CHARACTERIZING RADIO EMISSION FROM EXTENSIVE AIR SHOWERS WITH THE SLAC-T510 EXPERIMENT, WITH APPLICATIONS TO ANITA

by

Katharine B. Mulrey

A dissertation submitted to the Faculty of the University of Delaware in partial fulfillment of the requirements for the degree of Doctor of Philosophy in Physics

Winter 2018

CHARACTERIZING RADIO EMISSION FROM EXTENSIVE AIR SHOWERS WITH THE SLAC-T510 EXPERIMENT, WITH APPLICATIONS TO ANITA

by

Katharine B. Mulrey

Approved: ______________________________
Edmund R. Nowak, Ph.D.
Chair of the Department of Physics and Astronomy

Approved: ______________________________
George H. Watson, Ph.D.
Dean of the College of Arts and Sciences

Approved: ______________________________
Ann L. Ardis, Ph.D.
Senior Vice Provost for Graduate and Professional Education

I certify that I have read this dissertation and that in my opinion it meets the academic and professional standard required by the University as a dissertation for the degree of Doctor of Philosophy.

Signed: ______________________________

David Seckel, Ph.D.
Professor in charge of dissertation

I certify that I have read this dissertation and that in my opinion it meets the academic and professional standard required by the University as a dissertation for the degree of Doctor of Philosophy.

Signed: ______________________________

Konstantin Belov, Ph.D
Member of dissertation committee

I certify that I have read this dissertation and that in my opinion it meets the academic and professional standard required by the University as a dissertation for the degree of Doctor of Philosophy.

Signed: ______________________________

John Clem, Ph.D.
Member of dissertation committee

I certify that I have read this dissertation and that in my opinion it meets the academic and professional standard required by the University as a dissertation for the degree of Doctor of Philosophy.

Signed: ______________________________

Thomas K. Gaisser, Ph.D
Member of dissertation committee

ACKNOWLEDGEMENTS

I would like to thank my advisor, David Seckel, who has been a source of advice and creativity throughout my years at the University of Delaware, and who encouraged me to join exciting experiments that took me all over the world. Thanks also go to John Clem, who helped me navigate my way though the hardware side of my research.

To the SLAC T-510 collaboration, thanks for the opportunity to participate in the project where I had my first real foray into experimental physics. I am especially grateful to Anne Zilles, with whom I spent many hours pouring over details of the experiment, and Stephanie Wissel, who was a friend and guide throughout the analysis process.

Many thanks to the ANITA collaboration, especially to Peter Gorham, for helping me get involved in the experiment right away. The crew in Hawaii, especially Christian Miki, Brian Hill, Harm Schoorlemmer, Ben Rotter and Jarred Roberts, welcomed me and taught me so much about both the hardware and theory components of the ANITA experiment. Special thanks to Ben Strutt, with whom I first learned how to solder cables.

I would also like to thank my friends at the University of Delaware who made my time there very enjoyable, particularly my 306 officemates. Thanks also to my wonderful family who gave me lots of support throughout the years and enthusiastically listened to stories about my adventures in physics.

TABLE OF CONTENTS

LIST OF TABLES . . . . **x**
LIST OF FIGURES . . . . **xi**
ABSTRACT . . . . **xxi**

Chapter

1 INTRODUCTION **1**

2 HIGH ENERGY COSMIC RAYS AND NEUTRINOS **5**

2.1 Introduction 5
2.2 Brief History of Cosmic Ray and Neutrino Detection 6

2.2.1 Cosmic Ray Detection 6
2.2.2 Neutrino Detection 7

2.3 Cosmic Rays 8

2.3.1 Spectra and Composition 8
2.3.2 Sources and Acceleration 13
2.3.3 Propagation in the Galaxy 19
2.3.4 Propagation in the Cosmos 20
2.3.5 Detection 21

2.3.5.1 Direct Detection 21
2.3.5.2 Indirect Measurement 22

2.4 Neutrinos 24

2.4.1 Production 24
2.4.2 Interactions 25
2.4.3 Oscillations 26

2.4.4 Sources and Spectrum . . . 27

2.4.4.1 Solar Neutrinos . . . 28
2.4.4.2 Atmospheric Neutrinos . . . 30
2.4.4.3 Astrophysical Neutrinos . . . 31
2.4.4.4 Cosmogenic Neutrinos . . . 32

2.4.5 Detection . . . 33

3 HISTORY OF RADIO DETECTION OF COSMIC RAYS AND NEUTRINOS . . . 36

3.1 Introduction . . . 36
3.2 Early Radio Efforts . . . 36
3.3 Modern Efforts . . . 38
3.4 SLAC Radio Development . . . 40

3.4.1 Askaryan Radiation in Silica Sand . . . 40
3.4.2 Askaryan Radiation in Rock Salt . . . 43
3.4.3 Askaryan Radiation in Ice . . . 45

3.5 ANITA . . . 47
3.6 Ground Based Radio Efforts . . . 52

3.6.1 Cosmic Ray Air Shower Detection . . . 53

3.6.1.1 LOPES . . . 53
3.6.1.2 CODALEMA . . . 54
3.6.1.3 LOFAR . . . 54
3.6.1.4 AERA . . . 55
3.6.1.5 Tunka-Rex . . . 55

3.6.2 Detection of Cascades in Solid Media . . . 56

3.6.2.1 ARA . . . 56
3.6.2.2 ARIANNA . . . 56
3.6.2.3 Lunar Techniques . . . 57

4 PRODUCTION OF RADIO EMISSION FROM AIR SHOWERS . . . 58

4.1 Introduction . . . 58

4.2 Particle Cascades 60

4.2.1 Electromagnetic Cascades 62
4.2.2 Hadronic Cascades 64
4.2.3 Cascades in Dense Media 65

4.3 Radio Emission from Particle Cascades 66

4.3.1 Calculation of the Electric Field 69
4.3.2 Askaryan Emission 73
4.3.3 Geomagnetic Emission 74

4.4 Simulations 75

4.4.1 Monte Carlo Simulation Packages 76
4.4.2 Detector Simulations 77
4.4.3 Particle Level Radio Emission Simulations 78
4.4.4 SLAC T-510 Simulations 79

5 SLAC EXPERIMENTAL SETUP 81

5.1 Introduction 81
5.2 Experimental Design 81
5.3 SLAC Facility 84
5.4 Beam 85

5.4.1 Integrating Current Transformer 85
5.4.2 Collimator 86

5.5 Target 87
5.6 Antenna Set-Up 90
5.7 Signal Path Calibration 92
5.8 Trigger and Data Collection 93
5.9 Magnetic Field 95
5.10 Runs and Antenna Geometry 98

6 SLAC ANALYSIS 100

6.1 Introduction 100
6.2 Electric Field Simulations 101

6.2.1 Simulation Formalism 101
6.2.2 Propagation 102

6.2.3 X_{max} . . . 106
6.2.4 Contributions From Different Segments of Target . . . 107
6.2.5 Comparing Formalisms . . . 114

6.3 Convolving the Simulated Electric Field with the System Response . 116

6.3.1 End-to-End System Response . . . 118

6.4 T-510 Data . . . 120

6.4.1 Systematic Uncertainties . . . 121

6.5 Results . . . 123

6.5.1 Comparing Simulation and Data . . . 123
6.5.2 Mapping the Radiation Pattern . . . 125
6.5.3 Magnetic Effects . . . 128
6.5.4 Reflections . . . 130
6.5.5 Wavefront . . . 141

6.6 Conclusions . . . 142

7 ANITA 3 . . . 144

7.1 Introduction . . . 144
7.2 ANITA 3 Concept . . . 144
7.3 ANITA Gondola . . . 145
7.4 RF Signal Chain . . . 148

7.4.1 Seavey Antennas . . . 148
7.4.2 ANITA Instrument Box . . . 150
7.4.3 Sampling and Data Acquisition . . . 156
7.4.4 Trigger System . . . 156

7.5 Flight Software . . . 158
7.6 GPS and Positioning . . . 158
7.7 Power System . . . 159
7.8 Communication Systems . . . 159
7.9 Data Viewing Software . . . 160
7.10 System Calibration and Testing . . . 161

7.10.1 EMI Testing . . . 161
7.10.2 Instrument Calibration . . . 162

7.10.3 Ground Pulsers 163
7.10.4 HiCal 164

7.11 Analysis and Simulation 165
7.12 2015 Flight 167

8 ANITA CONTRIBUTIONS 169

8.1 Introduction 169
8.2 GPS Calibrations 169
8.3 SHORTs 171

8.3.1 Hardware Adjustments 171
8.3.2 Tunnel Diode Gains and Range of Operation 174

8.4 Temperature Sensors 176
8.5 ANITA 3 Integration and Campaign 178

9 SUMMARY 180

Appendix

A ACRONYM GUIDE 183
B T-510 RUN INFORMATION 187
C CALCULATION OF ANTENNA RESPONSE 191

C.1 Derivation 191
C.2 Seavey Data 193

D REFLECTION MEASUREMENT 195
E REFLECTIONS FROM THE BACK OF THE TARGET 198
F VHF DATA 201
G GLOBAL POSITIONING SYSTEM OPERATIONS 203

LIST OF TABLES

6.1 Summary of systematic uncertainties in the T-510 data. 122

6.2 Summary of systematic uncertainties in the T-510 simulations. . . . 123

B.1 T-510 Run Geometry for Seavey Antennas. 188

B.2 T-510 Run Geometry for Vpol Bicone antennas. 188

B.3 T-510 Run Geometry for Hpol Bicone antennas. 189

B.4 T-510 Run Geometry for Vpol LPDA antennas. 189

B.5 T-510 Run Geometry for Hpol LPDA antennas. 190

LIST OF FIGURES

2.1 Cosmic Ray Spectrum [64], updated in [65]. 9

2.2 Relative abundances of galactic cosmic ray composition with energies up to 0.5 GeV/nucleon [70] [71][72]. 11

2.3 Cosmic ray energy spectrum above the knee [73]. 12

2.4 Xmax as a function of energy [79]. 13

2.5 The Hillas Plot gives potential sources of cosmic rays. Above the diagonal lines are possible sources for Fe at 100 EeV, protons at 100 EeV, and protons at 1 ZeV [83]. 15

2.6 First order (left) and second order (right) Fermi Acceleration [88]. . 18

2.7 A schematic of the region in which cosmic rays diffuse in the galaxy [96]. 19

2.8 Flux of neutrinos over the full energy spectrum [122]. 28

2.9 Solar Neutrino Spectrum [123]. Solid lines represent spectra from the *pp* chain, and dashed lines represent spectra from reactions with carbon, nitrogen, and oxygen isotopes. 29

2.10 UHE neutrino limits set by various experiments [135]. 33

2.11 A PeV neutrino event detected by IceCube. Each point represents an optical detector. The size of the point shows the strength of the signal and the color indicates the detection time with red being earlier [141]. 34

3.1 Portrait of Gurgen Askaryan 37

3.2 Experimental set up for the 2000 SLAC run designed to measure Askaryan radiation in silica sand [25]. 41

3.3 Askaryan pulse measured in the 2000 SLAC run [25]. 42

3.4 Image of the 2002 SLAC run to measure Askaryan radiation in salt, a natural medium that could provide a viable experiment target [26]. 43

3.5 The measured amplitude of RF pulse is shown as a blue square. The normalized predicted strength of emission (based on the lateral and longitudinal particle distribution predicted by EGS) is shown as a solid line [26]. 44

3.6 Askaryan pulse due to excess charge in the particle shower as a function of cascade energy [26]. 45

3.7 Schematic of the 2006 SLAC experiment designed to detect Askaryan radiation in ice using the ANITA instrument as a detection tool [27]. 46

3.8 Top: Impulse response of the ANITA experiment, raw and partially-deconvolved. Bottom: Pulse observed near the peak of the Cherenkov cone, raw and partially-deconvolved. The deconvolution process removes ringing in the signal caused by filters in the signal chain [27]. 46

3.9 Experimental results for field strength as a function of frequency and radiated Cherenkov power as a function of shower energy [27]. . . . 47

3.10 Diagram of the ANITA concept. A neutrino interacts in Antarctica ice. ANITA's radio array detects Askaryan radiation [166]. 48

3.11 Left: Antarctic ice attenuation at 0.6 GHz [167]. Right: Attenuation length as a function of radio frequency, as measured at the South Pole [168]. 49

3.12 Neutrino flux limits set by ANITA 1 and ANITA 2 flights [23]. . . . 51

3.13 Results of the energy estimation for the 14 reflected cosmic ray events from the ANITA 2 flight [22]. 52

3.14 Overhead view of the Superterp at the LOFAR Radio Telescope [178]. 55

3.15 ARA detector based at South Pole Station [14]. 56

4.1 Example of a particle cascade induced by a primary cosmic ray [184]. 61

4.2 Modeled geometry of a high energy particle cascade. The charge excess is treated as a thin pancake with a width $\delta(z' - vt')$ [196]. . . 68

4.3 Frequency spectrum of the electric field amplitude for observation angles on and off the Cherenkov cone for a 10 TeV electromagnetic shower in ice. Details of the simulation are discussed in Section 4.4 [156]. 72

4.4 Simulated lateral distribution of electric field amplitude using ZHAireS and CoREAS compared with AERA data [208][209]. . . . 79

5.1 Schematic of the SLAC T-510 experiment (not to scale) [28]. 82

5.2 Overhead view of the SLAC End Station A Facility. The red line indicates the beam path and End Station A is circled in blue. . . . 84

5.3 Integrating Current Transformer used to calibrate beam charge during T-510 run. 86

5.4 Charge Measured by the Integrating Current Transformer with the collimator (1 cm opening, in black) and without the collimator (10 cm opening, in red). The beam charge was found to be more consistent with wide collimator gates. 87

5.5 Detailed diagram of the T-510 target. Not pictured, but important to the experiment was a 0.6 cm thick radio frequency absorbing mat placed beneath the target. A plywood support was beneath both the mat and the target. The Cherenkov and refracted Cherenkov angles θ_c and $\theta_{c,r}$ are given for n=1.53. 88

5.6 T-510 target in situ as it was during the experiment. The HDPE bricks sit above coil magnets, cooled by water via the orange tubing. 89

5.7 Internal view of the target taken after the second T-510 run. Radiation burn from the particle cascade can be seen. 90

5.8 Antenna measurements and geometry. Far left: Seavey antennas mounted in a vertical array. Center: Mounting geometry of Bicones and LPDAs. Right: Antenna mount dimensions. Measurements of the antenna array heights were made with reference to the floor of End Station A. Antenna positions described in Appendix B give the position of the antenna faces with reference to the coordinate system with y=0 at the front of the target and z=0 at beam height. 91

5.9 Polarizations of Askaryan and magnetically induced radiations. The red line shows the position of the Cherenkov cone. The green arrows show the radial polarization of the Askaryan radiation, and the blue arrows show the horizontal polarization of the magnetically induced radiation. 92

5.10 Geometry of the S-Band antenna triggering system. The antenna captured transition radiation generated as the beam left the beam pipe. 94

5.11 Linearity between the ICT charge and signal seen by a monitoring S-band antenna. 95

5.12 Overhead view of magnetic coils underneath the target. The water cooling system is in place, as seen by the orange tubing. 96

5.13 The magnetic field linearity, as controlled by current applied to the magnetic coils. 97

5.14 The measured magnetic field at the beam height along the vertical (z), longitudinal (y), and transverse (x) axes for a current of 2000A. 98

6.1 Fresnel Coefficient used in SLAC simulations. 104

6.2 Peak amplitude of the electric field for a 2D antenna array in an observer plane 1300 cm from the front of the target, as found using the endpoint formalism. The magnetic field has a maximum strength 970G. Left: total electric field. Center: horizontally polarized component. Right: vertically polarized component. The T-510 antenna closest to the peak of the radiation pattern is located at x=0 m, y=6.52 m in this coordinate system. The electric field is filtered to 200-1200 MHz, the T-510 bandwidth. 105

6.3 Position of maximum particle density from simulations. Plot by Andres Romero-Wolf. 106

6.4 Left: Ray tracing diagram of the emission on the Cherenkov angle arriving at antennas. Right: The emission point, relative to the beginning of the target, corresponding to different antenna heights. 107

6.5 Electric field contributions from different segments of the target. Vertical polarization is on the top and horizontal is on the bottom. The antenna height is 652 cm above the beam, which corresponds to the point of maximum radiation. The time t=0 refers to time the beam enters the target [214]. 108

6.6 Electric field contributions from different segments of the target, filtered to 200-1200 MHz using a software Butterworth filter [217]. Vertical polarization is on the top and horizontal is on the bottom. The antenna height is 652 cm above the beam, which corresponds to the point of maximum radiation. 109

6.7 Electric field contributions from different segments of the first 50 cm of the target at an antenna height of 319 cm. Vertical polarization is on the top and horizontal is on the bottom. 111

6.8 Electric field contributions from different segments of the first 50 cm of the target at an antenna height of 652 cm. Vertical polarization is on the top and horizontal is on the bottom. 112

6.9 Electric field contributions from different segments of the first 50 cm of the target at an antenna height of 747 cm. Vertical polarization is on the top and horizontal is on the bottom. 113

6.10 Electric field contributions from different segments of the first 50 cm of the target at an antenna height of 935 cm. Vertical polarization is on the top and horizontal is on the bottom. 114

6.11 Ratio in peak amplitude of total electric field in time domain for a 2D antenna array defined as $\frac{E_{ZHS}-E_{endpoint}}{E_{ZHS}}$: Left: difference in total electric field; Center: difference in horizontally polarized component; Right: difference in vertically polarized component [219]. 115

6.12 Comparison of ZHS and endpoint formalisms for a single antenna position 6 meters above the beam in the time domain (left) and frequency domain (right). The electric field is filtered to 200-1200 MHz using a software filter. 116

6.13 Schematic of T-510 electric field to voltage convolution. 117

6.14 Measured cable and filter losses for each channel. 118

6.15 Raw electric field from endpoint formalism at position (0,1329,747) cm from the beginning of the target. 119

6.16 Antenna response, which is applied in the frequency domain, but data is stored in the time domain. 119

6.17 Left: Simulated electric field. Right: Electric field convolved with the system response, resulting in the simulated voltage at the oscilloscope. The time base for the left panel is relative to the start of the simulation. The time base for the right panel is arbitrary. . . . 120

6.18 Top: Waveforms for horizontally polarized data and simulation at an antenna position of 652 cm, which is close to the point of peak field intensity, and B=970 G. Bottom: Power spectra of the same data. . 124

6.19 Top: Waveforms for vertically polarized data and simulation at an antenna position of 652 cm, which is close to the point of peak field intensity, and B=970 G. Bottom: Power spectra of the same data. . 125

6.20 Radiation is mapped by peak amplitude of the signal. Left: Vertical and horizontal polarizations in the case B=0 G. Right: Vertical and horizontal polarizations in the case B=970 G. Note, the antenna heights referenced on the x-axis do not all lie at the same distance from the target, but are offset as seen in Figure 6.4. 126

6.21 The radiation pattern is mapped by peak amplitude of the signal, normalized by maximum amplitude. 127

6.22 Power for horizontally polarized signals (B=970 G), for frequency bands 300-600 MHz, 600-900 MHz, and 900-1200 MHz, as a function of antenna height. Each profile is normalized by total power. 128

6.23 Power for vertically polarized signals (B=970 G), for frequency bands 300-600 MHz, 600-900 MHz, and 900-1200 MHz, as a function of antenna height. Each profile is normalized by total power. 128

6.24 Horizontally polarized data and simulations for magnetic field strengths of ±970,±730,±490,±240 G, and at antenna position of 652 cm above beam height. 129

6.25 The ratio of horizontally polarized signal to vertically polarized signal is shown for the antenna at 652 cm. The dashed line is the simulated ratio, and the black line is the linear fit to measured data. 130

6.26 Reflections seen in SLAC data. Black points represent antenna positions. This diagram shows reflections that land in the antenna at 652 cm above beam height. The primary signal is shown in blue, the first reflection in green, and second and third reflections in yellow and red. 131

6.27 Horizontal signal at B=970 at a position of 652 cm above the beam height. The blue line indicates the measured signal. The green line indicates the simulation, and the orange line indicates the simulation with the addition of the first reflection. 133

6.28 Vertical signal at B=970 at a position of 652 cm above the beam height. The blue line indicates the measured signal. The green line indicates the simulation, and the orange line indicates the simulation with the addition of the first reflection, $\sim$ 1 ns delayed from the primary signal, inverted with a reflection coefficient of 1.0 at the mat. 134

6.29 Radiation pattern mapped by peak amplitude of signal. Amplitudes are shown for data (blue), simulation (orange), and simulation corrected for the first reflection (green). Left: horizontally polarized data with magnetic field B=970 G. Right: vertically polarized data with magnetic field B=970 G. 136

6.30 Power for horizontally polarized signals (B=970 G), for frequency bands 300-600 MHz, 600-900 MHz, and 900-1200 MHz, as a function of antenna height. Each profile is normalized its total power. 137

6.31 Power for vertically polarized signals (B=970 G), for frequency bands 300-600 MHz, 600-900 MHz, and 900-1200 MHz, as a function of antenna height. Each profile is normalized by its total power. . . . 137

6.32 The ratio of horizontally polarized signal to vertically polarized signal is shown for the antenna at 652 cm. The dashed line is the simulated ratio without reflection, and the black line is the linear fit to measured data, and the green crosses indicate the simulation with the first reflection added. 138

6.33 Horizontal signal at B=970 G at a position of 652 cm above the beam height. The blue line indicates the measured signal. The green line indicates the simulation. The orange line indicates the simulation with the addition of the first reflection, and the red line indicates the addition of the second and third reflections. 140

6.34 Vertical signal at B=970 G at a position of 652 cm above the beam height. The blue line indicates the measured signal. The green line indicates the simulation. The orange line indicates the simulation with the addition of the first reflection, and the red line indicates the addition of the second and third reflections. 141

6.35 Relative arrival times of horizontally (blue) and vertically (red) polarized signals for different antenna positions. 142

7.1 Fully assembled ANITA 3 gondola at the hang test in Palestine, TX. 146

7.2 Layout of the ANITA 3 payload. 147

7.3 Seavey antenna beam pattern. Antenna gain is measured for each antenna of each ANITA flight, but anechoic chamber beam pattern measurements were only made for ANITA 1 [223]. 149

7.4 Seavey antenna gain for ANITA 1 antennas [223]. 149

7.5 Effective height measured for Seavey antennas for ANITA 1, also used for the T-510 experiment [223]. 150

7.6 ANITA 3 signal chain. Radio signal enters AMPAs directly after going through Seavey antennas. 151

7.7 Internal Radio Frequency Conditioning Module in production. . . . 152

7.8 SHORT boards mounted on the lid of the instrument box. Photo by Ryan Hupe. 153

7.9 AMPA responses, measured in Palestine. 154

7.10 iRFCM responses, measured in Palestine. 155

7.11 Inside of the instrument box. 155

7.12 Trigger efficiency, as measured at LDB. 158

7.13 RF shield testing inside a EMI-shielded tent. Both the ANITA instrument box and the CSBF SIP were tested. Photo by David Saltzsberg. 161

7.14 Callibration schematic as set up at the LDB facility. 163

7.15 ANITA ground pulser system at LDB. Here LDB Payload 2 refers to a position of the ANITA instrument when it was taken outside the hanger. 164

7.16 HiCal instrument, flown shortly after ANITA launched, with builders Jessica and Mark Stockham. 165

7.17 ANITA 3 launch on December 17, 2014. 167

7.18 Trajectory of ANITA 3 flight. 168

8.1 Multipath interference created by the difference of the path length between the direct signal and the reflected signal [225]. 170

8.2 SHORT boards before alteration. The circled resistors were removed, and the existing signal chain was broken to avoid signal contamination. 172

8.3 SHORT boards after alteration. The circled resistors were removed, and the existing signal chain was broken to avoid signal contamination. 173

8.4 Sample SHORT S11 measurement. Substantial power is not lost in the w.fl cable over the relevant frequency band. 174

8.5 SHORT testing setup. 175

8.6 SHORT SNR response. 176

8.7 SHORT output RMS compared to the input RMS, used to determine proper operating range. 177

8.8 Temperature sensor for ANITA. 178

B.1 Measuring the antenna positions. 187

C.1 Experimental Setup for Seavey Effective Height measurements taken at UH. 193

C.2 Transmitted pulse from Seavey antenna, used to calculate antenna response. 194

C.3 Received pulse from Seavey antenna, used to calculate antenna response. 194

D.1 Schematic of the reflection measurement set up (S. Wissel). 196

D.2 Horizontally polarized reflection measurement signals. The blue line indicates the signal without absorber, and the green with absorber (C. Paciaroni and S. Wissel). 197

E.1 Close up view of back reflections within the target. Dark colors indicate a direct path, and light indicate reflected paths. 199

E.2 Reflections from the back of the target seen in SLAC data. Black points represent antenna positions. Different color trajectories represent different paths emission can take to the antennas. Dark colors indicate a direct path, and light indicate reflected paths. 200

F.1 VHF waveform (left) and power spectrum (right) for antennas at 662 cm for Vpol and 678 cm for Hpol, B=970 G. Vertically polarized data is shown in red and horizontally polarized in blue. 201

F.2 Mapping of the Cherenkov cone with VHF antennas, with B=970 G. 0° is at the peak of the radiation pattern. Vertically polarized data is shown in red and horizontally polarized in blue. 202

ABSTRACT

Neutrino and cosmic ray astronomy allow scientists to gather information about the highest energy processes in the universe. However, since cosmic rays are charged nuclei moving in astrophysical magnetic fields, it has not been possible to determine their sources by studying their arrival directions. A pointed neutrino flux is expected at such energies, either direct from the sources or due to the GZK process, where high energy cosmic rays interact with cosmic microwave photons as they travel through the universe. Detection methods make use of particle cascades initiated by these high energy primaries. In particular, the electromagnetic radiation in radio frequencies generated by particle cascades is a powerful tool. Particle cascades emit radiation by the Askaryan process, where a charge excess in the cascade emits coherently. In the presence of a magnetic field, a transverse current develops which also emits coherently in the radio regime. Theoretical models describe this radiation and are widely used to reconstruct the energy, geometry, and composition of observed events. Therefore, understanding and validating models describing this radiation is of great importance to neutrino and cosmic ray astronomy.

The SLAC T-510 beam test is the first experiment to produce a particle cascade in a controlled setting in the presence of a magnetic field. Radio-frequency (RF) emission is collected in the region of the Cherenkov cone in two polarizations designed to separately capture Askaryan and magnetically induced radiation. Field intensity, linearity with magnetic field, and spectral content are compared to particle-level simulations. The data provide experimental evidence supporting theoretical models, and show the first laboratory results of the scaling of the radiative strength with the magnetic field.

SLAC T-510 grew out of a need to calibrate the sensitivity of the ANITA (Antarctic Impulsive Transient Antenna) experiment to cosmic ray air showers. ANITA uses radio techniques to detect the highest energy neutrinos and cosmic rays. An array of broadband antennas flies over Antarctica looking for signals from neutrinos interacting in ice and cosmic rays interacting in the atmosphere. The ANITA 3 flight took place in the austral summer of 2014-2015.

In this dissertation I describe the SLAC T-510 experiment and results, as well as preparation and flight from the 2014 ANITA 3 campaign.

Chapter 1

INTRODUCTION

Scientists learn about the extraterrestrial world by collecting electromagnetic radiation and cosmic particles that are incident on the Earth. The field of astronomy started when humans collected light from celestial objects and began mapping the night sky visible to the naked eye. In the last century new technologies have made it possible to collect photons from different frequencies, including the gamma-ray, radio, x-ray, and microwave regimes. The field of astroparticle physics developed simultaneously, with the discovery of cosmic rays in 1912 [1] and the first detection of solar neutrinos in the 1960s [2]. Gravitational waves due to extragalactic black hole mergers have recently been detected [3]. The combination of multiple observables allows scientists to paint a fuller picture of the universe.

Ultra high energy (10^{18} eV) cosmic rays and neutrinos are the most energetic particles known to man. Ultra high energy cosmic rays (UHECR) are believed to be accelerated in the most energetic events and structures in the universe, including black holes at the center of active galactic nuclei, neutron stars, and gamma ray bursts. Shock waves from magnetic field fronts transfer energy to particles as they move through turbulent sources. High energy neutrinos can come from the same events, and they can also be produced as byproducts of cosmic ray interactions. Questions about the origins, acceleration mechanisms, and propagation of high energy particles drive the field of high energy astrophysics [4].

Determining the sources of cosmic ray primaries is difficult because they are charged particles and lose directional information while propagating. Neutrinos, on the other hand, provide directional information about their sources. They are not charged and their paths are not distorted in the intergalactic magnetic fields. This means they point back to their origins without disruption, giving information about high energy accelerators. Furthermore, when UHECRs interact with cosmic microwave background photons, they produce neutrinos. These "cosmogenic" neutrinos can also give us information about origins of these cosmic rays, as the gyroradius of an UHECR is large and the position and direction of the cosmic ray at the interaction point may still give information about its origin [5][6].

UHE particles are scarce, and therefore detecting these particles directly is not effective on reasonable time scales. When cosmic rays enter the Earth's atmosphere they interact, creating particle cascades. Cascades are detected in a number of different ways. For direct secondary particle detection, particle detectors can be placed in a grid on the surface of the Earth to capture muons and other particles generated by the shower. Ionizing energy loss leading to fluorescence radiation and direct radiation by relativistic cascade particles both allow for remote detection of the cascades by radio and optical methods.

Radio techniques have proven to be effective for detecting cascades induced by UHE particles. Predicted by Gurgen Askaryan in the 1960s [7], Askaryan radiation is generated from a charge excess that forms as a particle cascade develops in a medium. Like Cherenkov radiation, Askaryan radiation forms a specific pattern that can be seen by detectors. Askaryan also noted that radiation should be generated due to the movement of charged cascade particles in the Earth's magnetic field. Radio emission from cosmic ray air showers was observed by Jelley et al. as early as the 1960s [8], however this observing method was not widely used until digital techniques became available decades later. Several modern experiments aim to exploit this radio emission from atmospheric air showers, including as the Pierre Auger Observatory [9], LOPES [10], CODALEMA [11], and LOFAR [12].

Neutrinos are more likely to interact in dense media and generate cascades that emit primarily Askaryan radiation. Experiments searching for neutrino induced Askaryan radiation in Antarctic ice include RICE [13], ARA [14], ARIANNA [15], and

ANTIA [16]. Experiments also utilize other large volumes of uniform material, including the lunar regolith (Parkes [17], Goldstone [18], VLA [19], and Westerbork [20]), and salt mines (SalSA [21]).

The ANITA (ANtarctic Impulsive Transient Antenna) experiment is unique in that it uses radio emission to detect both neutrinos interacting in the Antarctic ice and cosmic rays interacting in the atmosphere [22]. Askaryan radiation is present in both situations and is dominant for neutrino induced cascades in ice, whereas magnetically induced radiation is dominant in air showers, and is most useful for detecting cosmic rays. Three ANITA instruments have flown, in the austral summers of 2006, 2008, and 2014. No neutrinos have been detected, but new limits for neutrino flux at high energies have been set [23]. ANITA 1 saw 16 UHE cosmic rays. ANITA 2 was optimized for neutrino detection and set new flux limits on neutrinos, while contributing an additional 4 cosmic ray events. ANITA 3 data is in the analysis stage.

The geomagnetic and Askaryan emission mechanisms for coherent RF radiation had been used to detect UHE particles in nature, however, simulations had not been validated by a controlled experiment. Although Askaryan radiation was qualitatively understood when it was first hypothesized, Monte Carlo simulation techniques were not available to validate predictions. The Zas Halzen Stanev (ZHS) formalism, developed in the early 1990's, was the first to use numerical methods to simulate neutrino induced Askaryan radiation in a dense medium [24]. In the 2000's it became clear that geomagnetic radio emission was also effective for detecting cosmic rays, although the emission mechanism wasn't well understood. Even as the first ANITA cosmic ray results were analyzed, no validated simulation package existed.

The Askaryan charge excess effect has been demonstrated in a lab setting in several SLAC runs [25][26][27], but magnetically induced effects had never been characterized in a controlled setting. The purpose of the SLAC T-510 experiment was to create a particle cascade in a lab setting and observe the resulting radiation. The experiment was designed to be compared to results from particle level simulation packages used in the reconstruction of UHE particle cascades [28].

This dissertation aims to provide a verification of simulation of radio emission from particle cascades and show their relevance to modern cosmic ray and neutrino astronomy. Two primary experiments I participated in are described. The SLAC T-510 experiment took place in January and February of 2014, and the ANITA 3 experiment took place during the austral summer of 2014-2015.

The dissertation begins with an overview of the current state of cosmic ray and neutrino physics. Chapter 2 gives a history of UHE particle detection, spectra, sources, acceleration mechanisms for the particles, and a description of the most recent flux measurements and experiments in operation. Chapter 3 introduces radio detection of UHE particles. Earlier SLAC and ANITA experiments are outlined. The final introductory chapter is Chapter 4, which describes particle cascades and the resulting radio emission, as well as first principle simulations that predict radio features of particle cascades.

The following two chapters (5 and 6) are about the SLAC T-510 experiment. The experimental controls, data runs, and technical information about the apparatus are explained. T-510 data analysis includes a careful understanding of simulations and experimental data, and the relationship between the two. Data analysis is explained and science results are presented.

The ANITA 3 experiment is then presented. ANITA 3 builds on the legacy of ANITA 1 and 2. Chapter 7 discusses the overall goals of ANITA and presents components of the experiment, including trigger methods, signal chain, and data acquisition. Chapter 8 speaks to my direct contributions to the ANITA 3 integration and campaign.

Finally, I draw the relation between the two experiments presented in the dissertation and discuss the impact of the results on the field of high energy astrophysics.

Chapter 2

HIGH ENERGY COSMIC RAYS AND NEUTRINOS

2.1 Introduction

The information we know about the universe travels to us via particles. Most familiar is the photon, which lets us view stars at night. However, there are many more particles that allow us to better understand the universe. Scientists have turned to searching for high energy cosmic messengers.

Cosmic rays are highly energetic charged particles that propagate through space from the sources that accelerate them. The cosmic ray energy spectrum spans more than twelve decades of energy above the sub-GeV region. Sources of cosmic rays from different parts of the energy spectrum vary widely, from local sources at the lower energies to exotic extragalactic sources at the other extreme. The energy spectrum shows interesting features that are associated with galactic to extragalactic source transitions. UHECRs (above 10^{18} eV) are thought to be extragalactic in origin [29].

Likewise, astrophysical neutrinos have different populations and sources. Hadronic sources of UHECRs are likely to produce neutrinos. UHE neutrinos can also be produced as a product of UHECR interacting with cosmic microwave background (CMB). Neutrino astronomy is particularly attractive because neutrinos are not charged, and therefore point back to their sources. They also travel from the interiors of their sources, whereas photons only provide information about the surface. They are, however, difficult to detect.

Basic high energy astroparticle physics is introduced in this chapter. A brief history of neutrino and cosmic ray detection is presented, followed by a discussion of the flux, composition, spectrum, acceleration, and propagation of cosmic rays and neutrinos. Recent and current UHE particle experiments are also reviewed.

2.2 Brief History of Cosmic Ray and Neutrino Detection

2.2.1 Cosmic Ray Detection

Victor Hess won the 1936 Nobel Prize for the discovery of cosmic radiation [1]. Physicists noticed that ionizing radiation was changing the results of their experiments. Records of electroscopes spontaneously discharging date back to Coulomb. To characterize the radiation, Hess travelled to a height of 5 km in a hot air balloon. He discovered that the rate of ionization actually increased with altitude, indicating that the radiation did not originate from Earth as previously thought. The name "cosmic ray" is a bit of a misnomer. It was first hypothesized that cosmic rays were gamma rays and the name stuck even after most cosmic rays were found to be low energy protons. Further studies of the cosmic ray phenomenon led to the discovery of positrons [30], muons, and other fundamental particles [31].

Cosmic ray astronomy advanced further in 1939 when Pierre Auger noticed two particle detectors he had set up in the Alps detected radiation in coincidence. This experiment opened up the study of Extensive Air Showers (EAS), which are created when cosmic rays interact with particles in the atmosphere [32].

In 1962 John Linsley used a particle detector array at the Volcano Ranch site in New Mexico to detect a 10^{20} eV cosmic ray, which was the highest energy particle detected at the time [33]. This detection led to the idea that the sources of UHECRs might be extragalactic. Once there were enough statistics at high energies, it became clear that the shape of the cosmic ray energy spectrum had notable features in the "knee" and "ankle" region, which correspond to 3 PeV and 3 EeV respectively [34].

Meanwhile, theoretical cosmic ray physics developed. In 1949 Enrico Fermi proposed the supernova shock acceleration model that explained how cosmic rays below the knee might reach their energies [35]. This acceleration mechanism, along with improved experimental composition data, led to the development of galactic propagation models and questions of galactic confinement [36]. A critical development was made in 1966 when Greisen, Zatsepin, and Kuzmin published papers limiting the energy of cosmic rays coming from distant sources (about 150 million light years) to 5×10^{19} eV, due to interaction with the CMB [5][6]. The "GZK" cutoff also predicts the presence of an UHE neutrino flux, which was realized by Stecker in 1968 [37] and Berezinsky and Zatsepin in 1969 [38].

In the early 1990s, the AGASA experiment claimed to see a cosmic ray spectrum continuing beyond the GZK cutoff. The HiRes experiment, which was complementary but had a longer exposure time, eventually reported a distinct suppression of cosmic rays at the highest energies. Although this discrepancy was ultimately attributed to calibration differences, it highlighted the importance of using large detectors that could measure the flux of UHECR at higher energies [39].

Current ground based detectors use multiple types of detection, including Cherenkov light, particle detectors, fluorescence, and recently, radio signals, to aid with calibration and increase the exposure of the experiment.

2.2.2 Neutrino Detection

In 1930 it was observed that in beta decay the resulting electron did not account for the total mass left after decay. Wolfgang Pauli famously penned a letter to a conference in Tubingen that hypothesized a 1/2 spin particle with very low mass [40]. Enrico Fermi named the particle and developed a theory for beta decay using the neutrino in 1933 [41]. Reines and Cowan finally detected the neutrino in the 1950s using inverse beta decay and a detector shielded from cosmic ray background [42]. In 1957 Bruno Pontecorvo predicted neutrino flavors [43]. The electron and muon neutrino were experimentally confirmed in 1962 at Brookhaven National Laboratory. The tau lepton, which led to the tau neutrino, was discovered at SLAC in 1975. The 1995 Nobel prize went to Martin L. Perl and Frederick Reines for these discoveries [44].

Neutrino astronomy started with the Homestake (Davis and Bahcall) experiment's detection of solar neutrinos in the late 1960s. A deficit of solar electron neutrinos was measured, which was not compatible with massless neutrino models [45]. This discrepancy was known as the "solar neutrino problem." Neutrino flavor oscillations provided a solution and were finally measured by both Kajita and McDonald who won the 2015 Nobel prize [46]. Around the same time as the first solar neutrinos were measured, the first atmospheric neutrinos were detected by both the Reines and Bombay-Osaka-Durham groups [47] [48]. Atmospheric neutrinos produced by cosmic rays in the Earth's atmosphere provide further information about neutrino masses that can't be determined from terrestrial accelerator experiments [49]. Low energy neutrinos ($\sim$ 10 MeV) from Supernova 1987a were observed simultaneously at the Kamiokande II [50], IMB [51], and Baksan [52] observatories, and marked the first time neutrinos from an supernova were detected. This discovery was important for the validation of supernova core collapse models [53]. Current experiments such as IceCube search for neutrinos from the high energy astrophysical processes. Cosmogenic neutrinos result from interactions of UHECRs with CMB and will yield information about the highest energy standard model interactions and sources of UHECRs [5][6].

2.3 Cosmic Rays

Cosmic rays are charged particles that are accelerated to high energies. The composition of the cosmic ray tells us about the make up of the particle's source and the energy tells us about the acceleration mechanism. Cosmic rays fall into two categories: galactic and extragalactic. The following subsections discuss the spectra and composition, sources, acceleration and propagation processes, and methods of detection for each class of cosmic ray.

2.3.1 Spectra and Composition

The cosmic ray energy spectrum spans 12 orders of magnitude above 1 GeV. Between 10^9 and 10^{15} eV the energy spectrum follows an $E^{-(\alpha+1)}$ power law where $\alpha = 1.7$. The spectrum steepens at the "knee" ($10^{15.5}$ eV) to $\alpha = 2.0$, and then softens at the "ankle" ($10^{18.5}$ eV). The spectrum falls off above 10^{20} eV. Figure 2.1 shows the measured energy spectrum from LEAP [54], Proton Satellite [55], Yakutsk ESA [56], Haverah Park [57], AGASA [58], Fly's Eye [59], HiRes [60], and Pierre Auger Observatory [61]. The changes in the energy spectrum are associated with changes of propagation and sources. Cosmic rays with energies below the ankle are thought to be galactic in origin. The shape of the spectrum below the knee can be described by nuclei accelerated in supernova remnants in the galaxy in Fermi acceleration processes [62], and the flux of observed cosmic rays at these energies can be accounted for with known supernova energy density in the Milky Way [63]. The transition of sources between the knee and the ankle is an ongoing area of research, and is discussed later in this section.

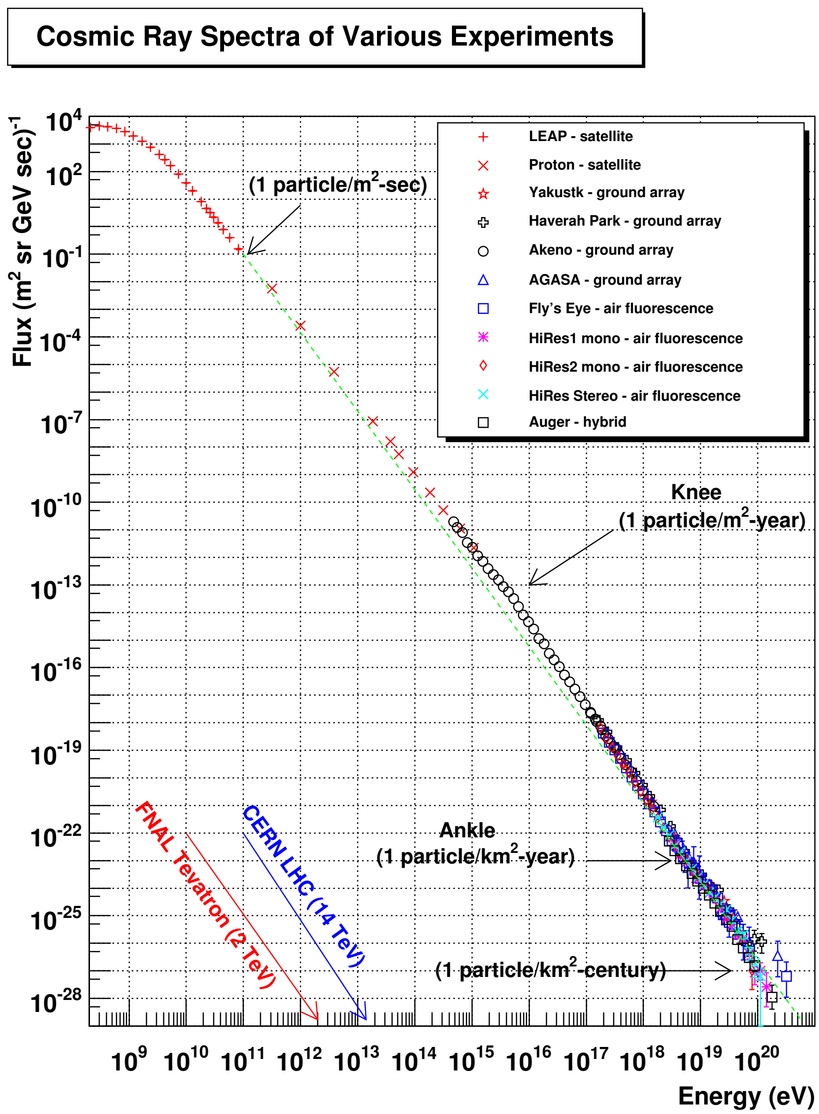

Figure 2.1: Cosmic Ray Spectrum [64], updated in [65].

The composition of cosmic rays well below the knee (with energies around one GeV / nucleon) is well known because direct detection is possible using balloons, spacecraft, and satellite based experiments. Closer to the knee, the question of secondary to primary ratios is not yet settled [66]. Figure 2.2 shows the relative abundances of galactic cosmic rays compared to abundances of chemicals in the solar system. Most notably, the cosmic ray abundances of Li, Be, and B are higher than the solar system abundances. This is due to cosmic ray interaction with interstellar media, or spallation, and supernova nucleosynthasis [67].

Mass density in the disk of the Milky Way galaxy is roughly 1 proton per cm^3. Cosmic rays are estimated to travel through about 5 g/cm^2 of material before diffusing out of the galaxy. Assuming the velocity is the speed of light, the average lifetime of a cosmic ray travelling through the galaxy is 3×10^6 years. Then a cosmic ray travelling at the speed of light will traverse the galactic disc, which is $\sim$ 30 kpc in diameter and $\sim$ 1 kpc thick, thousands of times before escaping [68].

The observed cosmic ray composition below the knee sheds light on the lifetime of cosmic rays travelling through the galaxy. For example, some nuclei have lifetimes that are less than the estimated travel times. Beryllium (^{9}Be) has a lifetime of 1.5×10^6 years. This supports Be being a product of cosmic ray spallation. The observed cosmic ray composition is commensurate with that idea, showing greater relative abundance of Be than lighter particles like Hydrogen and Helium when compared to solar atomic makeup [68] [69].

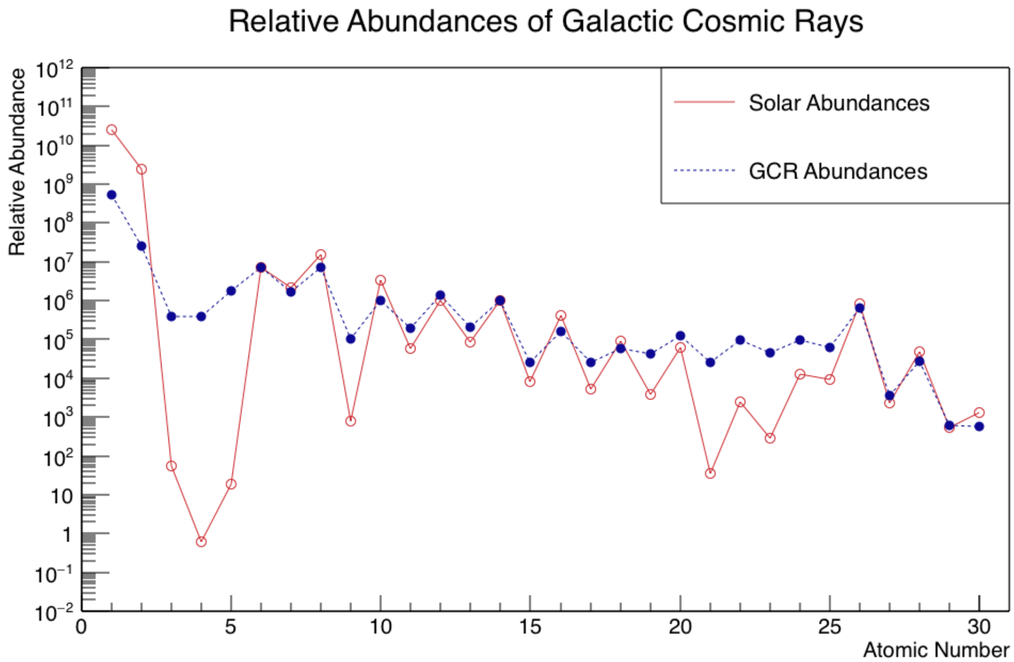

Figure 2.2: Relative abundances of galactic cosmic ray composition with energies up to 0.5 GeV/nucleon [70] [71][72].

At higher energies, composition becomes a more difficult question because the primary cosmic rays cannot be detected directly. Instead, features of the air showers created when a cosmic ray enters the atmosphere are measured with particle, Cherenkov, fluorescence, and radio detectors. Reconstructing the primary composition involves comparing experimental data with simulations. Simulations rely on hadronic interaction models, which have not been experimentally validated at these energies. The composition of high energy cosmic rays can be studied by measuring the depth of shower maximum in the extensive air shower (X_{max}) or by determining the ratio of muons to electromagnetic particles in the air shower.

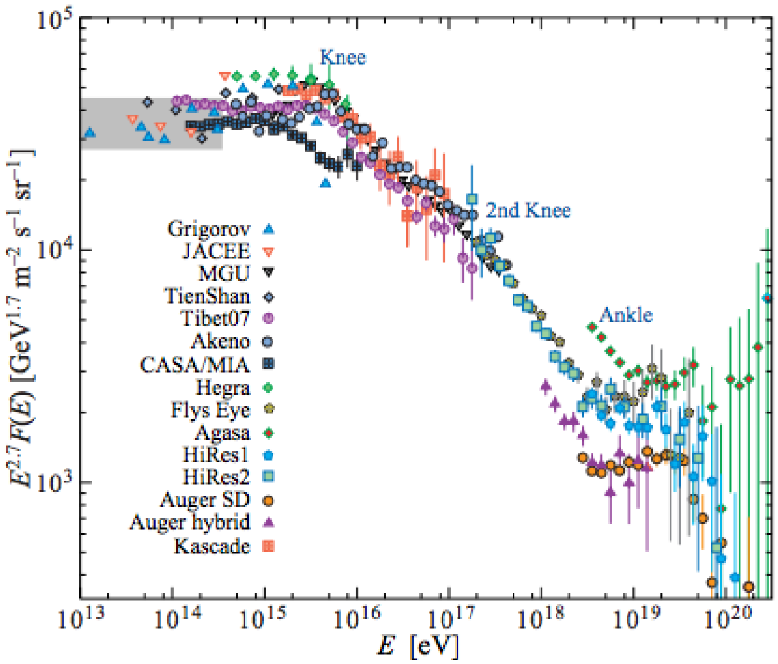

Figure 2.3: Cosmic ray energy spectrum above the knee [73].

There are different viewpoints about why the energy spectrum changes at the knee and ankle (see Figure 2.3). A transition between galactic and extragalactic sources may explain the shape and composition above 10^{15} eV. At high energies, cosmic rays can escape the magnetic confine of the galaxy. There are also distinct knees in the energy spectra of heavy and light cosmic rays [74]. This suggests a maximum energy of galactic accelerators, as the maximum energy a cosmic ray can reach is proportional to its atomic charge.

The 'dip' model explains the energy spectrum above the ankle using an extragalactic composition of only protons [75]. The ankle then would exist due to energy losses in proton propagation through the intergalactic medium [76]. A mixed composition model suggests that the composition of UHECRs is the same as that of galactic cosmic rays through the ankle. This model requires more acceleration sites or sites that can accelerate particles to a higher energy in the galaxy than are currently accounted for [77]. Finally, the ankle can be described using a steeply falling galactic composition on top of a flat extragalactic contribution. Again, this model requires higher energy acceleration sources in the galaxy. There is a sharp cutoff above 10^{20} eV that is attributed either to the GZK effect [78] or the maximum energy provided by accelerators, which is discussed later in this chapter.

Measurements of cosmic ray composition at high energies help constrain these models, as different models require different energy dependant compositions. Already, there is an observed trend from light to heavy composition in the knee region and heavy to light in the ankle region (Figure 2.4).

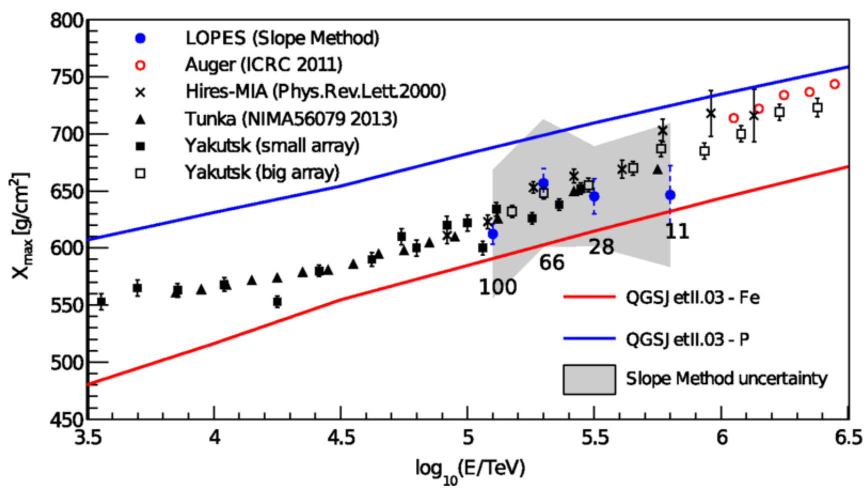

Figure 2.4: Xmax as a function of energy [79].

2.3.2 Sources and Acceleration

In this section we discuss sources and acceleration mechanisms for cosmic rays. Below the ankle, cosmic rays are accelerated in sites of large magnetic fields in the galaxy. Requirements for plausible acceleration sites are [80]:

- The particle must remain in the area of the acceleration mechanism during the acceleration process.
- The accelerator has to have enough power to accelerate particles to observed energies.
- The particle must gain more energy from acceleration than it loses from interacting with other particles.

- There must be a high enough density of acceleration sources in the galaxy to account for the flux of observed cosmic rays.

As the particle gains energy in the accelerator, its Larmour radius increases as

$$r_L = \sqrt{\frac{1}{4\pi\alpha}}\frac{E}{ZeB} = \frac{1.1}{Z}\left(\frac{E}{EeV}\right)\left(\frac{B}{\mu G}\right)^{-1}\text{kpc} \tag{2.1}$$

and so the maximum energy achievable is given by

$$E_{max} < Z\left(\frac{B}{\mu G}\right)\left(\frac{R_{source}}{kpc}\right) \times 10^9 \text{ GeV}. \tag{2.2}$$

Galactic cosmic rays are presumed to be accelerated in supernova remnants. These sites have strong magnetic fields necessary for containment and contain enough power to supply the observed cosmic ray flux below the knee [81]. However, it is more difficult to find possible sources for cosmic rays above 10^{18} eV, or UHECRs.

The Hillas plot (Figure 2.5) shows the magnetic field of acceleration sources plotted against the radius of the source to show possible accelerators for UHECRs. The actual capability of an accelerator also depends on it's lifetime. SNRs, for example, may only last for 10^4 years [82]. Using the Hillas criteria, SNRs are not viable sources for UHECRs. There are some galactic sources that do meet the criteria for EeV photons, such as white dwarf and neutron stars, however, most candidates are extragalactic.

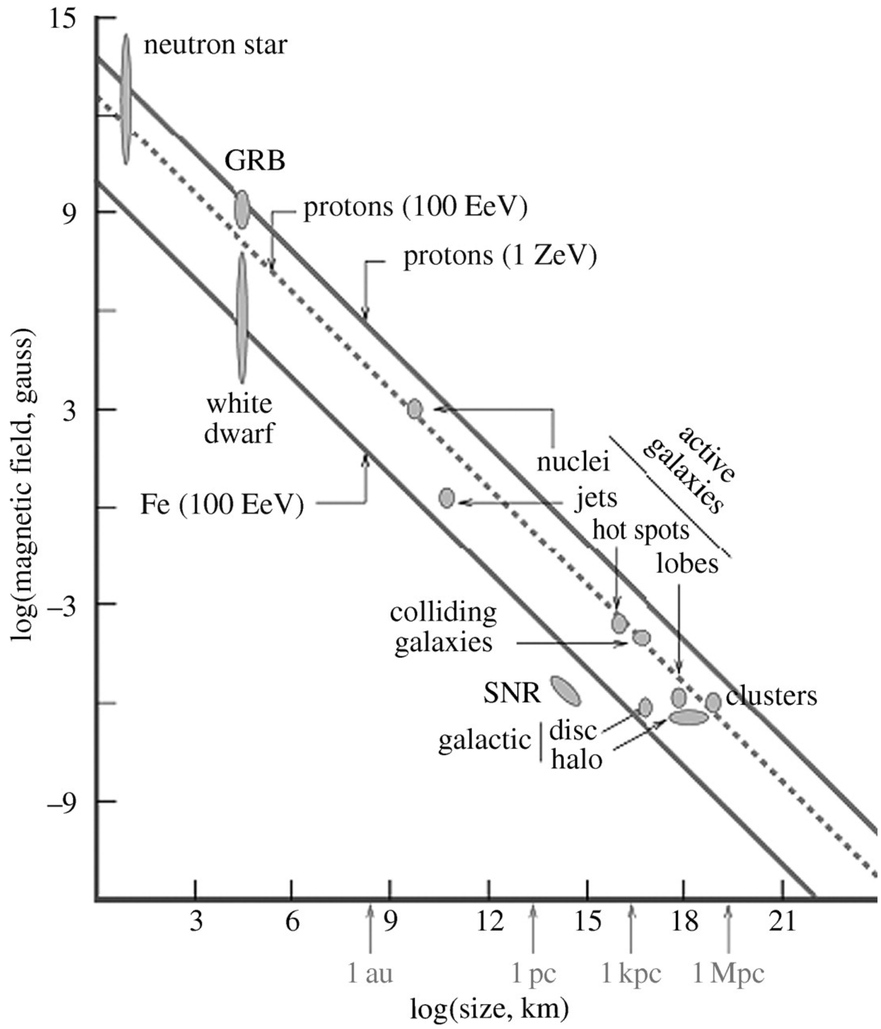

Figure 2.5: The Hillas Plot gives potential sources of cosmic rays. Above the diagonal lines are possible sources for Fe at 100 EeV, protons at 100 EeV, and protons at 1 ZeV [83].

Two potential extragalactic sources for UHECRs are active galactic nuclei (AGN) and gamma ray bursts (GRB). In an AGN, an accretion disc of cold material forms around a black hole. Jets of relativistic material can emerge from the disc and provide acceleration sites for cosmic rays. This method of injecting particles into acceleration sources to achieve high energies is know as the bottom up approach.

One can also take the “top down” approach, where UHECR are the products of interaction or decay of more exotic particles from the early universe. However, this approach has several problems [84]. Such objects have lifetimes that have to be adjusted ad-hoc so that they can produce the cosmic rays observed today. Also, top down models predict a higher flux of ν and γ than is observed.

For bottom up approaches, acceleration is assumed to take place in regions of high magnetic fields. Fermi posed first and second order models to describe the acceleration process [35]. Second order Fermi acceleration describes the interaction of charged particles with interstellar clouds, which can be thought of as magnetic mirrors [85]. The average change in energy per collision is given by

$$\left\langle \frac{\Delta E}{E} \right\rangle = \frac{8}{3}\left(\frac{v}{c}\right)^2 \tag{2.3}$$

where v is the velocity of the cloud and c is the velocity of the particle. The exponent is the reason for the name "second order Fermi acceleration." Given an average time between collisions dt and a mean free path L between magnetic clouds, the rate of energy gain is

$$\frac{dE}{dt} = \frac{4}{3}\left(\frac{v^2}{cL}\right) E = \alpha E. \tag{2.4}$$

Assuming a steady-state diffusion loss, the flux is then

$$N(E)dE = \text{constant} \times E^{1+\frac{1}{\alpha\tau_{esc}}} dE \tag{2.5}$$

where τ_{esc} is the time the particle is in the acceleration region. This produces a power law spectrum, but since magnetic cloud densities are low, energy gain is also low.

First order Fermi acceleration (or diffuse shock acceleration) takes place when particles cross magnetic shock waves. Particles generated in a supernova explosion have a certain starting energy, E_0. The particles encounter magnetic shock waves and gain energy $E = \beta E_0$ at each encounter. At each juncture, the probably that the particle remains in the acceleration region is P. (The energy dependence of P leads to the cutoff in the resulting spectrum, as particles of high enough energy cannot be contained by the accelerator and therefore are accelerated to a maximum energy.) There are then $N = N_0 P^n$ particles with energy $E = E_0 \beta^n$ after n collisions.

To eliminate n, we can take

$$\frac{\log(N/N_0)}{\log(E/E_0)} = \frac{\log(P)}{\log(\beta)} \tag{2.6}$$

and

$$\frac{N}{N_0} = \frac{E}{E_0}^{\frac{\log(P)}{\log(\beta)}}. \tag{2.7}$$

The differential flux is then

$$N(E)dE = \text{constant} \times E^{-1+\frac{\log(P)}{\log(\beta)}} \tag{2.8}$$

The average energy gain from a shock crossing is $\frac{2}{3}\frac{v}{c}$ [86], so the energy gain for particle passing through a shock and then back again is $\frac{4}{3}\frac{v}{c}$ and

$$\beta = 1 + \frac{4}{3}\frac{v}{c}. \tag{2.9}$$

Then $\log(\beta)$ can be approximated as

$$\log(\beta) \approx \frac{4}{3}\frac{v}{c} \tag{2.10}$$

The probability of the particle escaping the shock is $P_{esc} = \frac{4}{3}\frac{v}{c}$, so

$$P = 1 - \frac{4}{3}\frac{v}{c} \tag{2.11}$$

and $\log(P)$ can be approximated as

$$\log(P) \approx -\frac{4}{3}\frac{v}{c}. \tag{2.12}$$

Thus, first order Fermi acceleration gives a power law of

$$N(E)dE = \text{constant} \times E^{-2}dE \tag{2.13}$$

which does not quite produce the observed spectrum, but does have fixed exponent in the region of observed spectrum [87].

Figure 2.6 shows a schematic view of first order (left) and second order (right) Fermi accelerations.

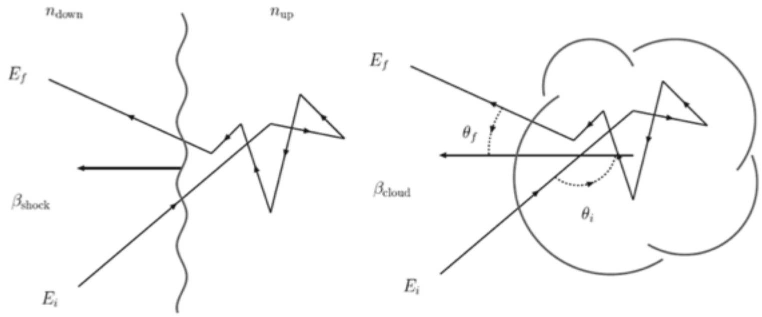

Figure 2.6: First order (left) and second order (right) Fermi Acceleration [88].

The acceleration of cosmic rays to energies above $E \approx Z \times 100$ TeV, where Z is the particle charge, using SNR and galactic sources remains an open question [89]. The knee of the cosmic ray energy spectrum, which is thought to indicate the beginning of the transition from galactic to extragalactic sources, occurs at ~ 3 PeV, which is above the maximum energy traditionally given for galactic acceleration sources. An extra order of magnitude in energy can be gained with new source analyses [90] and magnetic field amplification at acceleration sites [91]. Since accelerators work to a maximum rigidity, the transition from galactic to extragalactic sources should be later for larger Z. KASCADE experimental data first showed that the knee feature is due to the fall-off of a proton flux, and the fall-off of heavier primaries at higher energies proportional to Z [92]. Near the ankle, the composition trends back from heavy to light (as seen in Figure 2.4), presumably after the galactic sources are exhausted.

It is also possible that at energies above the knee, the lack of confinement time in the galaxy plays a role in the declining flux. A proton at 10^{17} eV has a Larmor radius r_L =100 pc, which is on the order of the length scale of the random galactic magnetic fields, L. Scattering in the magnetic fields, which contains cosmic rays in the galaxy, stops being efficient when $r_L \gg L$ [93].

Outside of the galaxy, there are more possibilities for acceleration sites, including merger shocks in galaxy clusters and the relativistic shocks of active galactic nuclei [94], as seen on the Hillas plot (Figure 2.5). Measuring cosmic ray composition is a high priority now, as composition provides more information about acceleration sites, as well as propagation, as discussed in the next section.

2.3.3 Propagation in the Galaxy

Up to energies of 10^{15} x Z eV, where Z is the atomic number of the cosmic ray, the energy spectra and composition of observed cosmic rays can be described by a galactic diffuse propagation model. Cosmic rays below the knee are contained in the galaxy and isotropic. The spatial diffusion is caused by the random galactic magnetic fields, and for energies where the Larmor radius of a cosmic ray primary is of the same scale as interstellar magnetic turbulence ($\sim$ 100 pc) [95], cosmic rays below the ankle are well isotropized.

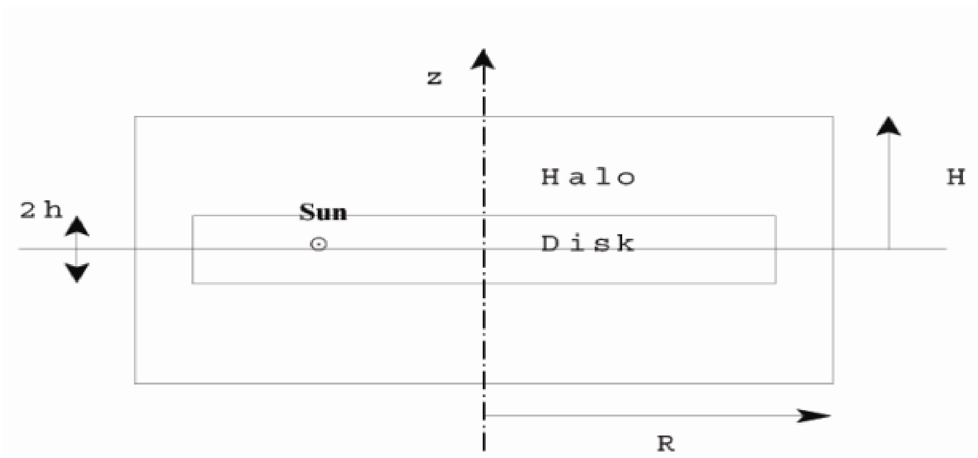

Figure 2.7: A schematic of the region in which cosmic rays diffuse in the galaxy [96].

The propagation of a nucleus of type i is given by [68]

$$\begin{aligned}\frac{\partial N}{\partial t} &= \nabla \cdot (D_i \nabla N) - \frac{\partial}{\partial E}(b_i(E)N_i(E)) - \nabla \cdot \mathbf{u}N_i(E) \\ &+Q_i(E,t) - p_i N_i + \frac{v\rho}{m}\sum_{k\geqslant i}\int \frac{d\sigma_{i,k}(E,E')}{dE}N_k(E')dE'.\end{aligned} \tag{2.14}$$

In Equation 2.14, $N(E, \mathbf{x}, t)dE$ gives the particle density at a given position, time, and energy range. The $\nabla \cdot (D_i \nabla N)$ term represents diffusion, with $D = \frac{1}{3}\lambda_D v$

where v is the particle velocity and λ_D is the diffusion mean free path. The second term describes energy change, where $b_i(E) = dE/dt$ being the rate of energy gain or loss. $\nabla \cdot \mathbf{u} N_i(E)$ accounts for convection at velocity $\mathbf{u}$. Q_i is the source intensity, which gives the density of particles of type i at a given time and for a given energy. The $p_i N_i$ term gives the loss of nuclei due to collisions or decay, where p_i is the probability of the cosmic ray colliding in ISM or decaying. The final term is the cascade term, and accounts for production of nuclei i from nuclei k colliding with the ISM, with $\sigma_{i,k}$ the production cross section for nuclei type k from spallation reactions of nuclei type i, and ρ the gas density with a mean particle mass m [68][97]. This model where the galaxy is homogeneous and cosmic rays propagate until they escape or lose energy is called the Leaky Box Model (see Figure 2.7).

The relative abundances of nuclei of observed cosmic rays allow one to probe the propagation time from source to observer. For cosmic rays that can be observed directly, the ratio of secondary to primary (that is, nuclei created in spallation processes compared to nuclei from the source) gives information about how far a cosmic ray has traveled. Secondary to primary ratios are energy dependent, which suggests that the distance a particle travels before undergoing spallation is also energy dependent [98].

2.3.4 Propagation in the Cosmos

Tracking UHECRs involves propagation through the intergalactic medium. In this case, magnetic fields and background photons are the most important factors. Using the Dip Model [75], which gives an UHECR proton component of over 85%, the ankle feature in the cosmic ray spectrum can be attributed to pair production due to proton propagation in the CMB, as

$$p + \gamma_{CMB} \rightarrow e^+ + e^- + p. \tag{2.15}$$

In the energy range $10^{18} - 10^{19}$ eV, the interaction length of UHECR is typically around a Gpc. For this reason, adiabatic expansion of the universe must also be taken into account. Photo-disintegration is also an important when considering the composition of UHECR. Nuclei with atomic mass A>1 interact with CMB, losing nucleons in the process and changing the composition of observed UHECRs [99].

The CMB photons have an average energy of 10^{-3} eV. Pions are created in collisions of nucleons with CMB, as $N + \gamma \rightarrow N + \pi$, with an energy threshold of

$$E_{thres}^{N,\pi} = \frac{m_\pi(m_N + m_\pi/2)}{2\epsilon} \approx 6.8 \times 10^{19} (\frac{\epsilon}{10^{-3}\text{eV}})^{-1}\text{eV} \tag{2.16}$$

where m_N and m_π are the masses of incident nucleon and resulting pion, and ϵ is the energy of an average CMB photon [100]. Thus, at energies above 10^{20} eV, cosmic rays will interact with CMB. This "GZK" effect was first hypothesized in the 1960s by Greisen, Zatsepin, and Kuzmin [5][6]. The GZK effect yields UHE neutrinos, as discussed later in this chapter. Infrared and optical photon backgrounds (IRB) are also important to consider. Although the density of IRB is more than two orders of magnitude lower than CMB, cosmic rays with energies below 10^{20} eV can interact with it, and so the interactions produce a non-negligible flux of cosmogenic neutrinos [101].

2.3.5 Detection

Cosmic rays from different parts of the energy spectrum are most efficiently detected using different techniques. Below 10^{14} eV it is possible to effectively measure cosmic rays directly. This is commonly done with detectors aboard high altitude balloons or on spacecraft. At higher energies it is more efficient to use ground based detectors that utilize the particle air shower that results when the primary cosmic ray interacts in the atmosphere. This section discusses recent and current cosmic ray experiments.

2.3.5.1 Direct Detection

Direct detection methods successfully measure composition and energy of cosmic rays before they interact in the Earth's atmosphere. The following experiments have made significant contributions to our understanding of cosmic ray physics below the knee.

- The TIGER (Trans-Iron Galactic Element Recorder) is a balloon based experiment that uses charge identification to resolve the charge of specific elements heavier than iron ($26 < Z < 40$) [102]. TIGER had two successful flights in the austral summer of 2001-2002 and one in the summer of 2003-2004. It's successor, SuperTIGER (Super Trans-Iron Galactic Element Recorder) had better charge resolution and extended the elemental reach to $Z = 60$ [103]. SuperTiger detected over 50×10^6 cosmic ray nuclei today.

- The CREAM (Cosmic Ray Energetics and Mass) balloon based experiment that aims to measure lower mass nuclei at high energies to bridge direct and indirect detection methods (between $10^{11} - 10^{15}$ eV). This would provide a calibration source for ground based experiments. CREAM also uses a charge identification system to measure nuclei from $1 < Z < 26$. CREAM has had 6 successful flights to date [104] [105].

- PAMELA (Payload for Antimatter Matter Exploration and Light-nuclei Astrophysics) is a space-based detector aboard the Russian Resurs-DK1 satellite. PAMELA uses a permanent magnet spectrometer to measure the antiparticle component of the cosmic radiation. An excess in positron fraction was found between 400 MeV and 200 GeV [106].

- AMS-02 (Alpha Magnetic Spectrometer) is aboard the International Space Station. It was launched in 2005 and has recorded over 60 billion cosmic ray events. Like PAMELA, it searches for cosmic ray antimatter that could indicate the presence of dark matter [107]. It's prototype AMS-01 was launched in 2001 and placed an upper limit on antihelium [108].

2.3.5.2 Indirect Measurement

The cosmic ray energy spectrum is steeply falling, and so it is not practical to detect cosmic rays above 10^{15} eV using direct methods. Instead, features of the extensive air shower are detected. Extensive air showers are discussed further in Chapter 4. Particle detector arrays can measure electromagnetic particles, muons, and hadrons that make it to ground level. Particle detectors are often scintillators or Cherenkov water tanks. These detectors probe the lateral distribution of the shower footprint which can be used to reconstruct the energy of the primary. Timing methods can be used to measure the direction of arrival, signal intensity can yield the position of the shower core. If particle detectors can distinguish between muons and electrons, the ratio between the two can be used to determine the composition of the primary.

Air Cherenkov, fluorescence, and radio detectors are used to measure the longitudinal development of air showers. In particular, $X_{\max}$, which is the atmospheric depth at which the air shower is at a maximum, is an important parameter which is sensitive to the primary mass, as heavier nuclei are likely to interact higher in the atmosphere. Fluorescence light is generated in the shower when Nitrogen molecules in the atmosphere are excited by particles in the shower and emit UV light. Light is captured in mirrors focused on an array of PMTs to image the development of the shower. This has proven to be a successful way to accurately measure $X_{\max}$, however the duty cycle is low because fluorescence detection requires dark conditions. Radio arrays are also used effectively to measure geomagnetic radiation generated by the transverse drift of charged particles in the Earth's magnetic field. Radio measurement can be used to reconstruct the primary cosmic ray's energy, geometry, and composition with a high duty cycle. Radio detection is discussed in depth in Chapter 3.

- The Pierre Auger Observatory is located in Argentina and has a detection area of 3,000 km^2. It was completed in 2008 and consists of 1,600 water Cherenkov surface detectors and 24 atmospheric fluorescence detectors. The combination of two detector types allows for cross calibration. Auger contributes to the current flux measurements of UHECRs up to 10^{20}eV [109]. There are various extensions being implemented at the Auger site, including a radio array (AERA) that is discussed further in the next chapter.

- The Telescope Array (TA) is a complementary experiment to Auger in the northern hemisphere. It is the next generation of the Fly's Eye/ HiRes experiments. TA is based in Utah and covers over 750 km^2. Cosmic rays above 10^{18} eV are detected using scintillators to map the particle footprint of the air shower and fluorescence detectors to map the longitudinal development of the air shower. TA is developing a low energy extension to measure cosmic rays in the galactic-extragalactic transition region [110][111].

- The Tunka-133 experiment consists of a 1 km^2 ground array of particle detectors and a photomultiplier array to capture Cherenkov light emitted by air showers. Like Auger and TA, this allows for shower reconstruction both from particle information on the ground and longitudinal development, but in this case from Cherenkov light. The Cherenkov technique allows for reconstruction of X_{max} using the lateral distribution of the photons at the ground. Tunka also added a radio extension, Tunka-Rex, that is discussed in the following chapter [112][113].

- IceTop is a 1 km^2 array of 81 particle detectors located at the South Pole on the ice surface above the IceCube experiment. Each station consists of two ice Cherenkov detectors separated by 10 meters. IceTop can be used in conjunction with IceCube or as a stand alone cosmic ray detector. In particular, muons with high enough energy (∼TeV) are seen by IceCube, and provide more information about air showers than is available from surface detectors alone [114].

2.4 Neutrinos

Neutrinos are neutral fermions that interact via the weak interaction. They are part of the Standard Model, which governs strong, weak, and electromagnetic interactions. The Standard Model includes gauge boson (spin 1) force carriers that mediate the interactions. The W$^{\pm}$ (with $\pm$ 1 charge) and Z^0 bosons mediate weak interactions. The weak interaction is named as such because the range at which it is effective is orders of magnitude smaller than that of the strong or electromagnetic forces. The high masses of the W and Z bosons (90 GeV/c^2) lead to the short range interactions. It also differs from the other fundamental forces in that it violates parity and charge-parity symmetries [115]. Neutrinos come in three flavors associated with the electron, muon, and tau leptons, and can oscillate between flavors. In this section the neutrino energy spectrum, sources, interactions, flavor oscillations, and detection experiments are discussed.

2.4.1 Production

Neutrinos can be generated in beta decay, nuclear reactions (such as fusion in the sun), and in high energy hadron collisions that result in pion decay [116].

Beta decay can occur in two ways. In a β^+ decay, a proton is converted into a neutron and a positron and ν_e are created in the process. In a β^- decay, a neutron converts to a proton and an electron and $\bar{\nu_e}$ are created [117]. The generic equations for β^+ and β^- are

$$^A_ZX \rightarrow ^A_{Z-1} X' + e^+ + \nu_e \tag{2.17}$$

$$ {}^{A}_{Z}X \rightarrow {}^{A}_{Z+1}X' + e^- + \bar{\nu}_e. \quad (2.18) $$

Neutrinos can also be created in nuclear fusion processes. For example, neutrinos can come from proton-proton reactions as

$$ p + p \rightarrow d + e^+ + \nu_e. \quad (2.19) $$

This reaction accounts for most neutrinos produced in the sun [118]. Finally, neutrinos can be the product of collisions between hadrons. This is the case for neutrinos produced in particle accelerators and cosmic ray air showers. The collision results in charged pions and kaons that decay into neutrinos as

$$ \begin{aligned} \pi^{\pm} &\rightarrow \mu^{\pm} + \nu_\mu(\bar{\nu}_\mu) \\ K^{\pm} &\rightarrow \mu^{\pm} + \nu_\mu(\bar{\nu}_\mu). \end{aligned} \quad (2.20) $$

At high energies, the $K^{\pm} \rightarrow \pi^0 l^{\pm} \nu_l(\bar{\nu}_l)$ decay channel is also important. More details about neutrino production for specific sources can be found in Section 2.4.4.

2.4.2 Interactions

Neutrinos interact via the weak neutral current interaction and charged current interaction. The neutral current interaction is mediated by the Z^0 boson. The charge and mass of the original particles remain the same, however there is a transfer of momentum, spin, and energy between them. For fermions other than neutrinos, this interaction is masked by the electromagnetic interaction. For neutrinos, which don't interact by the electromagnetic force, the neutral current interaction plays an important role in detection. The transfer of energy may boost particles in the detection medium to relativistic energies, which allows them to emit Cherenkov light that can be detected. All three flavors of neutrino can participate in this interaction, but no flavor information can be deduced from the product.

The charged current interaction is mediated by the W$^{\pm}$ boson. Neutrinos transform into their partner lepton. For example, a $\bar{\nu}_e$ entering a detection medium may interact as

$$\bar{\nu}_e + p \rightarrow n + e^{+}. \tag{2.21}$$

For this interaction to take place the initial neutrino must have sufficient energy to create the partner's mass. Detectors that can distinguish between the resulting electron, muon, or tau can measure the flavor of the incident neutrino.

2.4.3 Oscillations

Neutrinos can be described using mass eigenstates $|\nu_i\rangle$ with mass m_i or weak interaction eigenstates $|\nu_e\rangle$, $|\nu_\mu\rangle$, $|\nu_\tau\rangle$. $|\nu_\alpha\rangle = \sum U_{\alpha i}|\nu_i\rangle$ where U is the PMNS mixing matrix [119]. For simplicity oscillations here are discussed in a 2-flavor model.

$$|\nu_e\rangle = \mathrm{cos}\theta_\nu|\nu_1\rangle + \mathrm{sin}\theta_\nu|\nu_2\rangle \tag{2.22}$$

$$|\nu_\mu\rangle = \text{-}\mathrm{sin}\theta_\nu|\nu_1\rangle + \mathrm{cos}\theta_\nu|\nu_2\rangle. \tag{2.23}$$

Here, θ_ν is the vacuum mixing angle and is nonzero. At time $t = 0$ the neutrino is in a known state

$$|\nu(t=0)\rangle = |\nu_e\rangle = \mathrm{cos}\theta_\nu|\nu_1\rangle + \mathrm{sin}\theta_\nu|\nu_2\rangle. \tag{2.24}$$

After some propagation time, the oscillation probability depends on the neutrino's mass as seen in the phase term

$$e^{i(\vec{k}\cdot\vec{x}-\omega t)} = e^{i[\vec{k}\cdot\vec{x}-\sqrt{m^2+k^2}t]}. \tag{2.25}$$

Because the neutrino mass is small compared to the energy, this can be written

$$|\nu(t)\rangle = e^{i(\vec{k}\cdot\vec{x}-kt-(m_1^2+m_2^2)t/4k)}\left(\mathrm{cos}\theta_\nu|\nu_1\rangle e^{i\delta m^2 t/4k} + \mathrm{sin}\theta_\nu|\nu_2\rangle e^{-i\delta m^2 t/4k}\right). \tag{2.26}$$

The probability of a neutrino remaining in a state for some time is then

$$P_{\nu_e}(t) = |\langle\nu_e|\nu(t)\rangle|^2 = 1 - \mathrm{sin}^2 2\theta_\nu \mathrm{sin}^2\left(\frac{\delta m^2 c^4 x}{4cE}\right) \tag{2.27}$$

indicating that the probability of the original electron neutrino remaining in the same state in vacuum conditions oscillates from 1 to $1-\sin^2 2\theta_\nu$ and back to 1 over the length

$$L_o = \frac{4\pi\hbar c^2 E}{\delta m^2 c^4}. \tag{2.28}$$

This probability remained too small to account for neutrino oscillations by solar neutrinos until it was noted that neutrinos interacting with matter in the sun change their effective mass. This effect is called the MSW (Mikheyev, Smirnov, and Wolfenstein) mechanism and accounts for oscillations seen from solar neutrinos [120].

2.4.4 Sources and Spectrum

The neutrino energy spectrum extends from 10^{-6} eV to 10^{19} eV (see Figure 2.8). Neutrinos at the lowest energies are left over from the big bang and are known as relic neutrinos of the cosmic neutrino background. Solar neutrinos and neutrinos originating from supernovae dominate between 1 keV and a few 10s of MeV. Atmospheric neutrinos, with energies up to 100 TeV, come from cosmic ray interactions in the Earth's atmosphere. Between a few GeV and 100 PeV, neutrinos can come from extreme astrophysical objects such as black hole accretion discs or neutron stars. In the highest UHE regime, neutrinos may be astrophysical or cosmogenic, that is, produced via the GZK process [121].

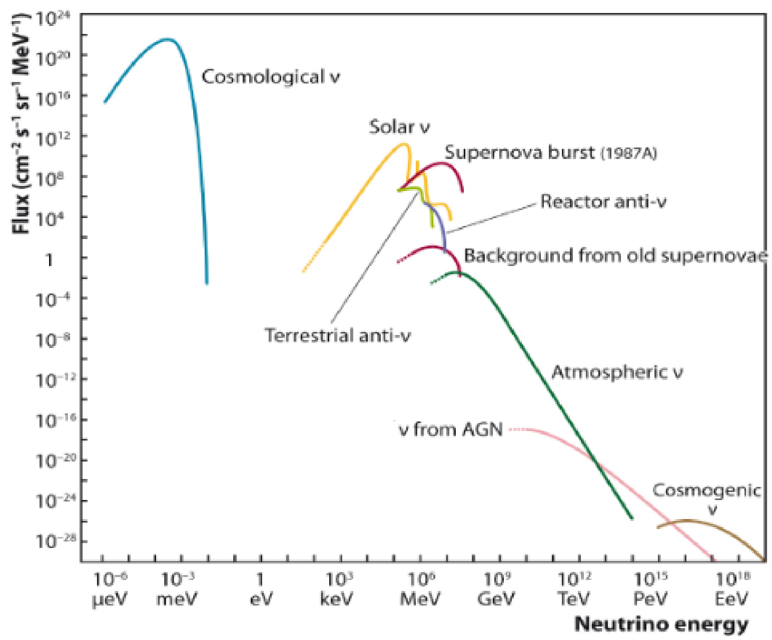

Figure 2.8: Flux of neutrinos over the full energy spectrum [122].

2.4.4.1 Solar Neutrinos

Solar neutrinos are produced by fusion processes in the sun. The energy spectrum of solar neutrinos is shown in Figure 2.9.

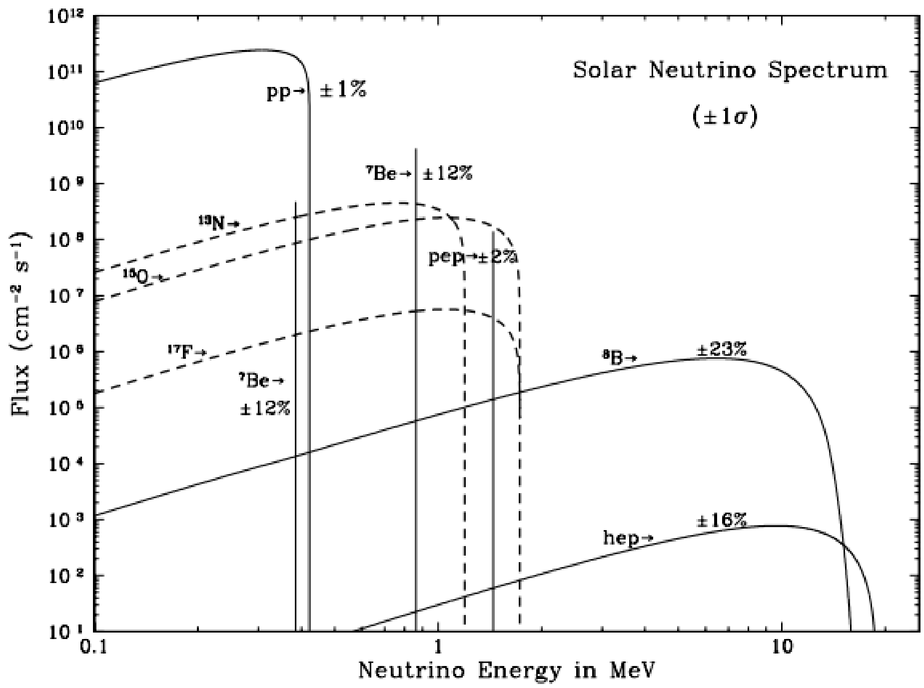

Figure 2.9: Solar Neutrino Spectrum [123]. Solid lines represent spectra from the *pp* chain, and dashed lines represent spectra from reactions with carbon, nitrogen, and oxygen isotopes.

The *pp* reaction in the sun that produces 86% of solar neutrinos is

$$p + p \rightarrow {}^{2}H + e^{+} + \nu_e. \tag{2.29}$$

Although the majority of solar neutrinos come from *pp* interaction, they have energies below the detection threshold of most experiments (such as the ^{37}Cl detector used at Homestake, which had a detection threshold of 0.814 MeV). The primary reaction for neutrinos with high enough energy for detection is

$$\begin{aligned}
&{}^{3}\mathrm{He} + {}^{4}\mathrm{He} \rightarrow {}^{7}\mathrm{Be} + \gamma \\
&{}^{7}\mathrm{Be} + p \rightarrow {}^{8}\mathrm{B} + \gamma \\
&{}^{8}\mathrm{B} \rightarrow {}^{8}\mathrm{Be}^{*} + e^{+} + \nu_e \\
&{}^{8}\mathrm{Be}^{*} \rightarrow 2\alpha
\end{aligned} \tag{2.30}$$

which occurs in about one of every 5000 terminations of the *pp* chain. The resulting ν_e's have maximum energies of 15 MeV.

The lack of electron neutrinos measured from the sun brought attention to the phenomena of flavor oscillations, as discussed earlier in this chapter. In particular Homestake experiment measured a deficit of electron neutrinos from the sun in the 1970s, leading to the "solar neutrino problem [124]." Neutrino oscillations were confirmed by the both Super-Kamiokande Observatory and Sudbury Neutrino Observatories. The SNO detects neutrinos interacting in a heavy water detector through charged current interactions ($\nu_e + d \rightarrow p + p + e^-$), neutral current interactions ($\nu_x + d \rightarrow p + n + \nu_x$), and elastic scattering ($\nu_x + e^- \rightarrow \nu_c + e^-$), although the elastic scattering interaction has reduced sensitivity to ν_τ and ν_μ. Since the neutral current is sensitive to all flavors of neutrinos, and the charged current is only sensitive to electron neutrinos, the solar electron neutrino component can be distinguished from the total solar neutrino flux, and the probability of oscillation can be measured [125].

2.4.4.2 Atmospheric Neutrinos

Hadronic cosmic rays entering the Earth's atmosphere interact and produce a cascade of particles, including muons, pions, and kaons. Neutrinos with GeV energies are produced primarily by the secondaries, which decay before re-interacting by

$$\begin{aligned} \pi^\pm &\rightarrow \mu^\pm + \nu_\mu(\bar{\nu}_\mu) \\ K^\pm &\rightarrow \mu^\pm + \nu_\mu(\bar{\nu}_\mu) \\ \mu^\pm &\rightarrow e^\pm + \nu_e(\bar{\nu}_e) + \bar{\nu}_\mu(\nu_\mu) \end{aligned} \tag{2.31}$$

with the resulting ratio

$$r = \frac{\nu_e + \bar{\nu}_e}{\nu_\mu + \bar{\nu}_\mu}. \tag{2.32}$$

This production ratio is close to $r \approx 0.45$, as calculated using monte carlo simulations [121]. At higher energies, the $K^\pm \rightarrow \pi^0 l^\pm \nu_l(\bar{\nu}_l)$ channel is relevant, where l is

e or μ. This is the dominant source of ν_e for $E_\nu \gg 1$ GeV, where muon decay isn't important [68]. Atmospheric neutrinos are an interesting source because they don't depend on absolute astrophysical fluxes and are uniformly distributed over the Earth. Experiments can look through the Earth in different angles to achieve a variety of experimental baselines to measure flavor mixing.

Atmospheric neutrinos also played an important role in the discovery of flavor oscillation. Neutrino masses are small, so flavor oscillations have to be measured over long baselines. In the 1980s, Kamiokande and IMB saw a deficit of atmospheric ν_μ while seeing the predicted number of ν_e [126]. The deficit was energy and zenith angle dependent. By 1994 enough data had been collected to demonstrate that a deficit existed for neutrinos that had traveled through the Earth, corresponding to a long flight path, whereas no deficit existed for neutrinos that hadn't traveled through the Earth. This data provided strong evidence for neutrino oscillations from $\nu_\mu \rightarrow \nu_\tau$ [127][128].

2.4.4.3 Astrophysical Neutrinos

The first observation of astrophysical neutrinos from a known source other than the sun was the observation of Supernova SN1987a. Three observatories coincidentally detected neutrinos consistent with a thermal spectrum, and a few hours prior to the observed visible light [53].

Any astronomical object that has nuclei interacting with a plasma or radiation field can produce neutrinos. The interaction produces pions, which decay into neutrinos, as described the previous section. Possible sources include AGN and gamma ray bursts, the same sources that could produce UHECRs. Unlike cosmic rays, astrophysical neutrinos point back to their sources, opening the door for neutrino astronomy. The challenge is detecting a large enough flux of neutrinos at high energies [129] [130].

In four years of IceCube data (through 2015) an astrophysical neutrino flux of 58 neutrino events above 30 TeV has been found. The astrophysical neutrino observations do not exhibit any significant anisotropy, which suggests the sources are extragalactic [131][132].

2.4.4.4 Cosmogenic Neutrinos

The highest energy neutrinos are thought to be a product of cosmic ray nuclei interacting with the cosmic microwave background, given as

$$\gamma_{CMB} + p \rightarrow \Delta^{+} \rightarrow p + \pi^{0} \tag{2.33}$$

$$\gamma_{CMB} + p \rightarrow \Delta^{+} \rightarrow n + \pi^{+}. \tag{2.34}$$

The resulting charged pions then decay as

$$\begin{aligned} \pi^{+} \rightarrow & \mu^{+} + \nu_{\mu} \\ & \hookrightarrow e^{+} + \bar{\nu_{\mu}} + \nu_{e}. \end{aligned} \tag{2.35}$$

There is also a $\pi^0 \rightarrow 2\gamma$ decay mode which produces intergalactic electromagnetic cascades. Eventually the energy cascades off the CMB down to 0.1-1 TeV photons, which are detectable and can constrain propagation models.

The characteristic energy at which photo-pion production dominates energy loss for a proton primary in CMB is $\sim 6 \times 10^{19}$ eV. (When considering red-shifted primaries, this limit is shifted by a factor of $(1 + z)$ to lower energies because the CMB photon energies increase as $(1 + z)$ [133]). This is the cause of the GZK cutoff, which describes the fall-off of the cosmic ray energy spectrum above 10^{20} eV. Below this limit, the dominant source of energy loss for protons is pair production, however, this effect is 200 times smaller than the energy loss due to pion production. Below $\sim 10^{18}$ eV, adiabatic energy losses dominate [134].

The photo-pion interaction limits the distance a proton with an energy at this threshold can travel to 50 Mpc. Assuming UHECRs are coming from extragalactic sources, this also guarantees an UHE neutrino flux. The current generation of neutrino detectors are closing in on limits for a GZK flux [5][6] (Figure 2.10). Fluxes by current experiments, including IceCube, are shown in light gray. The next generation of neutrino experiments (EVA, ARIANNA, ARA37) is in development, and expected sensitivities are shown in color. An overview of radio neutrino experiments is given in Chapter 3.

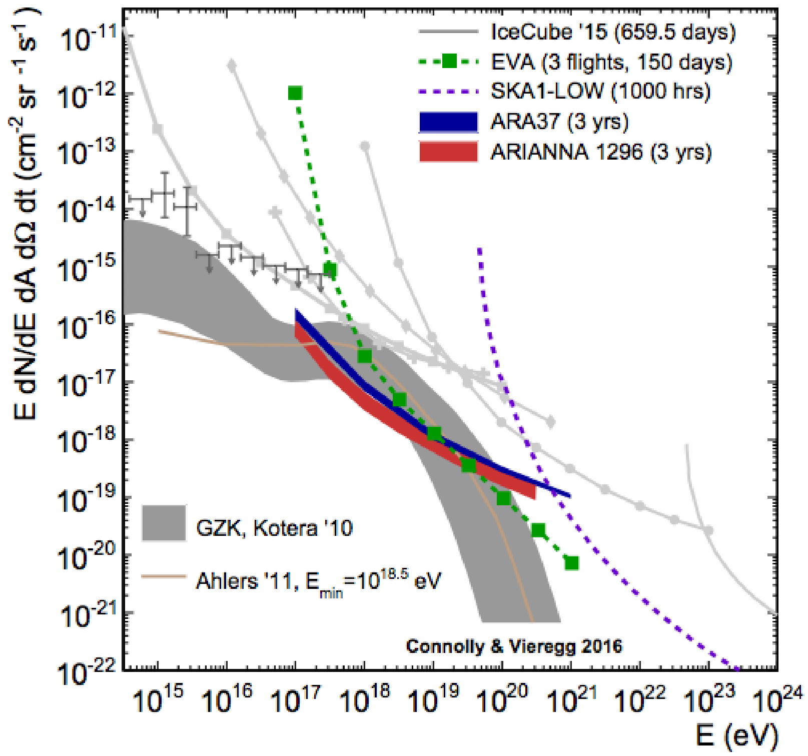

Figure 2.10: UHE neutrino limits set by various experiments [135].

2.4.5 Detection

Neutrino detection is notoriously difficult because neutrinos only weakly interact with other particles. Since these interactions are rare, experiments utilize large target masses to maximize the chance of a detection.

- The Sudbury Neutrino Observatory (SNO) used 1,000 tons heavy water buried in a mine to detect Cherenkov emission from solar neutrinos. The heavy water allows for both charged and neutral current interactions. Only solar electron neutrinos are able to interact via the charged current interaction, while all neutrino flavors interact through the neutral current. This allows for neutrino oscillations to be measured with the same experiment. SNO provided experimental evidence of neutrino oscillations (and therefore neutrino mass) in 2001, complementary with the Super-K 2001 results, thereby solving the solar neutrino problem [118].

- The Super-Kamiokanda experiment is located under Mount Ikeno in Japan. It uses 50,000 tons of ultra-pure water to detect Cherenkov light from the product of a neutrino interaction. Super-K detects solar, atmospheric, and Supernova neutrinos. Super-K found strong evidence of atmospheric neutrino oscillations in 1998 and solar neutrino oscillations in 2001 [136][137].

- IceCube is the current state of the art high energy neutrino experiment. An array of optical detectors cover a cubic kilometer of ice located 1450m - 2450m beneath the south pole. Detectors are arranged in a grid to evenly cover the volume. There is also a DeepCore infill to detect lower energy neutrinos and a surface array to detect cosmic rays. As mentioned previously, IceCube detected the first high energy astrophysical neutrino flux [138]. IceCube also detected three neutrinos in the PeV energy region, the highest seen to date [139]. Figure 2.11 shows a 2 PeV neutrino event. IceCube's geometry (and the planned IceTop surface array) allow the experiment to distinguish astrophysical neutrinos from atmospheric neutrinos. The deep core also has the possibility of detecting neutrinos coming from the decay of dark matter [140]. IceCube is currently planning an extension to reach a higher energy region and improve sensitivity at GeV energies to study neutrino mass mixing.

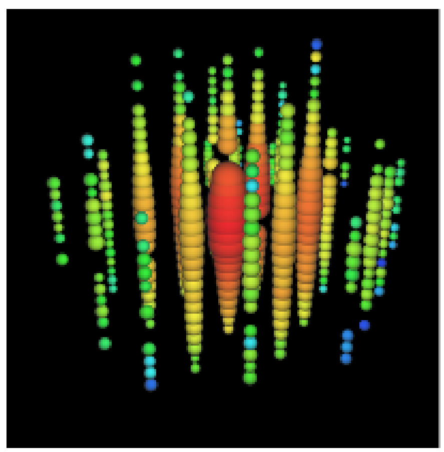

Figure 2.11: A PeV neutrino event detected by IceCube. Each point represents an optical detector. The size of the point shows the strength of the signal and the color indicates the detection time with red being earlier [141].

- KM3NeT is a planned neutrino detector based in the Mediterranean Sea. An array of optical detectors will measure Cherenkov light generated by neutrino secondary interactions in the water. KM3NetT will cover several cubic kilometers. The first phase of KM3Net construction is expected to be operational in 2017. There are two major components of the experiment. The ARCA (Astroparticle Research with Cosmics in the Abyss) array is optimized for angular resolution and will study source anisotropies. The ORCA (Oscillation Research with Cosmics in the Abyss) array will measure atmospheric neutrino oscillations with high precision [142][143].

In addition, the ANTARES [144] and Baikal [145] detectors were also important for developing large are neutrino telescope technology.

The aforementioned experiments use optical detection methods. Radio detection is also an effective detection technique, since radio signals travel long distances without significant attenuation. Chapter 3 gives an overview of radio detection experiments. Chapter 4 discusses the radiation mechanisms in detail.

Chapter 3

HISTORY OF RADIO DETECTION OF COSMIC RAYS AND NEUTRINOS

3.1 Introduction

Radio detection of high energy particles was hypothesized in the 1960s. The first experimental radio detection of cosmic ray air showers was made shortly thereafter. In the 1960s radio detection used an analogue technique and measured emission from air showers at single frequencies. Energy and direction of cosmic ray primaries could be reconstructed. In 1970s other techniques such as particle detector arrays were preferred for measuring air showers, as they were better understood. Radio detection gained popularity again in the 1990s when it was hypothesized that neutrinos could be detected using Askaryan radiation. This radiation was experimentally confirmed at SLAC in 2000. Interest in geomagnetic radiation also resurfaced for the detection of cosmic rays. Now, radio detection of high energy particles is one of the most promising techniques available. The emission mechanisms are well understood and simulated [146]. This chapter reviews the development of radio detection of cosmic rays and neutrinos. We begin with the original predictions for radio emission in the 1960s and discuss early experimental results. Then, modern approaches to radio detection and simulation are reviewed. The SLAC beam tests for Askaryan radiation and the ANITA experiment are presented in detail, as they are of particular interest for this thesis. Current radio experiments are also discussed.

3.2 Early Radio Efforts

In 1962 Gurgen Askaryan published a paper predicting the production of radio emission from electron-positron particle showers in a dense medium [7]. After narrowly missing a Noble Prize for the development of the Bubble Chamber, Askaryan focused on different effects generated by high energy particles injected into media. Specifically, he proposed that a) the resulting cascades of $e^+e^-\gamma$ would develop a charge asymmetry, and b) since the cascade travelled faster than the speed of light in the medium, it would emit coherently in the radio regime. This is the Cherenkov effect, where a net charge moving faster than the velocity of light in the medium produces coherent radiation, which peaks on an index of refraction dependant emission angle. A consequence of the coherence of the radiation is that the radiated power scales as the square of the energy of the primary, and is beamed into a Cherenekov cone [73]. Askaryan also noted that magnetically induced radiation would be seen due to the presence of Earth's magnetic field in cosmic ray air showers. It is now understood that air showers also exhibit Cherenkov like effects [147]. These radio emission mechanisms are discussed further in Chapter 4.

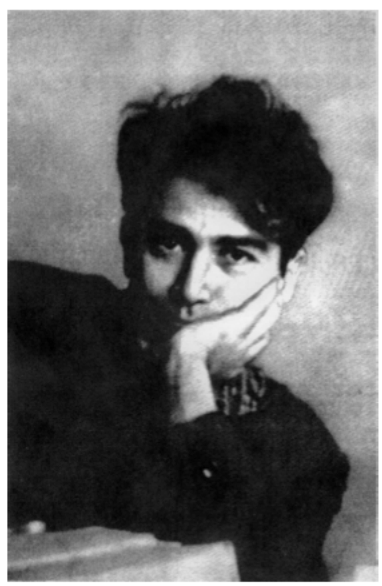

Figure 3.1: Portrait of Gurgen Askaryan

In 1965 Jelley, et al. made further contributions to the field by demonstrating a strong radio signal from a cosmic ray air shower at 44 MHz [8]. In the next five years simple radio experiments followed at the Haverah Park air shower Cherenkov detector [57]. Minimal bandwidth antennas continued to detect radio emission from high energy showers [148][149][150][151]. These experiments detected faint signals and required an extremely quiet background, and wouldn't be possible now due to the large number of radio noise sources. Basic features of cosmic ray air showers could be reconstructed with these experiments, including primary energy and arrival direction. However, the emission mechanisms were not well understood and overall strength of the radio signal was not well calibrated between experiments [113]. Radio detection picked up again in the 1980s with radio antennas installed at the Yakutsk site [152]. AGASA and EAS-TOP made early digital radio measurements in the late 1980s [153].

As radio detection gathered interest, it was necessary to have models which could provide detailed theoretical predictions to compare to data. Analytic models, for example Kahn and Lerche (1966), included magnetically induced radiation from cosmic ray air showers [154], but lacked the microscopic physics to make detailed predictions.

3.3 Modern Efforts

The early efforts to detect radio emission from air showers relied on analog electronics and analytic models, which limited the information that could be extracted from experimental data. For that reason, along with the fact that radio emission from air showers wasn't well understood, radio detection of cosmic rays was set aside in favor of the more promising fluorescence technique. The availability of digital electronics and numerical simulation methods in the 1990s renewed interest in the field.

In the 1990s new theoretical models were developed for radio emission from particle cascades in dense media, which was relevant for neutrino interactions in Antarctic ice. Specifically, the ZHS (Zas, Halzen, and Stanev) algorithm [24][155] motivated the RICE experiment at the South Pole [13]. In the late 1990s simulation techniques developed by Alvarez-Muniz et al. extended simulations to EeV energies [156]. Simultaneously, efforts were made to characterize radio emission in dense media phenomenologically by Razzaque et al. [157] and theoretically by Buniy and Ralston [158]. These developments were important in the interpretation of the original SLAC Askaryan experiments discussed in Section 3.4, where Askaryan radiation was generated and detected in a controlled lab setting. The success of these experiments paved the way for modern experiments, like ANITA [16], which aims to detect radio emission from neutrino cascades over large volumes of Antarctic ice.

Predictions for geomagnetic radiation in air showers also helped revive interest in radio detection of cosmic rays [159]. However, until $\sim$ 2009, radio emission mechanisms of cosmic ray air showers were not well understood [146]. Early particle simulations assumed that the magnetically generated component of air shower radiation was due to the synchrotron effect. Using an incorrect emission mechanism, macroscopic calculations were not correct. Time domain microscopic simulations also omitted contributions to the emission, which produced inconsistencies with simulations carried out in the frequency domain [146]. The nature of the Cherenkov cone due to a varying index of refraction in air was also not understood. For these reasons, simulations did not agree and interpretation of radio data from cosmic ray air showers was difficult.

Now there are a number of modern macroscopic and microscopic simulations in use. A primary macroscopic approach is MGMR, which uses the time derivative of drift currents developing in the shower to derive the radio emission [160]. Drawbacks of this approach include the fact that assumptions are made about the emissions mechanisms and approximations have to be made about the air shower conditions [146]. Macroscopic approaches have the advantage of speed, and provide insight into the contributions to radio emission from air showers.

Two complementary microscopic approaches are CoREAS [161] and ZHAireS [162]. Both track individual particles in the shower and sum the radio emission at the point of the observer. No emission mechanisms are assumed and coherence effects are automatically accounted for. CoREAS builds off the endpoint formalism developed for REAS3 [163] and uses CORSIKA to generate Monte Carlo air shower simulations. ZHAires uses the ZHS formalism with the AIRES Monte Carlo [164]. The two methods are in good agreement and are discussed further in Chapter 4.

The geomagnetic emission process has been confirmed experimentally. The

LOPES [10] and CODALEMA [11] experiments validated radio detection of cosmic rays as a technique, and the current generation of radio experiments measure energy, direction, and composition of cosmic rays, relying on simulations to reconstruct parameters. Recent and current experiments are discussed in Section 3.6.

3.4 SLAC Radio Development

The Stanford Linear Accelerator (SLAC) National Laboratory facility has proven a useful environment in which to probe the features of Askaryan radiation. SLAC provides a test beam of photons, electrons, or positrons at a known energy. This beam can be directed into some target material, at which point a particle shower will be generated and various radiation will be produced. Askaryan radiation experiments done using ice, silica sand, and salt validated Askaryan predictions and are discussed here. The T-510 experiment used high density polyethylene as a target and is discussed in Chapters 5 and 6.

3.4.1 Askaryan Radiation in Silica Sand

The first experiment to directly measure Askaryan radiation took place at the SLAC National Laboratory Final Focus Test Beam facility in 2000 [25]. Picosecond pulses of 28.5 GeV bremsstrahlung photons were directed into a 3.5 ton silica sand target. Antennas spanning 0.3 to 6 GHz were used to detect nanosecond radio pulses. Figure 3.2 shows the experimental set up.

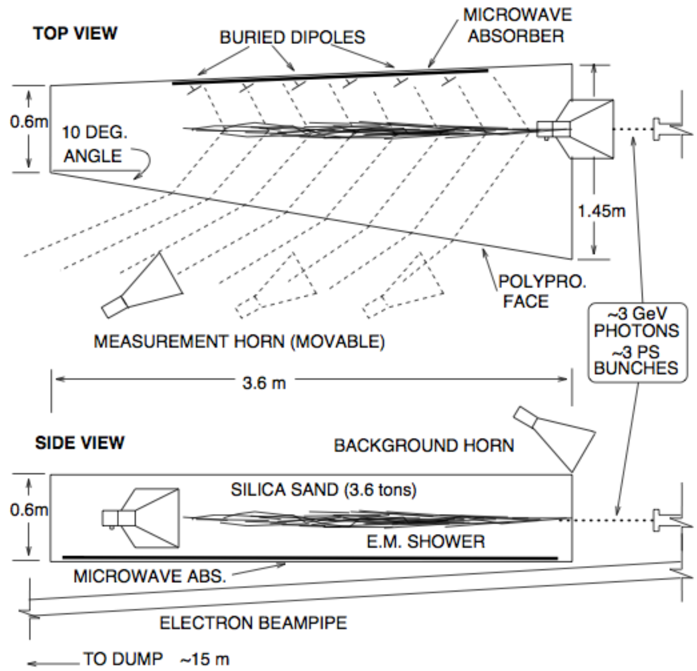

Figure 3.2: Experimental set up for the 2000 SLAC run designed to measure Askaryan radiation in silica sand [25].

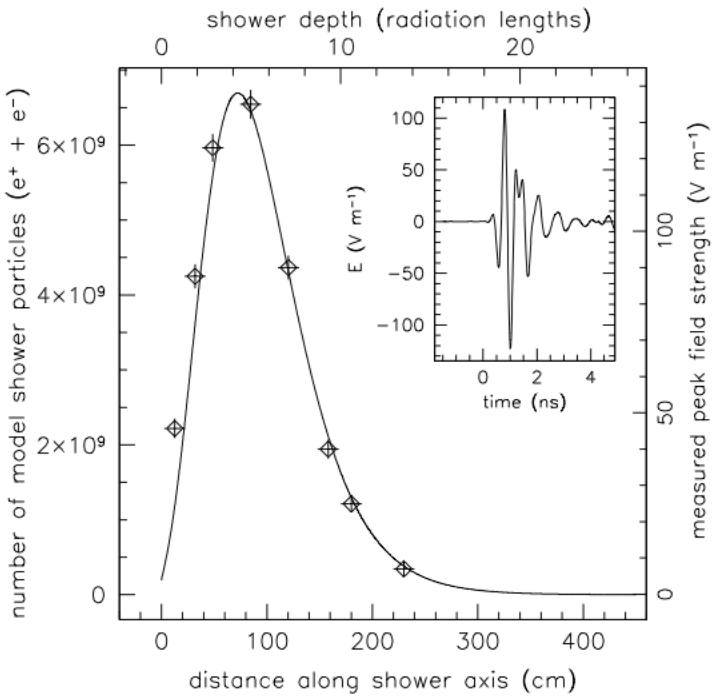

Figure 3.3: Askaryan pulse measured in the 2000 SLAC run [25].

The pulses were determined to be linearly polarized and the field strength scaled linearly with the local particle count in the shower, as shown in Figure 3.3. The field strength was characterized as

$$R\vec{E} = A_0 K \epsilon \left(\frac{W_T}{1\mathrm{TeV}}\right) \frac{\nu}{\nu_0} \left(\frac{1}{1 + 0.4\left(\frac{\nu}{\nu_0}\right)^{\delta}}\right) \left(\mathrm{Vm}^{-1}\mathrm{MHz}^{-1}\right) \tag{3.1}$$

where R is the distance to the source, ν is the radio frequency, and the decoherence frequency is $\nu_0 = 2500$ MHz for silica sand. The coefficients were determined empirically, as $A_0 = 2.53107$, and $\delta = 1.44$. The cascade energy is given as $W_T = N_e \eta W_e$, where N_e is the total number of electrons, η is the thickness of the radiator in radiation lengths, and W_E is the electron energy. Since Equation 3.1 was originally developed for cascades in ice, the factor K is introduced to account for the differences in density and radiation lengths between ice and silica sand. The antenna apertures are only sensitive to ~ 0.5 of the field strength, which is captured in $\epsilon = 0.5$. The form of the equation comes from efforts from Alvarez-Mũniz, Vázquez, and Zas to calculate radio emission from UHE cascades in dense media numerically and in the Fraunhofer limit in the early 2000s [156].

This lab measurement of Askaryan radiation helped justify the first generation of Askaryan cosmic ray and neutrino experiments.

3.4.2 Askaryan Radiation in Rock Salt

The second SLAC Askaryan experiment, located at the Final Focus Test Beam facility in June 2002, used rock salt as a target medium [26]. Rock salt was first suggested as a viable material in which to detect neutrinos by Askaryan. The SalSA concept aimed to make use of salt rock as it is naturally occurring and has a long attenuation length of $\sim$ 250 meters at 200 MHz [21]. Again, bremsstrahlung photons were used to generate the particle showers in the target. Figure 3.4 shows researchers installing antennas in the rock salt target.

Figure 3.4: Image of the 2002 SLAC run to measure Askaryan radiation in salt, a natural medium that could provide a viable experiment target [26].

The 2002 experiment simulated the longitudinal charge excess in the cascade and compared that to the RF amplitude profile (Figure 3.5), confirming charge excess as the source of the Askaryan effect. The Electron Gamma Shower 4 (EGS4) Monte Carlo code was used as a baseline simulation with which to compare the results of the experiment [165]. RF emission wasn't included in this simulation, but estimates were made from the longitudinal and lateral distribution of particles in the cascade. This was an important first step in comparing experimental results to simulation.

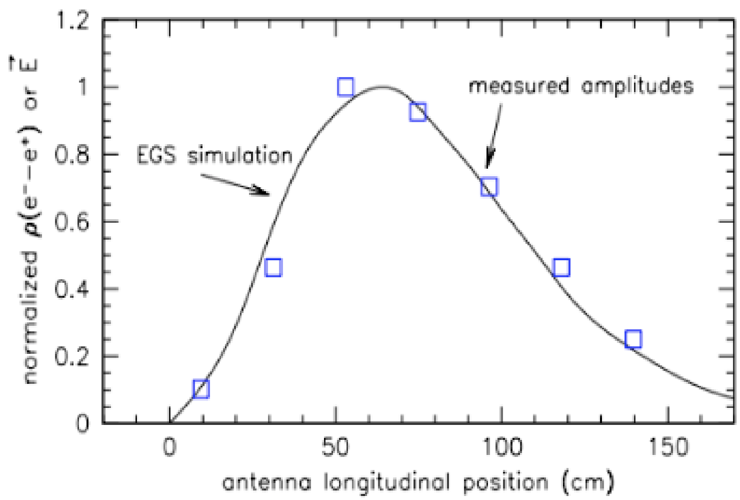

Figure 3.5: The measured amplitude of RF pulse is shown as a blue square. The normalized predicted strength of emission (based on the lateral and longitudinal particle distribution predicted by EGS) is shown as a solid line [26].

Finally, the power contained in a Cherenkov pulse was shown to scale quadratically with electromagnetic cascade energy, as seen in Figure 3.6.

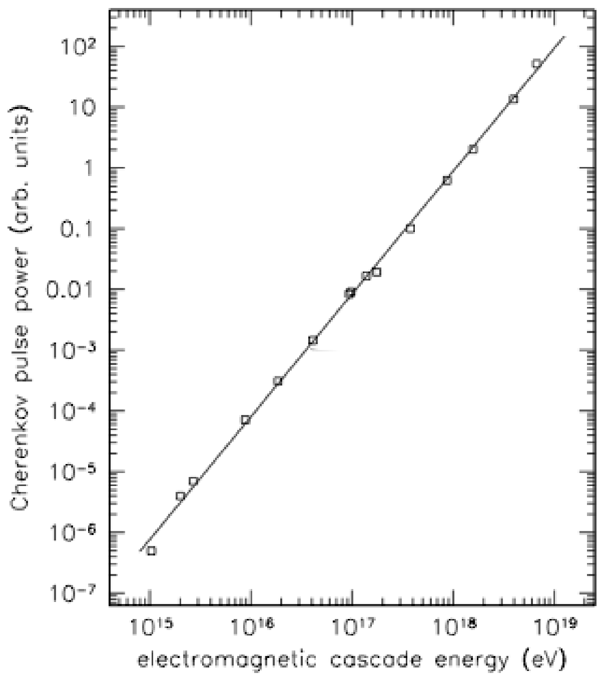

Figure 3.6: Askaryan pulse due to excess charge in the particle shower as a function of cascade energy [26].

3.4.3 Askaryan Radiation in Ice

Following the success of the rock salt experiment the ANITA collaboration designed an experiment to detect Askaryan radiation using carving grade ice as a target material in 2006 [27]. As part of the ANITA I pre-flight integration, a 1.5 by 2 by 5 meter ice target was used to beam Askaryan radiation onto the ANITA instrument (Figure 3.7). The ice was sloped at an 8° angle to avoid total internal reflection.

Electrons of energy 28.5 GeV produced showers on a 10 nanosecond time scale in bunches of 10^9 particles. It is estimated that 90% of the shower developed in the target. EGS simulations predicted a 20% charge asymmetry.

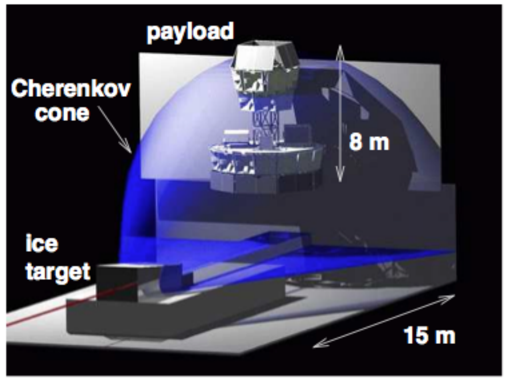

Figure 3.7: Schematic of the 2006 SLAC experiment designed to detect Askaryan radiation in ice using the ANITA instrument as a detection tool [27].

The ANITA payload was used to detect the radio emission in the range between 200 − 1200 MHz. The layout of antennas on the ANITA frame allowed for multiple antennas to sample a single wavefront in two polarizations. A sample radio pulse is shown in Figure 3.8.

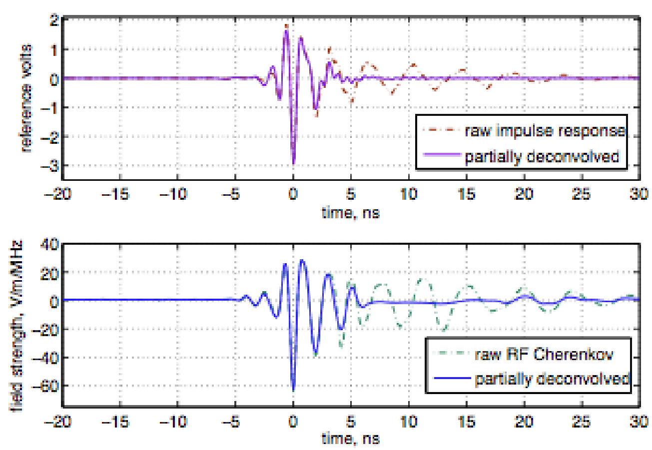

Figure 3.8: Top: Impulse response of the ANITA experiment, raw and partially-deconvolved. Bottom: Pulse observed near the peak of the Cherenkov cone, raw and partially-deconvolved. The deconvolution process removes ringing in the signal caused by filters in the signal chain [27].

Results showed that the observed Cherenkov power in the 200-1200 MHz frequency band scaled quadratically with shower energy (Figure 3.9) and provided proof of principle for radio detection of Askaryan radiation in ice.

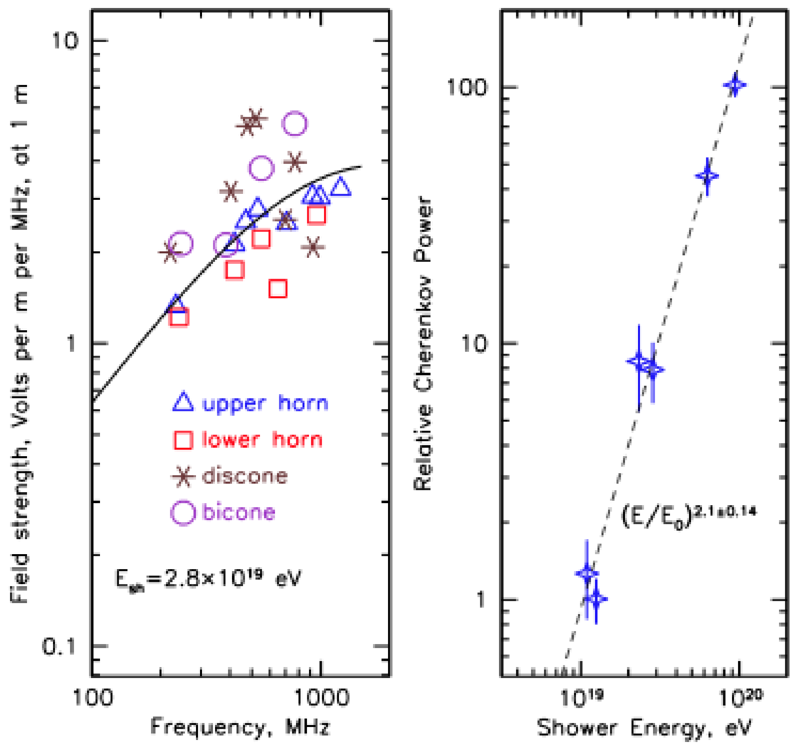

Figure 3.9: Experimental results for field strength as a function of frequency and radiated Cherenkov power as a function of shower energy [27].

The SLAC experiments paved the way for the SLAC T-510 experiment that probed the nature of magnetically induced and Askaryan radiation. SLAC T-510 is discussed at length in Chapters 5 and 6.

3.5 ANITA

ANITA (ANtarctic Impulsive Transient Antenna) is a balloon borne antenna array that was designed to detect Askaryan radiation from neutrinos interacting in Antarctic ice. The geometry of an ANITA neutrino event is shown in Figure 3.10. UHE neutrinos skim the surface of the Antarctic continent and interact in the ice, producing a particle cascade. Askaryan radiation is generated and refracts out of the ice. Because radio wavelengths have a long attenuation length in ice, this radiation can be seen by antennas suspended on a balloon floating 35 km in the air, giving it a large field of view. ANITA was also found to detect radiation from UHECRs in the atmosphere, either directly, or from the radiation reflecting off of the ice [22].

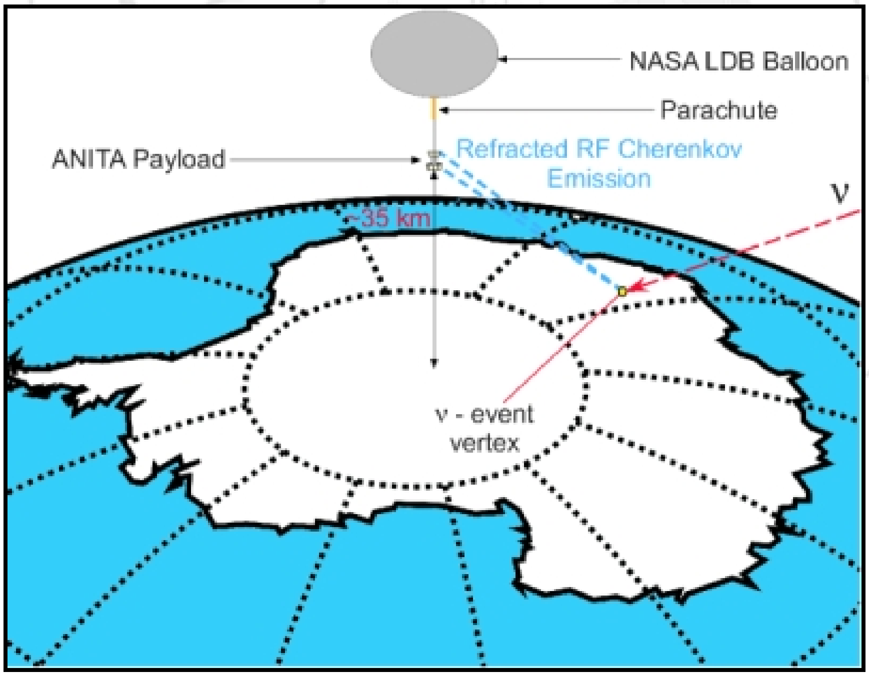

Figure 3.10: Diagram of the ANITA concept. A neutrino interacts in Antarctica ice. ANITA's radio array detects Askaryan radiation [166].

Ice makes a good target medium because it is a radio-frequency dielectric with low attenuation and naturally occurs in large volumes. The attenuation in ice can be expressed as

$$\alpha(dB/m) \approx 8.686\sqrt{\frac{\mu_0}{\epsilon_0\epsilon'}}\frac{\sigma}{2} \tag{3.2}$$

where μ_0 is the permeability of free space, ϵ_0 is the permittivity of free space, ϵ' is the real part of the relative permittivity of ice, and σ is the conductivity of the ice [167]. The conductivity depends on ice temperature and impurities. A map of the attenuation in Antarctic ice at 0.6 GHz is given in the left panel of Figure 3.11. The data presented

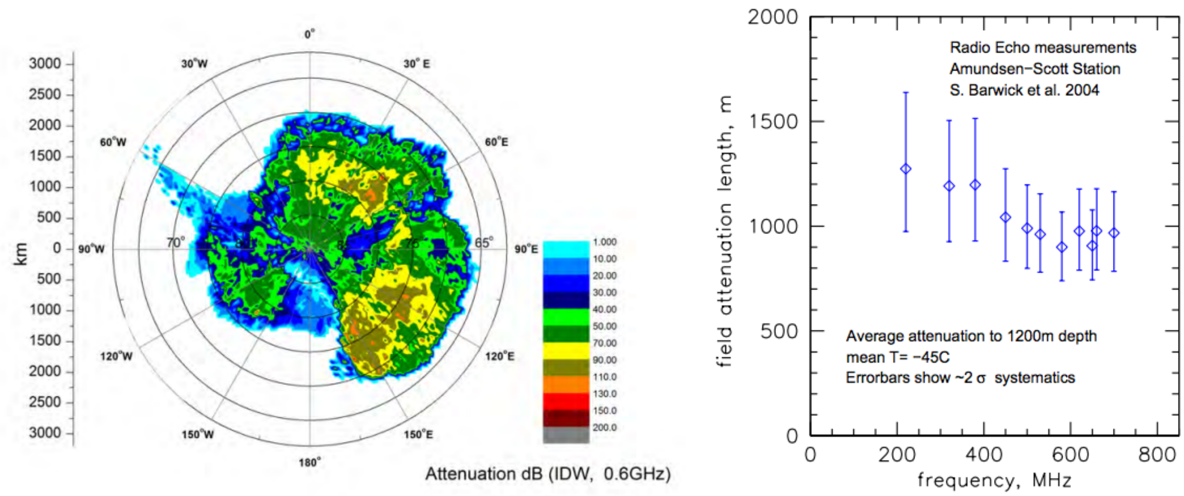

Figure 3.11: Left: Antarctic ice attenuation at 0.6 GHz [167]. Right: Attenuation length as a function of radio frequency, as measured at the South Pole [168].

is interpolated from measurements made of the return power of a signal reflecting off of the bedrock. More details can be found in [167]. The right panel of Figure 3.11 shows field measurements of the attenuation length of ice at the South Pole between 200 and 700 MHz made by Barwick et al [168]. From Equation 3.5, we estimate that the ice attenuation at the pole is ~ 0.03 dB/m, which is consistent with the right and left panels in Figure 3.11.

Through 2015, there have been three ANITA flights and a prototype mission. ANITA-LITE flew for 18.5 days in the austral summer of 2003 piggybacking on the TIGER experiment. The 2003 payload included two antennas and preliminary electronics. A primary measurement made during this flight was the radio background in Antarctica [169]. ANITA 1 consisted of a full payload of 32 antennas distributed in 16 phi sectors and two levels to have a uniform view of ice. ANITA 1 flew in 2006 for 35 days. ANITA 2 included another layer of antennas bringing the total to 40. The ANITA 2 flight lasted 31 days. ANITA 3 had 48 antennas and flew for 22 days in the austral summer of 2014 and is discussed further in Chapter 7.

ANITA uses dual polarization quad-ridged Seavey horn antennas with a bandwidth of 200-1200 MHz. As with all remote experiments detecting impulsive events, triggering is critical and is built into the ANITA instrument. If antennas in coincident phi (azimuthal) sectors detect a plausible signal, the data is recorded. Extensive offline data analysis is required to rule out anthropogenic noise and continuous waveforms (CW). No neutrinos have been detected, but new neutrino limits were set. ANITA-lite and ANITA-1 both transformed the linearly polarized Seavey signals into left and right handed circularly polarized signals for triggering purposes. This allowed for the unintended result that ANITA 1 saw 16 UHECRs. The neutrino signal has primarily vertical polarization for ANITA geometry. Because of the orientation of the magnetic field in Antarctica, the cosmic ray signal is predominantly horizontally polarized, so the mixing of the signal allowed for triggers from cosmic rays [16]. ANITA 2 used a trigger optimized for the vertical neutrino signal, and so was not able to see many cosmic rays, although a few high energy events were strong enough to trigger. Again though, a new neutrino limit was set [23]. Figure 3.12 shows the limits set by both ANITA 1 and ANITA 2. At the time of flights ANITA was able to set the most stringent limits on UHE neutrino fluxes above 10^{19}eV, putting tension on the most optimistic neutrino flux models [170].

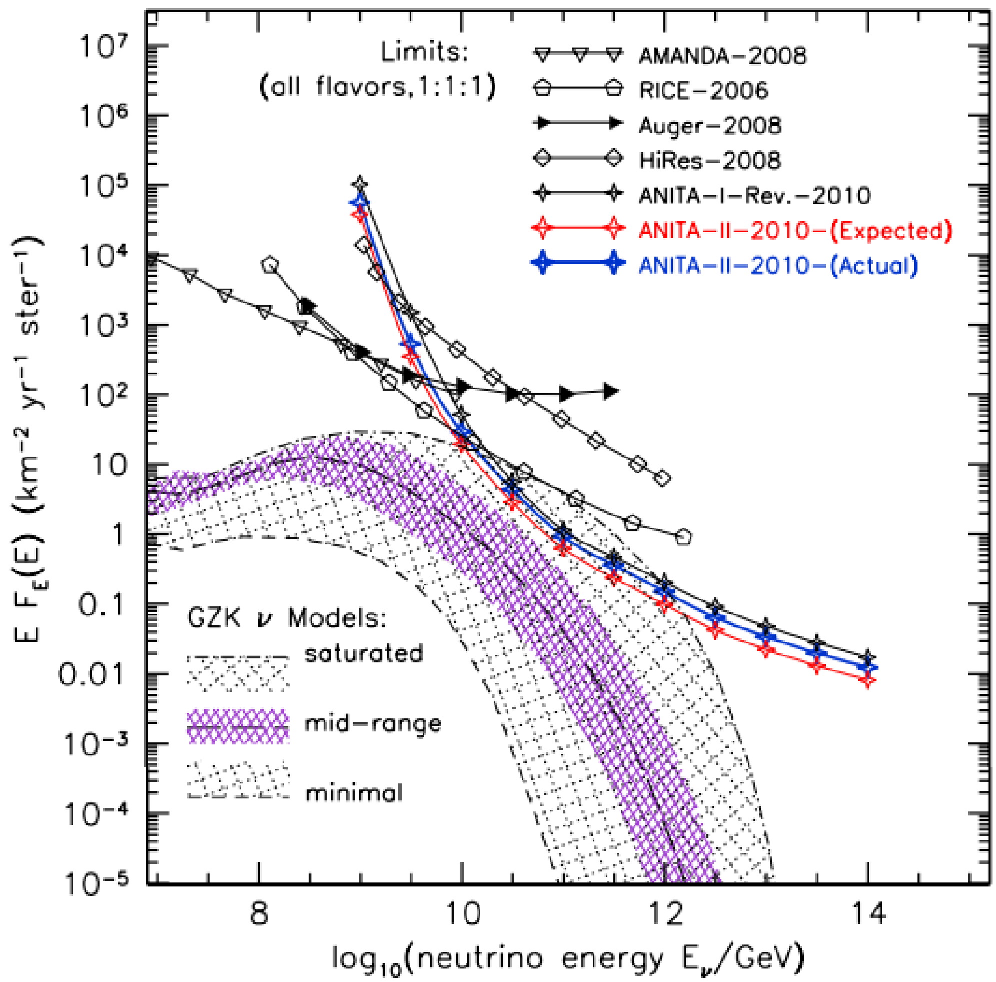

Figure 3.12: Neutrino flux limits set by ANITA 1 and ANITA 2 flights [23].

ANITA 1 cosmic ray events have been under analysis since they were identified. Reconstructing the energy of such events relies on accurate simulations, which were not available at the original time of discovery. Since then, the simulation code ZHAires [162] has been used to produce a library of high energy cosmic ray events. Features of the measured frequency spectrum were compared to simulations to estimate the original energy, as described in [171]. Figure 3.13 shows the results of ANITA 1 energy reconstruction, which are compatible with the Auger and TA experiments which detect CRs in the same energy regime. ANITA 3 flew a trigger which was redesigned to include signals from CRs.

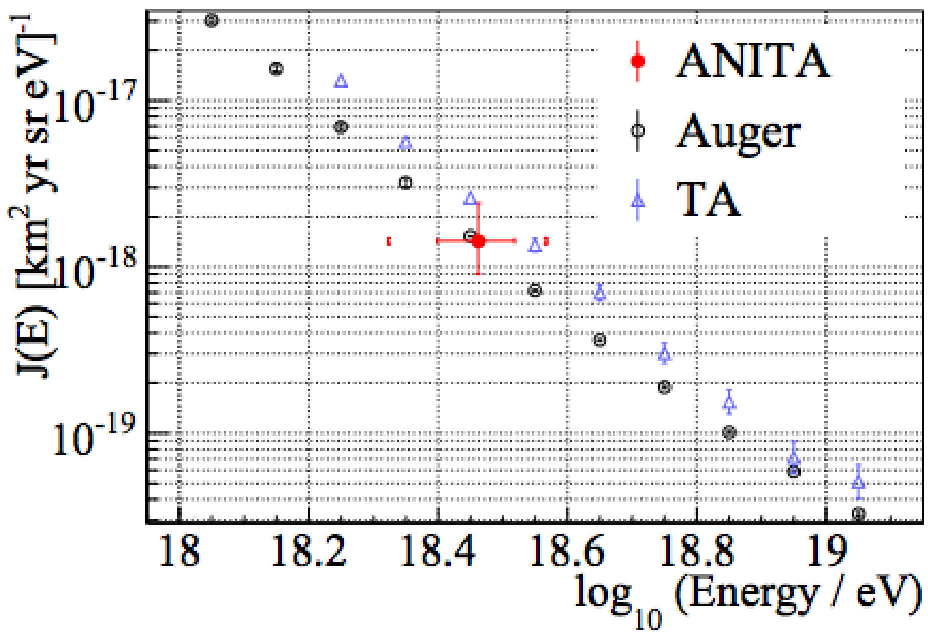

Figure 3.13: Results of the energy estimation for the 14 reflected cosmic ray events from the ANITA 2 flight [22].

ANITA is the first experiment to detect cosmic ray air showers so inclined that they don't intersect with the Earth. This allows for comparison of radio emission directly from the air shower, in the case of highly inclined showers, to radio emission from showers with steeper zenith angles that has reflected off of the ice. The change in sign of the electric field for reflected events is important for the signal identification of cosmic ray events. ANITA has also been among the first experiments to characterize radio events using Stokes parameters. This formalism makes it convenient to look at intensity, linearity, and component mixing of the signal in an intuitive way [172].

3.6 Ground Based Radio Efforts

Ground based radio detectors are effective for a number of reasons. Antenna arrays are relatively inexpensive to build and have a high duty cycle compared to optical and fluorescence detectors. Radio telescopes built for astronomy purposes are already in place, and can also be used for cosmic ray air shower detection. Radio arrays can also be built on large scales, allowing for detection of UHE particles. This section describes current efforts to use radio detection for cosmic ray air showers and neutrino induced cascades in dense media.

3.6.1 Cosmic Ray Air Shower Detection

The primary source of radio emission from air showers arises from the geomagnetic effect, where electrons and positrons in the shower drift in opposite directions. The Askaryan, or charge excess, effect, exists in air showers but it is non-dominant. The superposition of these two effects is detected by radio antenna arrays, and contains information about the direction, energy, and composition of the cosmic ray primary. The radiation is forward beamed because the shower is traveling at relativistic speeds, and compressed in time, and therefore coherent at high (GHz) frequencies for an observer on the Cherenkov cone [146]. The radio experiments discussed in the following sections have moved past proof of principle and use radio techniques to detect multiple observables of UHE particles.

3.6.1.1 LOPES

LOPES (LOFAR Prototype Station) was a prototype radio experiment associated with LOFAR [10]. It consisted of 40-80 MHz antennas and operated in coincidence with the existing KASCADE-Grande air shower experiment [173] located at the Karlsruhe Institute of Technology. KASCADE-Grande used ground level particle detectors to measure air shower energies ranging from 100 TeV to 1 EeV. LOPES radio data provided new, complementary information that was useful in precise reconstruction of air showers. Thirty quasi-omnidirectional dipole antennas were arranged in an array on top of the existing KASCADE detectors. LOPES demonstrated the ability of an array of radio antennas to detect UHECRs and provided a proof of concept for future radio arrays that would operate in a more radio quiet area, making triggering and reconstruction of features of the primary particle feasible. LOPES disbanded in 2009.

3.6.1.2 CODALEMA

The CODALEMA (Cosmic-ray Detection Array with Logarithmic Electro--Magnetic Antennas) experiment in Nancay, France, uses a combination of scintillation and radio self-triggering methods. It provided early experimental evidence for geomagnetic and Askaryan emission mechanisms [11] [174]. There is a sparse scintillator array to cross check radio data. CODALEMA operates in the 20-200 MHz frequency range. The experiment is still running and extensions are looking for transition radiation from air showers terminating at ground level [175].

3.6.1.3 LOFAR

The LOFAR (Low Frequency Array, Figure 3.14) antenna array is based in the Netherlands, with satellite stations across Europe. A densely packed super-terp contains 24 stations of 96 antennas in the 30 - 80 MHz band. LOFAR is primarily designed for interferometric radio astronomy, but has recently proven very useful as an UHECR detector in the range of 10^{17}eV. A scintillator array is used to trigger radio readout and provide energy and direction information [176]. A few hundred antennas across multiple stations contain data for a typical cosmic ray event [12]. Because of its dense spacing, LOFAR has been used to provide high precision X_{max} reconstructions (up to 20 g/cm^2) comparable with the fluorescence technique [177].

Figure 3.14: Overhead view of the Superterp at the LOFAR Radio Telescope [178].

3.6.1.4 AERA

The AERA (Auger Engineering Radio Array) antenna array is operated at the Pierre Auger Observatory [9]. The array covers 17 km^2. Like LOFAR, it operates between 30-80 MHz. AERA radio data can be correlated with data from Cherenkov water detectors and underground muon detectors. Fluorescence detectors also make measurements of X_{max}, and so provide a source of cross calibration.

3.6.1.5 Tunka-Rex

The Tunka-Rex (Tunka-Radio EXtension) experiment consists of 38 dual-polarized antennas that operated in conjunction with the Tunka-133 and Tunka-Grande cosmic ray experiments at Lake Baikal in Siberia. This set of experiments operates in the EeV energy range [112]. Cosmic ray air showers are simultaneously detected with radio antennas, water Chernekov detectors, and surface and underground scintillator stations. Tunka-Rex aims to measure X_{max} with both radio and Cherenkov techniques.

3.6.2 Detection of Cascades in Solid Media

The Askaryan effect is the primary emission mechanism for cascades in dense medium due to the shortened cascade length, but the underlying physics principles are the same as the case for air showers. Neutrino detection experiments make use of naturally occurring dense media such as Antarctic ice or the lunar regolith.

3.6.2.1 ARA

The Askaryan Radio Array (ARA) is a radio detector based at the south pole. An array of buried antennas is designed to detect Askaryan radiation induced by neutrinos interacting in the Antarctic ice. The antennas are organized in stations spaced 2 km apart and buried in the ice 200 meters deep to avoid refractive shadowing effects. Radio signals are detected in a frequency range of 150 - 850 MHz. The location of ARA allows it to work in coincidence with other neutrino experiments at the south pole, such as IceCube. Currently, there are 3 operating stations, with a plan for a larger grid of 37 stations once the concept has been established (Figure 3.15) [14].

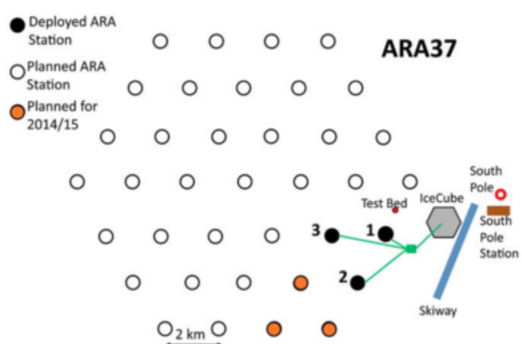

Figure 3.15: ARA detector based at South Pole Station [14].

3.6.2.2 ARIANNA

The ARIANNA (Antarctic Ross Ice Shelf Antenna Neutrino Array) also looks for neutrino signals generated in ice. In this case antennas on the surface look for neutrino signals bouncing off the bottom of the Ross Ice Shelf which acts as a mirror. The frequency range is 50 1000 MHz. There are currently 8 stations with 4 antennas each with plans to eventually have a 36 x 36 station array with 1 km spacing. ARIANNA will be sensitive to energies higher than 2×10^{17} eV [15][179].

3.6.2.3 Lunar Techniques

The lunar regolith is also a promising detection medium. Cosmic rays and neutrinos interact in the fine material from meteorite impacts that covers the entire surface of the moon [180]. The moon provides a natural large detection area, with a visible area of 1.9×10^7 km^2 [181]. Multiple experiments have already provided a proof of concept and early limits for neutrino fluxes from the moon, including Parkes [17], Goldstone [18], VLA [19], and Westerbork [20]. Currently, the NuMoon experiment is in development at the LOFAR radio telescope [182] and lunar detection of UHE particles is planned for the future SKA radio telescope [181].

Chapter 4

PRODUCTION OF RADIO EMISSION FROM AIR SHOWERS

4.1 Introduction

High energy particles interact in media they encounter, such as ice or air, and produce a cascade of secondary particles. Depending on the type of primary particle, the cascade can be electromagnetic, hadronic, or a combination of the two. The charged components of the cascade, dominated by electromagnetic components, emit in the radio regime. The features of radio emission from particle cascades were predicted by Askaryan in 1962 [7]. Radio emission can be qualitatively described as developing from two primary mechanisms. The Askaryan effect refers to the charge excess that develops in the cascade due to positron annihilation and Compton scattering, among other processes. This charge excess moving at relativistic speeds produces coherent radiation at locations that satisfy an approximate Cherenkov-cone geometry. In the presence of a magnetic field, positrons and electrons in the cascade separate due to the Lorentz force, creating a transverse current, which also radiates coherently [146]. In both cases the coherence of the radiation is dictated by the motion and dimensions of the cascade as projected to the observer. The direction and intensity of the currents affects the polarization and strength of the radiation.

The emission mechanisms manifest differently in different media. In a dense medium, such as ice, the Askaryan effect is more pronounced, and is effective for neutrino detection. In a low density medium like the atmosphere, an air shower develops over a longer distance and the Earth's magnetic field is strong enough to provide a transverse current that produces coherent radiation detectable with ground based and airborne detectors [159]. Properties of observed radio emission can be used to reconstruct parameters of the primary particle. The amplitude of the radio emission scales with the number of particles in the cascade, and thus with the primary particle energy. The arrival direction of the radiation can be reconstructed using timing differences between antennas in a given experiment. For ground arrays, imaging the Cherenkov cone allows for the reconstruction of the shower axis. For airborne instruments like ANITA, the polarization and frequency spectrum must be used, as the full cone cannot be imaged. For in-ice cascades, the polarization, spectrum and amplitude of the signal are used to reconstruct the cascade geometry. Recently, radio signals have been used to reconstruct the shower maximum of cosmic ray air showers, which yields information about the composition of the primary cosmic ray [177].

Physics results rely on comparing simulations to experimental data. With increasing levels of detail, simulations include modeling cosmic ray and neutrino flux models and their interactions in target materials, the resulting particle cascades with the production of radio frequency radiation, and detailed response of detector instrumentation. The particle cascades and radio emission may be modeled analytically or by particle Monte Carlos. Such simulations track individual particles in the cascade and calculate and sum the electromagnetic fields to find the field strength at a defined observer position [24][161]. A major goal of T-510 was to test the paradigms of the emission models and validate the most detailed particle Monte Carlo codes.

This chapter gives an overview of particle cascades and radio emission, as well as current approaches to simulation. Section 4.2 introduces particle cascades with a focus on cosmic ray air showers. Electromagnetic and hadronic cascades are discussed, as well as the differences between cascades in air and in solid media. A derivation of the electric field generated from a current density is given in Section 4.3, which is the form used to calculate radio emission from particle cascades. This formalism is developed without assumptions about emission mechanisms. Askaryan and geomagnetic emission mechanisms are introduced later in Section 4.3. Finally, Section 4.4 gives an overview of current simulation techniques, specifically the ZHS and endpoint formalisms relevant to the discussion of SLAC T-10 in Chapter 6.

4.2 Particle Cascades

Particle cascades are critical for detection of UHE particles. As a primary particle enters a medium, it has a chance to interact, depending on its energy and cross section. UHECRs interact with the Earth's atmosphere shortly after entry, and neutrinos interact via charge or neutral current interactions in dense media [183]. After the first interaction, secondaries are produced. Gammas, electrons, or positrons produce electromagnetic cascades, and hadronic secondaries produce hadronic cascades. Neutrinos can undergo deep inelastic scattering where they produce a"recoil" hadronic cascade and an outgoing lepton, which depending on the interaction details and neutrino flavor, may initiate additional cascades. Hadronic cascades consist primarily of pions and kaons interacting with nuclei. As hadronic cascades evolve, they develop electromagnetic components via π^0 decay, and leptons and neutrinos through $\pi^{\pm}$ and $K^{\pm}$ decay.

Figure 4.1 shows an example of a cosmic ray induced cascade from two points of view. On the left, the particle development from a proton induced shower is sketched. In this example, the proton primary initiates a hadronic cascade with electromagnetic components developing after the first interaction. A muon component resulting from $\pi^{\pm}$ decay is also visible. On the right, the physical dimensions of the shower are shown in relation to ground detectors.

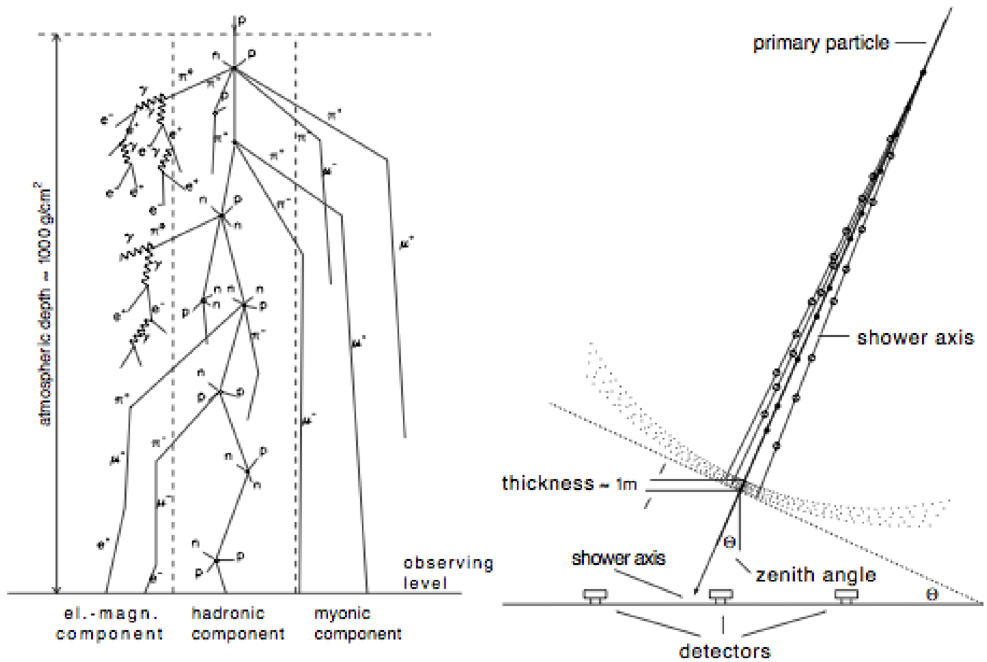

Figure 4.1: Example of a particle cascade induced by a primary cosmic ray [184].

Cascades can be characterized by their longitudinal development, transverse size, and shower thickness. The particle density for species i is

$$\rho_i(x, y, z, t) = n_i(t) f_i(r, t) h_i(\tilde{z}, r, t) \tag{4.1}$$

where $n_i(t)$ is the number density and describes the longitudinal development, $f_i(r, t)$ the transverse, and $h_i(\tilde{z}, r, t)$ the shower thickness, where $\tilde{z} = z - ct$.

When considering the current distribution, as is done in Section 4.3, the velocity vector $\mathbf{v_i}(\tilde{z}, r, t)$ of the cascade is also taken into account,

$$\mathbf{J} = \sum_i q_i n_i \mathbf{v_i} \tag{4.2}$$

where q_i is the charge of particle species i. Equations 4.1 and 4.2 are implicitly integrals over energy and phase space. Finding a precise definition for the particle density in a cascade becomes complicated when including things like magnetic fields and changing density of the material in which the cascade develops. Analytic simulations use parameterizations like Equation 4.1, but particle simulation techniques are required to capture the full complexity of cascade development.

Electromagnetic and hadronic cascades, with a focus on air showers, are discussed in Sections 4.2.1 and 4.2.2 respectively. Cascade development in dense media is discussed in Section 4.2.3. Simulations are discussed further in Section 4.4.

4.2.1 Electromagnetic Cascades

We look at electromagnetic cascades using Heitler's qualitative approach [185], and begin by establishing standard cascade terminology. The radiation length, X_0, is the traversed amount of matter over which a high energy electron loses $1/e$ of its energy by bremsstrahlung and pair production processes, and also 7/9 the mean free path for a high energy photon's pair production. It is measured in units g/cm^2 to remain density independent. The critical energy, E_c, of an electron refers to the energy at which bremsstrahlung energy losses and ionization energy losses are equal [73].

As the electromagnetic cascade develops, interactions occur after each radiation length, and the cascade grows as 2^{n} particles after n interactions. At the beginning of the cascade, shower evolution is dominated by bremstrahlung and pair production processes. At the critical energy, ionization losses and Compton scattering dominate and the cascade dies out. The radiation length depends on the medium in which the cascade takes place. The physical length of the cascade scales as X_0/ρ. As a reference for air showers, the radiation length for air is $X_0 \sim 37$ g/cm^2 [73].

Shower maximum, X$_{max}$, is the depth at which the number of particles is the greatest, given as

$$X_{max} \approx X_0 \ln(E_0/E_c). \tag{4.3}$$

The average particle energy at X (in g/cm^2) is

$$E(X) = E_0/N(X) \tag{4.4}$$

where E_0 is the energy of the primary particle. If X_0 is independent of energy, then conservation of energy suggests that the spectrum of secondaries in the cascade is close to $1/E^2$. The number of particles at X_{max} is

$$N(X_{max}) \sim \frac{1}{\ln(E_0/E_c)} \frac{E_0}{E_c}. \tag{4.5}$$

We see that N_{max} is proportional to the primary energy and X_{max} scales as $\ln(E_0)$. The longitudinal profile of the energy deposition can be described using a gamma distribution [186], as

$$\frac{dE}{dt} = E_0 b \frac{(bt)^{a-1} e^{-bt}}{\Gamma(a)} \tag{4.6}$$

where $t = \frac{x}{X_0}$. Estimating the energy deposition as $\frac{dE}{dt} = X_0 n \frac{E_c}{X_0} = nE_c$ and using $n_{max} \sim \frac{E_0}{E_c}$, Equation 4.6 can be used to model the shower profile n(t) in Equation 4.1 as a gamma function.

The lateral energy distribution of a cascade can be described as a narrow core, with a halo of more numerous lower energy particles, and is due to Coulomb scattering off the target nuclei. From [73], the distribution of angles for multiple scattering through small angles can be approximated as a Gaussian with an RMS given as

$$\theta_0 = \frac{13.6 \text{ MeV}}{\beta c p} q \sqrt{x/X_0}[1 + 0.038 \ln(x/X_0)] \tag{4.7}$$

where p is particle momentum, βc is velocity, and q is the charge of the incident particle. In the case that $x = X_0$, this reduces to $\theta_0 = \frac{13.6 \text{ MeV}}{\beta c p} z$. The transverse dimensions of the cascade are due to this scattering, and scale roughly as the Moliere radius,

$$R_M = X_0 \frac{E_S}{E_c}. \tag{4.8}$$

Here, $E_s \approx 21$ MeV [187]. This value differs from the aforementioned 1.63 MeV because the assumption that $E = E_c$ and $x = X_0$ as constant values is too simplistic. About 90% of the cascade energy is contained within a cylinder of radius R_M. Roughly 99% of the energy is contained within 3.5 R_M.

The lateral density in the shower front is given by the NKG function [188],

$$\rho_{NKG}(x,y) = \frac{1}{R_M^2} \frac{2.5}{2\pi} \left(\frac{r}{R_M}\right)^{-1} \left(1 + \frac{r}{R_M}\right)^{-3.5}. \tag{4.9}$$

This is related to the $f(r,t)$ term in Equation 4.1. For an atmospheric density of $\rho_{atm} = 0.82$ mg cm^{-3}, corresponding to a vertical height of 4 km (which is roughly where an air shower might reach X_{max}), $R_M \approx 117$m. In contrast, for the equivalent cascade in ice, the Moliere radius would be $R_M \approx 10$ cm.

Because the transverse dimensions of the cascade are due to small angle scattering, the shower front thickness scales roughly as $h \sim (1 - \cos(\theta))X_0$, where $\theta \sim R_m/X_0 \approx 1/4$ gives $h \approx .03X_0$. The true shower front thickness can only be calculated using simulations [189]. An estimate of the shower thickness near the core of a UHE cosmic ray air shower at X_{max} is of the order of a few meters [160].

The transverse coherence is dictated by R_m. For in-ice cascades the transverse coherence dominates. For air showers, the shower front coherence dominates, since $\theta_c \sim .01$ and $h/R_m \sim 0.1$. This suggests that ground level arrays at 50 MHz are sensitive to the whole shower, while ANITA with sensitivity of $\sim$ 300 MHz is only sensitive to higher energy secondaries in the cascade.

In the case of a particle cascade in a magnetic field, such as an air shower, the magnetic deflection of charged particles also has an effect. In this case, the cascade loses axial symmetry in the velocity distribution of the particles. This is the cause of the geomagnetic effect resulting in radio emission from air showers, discussed in Section 4.3.3.

4.2.2 Hadronic Cascades

Hadronic cascades can be the result of a cosmic ray nucleus interacting with an air molecule or a deep inelastic scattering charged or neutral current neutrino interaction. The details of hadronic cascades may differ depending on the initial interaction, but the essential characteristic is that outgoing quarks “fragment” to produce multiple particles, primarily pions and kaons. These secondaries have low transverse momentum characterized by the scale of strong interactions ($\Lambda_{QCD} \sim 300$ MeV), and so they propagate in the direction of the cascade. Approximating the hadronic cascade as a pion cascade, at each interaction 1/3 of the initial meson energy goes into producing neutral pions, π^0, which in turn decay to two photons, feeding electromagnetic cascades. The other 2/3 of the energy produce $\pi^{+/-}$, which may undergo additional interactions, or decay. For air showers, if the pions are above 100 GeV, they are likely to interact, producing more pions, again with 1/3 being π^0 and feeding the electromagnetic cascade. Below that energy, the $\pi^{+/-}$ decay into leptons, removing energy from the cascade [190]. The charged pions decay via

$$\begin{aligned} \pi^+ &\rightarrow \mu^+ + \nu_\mu \\ \pi^- &\rightarrow \mu^- + \bar{\nu}_\mu. \end{aligned} \tag{4.10}$$

Because of their heavy mass, muons don't lose as much energy via bremsstrahlung radiation as electrons. If their energy is above a few GeV they will survive to the ground. Neutrinos are weakly interacting and represent energy lost from the cascade. For these reasons, ground particle detectors are effective for reconstructing the primary composition using particle detectors. The primary energy can be estimated by considering a combination of electromagnetic particles and muons detected [191]. There are large fluctuations in the particle density in the shower front for hadronic cascades, and the transverse dimensions are wider. These considerations need to be modeled with Monte Carlo simulations, and the uncertainty in hadronic interaction models at high energies is currently a limitation.

4.2.3 Cascades in Dense Media

Much of the previous discussion has focused on particle cascades in air, but it is also important to consider particle cascades in dense media. Dense media such as salt and ice are often proposed as a target material for UHE neutrino interactions because they are found in large, naturally occurring volumes of uniform density and lave long attenuation lengths for radio frequencies.

In dense media, cascades develop in a similar way as in air, but the length scales are different. A typical radiation length is $X_0 \sim 37\text{g/cm}^2$. In air (at 4 km), this is around 400 m, and the Moliere radius at a height of 4km is $R_M \sim 117$ m. For ice, the radiation length becomes 40 cm, and the Moliere radius is closer to 10 cm [192].

Other differences arise in the hadronic cascade development. In air, charged pions below 100 GeV can decay to produce leptons before interacting. In dense media, the pions interact with the media before decaying, so cascade energy continues to be transferred to the electromagnetic component without significant losses to muons and neutrinos. For meson energies above a PeV, even the π^0's interact in a dense medium, so the cascade remains purely hadronic until the energy of secondary pions is below a PeV.

Furthermore, in modeling electromagnetic cascades in a dense medium, one has to consider the LPM effect [193]. At high energies, the cross sections for bremsstrahlung and pair-production decrease due to quantum effects. This effect lengthens the longitudinal development of the cascade [194].

Radio emission from a cascade in high density polyethylene was used in the T-510 experiment, which is discussed in Chapters 5 and 6. The T-510 experiment used an electromagnetic shower in the presence of a magnetic field, and so the main differences between the cascade in T-510 and air showers arise from length scales and the constant index of refraction of n = 1.53.

4.3 Radio Emission from Particle Cascades

Now that distributions of particles in cascades have been discussed, we can look at how the showers radiate in the radio regime. We start with the electric field as the derivative of the vector potential, **A**, which, in turn, depends on the current density in the cascade. In this context, the charges in the cascade are considered as a charge current distribution, **J**. In Section 4.3.1, the current distribution is quantized and an expression for the electric field is derived for an individual particle track. This is important for radio simulations, where the radiation from individual particles in a cascade is summed at the point of an observer. This can be done in either the time or frequency domain, as discussed in Section 4.4. In Sections 4.3.2 and 4.3.3, Askaryan and geomagnetic emission are discussed. These emission mechanisms result from the current distributions that develop in cascades.

The electric field can be written in terms of the vector potential, $\mathbf{A}$, as

$$\mathbf{E} = -\frac{1}{c}\frac{d\mathbf{A}}{dt}. \tag{4.11}$$

The vector potential at the position of an observer is derived directly from Maxwell's Equations by

$$\mathbf{A}(x,t) = \frac{\mu}{4\pi}\int_{\infty}^{-\infty}\frac{\mathbf{J}_{\perp}(x',t')}{|x-x'|}\delta\left(\sqrt{\mu\epsilon}|x-x'| - (t-t')\right)d^3\mathbf{x}'dt'. \tag{4.12}$$

The dielectric constant ϵ and magnetic constant μ are of the standard definition. The average velocity of the current distribution is primarily directed along the cascade axis. The times indicate the source time (t') and the observation time(t), and the delta function gives t delayed with respect to the time it takes the radiation to travel from the source point (x') to the observer point (x).

$\mathbf{J} = \sum q_i n_i \mathbf{v_i}$ is a current density vector, where q_i is the charge and n_i is the number density. $\mathbf{J}_{\perp}$ is the component of the current relevant to the radiation field (derived in [195]). This transverse current is given as

$$\mathbf{J}_{\perp} = -\hat{\mathbf{u}} \times (\hat{\mathbf{u}} \times \mathbf{J}) \tag{4.13}$$

where

$$\hat{\mathbf{u}} = \frac{x - x'}{|x-x'|} \tag{4.14}$$

is the unit vector from the source to observation point.

There are two relevant cascade velocities to consider. In Figure 4.2, we consider the shower velocity, v, along the z-axis and model the "pancake" shower front as $\delta(z' - vt')$. Here, t' is the retarded time that refers to the time the electric field was emitted from the source. (As a reference from Equation 4.1, here $\tilde{z} = z' - vt'$, as z' is the position of the charge pancake.) In Section 4.3.1,the discussion focuses on the spatial and temporal dependence of $\mathbf{J}(x,t)$ which determines the coherent properties of radiation, leading to the Cherenkov cone.

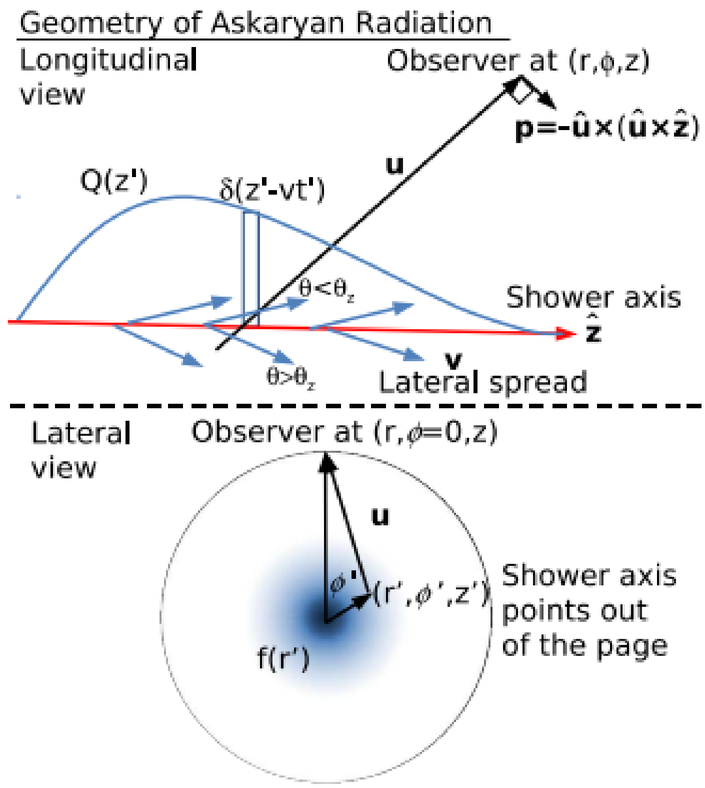

Figure 4.2: Modeled geometry of a high energy particle cascade. The charge excess is treated as a thin pancake with a width $\delta(z' - vt')$ [196].

The particle velocities within the shower determine the current density, which acts as the source for the vector potential and electric field. The current density is given in cylindrical coordinates as

$$\mathbf{J}(x', y', z', t') = \sum q_i n_i(t') \mathbf{v_i}(r', \phi', z') f_i(r', z') \delta_i(z' - vt') \tag{4.15}$$

where the $f_i(r', z')$ term is the lateral charge distribution in the plane perpendicular to the direction of the shower, n_i represents the longitudinal profile, and $\delta_I(z' - vt')$ models the shower front. The radius $r' = \sqrt{(x'^2 + y'^2)}$ is now used. This expression is comparable in form to Equation 4.1, where $\delta(z' - vt')$ now represents the width of the shower front rather than $h(\tilde{z}, r, t)$ in 4.1. This approach is used in macroscopic simulations, and offers an intuitive understanding of the shower progression. The observer sees coherent emission from the cascade on the Cherenkov cone, when emission from points along the track arrive in phase.

To calculate the electric field at the point of an observer, the current densities have to be well known. It is particularly difficult to find analytic forms for the lateral distribution and shower front profiles. For this reason, Monte Carlo techniques are often used, which only require knowledge of the emission produced by individual particles. (Monte Carlo simulations are discussed in Section 4.4.) In Section 4.3.1, we derive the electric field produced by particles in a cascade and discuss the coherence and Cherenkov cone that arise. In Sections 4.3.2 and 4.3.3, the Askaryan and Geomagnetic emission mechanisms are discussed.

4.3.1 Calculation of the Electric Field

We now use equation 4.12 to derive an expression for the electric field at the point of an observer. This discussion of radio emission from a particle cascade comes from [197]. In order to solve for the electric field at a time t and position $\mathbf{x}$, the current must be evaluated at the retarded time $t^{'}$. Since the wavelength of radiation in the shower is large compared to typical particle separations, treating the current in the shower as a smooth distribution is often a valid approach [160]. However, in reality the current distribution is discrete, as it is the sum of contributions from particles in the shower.

The transverse current density for a given particle track between times t_1 and t_2 is

$$\mathbf{J}_{\perp}(\mathbf{x'}, t') = e\mathbf{v}_{\perp}\delta^3\left(\mathbf{x'} - \mathbf{x_0} - \mathbf{v}t'\right)\left[\Theta(t' - t_1) - \Theta(t' - t_2)\right] \tag{4.16}$$

where e is the charge of an electron, $\mathbf{v} = \beta c$ and $\Theta(x)$ is the Heaviside step function defined as

$$\Theta(x) = \begin{cases} \Theta(x) = 1 \text{ if } x > 0 \\ \Theta(x) = 0 \text{ if } x < 0. \end{cases} \tag{4.17}$$

This can be substituted into Eq. 4.16, and the three dimensional delta function can be integrated by substituting $\mathbf{x'} = \mathbf{x_0} + \mathbf{v}t$ and approximating the distance between $\mathbf{x}$ and $\mathbf{x'}$ as

$$|\mathbf{x'} - \mathbf{x_0} - \mathbf{v}t'| \simeq R - \mathbf{v} \cdot \hat{\mathbf{u}}t' \tag{4.18}$$

where $R = |\mathbf{x} - \mathbf{x_0}|$. In one dimension, the delta function is $\delta(t'(1-n\beta\cos\Theta) - (t - \frac{nR}{c}))$ where θ is the angle between $\mathbf{v}$ and $\mathbf{u}$. Eq. 4.16 can then be integrated over t' with the result

$$\mathbf{A} = \frac{\mu e}{4\pi R}\mathbf{v}_\perp \frac{\Theta(t - \frac{nR}{c} - (1 - n\beta\cos\theta)t_1) - \Theta(t - \frac{nR}{c} - (1 - n\beta\cos\theta)t_2)}{(1 - n\beta\cos\theta)}. \tag{4.19}$$

(Note, because this equation diverges when $1 - n\beta\cos(\theta) = 0$, it is not well defined. A formal limit for $\theta \rightarrow \theta_C$ is found by multiplying numerator and denominator by δt, as discussed in [197].) The maximum of this function occurs when $(1-n\beta\cos\theta) = 0$, which corresponds to the Cherenkov angle (demonstrated by P.A. Cherenkov in 1934 [198]), given by

$$\cos\theta_C = \frac{c}{nv} = \frac{1}{n\beta}. \tag{4.20}$$

The corresponding electric field in the time domain is

$$R\mathbf{E}(t, \theta) = \frac{-\mu e}{4\pi\epsilon_0 c^2}\mathbf{v}_\perp \frac{\delta(t - \frac{nR}{c} - (1 - n\beta\cos\theta)t_1) - \delta(t - \frac{nR}{c} - (1 - n\beta\cos\theta)t_2)}{(1 - n\beta\cos\theta)}. \tag{4.21}$$

Using the Fourier transform [197]

$$\bar{f}(\omega) = 2\int_{-\infty}^{\infty} f(t)e^{i\omega t}dt \tag{4.22}$$

and substituting $k = \frac{n\omega}{c}$, the electric field can be written

$$\mathbf{E}(\omega, \mathbf{x}) = \frac{e\mu}{2\pi\epsilon_0 c^2} i\omega \frac{e^{ikR}}{R} e^{i(\omega - \mathbf{k}\cdot\mathbf{v})t_1}\mathbf{v}_\perp \left[\frac{e^{i(\omega - \mathbf{k}\cdot\mathbf{v})\delta t} - 1}{i(\omega - \mathbf{k}\cdot\mathbf{v})}\right]. \tag{4.23}$$

This result can also be derived directly from an explicitly Lorentz covariant approach based on the Lienard-Wiechert potentials, as was originally done in ZHS [24].

Explicit expressions for the electric field, like 4.23, are used in particle level simulations to find the electric field at the point on an observer. The electric fields from individual particles are tracked and summed at an observation point. This sum can be done in either the time or the frequency domain. The ZHS formalism, for example, originally calculated the electric field in the frequency domain. An example of this is Figure 4.3, which shows the simulated frequency spectrum of the electric field seen by observers at different viewing angles for a 10 TeV cascade. Since there is no magnetic field for this simulation, the radiation shown in Figure 4.3 is pure Askaryan radiation. The solid line is the full Monte Carlo simulation, and the dashed line is a one dimensional approximation that ignores the lateral distribution of the shower. The power is the strongest and covers the widest frequency band for an observing angle on the Cherenkov cone. As the observer moves away from the cone, the power decreases as $\sin(\theta)$ (see Section 4.3.2) and the bandwidth decreases due to coherence effects [156].

Close to the Cherenkov cone, the transverse dimensions of the cascade determine the frequencies observed, whereas at larger angular offsets the longitudinal dimensions determine coherence. For in-ice cascades, the shower thickness does not play a large roll. The width of the cone, $\delta\theta$, is inversely proportional to the observing frequency and the longitudinal size of the cascade, as $\delta\theta = \frac{1}{fL_{\parallel}}$. The peak power frequency is inversely proportional to the transverse size of the cascade, as $f_{max} \sim \frac{1}{L_{\perp}}$, so when considering the full frequency band, $\delta\theta = \frac{L_{\perp}}{L_{\parallel}} \sim \frac{R_M}{5X_0} \sim \frac{1}{20}$.

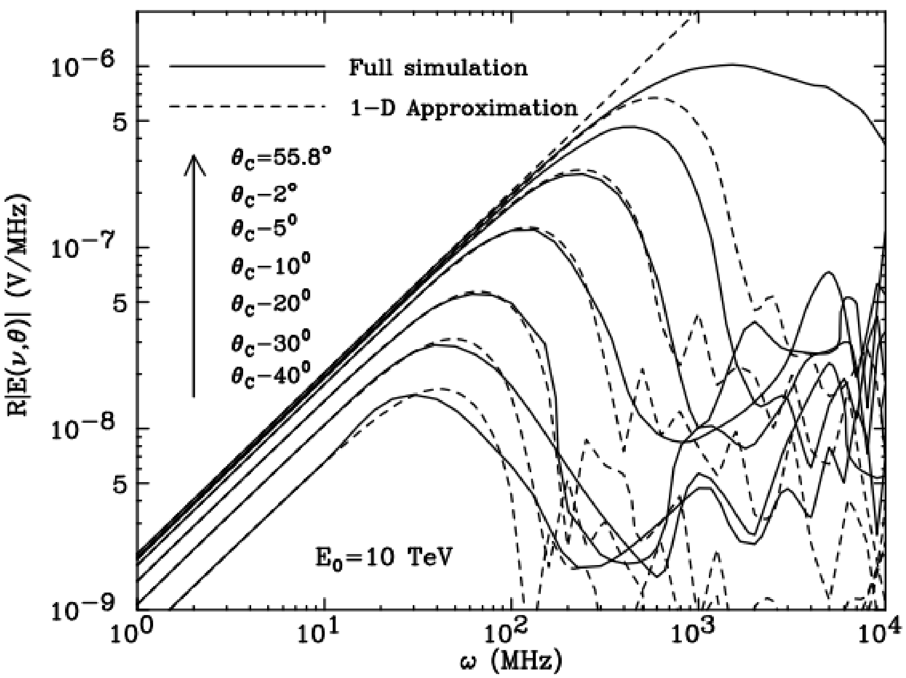

Figure 4.3: Frequency spectrum of the electric field amplitude for observation angles on and off the Cherenkov cone for a 10 TeV electromagnetic shower in ice. Details of the simulation are discussed in Section 4.4 [156].

The electric field generated by particle cascades depends on the index of refraction, n. For cascades in constant media, the Cherenkov angle is consistent. Air showers, however, take place in the atmosphere, which has changing density. In the case of an observer on a well defined Cherenkov cone, radiation from the cascade arrives at the same time, leading to coherent signal. For the case of a changing index of refraction, an observer will be on the Cherenkov cone for a specific emission region. Inside the cone, emission will arrive simultaneously, and therefore be compressed in time. Inside the cone, pulse widths are wider, and emission is also coherent at lower frequencies [146]. In simulation, this is dealt with in two ways. If the bending due to changing index of refraction is large, ray optics can be used to track the radiation. This is what is used for in ice simulations. If the bending is small, one can calculate the resulting phase delay along the line of sight from observer to emission point, as is done in CoREAS [161].

4.3.2 Askaryan Emission

Section 4.3.1 describes the radio emission from a charge current distribution. The Aksaryan effect is one way in which a charge distribution can develop in a particle cascade. As an electromagnetic cascade develops, positron annihilation, Compton scattering, and secondary ionization lead to a 20% negative charge asymmetry [7]. This component of the current distributinon $\mathbf{J}(x)$ is in the direction of the propagation of the shower, $\mathbf{J_q} = (\mathrm{dq})(\mathrm{u})\mathbf{v}$, where dq is the charge excess, n is the number density of charged particles in the shower front, and $\mathbf{v}$ is the vector along the shower axis. Askaryan radiation is polarized in the $\mathbf{u} \times \mathbf{u} \times \mathbf{J_q}$ direction, and so scales with $\sin(\theta)$, as seen in Figure 4.3, and is relatively small in air showers where the Cherenkov angle is small.

Electron-positron annihilation occurs when an electron from the medium in which the cascade is developing and a positron in the cascade annihilate. The process yields two photons to conserve linear momentum and energy

$$e^+ + e^- \rightarrow \gamma + \gamma. \tag{4.24}$$

The process removes a high energy positron from the cascade.

Compton scattering also takes place in the cascade. A photon is elastically scattered off of an atomic electron. In this case, energy from the photon is transferred to an electron. Electrons are further added to the shower via δ-ray scattering when highly energetic particles knock electrons from the medium into the cascade. Askaryan originally estimated the negative charge excess to be 10% in a high energy particle cascade. The charge excess is currently estimated to be $20 - 30\%$ [199]. The result of a charge excess moving at speeds greater than c in the particle shower is coherent radiation. The resulting electric field at the observer is of the form derived in Equation 4.23.

The radiative power at a particular frequency, ΔJ_f, is related to the primary particle energy as follows:

$$\Delta J_f = \left(\frac{e^2\nu^2}{c}\right) f\Delta f \approx 3x\left(10^{-16}E_0\right)^2 \mathrm{mW}. \tag{4.25}$$

The presence of Askaryan radiation in a dense medium was experimentally observed at the SLAC facility in 2000 by Saltzberg et. al (previously described in Chapter 3) [25].

4.3.3 Geomagnetic Emission

In his 1962 paper Aksaryan also hypothesized that a charge separation developing in a particle cascade in the presence of a magnetic field can emit radiation that will add coherently in the radio regime. The Lorentz force causes charged particles in the shower to accelerate along the axis perpendicular to the direction of the shower front and the magnetic field. Particles collide with air molecules, and the net effect is a drift velocity, and therefore an electric current, described as $\mathbf{J_m} = \mathrm{an}(\mathbf{v} \times \mathbf{B})$, where n is the particle density in the shower front, $\mathbf{B}$ is the magnetic field, $\mathbf{v}$ is the velocity along the shower axis. There is also a scale factor, a, that is related to the magnitude of the drift velocity. The drift velocity for charged particles in an air shower is proportional to their mean free path in the atmosphere [160]. For electrons with energy greater than 10 MeV, the mean free path is given as $L = X_0/\rho_{air}$. Geomagnetic radiation is polarized in the $\mathbf{u} \times \mathbf{u} \times \mathbf{J_m}$ direction, scales with $\cos(\theta_C)$, and so, unlike Askaryan emission, is unsuppressed for air showers where the Cherenkov angle is small.

The strength of the radiation scales with the track length of the particles and the transverse velocity. As with Askaryan radiation, the track length scales as $1/\rho$ and the transverse velocity as B/ρ, making the total scale factor B/ρ^2.

Magnetically induced radiation is not particularly useful for cascades developing in dense media, since the dimensions of the shower don't allow for significant transverse current development. It is, however, the primary mechanism by which cosmic rays developing in the atmosphere are detected. In the case of UHECRs, Askaryan radiation is present, but geomagnetic radiation dominates because of the long development of the cascade, and the suppression of Askaryan radiation at small emission angles..

4.4 Simulations

Simulations are critical to the understanding of radio signals from particle cascades, both in dense media and in air. In general, a simulation models a physical system. Particle physics simulations generally consist of a physics component and a detector component. The physics component simulates physical processes, for example, the development of an air shower. The detector component simulates an instrument response and provides a framework for the interpretation of measured data. To explore physics hypotheses, it is necessary to take a step back and consider where the particles included in simulations come from. In the case of cosmic rays, to simulate predicted flux one needs to include source models, cosmic ray energy spectra, realistic composition models, and other considerations discussed in Chapter 2.

Monte Carlo simulations model reality by drawing random numbers from probability distributions. For example, in a Monte Carlo simulation of a cosmic ray air shower, individual cascade particles are tracked. At each possible interaction point the outcome is decided based on a random number draw. The simulation can include different models for electromagnetic and hadronic interactions. After each interaction, more particles are generated and tracked until the particle exits the simulated volume, reaches a detector, or falls below a given energy threshold. Because the simulation is probability based, each simulated shower is different, which reflects fluctuations in real cosmic ray air showers.

In addition to Monte Carlo techniques, there are parameterized simulations for radio emission from cascades. In this case, individual particles are not tracked. Instead, the resulting signal is derived from input parameters such as primary energy, X_{max}, magnetic field, etc. Parameterized methods are much faster than Monte Carlo simulations, but don't capture the natural fluctuations in air shower development.

Parameterized simulations are frequently used for in-ice situations where the target material has constant density.

Before using simulations to interpret experimental data, it is necessary to validate that the simulations produce realistic results. This can be done by performing experiments with known parameters in controlled settings and comparing experimental and simulated results. This is a challenge for simulations involving cosmic rays, because air showers do not take place in a controlled setting. Particle interaction models are generally confirmed in an accelerator setting, and then applied to air showers. (For the highest energy cosmic rays, where the particle energies required in the interactions can not be manufactured in a lab setting, this poses a problem. In fact, there is a discrepancy in the simulated and measured muon content of air showers above 10^{18} eV [200].) As cosmic rays experiments using radio detection developed, there was a greater need for robust simulations of radio emission from particle cascades. Part of the work of this thesis involves validating radio emission simulation packages in a controlled setting, particularly in the presence of a magnetic field.

This section discusses Monte Carlo simulations and how they are implemented for different applications, such as experiment design and interpretation of results.

4.4.1 Monte Carlo Simulation Packages

Two relevant Monte Carlo simulation packages for air shower simulation are CORSIKA (COsmic Ray SImulations for KAscade) [201] and AIRES [164]. These programs track individual particles in the context of cosmic ray air shower propagation. Here, the user can define things like the atmospheric model and local magnetic field. Both use realistic physics processes, like particle interaction and decay, and rely on different models for high and low energy hadronic and electromagnetic interactions. Both packages can provide the user with information about particles at different stages of propagation.

Extensions to CORSIKA and AIRES can be used to derive more information.

For example, and relevant to this work, radio emission from each particle in the cascade can be calculated and propagated to an observation point. This is only possible because Monte Carlo simulations follow each particle in a cascade individually. Two examples of radio emission extensions for air shower simulations are CoREAS [161] and ZHAires [162], and are discussed further in Section 4.4.3.

Geant4 (GEometry ANd Tracking) is a more generic particle tracking Monte Carlo [202]. The Geant4 package propagates particles through a user defined system (material, geometry, magnetic field, etc.). It is used widely in the particle physics community for modeling detectors in accelerator based experiments. This tool was used for T-510 simulations, as the cascades took place in a dense material. In this case, both the endpoint and ZHS formalisms typically used for air shower simulations were adapted for use in Geant4, to provide radio emission from cascades in a polyethylene target.

4.4.2 Detector Simulations

In order to be useful for a specific experiment, realistic detector simulations need to be integrated into Monte Carlo physics simulations. The output of a simulation of a physical process is not necessarily the quantity that is measured in an experiment, and so detector simulations are critical for the interpretation of experimental results. Detector simulations can include features such as losses in cables, antenna models, digitization effects, and filtering. By including a realistic detector simulation, individual cascade events can be modeled end to end.

In order to predict the acceptance or effective area of an experiment, a variety of physics simulations can be run with varying input parameters, including different particle primary energies, compositions, and directions. The results of the simulated air showers would be propagated through the instrumentation, and one can determine whether or not the signal from the shower is large enough to be detected given the detector response. In designing an experiment one would make use of simulations to maximize the effective area of the detector.

4.4.3 Particle Level Radio Emission Simulations

In the early 1990's the ZHS code was developed and could simulate electromagnetic cascades up to the PeV energy range [24][203]. The original ZHS methodology tracks individual particles in an electromagnetic cascade and calculates the expected radiation from the Lienard–Wiechert potentials. Figure 4.3 is an example of the frequency spectrum obtained from a ZHS air shower simulation. The radiation from each particle track is summed, in the frequency domain, at the location of an observer. The endpoint technique is a second approach. Here the particles are also tracked, and radiation is calculated only at the beginning and end of each track and summed at the observer in the time domain. The endpoint formalism was originally implemented in the REAS Monte Carlo package used for high energy cosmic ray air showers [163][204].

Early comparisons of air shower data to simulations showed that some mechanics of the simulations weren't handled correctly. For example, prediction of the time domain pulse shape (from REAS) was not consistent with frequency domain predictions of a bipolar pulse from Falcke and Gorham [159]. The time-domain macroscopic approach from Werner and Scholten in 2007 did produce a bipolar pulse [205].

The radiation component missing from time-domain models was discovered to be due to the fact that the time variation of the number of particles in the cascade was not included [206]. This was accounted for in REAS3 [163]. Since then, both ZHS and endpoint formalisms have been shown to produce consistent results in both the time and frequency domains [156][197][207].

For application to air showers, ZHS and endpoint formalisms are coupled with particle tracking simulations. Currently in use are the simulation packages ZHAires and CoReas [161][162]. ZHAires uses the Aires [164] air shower simulation package and the ZHS formalism, and CoReas uses CORSIKA and the endpoint formalism. These approaches have been shown to be in good agreement, including absolute magnitude [208]. Figure 4.4 shows 2013 results comparing ZHAires and CoREAS results with AERA data [209].

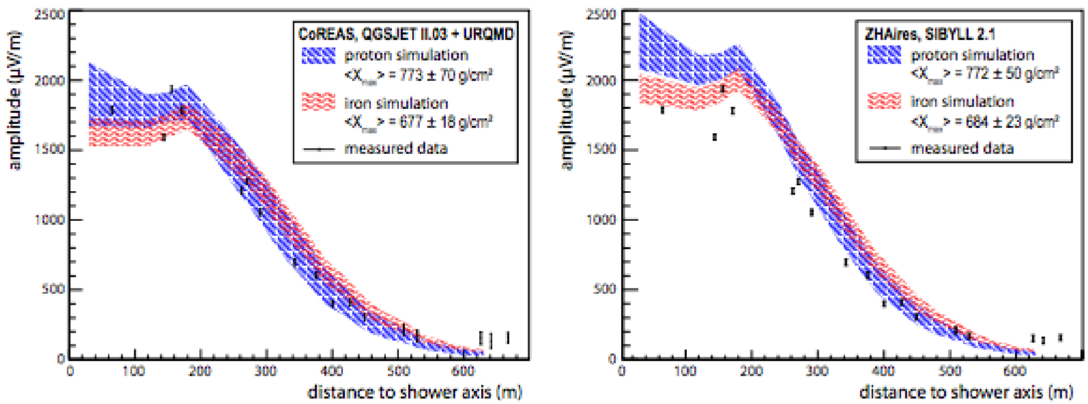

Figure 4.4: Simulated lateral distribution of electric field amplitude using ZHAireS and CoREAS compared with AERA data [208][209].

As mentioned in the previous section, models must be confirmed in order to be used in the interpretation of experimental data. The following two chapters indeed confirm that the ZHS and Endpoint formalisms accurately describe radio emission from particle cascades in a magnetic field.

4.4.4 SLAC T-510 Simulations

Section 4.4 has given an overview of the simulation techniques used in the SLAC T-510 experiment. The T-510 experiment was designed to measure radio emission from a particle cascade in a magnetic field and to compare that measured signal with simulations. In this case, the cascade developed in high density polyethylene, and then the signal propagated out of the target, through air, and to an antenna array. Geant4 was used to simulate the particle cascade. The endpoint formalism generally used for CoREAS air shower simulations was adapted for Geant4 by Anne Zilles at KIT and used to calculate radio emission from track segments. From there, ray tracing was used to propagate the radio signal from point of emission to the observing antenna. Once at the antenna, the electric field was fed through a realistic detector simulation, including antenna response, cable losses, and digitization. At that point, the simulation could be directly compared to experimental data. A more detailed overview of the experiment is discussed in Chapter 5, with the data analysis following in Chapter 6.

Chapter 5

SLAC EXPERIMENTAL SETUP

5.1 Introduction

The SLAC T-510 experiment is an extension of earlier beam experiments to measure the Askaryan radiation from a particle shower in a dense dielectric. Previous experiments have shown this radiation to exist in silica, salt and ice targets. T-510 was the first to introduce an applied magnetic field in the target and to measure its effects on the radiation pattern. The main goals of this experiment were to validate the simulations (specifically ZHS and endpoint formalisms) used to study the radio emission from cosmic ray extensive air showers in the Earth's atmosphere, and to map the RF emission. Understanding the nature of magnetically induced radiation was especially important as radio detection of cosmic ray air showers is becoming increasingly popular, for the reasons discussed in Chapters 3 and 4. The ANITA [210], LOFAR [12], and AERA [9] experiments, among others, have successfully used the radio technique to reconstruct cosmic ray parameters. This chapter covers the design and practical aspects of the experiment. T-510 results and data analysis are discussed in Chapter 6.

5.2 Experimental Design

As discussed in Chapter 4, radio emission from particle cascades is a promising way to detect cosmic rays. In order for the radio emission from a particle cascade to be interpreted, it must be compared to simulations. Radio simulation packages track particles in the cascade and calculate the radiation from each track segment, which is then summed up at the point of an observer. The particle tracks are supplied by simulations that rely on hadronic interaction models, and which have systematic uncertainties. For this reason, the only way to directly compare simulations of radio emission from a particle cascade to data is to perform a controlled experiment with a beam of electrons or gamma-rays. We can use two mechanisms to describe radio emission from secondary cascades: Askaryan and magnetically induced radiation. Askaryan radiation occurs when a charge excess develops in the cascade due to Compton scattering, positron absorption, and δ-ray production. This radiation is linearly polarized and $\vec{E}$ points towards the cascade axis. In the presence of a magnetic field the charges in the cascade form a transverse current, creating radiation that is polarized in the $\hat{\mathbf{u}} \times \hat{\mathbf{u}} \times (\mathbf{v} \times \mathbf{B})$ direction, where $\hat{u}$ is the direction to the antenna. The observer sees the coherent sum of both polarizations, resulting in constructive or deconstructive superposition depending on the geometry of the observer in relation to the cascade. The T-510 experiment was designed such that the beam parameters (energy, charge, etc.) were well known, the particle cascade was contained in the experimental area (i.e. not air shower dimensions) and in the presence of an adjustable magnetic field, and both Askaryan and magnetically induced radiation were present in comparable amplitudes and detectable in separate polarizations.

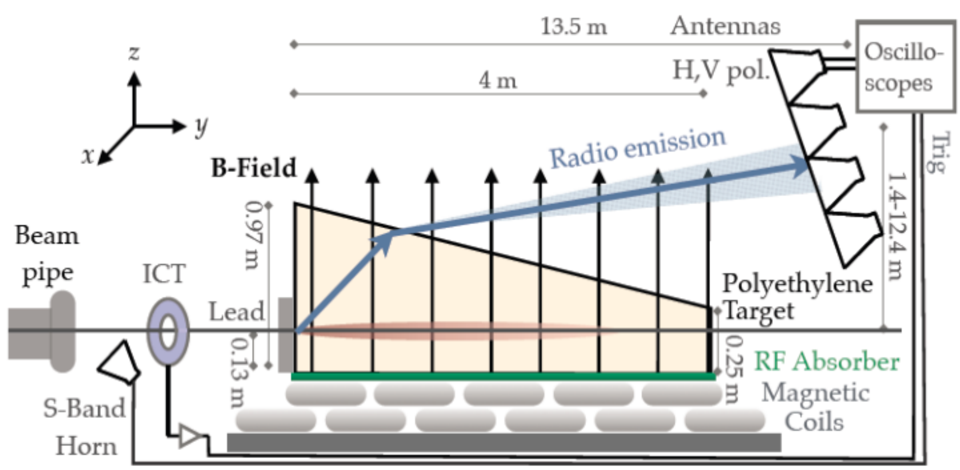

Figure 5.1: Schematic of the SLAC T-510 experiment (not to scale) [28].

A schematic of the experimental set up is shown in Figure 5.1. An electron beam entered through the beam pipe (on the far left), went through beam monitoring equipment, and started to cascade in a segment of lead placed directly before the target. The majority of radiation was generated in the HDPE target, and optionally, in the presence of a magnetic field. The radiation refracted out of the target and was observed by antennas placed in the far field so as to map the shape of the emission. The data was digitized and recorded using oscilloscopes that were controlled in a counting house adjacent to the experimental hall.

For T-510, radiation from the cascade was beamed in a Cherenkov cone pattern intersecting the plane of the observing antennas. Antennas had both horizontally and vertically polarized feeds. Since the cascade developed in a vertical magnetic field, the magnetically induced radiation at the position of the antennas was horizontally polarized. The Askaryan radiation, radially polarized, was present in the vertical polarization of the antenna at the position of observation.

To generate Askaryan and magnetic radiation in comparable amplitudes, the scaling of radiation strength as a function of magnetic field and target density was considered. With the primary beam charge kept constant, the Askaryan radiation scales with the particle track length, which in turn scales with radiation length X_0, and for light elements and compounds approximately as $1/\rho$, where ρ is the density of the target medium. Magnetically induced radiation, however, scales as the drift velocity (magnetic field strength per track length, B/ρ), and the particle track length $1/\rho$, for a total of B/ρ^2. The ratio of magnetic to Askaryan radiation is then B/ρ. For a typical air shower, values of magnetic field and medium density are 0.5 Gauss and 1.225×10^{-3} g/cm^3, respectively. For logistical reasons, the experimental field was scaled to a maximum 1000 G. A target material with a density of 0.97 g/cm^3 was used to maintain reasonable scaling between the T-510 experiment and an air shower while keeping the amplitudes of Askaryan and magnetic radiation comparable, and to contain the majority of the cascade in the target.

There are instances where the measured quantities of the experiment, those reported in publications, and those used in simulations differ. For example, the beam height above the bottom of the target is measured to be 10.2 cm, but 12.7 cm was used in simulations, and Figure 5.1 from [28] shows the beam height as 13 cm. Details of the target dimensions also differ. In this chapter these differences are mentioned where they arise, and estimates of the errors produced as a result of the differences are discussed in Chapter 6.

5.3 SLAC Facility

The SLAC National Accelerator Laboratory is one of ten Department of Energy labs. It is managed by Stanford University. SLAC has several experimental facilities including FACET (Facility for Advanced Accelerator Experimental Tests), NLCTA (Next Linear Collider Test Accelerator), ESTB (End Station (A) Test Beams), and ASTA (Accelerator Structure Test Area). The SLAC accelerator is two miles long, and at the time it was built in 1962 it was the largest particle accelerator in the world. T-510 was housed in End Station A (ESA) of ESTB and was provided a fraction of the beam used by Linac Coherent Light Source (LCLS). ESA provides a venue for large scale experiments, with a 60 meter long cement building and overhead cranes [211].

Figure 5.2: Overhead view of the SLAC End Station A Facility. The red line indicates the beam path and End Station A is circled in blue.

5.4 Beam

The SLAC beam is accelerated in a two mile linear accelerator, as seen in Figure 5.2. Radio waves guide electrons and positrons to high energies in copper cavities. The facility is capable of providing between 2-15 GeV of beam energy with a spread of 0.02%, with the energy being determined by users. The ESA beam piggybacks off of the LCLS beam at a rate of 5 Hz. The average charge per pulse is up to 0.35 nC. The beam is redirected from the LCLS station to the ESA using pulsed magnets. The T-510 beam was 4.35 GeV or 4.55 GeV with a charge of 131 pC corresponding to a 4×10^{18} eV electromagnetic cascade. Charge bunches arrived as picosecond pulses with a transverse structure controlled by a collimator. Calibration of the SLAC beam charge is discussed in this section

5.4.1 Integrating Current Transformer

Early runs indicated that the charge in each bunch was not consistent or known with the accuracy necessary for the T-510 experiment. An integrated current transformer (ICT) was inserted directly after the beam pipe to measure the beam charge pulse by pulse, as seen in Figure 5.3.

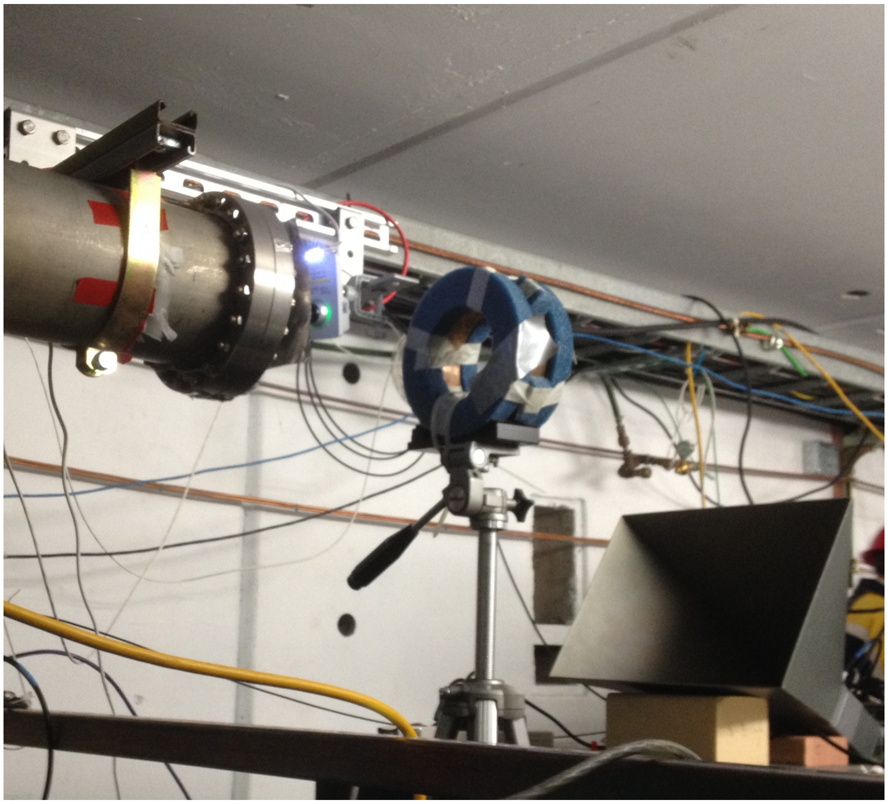

Figure 5.3: Integrating Current Transformer used to calibrate beam charge during T-510 run.

ICTs are special cases of standard current transformers used for applications with short pulse times between 1 ps and 1 μs. The charged bunch acts as a moving current inducing a magnetic field at the location of the current transformer, and therefore a secondary current in the coils of the transformer. Unlike a standard transformer, the ICT stores the charge in a capacitor before discharging it to secondary component of the transformer. Timing information is lost in the process, but charge information is saved [212]. The ICT used during the T-510 experiment was calibrated using an Avtech pulse generator that created pulses of a known charge.

5.4.2 Collimator

The SLAC facility uses a collimator to tighten the transverse dimensions of the beam. The SLAC collimator was set at two different widths during the T-510 runs: 1 cm and 10 cm. We found that the beam charge was more consistent with the collimator “open” to 10 cm, since charge was not “skimmed” off the side of the beam (Figure 5.4). Data was taken with the collimator opened and closed, but only open collimator data was used in analysis.

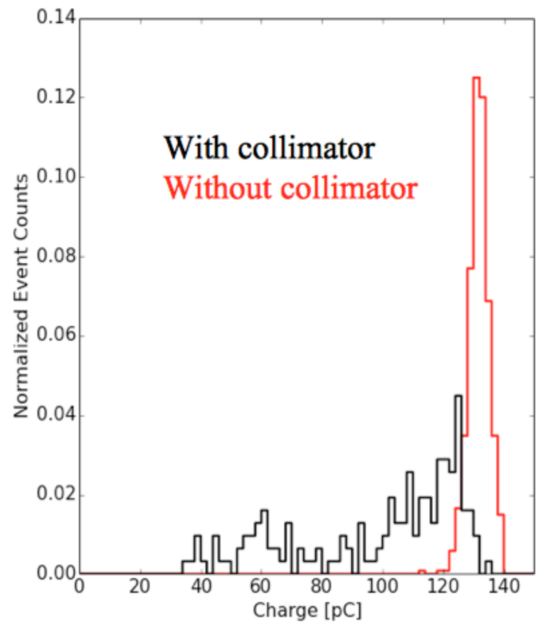

Figure 5.4: Charge Measured by the Integrating Current Transformer with the collimator (1 cm opening, in black) and without the collimator (10 cm opening, in red). The beam charge was found to be more consistent with wide collimator gates.

5.5 Target

The T-510 target, shown in Figure 5.5, consisted of over 1,200 bricks (5.08 cm x 10.16 cm x 30.48 cm) of high density polyethylene (HDPE), with index of refraction n=1.53 $\pm$ 0.005 [213]. An alumina target was originally considered, but simulations showed that it would require 10 kG magnetic field to produce the required magnetically induced radiation, which was not possible to create with the given resources. The target was 3.97 m long, 0.61 m wide, and 0.97 m tall and contained the majority of the particle shower. The top of the target was sloped at 10.16 degrees to prevent total internal reflection, so the angle at which Cherenkov radiation left the target was 28.6°, as shown in the figure. The radiation length of the target material was chosen so that the particle cascade would take place within the length of the target while maximizing the magnetically induced radiation. A 1.27 cm piece of lead (corresponding to 2.27 radiation lengths) was added at the front of the target to preshower the cascade. Simulations use a lead thickness of 1.2 cm, which corresponds to a 6 cm change in longitudinal shower development.

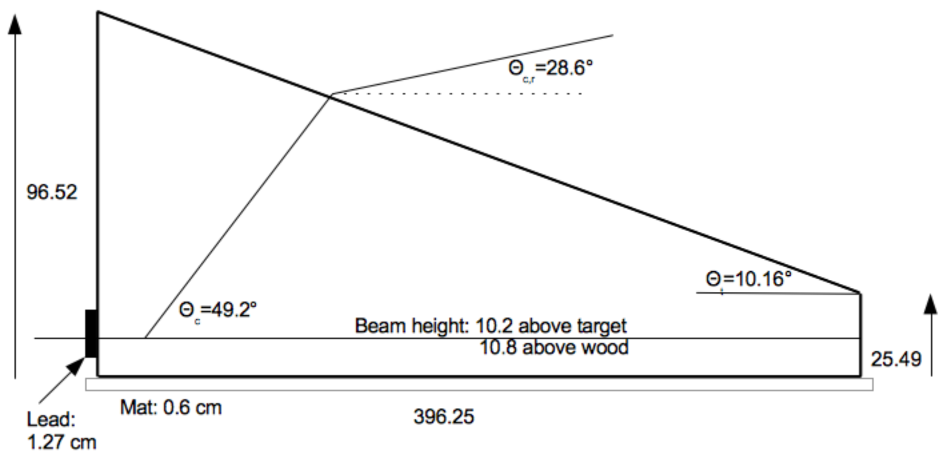

Figure 5.5: Detailed diagram of the T-510 target. Not pictured, but important to the experiment was a 0.6 cm thick radio frequency absorbing mat placed beneath the target. A plywood support was beneath both the mat and the target. The Cherenkov and refracted Cherenkov angles θ_c and $\theta_{c,r}$ are given for n=1.53.

Figure 5.6 is an image from the T-510 run showing the target in place at the end of the beam pipe. ANW-79 radio absorbing foam is seen at the end of the target, and a 0.6 cm thick RF absorbing mat is beneath the target. The target and mat were supported by a wooden platform above coil magnets, described below. After the runs were complete, some HDPE bricks were removed in the area of $X_{\max}$. Figure 5.7 shows burning on the target material along the line of the particle shower, which indicates that the height of the beam was 10.2 cm above the bottom of the target, and 10.8 cm above the wooden platform (including the thickness of the mat). During the experiment, it was estimated that the beam height was 12.7 cm above the wooden platform. That is the reason that in Figure 5.1 the beam height is given as larger than 10.8 cm above the platform, and the magnetic field, discussed in Section 5.9, was measured at 12.7 cm.

Figure 5.6: T-510 target in situ as it was during the experiment. The HDPE bricks sit above coil magnets, cooled by water via the orange tubing.

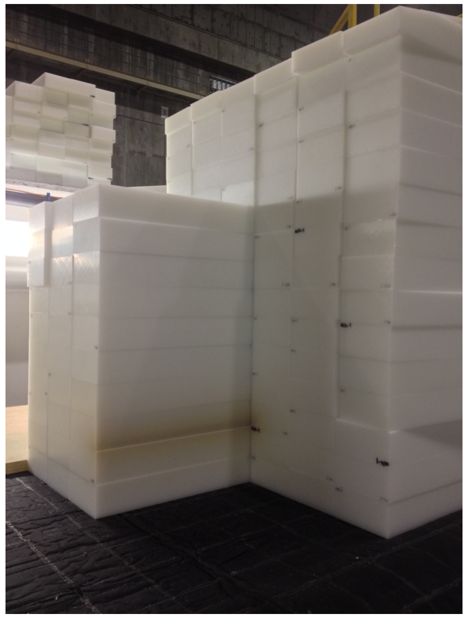

Figure 5.7: Internal view of the target taken after the second T-510 run. Radiation burn from the particle cascade can be seen.

The target shape was designed to beam the Cherenkov cone onto the back wall of ESA at a convenient height for antennas to receive the signal, and to ensure that the cascade stayed within the target. The Cherenkov cone was calculated to peak at 660 cm above the beam line.

5.6 Antenna Set-Up

The antennas used in T-150 were affixed to an adjustable array meant to capture a slice of the Cherenkov cone beamed from the radiation out of the target. The primary antennas used were four dual polarized Seavey antennas, the same as were used in the ANITA 1 experiment, and covered a frequency range of 200-1200 MHz. They were mounted vertically in a column and suspended from a crane that had three dimensional movement. The antennas were tipped towards the target at 19.6 degrees to face the radiation. Two commercially purchased Bicone antennas, one oriented with vertical polarization and one with horizontal polarization, were also mounted in a similar fashion, and covered 50-300 MHz. Finally, two high frequency (3 GHz) Logarithmic

Periodic Dipole Antennas were used, and also mounted to be vertically and horizontally polarized. Figure 5.8 shows the mounting geometry of each antenna. Details of the antenna positions are discussed in Appendix B.

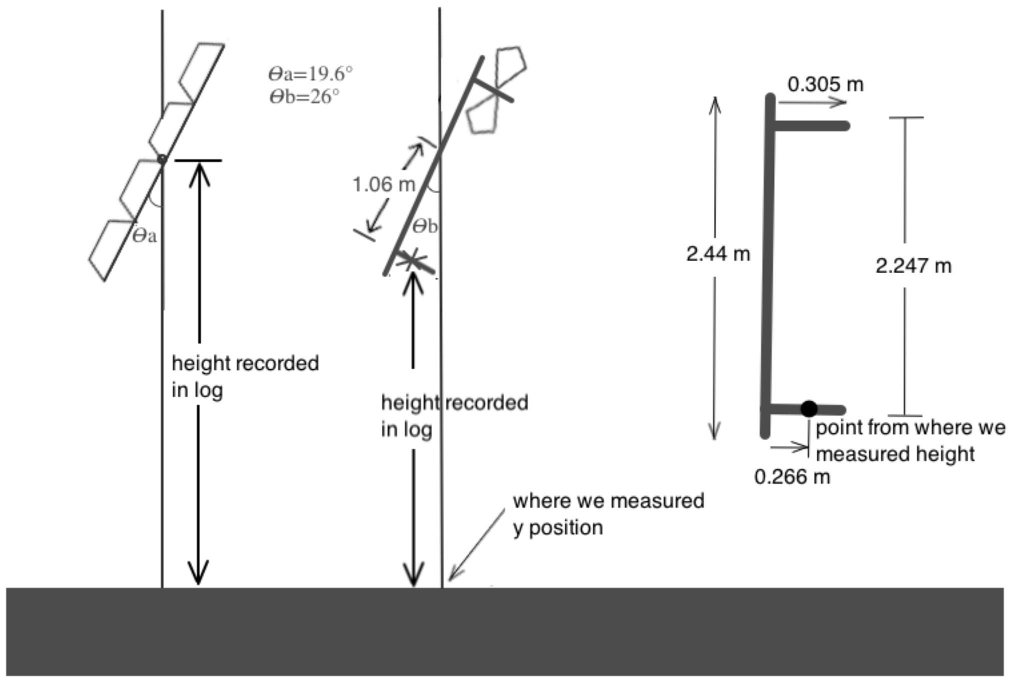

Figure 5.8: Antenna measurements and geometry. Far left: Seavey antennas mounted in a vertical array. Center: Mounting geometry of Bicones and LPDAs. Right: Antenna mount dimensions. Measurements of the antenna array heights were made with reference to the floor of End Station A. Antenna positions described in Appendix B give the position of the antenna faces with reference to the coordinate system with y=0 at the front of the target and z=0 at beam height.

As mentioned in the Section 5.2, an important aspect of the T-510 experiment was to identify each expected type of radiation. To that end, the polarization of the radiations was designed to be separated into horizontal and vertical components. Askaryan radiation is radial, and in the given geometry it will show up as vertically polarized in an antenna lined up with a vertical slice of the Cherenkov cone. The vertical magnetic field induced radiation manifests in the horizontal polarization. This technique allowed us to probe the two components of the RF emission as shown in Figure 5.9.

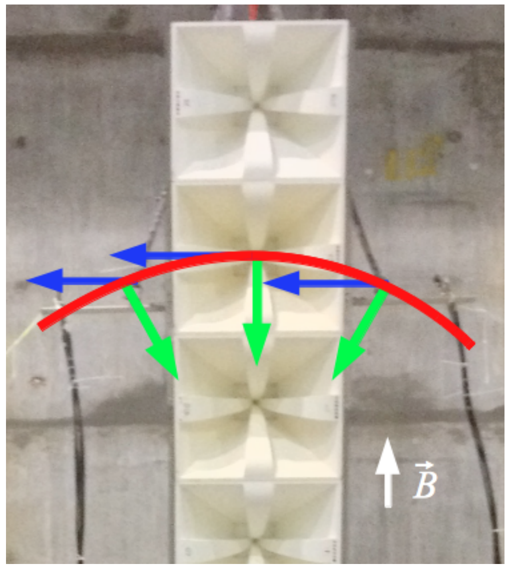

Figure 5.9: Polarizations of Askaryan and magnetically induced radiations. The red line shows the position of the Cherenkov cone. The green arrows show the radial polarization of the Askaryan radiation, and the blue arrows show the horizontal polarization of the magnetically induced radiation.

5.7 Signal Path Calibration

In order to reconstruct the electric field at the front of the antenna, the antenna response and cable responses in the system must be measured. Each antenna polarization output was attached to 240 feet of coaxial RF cable. The signal also went through a 200-1200 MHz bandpass filter. This response was characterized by S_{12} data taken on every channel to find the group delay and dispersion of the signal.

The antenna response was measured by P. Miocinovic at the University of Hawaii's anechoic chamber in 2005. Two Seavey antennas were mounted facing each other and in each others' far field region. A known signal was transmitted from antenna

1 to antenna 2, and the resulting voltage recorded. The complex antenna response is critical to data analysis, and details are discussed in Chapter 6.

5.8 Trigger and Data Collection

T-510 data was collected remotely and recorded on two 2.0 GHz (5 GSamples/second) Tektronix oscilloscopes that required an auxiliary trigger to record data. To provide a trigger, an S-Band antenna was placed 77.5 cm away from the beam pipe. This antenna captured transition radiation generated as the beam passed through a thin aluminum window from the beam pipe to air. The signal was sent to a third oscilloscope that generated a threshold trigger in real time. The oscilloscopes recorded 500 ns of data, so it was necessary for the trigger signal to arrive within that time window. Since the transition radiation was generated within 100 ns of the primary signal arriving at the antennas, and the cable lengths between both the S-Band and Seavey antennas and the oscilloscopes were compatible, the trigger signal arrived at the oscilloscope in time to form a trigger. A schematic of the triggering antenna is shown in Figure 5.10.

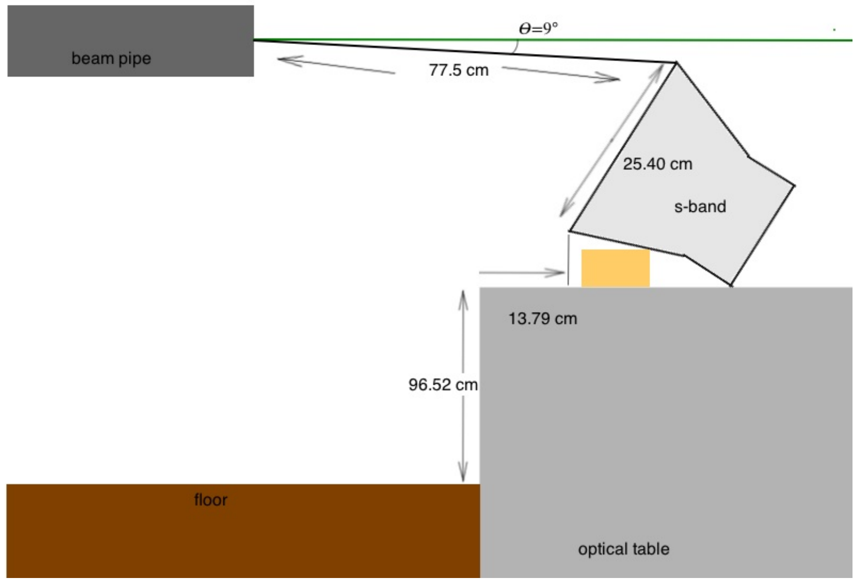

Figure 5.10: Geometry of the S-Band antenna triggering system. The antenna captured transition radiation generated as the beam left the beam pipe.

The S-band signal also served as a shot to shot relative calibration in conjugation with the ICT. Figure 5.11 shows the linearity between the charge measured by the ICT and the signal amplitude in the S-band antenna. As expected, the strength of the signal scales with beam charge.

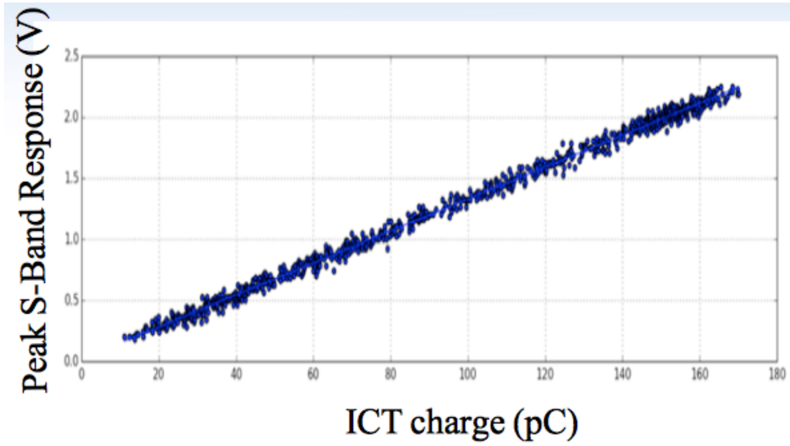

Figure 5.11: Linearity between the ICT charge and signal seen by a monitoring S-band antenna.

The oscilloscope that provided the trigger signal also recorded the ICT voltage, and a monitor voltage from an antenna placed after the beam pipe. The first primary data collection oscilloscope recorded antennas 1 and 4 on the array, vertical and horizontal polarizations. The second recorded antennas 2 and 3, both polarizations. This arrangement was designed to reduce cross talk between antenna channels.

The oscilloscope data was routed into the Counting House at ESA, a room above the main experimental hall. The scopes were controlled and data was collected through a LabView program.

5.9 Magnetic Field

Creating uniform and well measured magnetic field was crucial to the SLAC T-510 experiment. A primarily vertical magnetic field was generated using 15 water-cooled magnetic coils in two staggered rows that were placed on top of a 10.16 cm thick steel plate. Figure 5.12 shows the installation of the magnets.

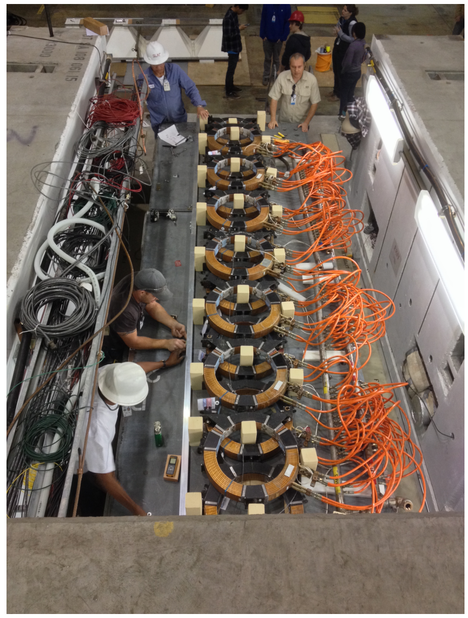

Figure 5.12: Overhead view of magnetic coils underneath the target. The water cooling system is in place, as seen by the orange tubing.

The magnetic field varied between -970 and 970 Gauss, and was controlled by varying the current provided to the coils. The linear relation between applied current and resulting magnetic field is shown in Figure 5.13.

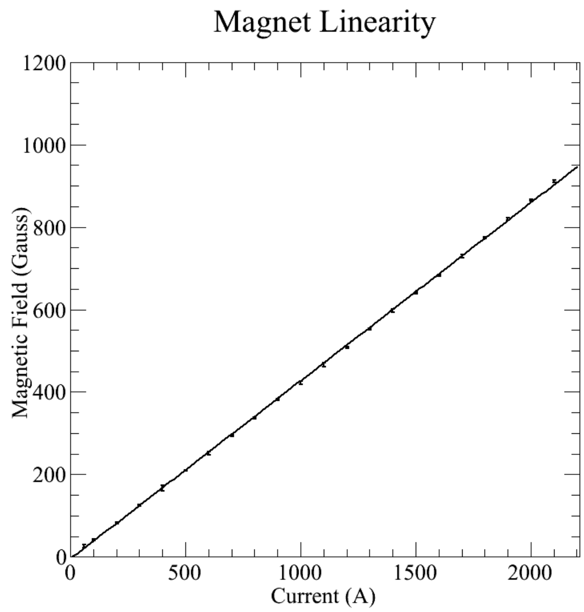

Figure 5.13: The magnetic field linearity, as controlled by current applied to the magnetic coils.

The magnetic field was measured using a Beehive Electric magnetic probe. Data points in all directions (x,y,z) were taken in a 5 cm by 5 cm grid 12.7 cm above the wooden platform across the area of the target. Sample measurements taken at different heights were collected to provide information about the magnetic field in the z direction. We found a 9% average difference in vertical fields measured at 11.56 cm and 15.06 cm above the wooden platform, at a displacement from the beam axis of x=5cm. The magnetic field was also monitored at one location within the target during the runs to ensure consistency. The magnetic field is shown in Figure 5.14 with position of the target overlaid in the center panel. The beam entered the target from the y=0 direction. The field was not perfectly symmetric around x=0, which could be explained if magnets were offset slightly on the x-axis by about $\sim$ 2cm. This resulted in a $5^{\circ} - 10^{\circ}$ tilt in the magnetic field. Since the beam height was actually at 10.8 cm above the wooden platform (including the radio absorption mat), the measured magnetic field is 1.9 cm above beam height. Based on the vertical field samples taken at different heights, we estimate an 8.6% difference between the measured field and the true field at beam height. Simulations include measured data, but the beam height was incorrectly assumed to be 12.7 cm.

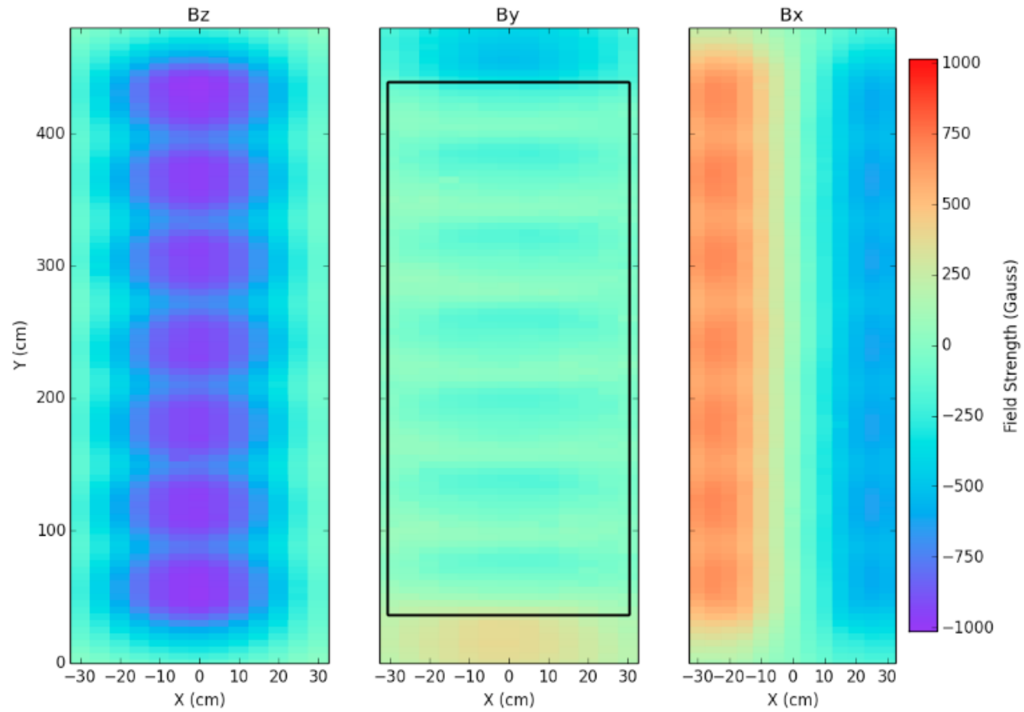

Figure 5.14: The measured magnetic field at the beam height along the vertical (z), longitudinal (y), and transverse (x) axes for a current of 2000A.

5.10 Runs and Antenna Geometry

T-510 was divided into two sets of runs. Runs 1-186 were taken during the first half of the experiment, and runs 187-378 were taken the second half. The second half of runs reflects a more stable and well understood beam. For each set of antennas (Seaveys, Bicone, and LPDA), data was taken with antenna positions covering a vertical slice through the Cherenkov cone. For each antenna position, runs were taken with the magnetic field off, and at each extreme (970 and -970 G). Additional runs were taken with the antennas in the region of the most intense radiation, ramping up the magnetic field from minimum to maximum in 250 Gauss steps. Runs were also taken with the collimator open and closed to compare the effects. Data was taken on the cone in the near field (with the center of the antenna array 2.8 m from the target), mid field (5.7 m from the target), and $\pm$ 3.2 m off of the x-axis. The tilt angle of the antenna array was consistently 19.6 degrees for all Seavey runs and 26 degrees for the other antenna models. Tables B.1, B.2, B.3, B.4, and B.5 in Appendix B show the positions of each antenna for the T-510 runs analyzed in Chapter 6.

Chapter 6

SLAC ANALYSIS

6.1 Introduction

The goals of the SLAC T-510 experiment were to validate simulations for radio emission from particle cascades and to identify and understand features of radio emission, specifically the magnetically induced radiation. This chapter covers details of the simulation, physics results of the experimental data, and the comparison between simulation and experiment.

First, a framework is introduced in Section 6.2 to simulate the electric field incident on the antenna array. The techniques used here are the same as discussed in Chapter 4. Specifically, the endpoint and ZHS formalisms were used to produce radio emission from a particle cascade, and a hardware simulation was used to model the detector response. T-510 simulations include realistic geometry, beam energy, magnetic field, and refraction effects. A discussion of electric field propagation from the point of emission to the antenna is included, as well as interpretation of simulation results. A comparison of the two simulation techniques is also discussed in this section.

Once the electric field is established at the antenna, it is necessary to model the electronics and response of the system. This is done in Section 6.3, where the simulated electric field is convolved with the antenna response to produce a voltage that may be compared to the T-510 data. The signal chain is described in detail in Chapter 5. Physics results are presented in Section 6.5, including a mapping of the signal strength and linearity of the signal strength with applied magnetic field. The qualitative features of magnetically induced radiation are confirmed, but the amplitude of the signal was $\sim 40\%$ greater than simulated. We believe that this is because the simulations did not include reflections off the bottom of the RF absorbing mat placed under the polyethylene target. The mat was placed underneath the target to prevent reflections within the target, however, it turned out that the characteristics of the mat within the T-510 frequency band were not well know. In order to understand the full amplitude of the measured voltage, it was necessary to model the effects of the mat and the reflections. The handling of these reflections is discussed in Section 6.5.4 and 6.6.

6.2 Electric Field Simulations

This section discusses T-510 simulations, which were developed and run by Anne Zilles at the Karlsruhe Institute of Technology [214]. A more general discussion of radio simulation packages is found in Chapters 3 and 4. Particle level simulations from Geant4 and calculation of the electric field using endpoint and ZHS formalisms are described in Section 6.2.1 and the propagation of the electric field from point of emission to observer in Section 6.2.2. In Sections 6.2.3 and 6.2.4, radiation from different emission points is looked at in detail to better understand the effects of coherence. Finally, in Section 6.2.5, the ZHS and endpoint are compared for the T-510 framework.

6.2.1 Simulation Formalism

Particle level radio emission simulations use existing Monte Carlo software to track individual particles in a cascade. The radiation from each particle track is calculated and summed at the point of an observer. Geant4 version 10.0 was used to simulate particle cascades for bunches of particles. This package tracks the propagation and interaction of particles through matter by splitting the motion of a particle into straight-line sub-tracks with known timing and position [202]. The experimental geometry was included in the Geant4 simulations, including target composition and realistic magnetic field. Energy cuts were incorporated in Geant4 by eliminating particle tracks from which the radiation would not be significant. For the T-510 case, this cut corresponded to track lengths of 0.1 mm. Radio emission from each sub-track was calculated using endpoint and ZHS formalisms. The endpoint formalism calculates the emission from a track as if the particle instantaneously accelerates from rest to its final velocity at the first endpoint and then decelerates from its velocity to rest at the second endpoint. The ZHS formalism integrates the vector potential at the antenna due to each particle over its full track length.

Simulated radio emission was collected at specified antenna positions in a 400 ns time window sampled at 100 GHz. To make computation time reasonable, 5000 electrons of energy 4.35 GeV were simulated and then the electric field was scaled up to the full charge of 131 pC.

6.2.2 Propagation

A challenge in simulating a realistic experimental setup is handling the propagation of the generated radiation accurately. The emission is tracked using ray optics as it propagates through the target and to the antenna. The amplitude of the electric field changes as it passes through the boundary of the target. The electric field here is of the form described in Equation 4.23. Radiation from each particle track segment has a different path to the antenna, and so Snell's law has to be applied separately for each track. Therefore, each track has a different reflection and transmission coefficient. The total transmitted electric field incident on the antennas is

$$\vec{E}_{ant} = \left(\vec{E}_{em} \cdot \hat{\vec{R}}_{\perp,in}\right) t_{\perp} \hat{\vec{R}}_{\perp,out} + \left(\vec{E}_{em} \cdot \hat{\vec{R}}_{\parallel,in}\right) t_{\parallel} \hat{\vec{R}}_{\parallel,out}. \tag{6.1}$$

$\vec{E}_{ant}$ refers to the total electric field, summed from the perpendicular and parallel components of the electric fields. $\vec{E}_{em}$ refers to the electric field at the point of emission. The $\hat{\vec{R}}$ unit vectors give the planes of incidence perpendicular and parallel to the electric field, including directions before and after refraction. The $t_{\perp}$ and $t_{\parallel}$ terms give the Fresnel coefficients in each direction, and are defined below.

Derived from [195], parallel and perpendicular reflection coefficients are given as

$$r_{\parallel} = \frac{n_{HDPE} \cdot \cos(\beta) - n_{air} \cdot \cos(\alpha)}{n_{HDPE} \cdot \cos(\beta) + n_{air} \cdot \cos(\alpha)} \tag{6.2}$$

$$r_{\perp} = \frac{n_{HDPE} \cdot \cos(\alpha) - n_{air} \cdot \cos(\beta)}{n_{HDPE} \cdot \cos(\alpha) + n_{air} \cdot \cos(\beta)} \tag{6.3}$$

where n_{air} is the index of refraction of air, n_{HDPE} is the index of refraction of the high density polyethylene, and α and β are the incident and transmitted angles, respectively. At Brewster's angle, $\tan(\theta_B) = n_{hdpe}/n_{air}$, the parallel reflection coefficient is $r_{\parallel} = 0$. Equation 6.2 adopts the convention that for head on incidence $\alpha = 0$ (and more generally $\alpha < \theta_B$), $r_{\parallel}$ and $r_{\perp}$ have the same sign, while for $\alpha > \theta_B$ they have opposite signs.

Assuming that α and β don't change over the face of the target, the Fresnel coefficients can be written as

$$t_{\parallel} = \sqrt{\frac{\tan(\beta)}{\tan(\alpha)} \left(1 - r_{\parallel}^2\right)} \tag{6.4}$$

$$t_{\perp} = \sqrt{\frac{\tan(\beta)}{\tan(\alpha)} (1 - r_{\perp}^2)}. \tag{6.5}$$

to yield the transmitted electric field close to the surface of the target. In the limit that the observer is far away from the boundary, the emission can be considered as coming from a point source, divergence effects are included [215][216], and the transmission coefficients become

$$t_{\parallel} = \sqrt{\frac{\tan(\alpha)}{\tan(\beta)} \left(1 - r_{\parallel}^2\right)} \tag{6.6}$$

$$t_{\perp} = \sqrt{\frac{\tan(\alpha)}{\tan(\beta)} (1 - r_{\perp}^2)}. \tag{6.7}$$

Equations 6.6 and 6.7 are used in the T-510 simulations. However, the antennas are not sufficiently far away that this approximation is accurate, and a 5% level correction is expected, but not included in this analysis.

Figure 6.1 shows the calculated Fresnel coefficients parallel and perpendicular (vertical) to the target as a function of emergent angle, that is, the angle resulting from refraction out of the target.

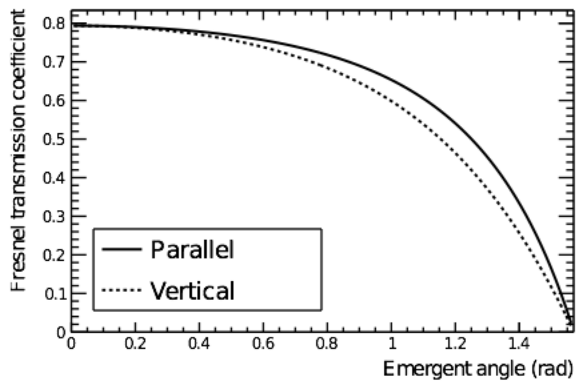

Figure 6.1: Fresnel Coefficient used in SLAC simulations.

Let d_{HDPE} be the distance between the particle track and refraction point on the target and d_{air} be the distance between the refraction point and the antenna. Then, the total propagation time t_{prop} from track to antenna is

$$t_{prop} = n_{HDPE} \cdot \frac{d_{HDPE}}{c} + n_{air} \cdot \frac{d_{air}}{c}. \tag{6.8}$$

The propagation time is added to the time the signal was generated before summing to find the total electric field for the observer.

Figure 6.2 shows the amplitude of the electric field as it appears in the antenna plane, the geometry of which is shown in Figure 5.1. As discussed in Chapter 5, the geometry of the experiment was designed so that the magnetically induced radiation would be isolated in the horizontally polarized direction and the Askaryan radiation would be isolated in the vertically polarized direction at the point of the observing antennas. For reference, the T-510 antennas fall along the x=0 axis of Figure 6.2 and are tilted 19.6° towards the target. The antenna closest to the peak radiation is located at x=0 m, y=6.52 m in this coordinate system. At this point, the horizontally polarized signal strength is about a third of the vertically polarized signal. The left panel of Figure 6.2 shows the total field strength, magnetically and charge excess induced, in the plane of the antennas. Off axis, asymmetries are primarily due to interference between magnetically induced and Askaryan radiation. Ideally, on the x=0 axis, the magnetic and charge excess radiation would be confined to independent polarizations. From the measured magnetic field maps discussed in Chapter 5 (Figure 5.14), it is clear that there are non-vertical components contributing to the magnetic field. These components contribute to a tilting of the cascade development, which introduces additional non-symmetrical effects. Since a realistic magnetic field is used in the simulations, these effects are accounted for in the simulated results. The offset in the symmetry of the horizontal radiation is seen in the center panel of Figure 6.2. The right panel shows the vertically polarized emission, and takes the shape of a radial cone, with an asymmetry introduced by the tilted magnetic field visible.

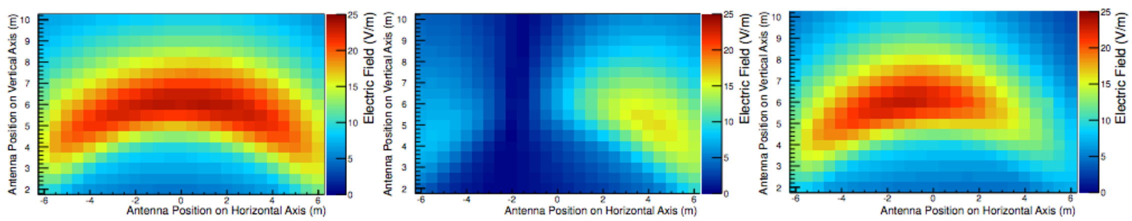

Figure 6.2: Peak amplitude of the electric field for a 2D antenna array in an observer plane 1300 cm from the front of the target, as found using the endpoint formalism. The magnetic field has a maximum strength 970G. Left: total electric field. Center: horizontally polarized component. Right: vertically polarized component. The T-510 antenna closest to the peak of the radiation pattern is located at x=0 m, y=6.52 m in this coordinate system. The electric field is filtered to 200-1200 MHz, the T-510 bandwidth.

This model only represents the direct path from emission point to antenna and not any reflections off target surfaces. These reflections have a significant impact on the resulting signal, and their treatment is discussed later in this chapter. Transition radiation from the beginning of the target was simulated and found to be two orders of magnitude below the simulated Askaryan signal, so it is not considered in the analysis [214].

6.2.3 X_{max}

In order to understand the point of peak radiation at the antenna, we look at the distribution of current in the target. For a distant observer and infinite target materials, the maximum radiation comes from the point of X_{max} in the cascade development. However, in the T-510 case, the geometry of the experiment is finite, and so the definition of the point of the peak radiation is not straight forward. In Figure 6.3 the x-axis represents the length along the target and the y-axis represents the number of $e^+ + e^-$ within a Moliere radius with a relativistic gamma factor above Cherenkov radiation threshold. The thickness of the lead for T-150 was close to two radiation lengths, so the cascade maximum was close to the emission at the target entrance.

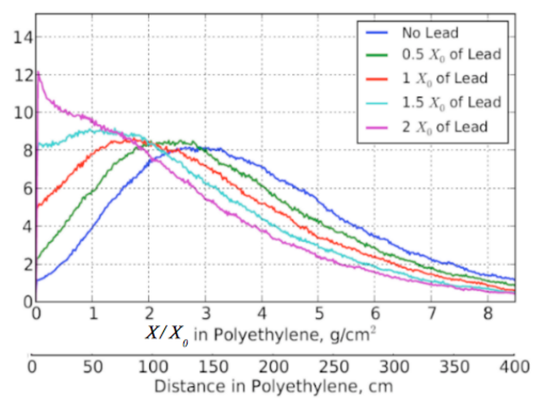

Figure 6.3: Position of maximum particle density from simulations. Plot by Andres Romero-Wolf.

Figure 6.4 indicates, for a given antenna position, where emission on the Cherenkov angle originates. The left panel shows the geometry signal path for antennas at heights of 652 cm and 747 cm. The right panel shows where along the x-axis the emission must originate in order to reach a particular antenna. From this, we see that the emitting region is quite spread out, and that for most antennas, the stationary point of emission is not from within the target. Therefore, we have to distinguish between the antenna on the Cherenkov cone (where emission arrives in phase), and the antenna that sees the most radiation due to cascade development in the target. For example, in Figure 6.4, the antenna at 747 cm sees radiation on the Cherenkov cone at a point of maximum cascade development, but much of the radiation is generated before the target, and therefore doesn't reach the antenna. The antenna at 652 cm sees a stationary emission point after the maximum cascade development, but it also sees emission from the entire target.

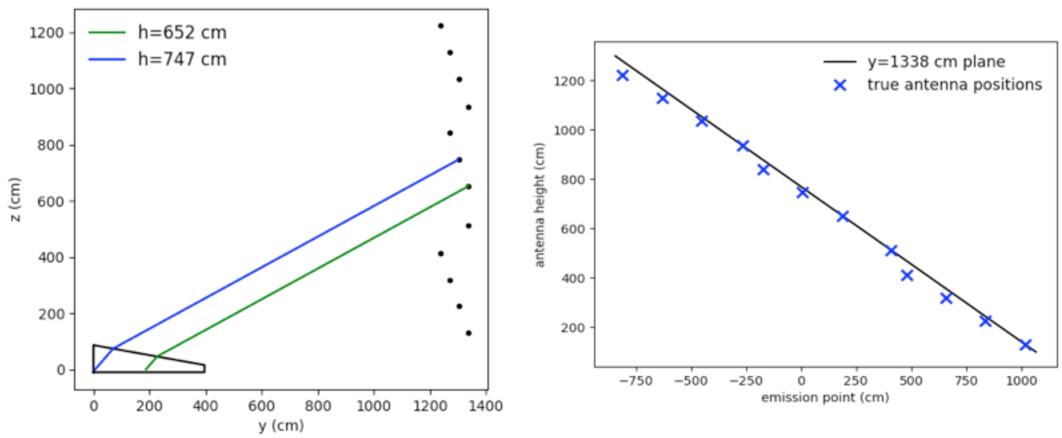

Figure 6.4: Left: Ray tracing diagram of the emission on the Cherenkov angle arriving at antennas. Right: The emission point, relative to the beginning of the target, corresponding to different antenna heights.

In the next section we examine the contributions from different parts of the cascade to antennas at both these locations.

6.2.4 Contributions From Different Segments of Target

To study coherence, we examine how different parts of the particle shower contribute to the electric field seen at the antenna. This was done by separating the target into five sections, $(0-50\text{cm}), (50-100\text{cm}), (100-150\text{cm}), (150-200\text{cm}), (200-400\text{cm})$, and running separate simulations that only summed the radiation from the specified track segments. Contributions from these five slices of the target for an antenna at 652 cm above the beam are shown in Figure 6.5. It is evident that most of the radiation comes from the first 50 cm of the target in the full frequency band, and that most power comes from high frequencies that are out of the T-510 bandwidth, which is 200-1200 MHz.

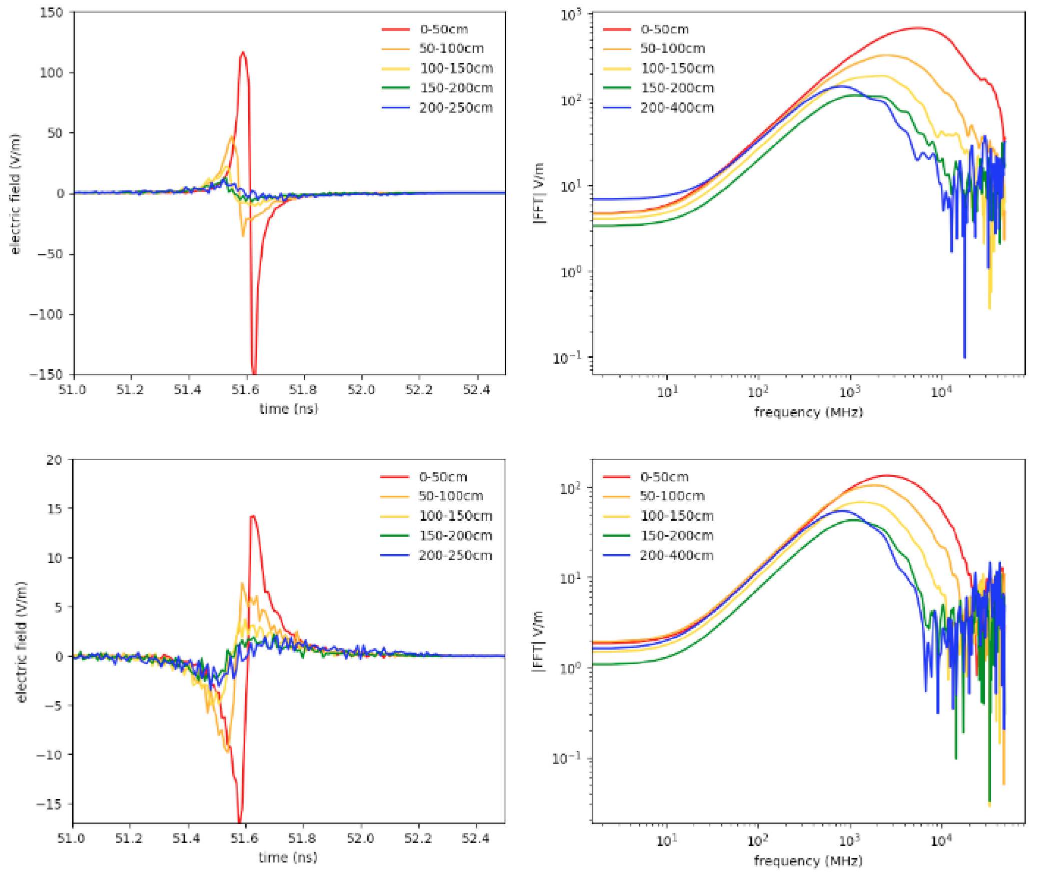

Figure 6.5: Electric field contributions from different segments of the target. Vertical polarization is on the top and horizontal is on the bottom. The antenna height is 652 cm above the beam, which corresponds to the point of maximum radiation. The time t=0 refers to time the beam enters the target [214].

Figure 6.6 shows the contributions in the 200-1200 MHz bandwidth. The electric field is reduced, and especially in the horizontal polarization, we see comparable contributions from the 0-50 cm track and the 50-100 cm track. This makes sense for the T-510 set up, since the charge excess contribution begins in the lead, however, the magnetically induced currents only develop in the magnetic field, later in the cascade.

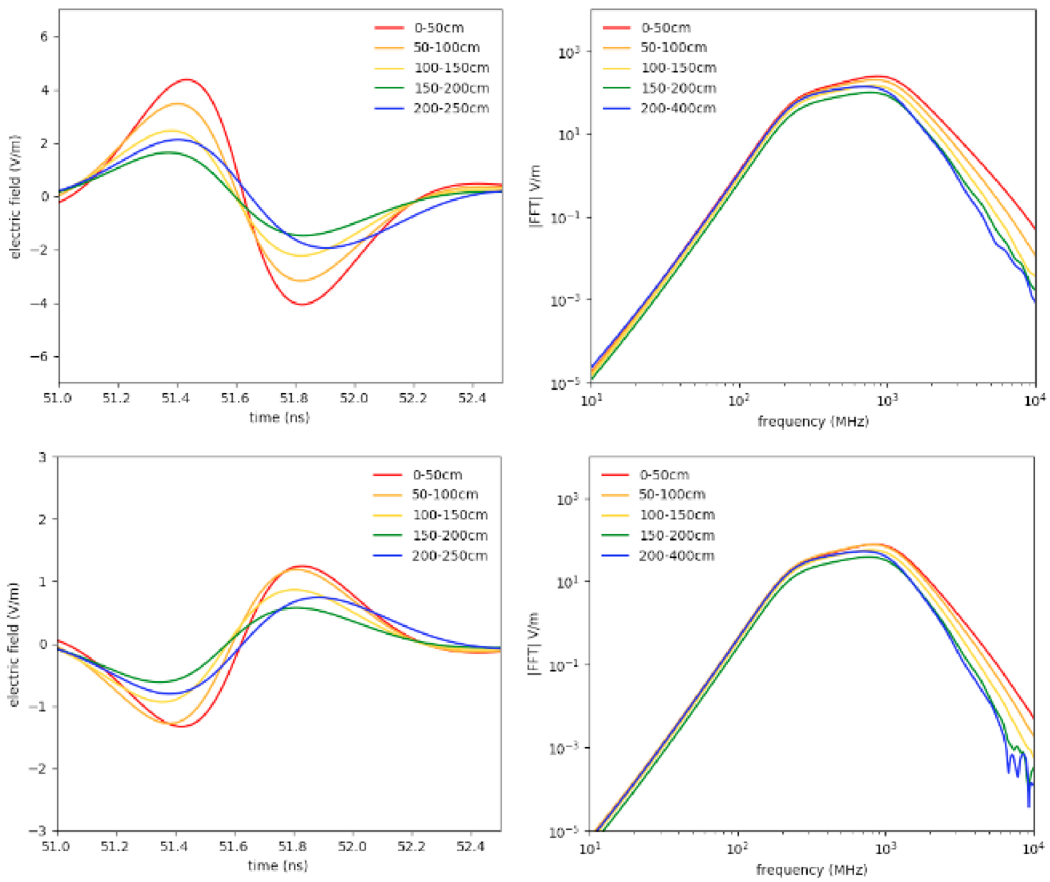

Figure 6.6: Electric field contributions from different segments of the target, filtered to 200-1200 MHz using a software Butterworth filter [217]. Vertical polarization is on the top and horizontal is on the bottom. The antenna height is 652 cm above the beam, which corresponds to the point of maximum radiation.

We can now take a closer look at emission from the first 50 cm of the target. Figures 6.7, 6.8, 6.9, and 6.10 show the contributions from 5 cm long segments of the target for the first 50 cm for antennas at 319 cm, 652 cm, 747 cm, and 935 cm above the beam height. The 747 cm position is closest to receiving emission on the Cherenkov cone, and it is evident that the contributions from different segments of the target arrive close together temporally, therefore adding coherently to give greater power. The horizontal polarization has significantly less radiation from the first 5 cm of the target than the vertical polarization, again indicating that the magnetically induced radiation develops after the charge excess. Although the 652 cm position is not directly on the Cherenkov cone, it still sees a comparable amount of power because it is able to integrate emission from the entire cascade inside the target. The contributions from the first 3 slices are close in amplitude, while the 747 cm position gets most of its power from the first 5 cm of the target. The 319 cm and 935 cm positions show the loss of coherence as you move away from the Cherenkov cone. The pulses arrive with opposite time ordering in the two cases, with the signal further in the target arriving first at the lower antenna, and last in the higher antenna, as dictated by the geometry of the target and antennas.

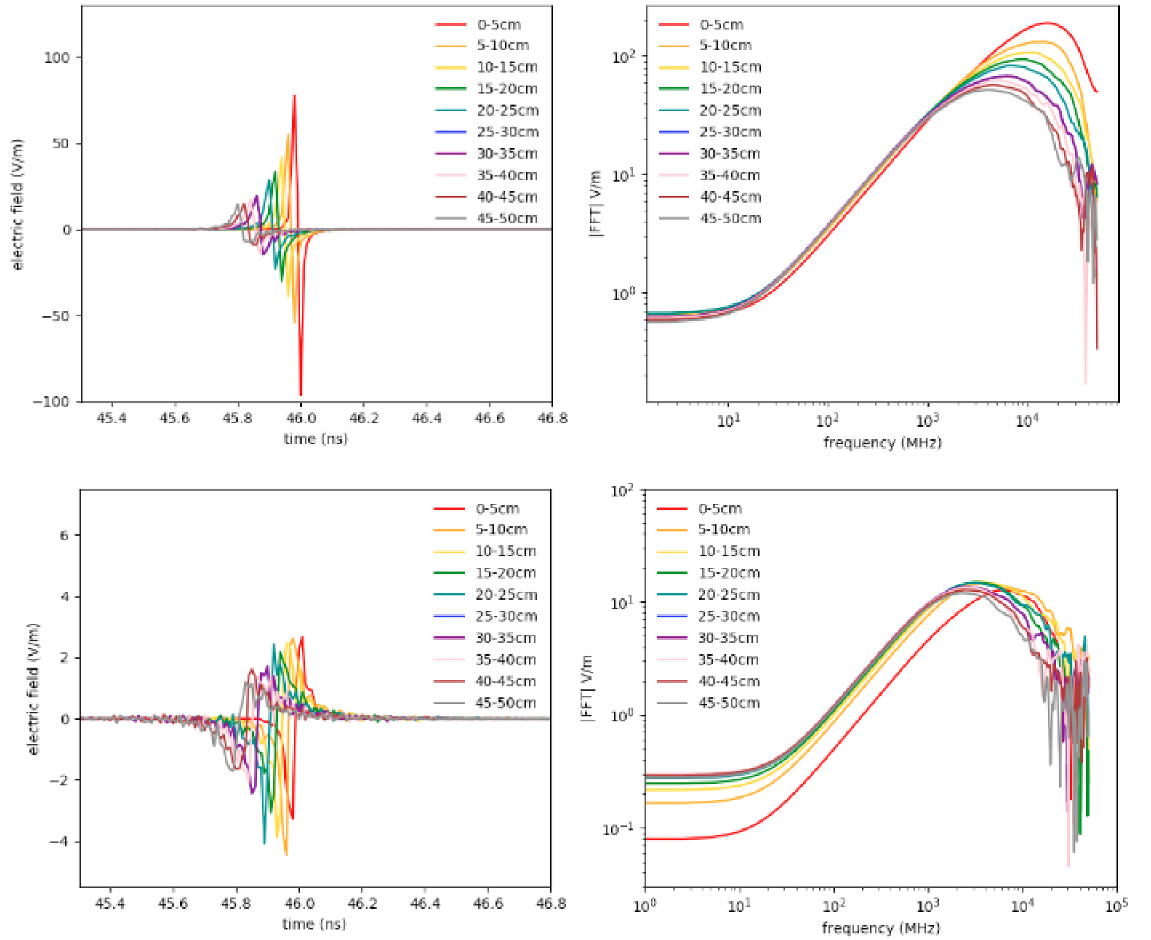

Figure 6.7: Electric field contributions from different segments of the first 50 cm of the target at an antenna height of 319 cm. Vertical polarization is on the top and horizontal is on the bottom.

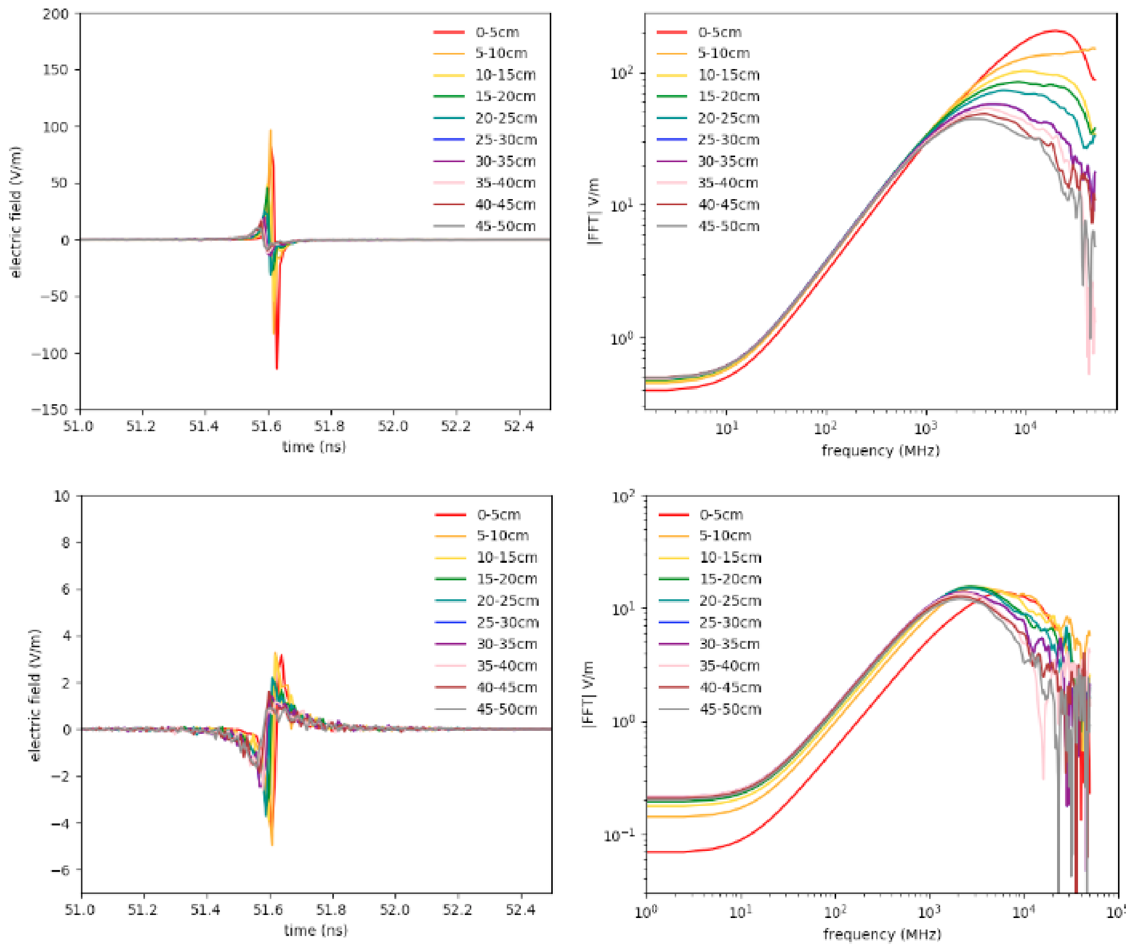

Figure 6.8: Electric field contributions from different segments of the first 50 cm of the target at an antenna height of 652 cm. Vertical polarization is on the top and horizontal is on the bottom.

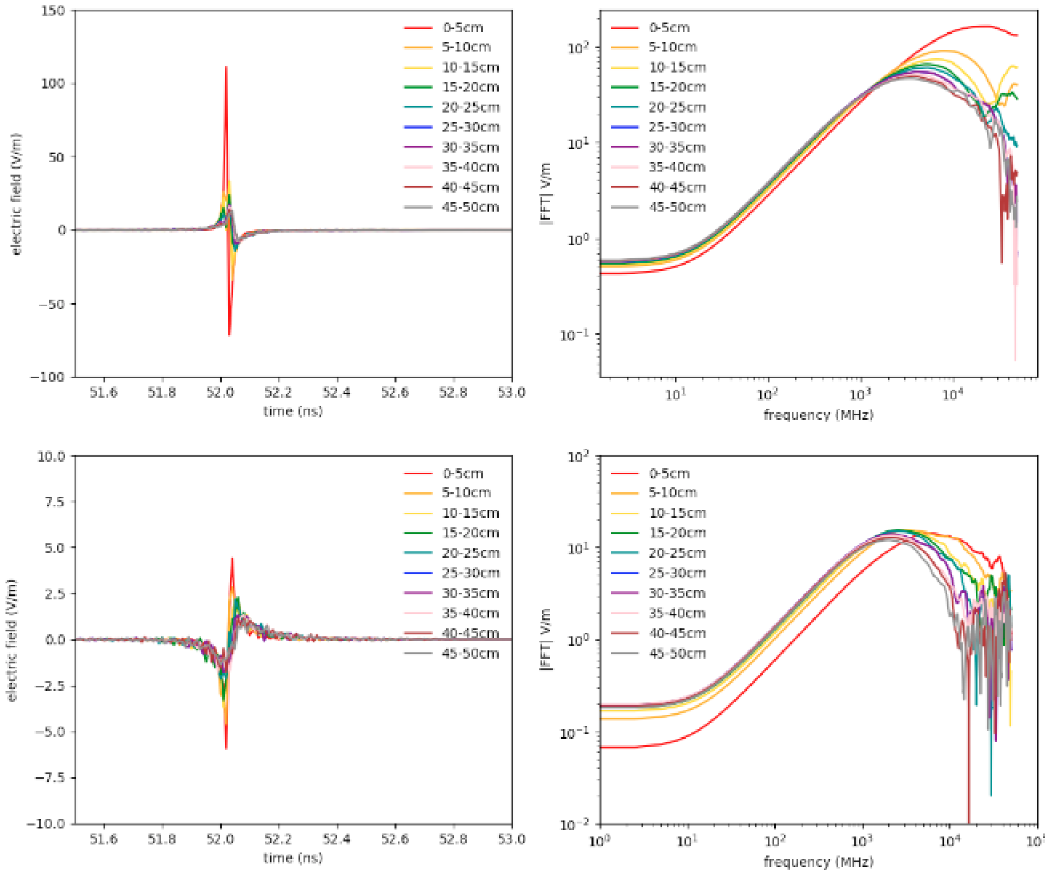

Figure 6.9: Electric field contributions from different segments of the first 50 cm of the target at an antenna height of 747 cm. Vertical polarization is on the top and horizontal is on the bottom.

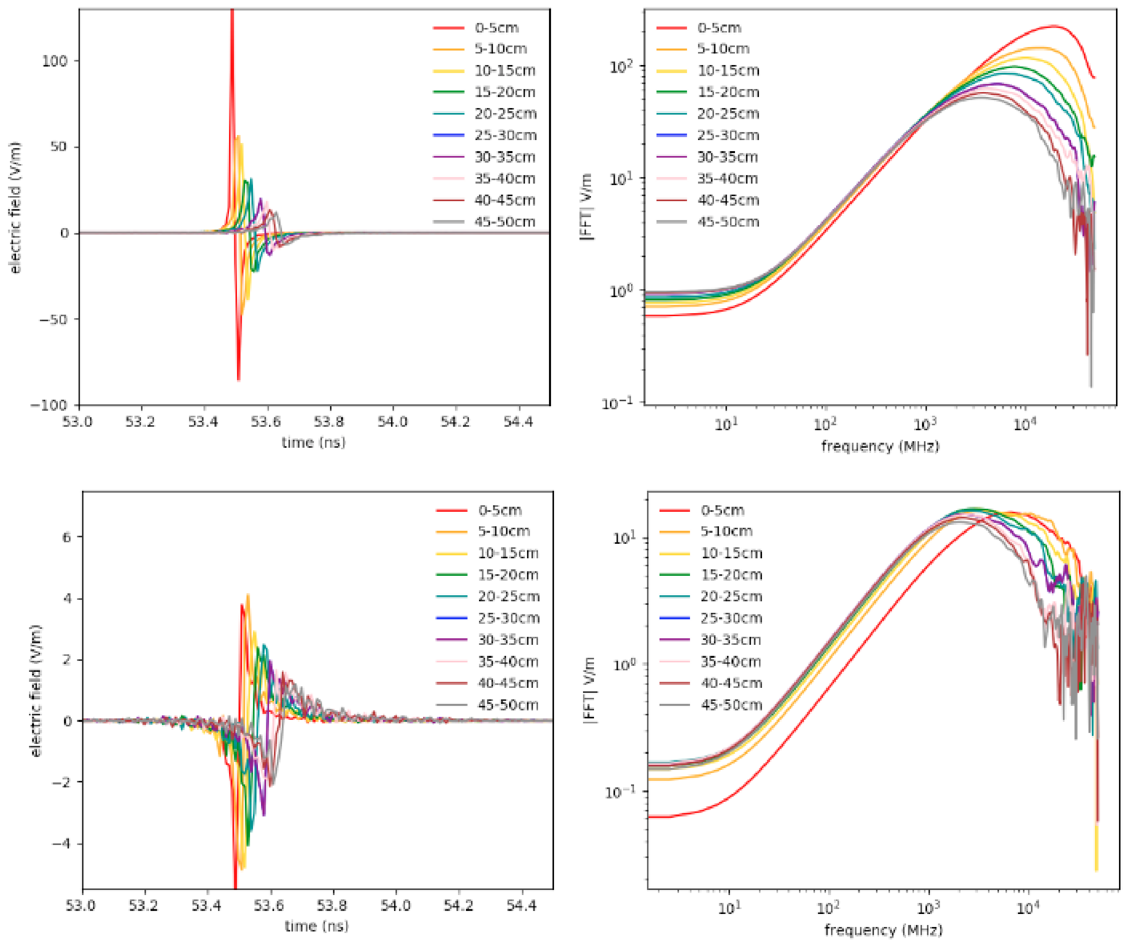

Figure 6.10: Electric field contributions from different segments of the first 50 cm of the target at an antenna height of 935 cm. Vertical polarization is on the top and horizontal is on the bottom.

6.2.5 Comparing Formalisms

Microscopic simulations are derived from first principle Maxwell equations with the assumption that the observer is in the far field. Mathematically, both ZHS and endpoint formalisms reach the same conclusion. The difference is in the way they approach the emission from track segments [218]. The ZHS formalism calculates the integrated vector potential of the particle over the whole path length. As the name suggests, endpoint uses the acceleration and state of the particle only at the beginning and end of each track segment. The endpoint approach breaks down directly on the

Cherenkov cone because the equation for the electric field has a singularity at that point, and the numerical algorithm reverts to ZHS methods for these track segments. More details about these simulations are discussed in Chapter 4. Figure 6.11 shows a comparison between the two formalisms with a 970 G magnetic field. The relative difference between the peak amplitude in ZHS and endpoint formalisms is plotted for observing antennas in a 2D array. Since there is little horizontal radiation at x = - 2 m (as seen in Figure 6.2), the ratio diverges at this location, as indicated by the white band.

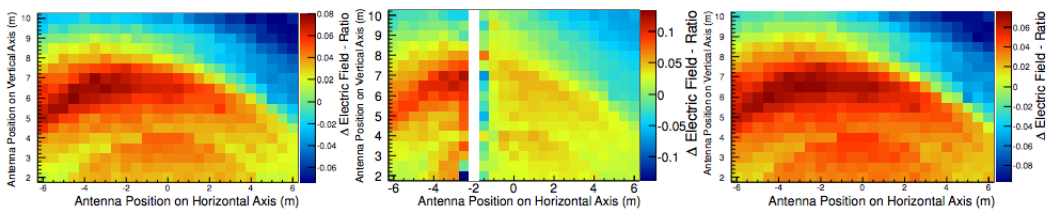

Figure 6.11: Ratio in peak amplitude of total electric field in time domain for a 2D antenna array defined as $\frac{E_{ZHS}-E_{endpoint}}{E_{ZHS}}$: Left: difference in total electric field; Center: difference in horizontally polarized component; Right: difference in vertically polarized component [219].

The radiation calculated from both formalisms is run in parallel, so there are no cascade to cascade fluctuations in this comparison. There is a 7% $-$ 8% difference in peak amplitude between formalisms, depending on the observer location. ZHS predicts slightly higher amplitudes inside the Cherenkov ring, while endpoint predicts higher results outside the ring. In the frequency domain the deviation ranges between 3%$-$7%.

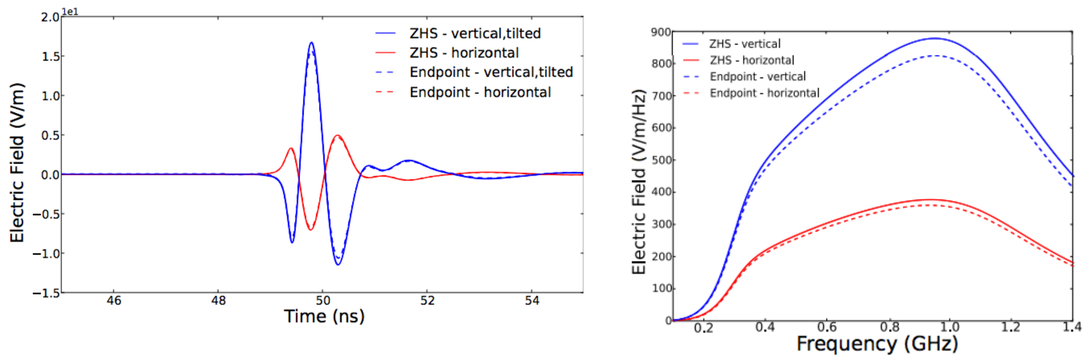

Figure 6.12: Comparison of ZHS and endpoint formalisms for a single antenna position 6 meters above the beam in the time domain (left) and frequency domain (right). The electric field is filtered to 200-1200 MHz using a software filter.

Figure 6.12 shows the simulated electric field for an antenna 6 meters above the beam. The notation "vertical, tilted" refers to the simulation being projected into the plane perpendicular to the incoming signal. There is a 4.4 % difference between peak amplitude in the horizontal polarization and 6.4% in the vertical polarization. There is a maximum 7% discrepancy in the frequency domain, although the spectral shapes agree well. The origin of the difference between formalisms is still an open question. Endpoint simulations are used for comparisons made in the remainder of this chapter, and the systematic error for simulations is taken to be 7%, which is the maximum difference between formalisms.

6.3 Convolving the Simulated Electric Field with the System Response

Now that we have established the simulation methodology, we look at how to compare the simulated electric fields with T-510 data. We choose to apply the system response to the simulated electric field to construct a simulated voltage. This approach is more stable than removing the system response from measured data, since the noise in the system isn't well characterized. Figure 6.13 shows a diagram of the components included in the convolution process.

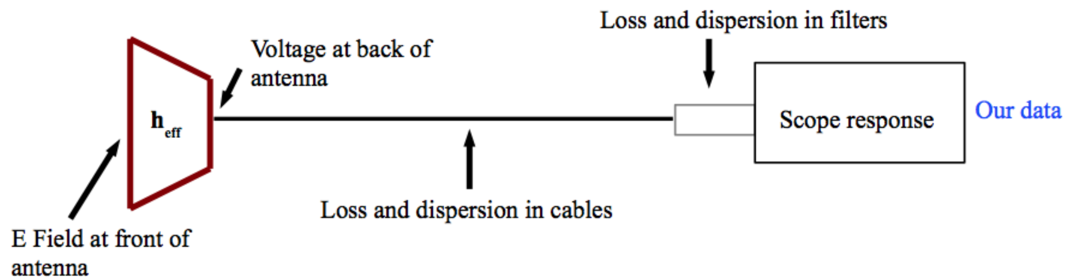

Figure 6.13: Schematic of T-510 electric field to voltage convolution.

The primary relation used to calculate the voltage at the oscilloscope is

$$V(t) = \mathbf{h_e}(\mathbf{t}) * \mathbf{E}(\mathbf{t}). \tag{6.9}$$

The $\mathbf{h_e}(\mathbf{t})$ term refers to the system response, or effective height of the system, which is described in detail in Appendix C. The simulated electric field is known, the system response (including antenna response and losses in the cables) is known, and so the simulated voltage can be calculated. The antennas used for T-510 are the same model as used for the ANITA experiment, and have been characterized in an anechoic chamber at the University of Hawaii in 2005. We use that measured effective height in this analysis.

Antenna response patterns vary for different angles between the normal to the antenna face and the incoming signal. The antenna response was measured in discrete steps. For antenna tilt angles close to bore sight this isn't a large problem, as the antenna response doesn't vary much in that range. For antenna tilt angles that haven't been measured directly, the response is interpolated.

The simulated electric field also needs to be adjusted for losses in the cables and the hardware low-pass filter on each channel with a 3dB point at 1250 MHz. Cable losses and filter responses for each data channel were measured at the time of the T-510 experiment and are shown in Figure 6.14.

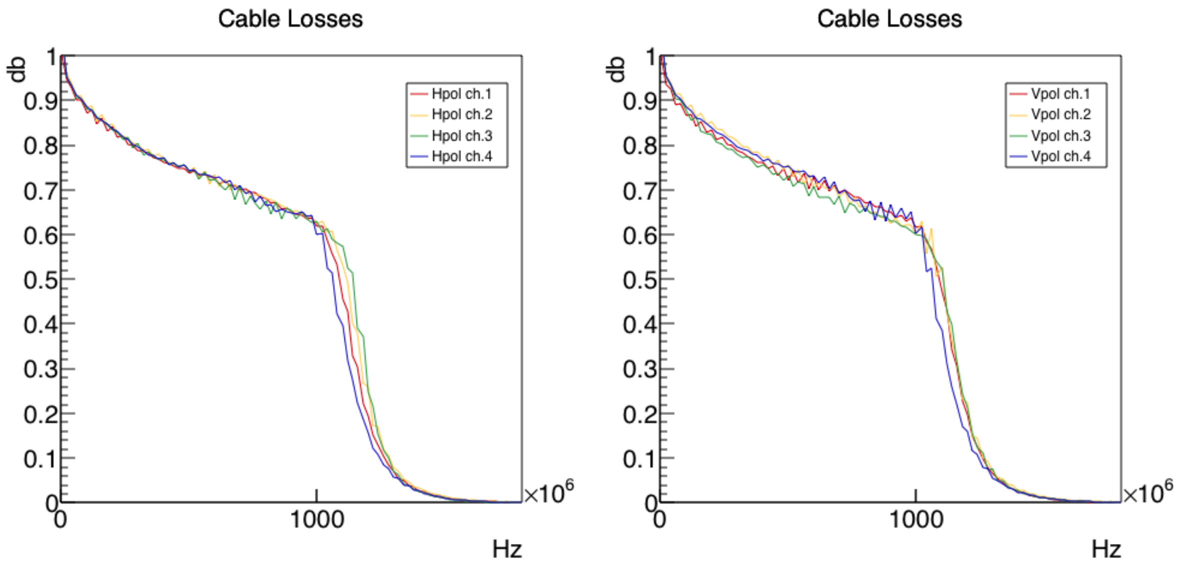

Figure 6.14: Measured cable and filter losses for each channel.

6.3.1 End-to-End System Response

For this analysis, we will take the coordinate system defined as follows: with x pointing horizontally away from the beam, y along the beam, and z vertical above the beam, with a diagram in Appendix B. The origin (0,0,0) is at x = 0 on beam, y = entrance to the target along beam, and z = beam height, as indicated in Figure 5.1.

As an example, we take the vertically polarized simulated electric field at an antenna 1329 cm away from the front of the target and 747 cm above the beam height with B=0. After convolution with the system response, this simulation is compared to the corresponding data from antenna #2 run 210, taken on February 12, 2014. We make the following transformation to change from the endpoint x, y, z to antenna vertical and horizontal polarizations, where $\theta = 19.6^{\circ}$ is the tilt angle of the antenna face.

$$E_{vpol} = -1 \times E_y \times \sin(\theta) + E_z \times \cos(\theta) \tag{6.10}$$

$$E_{hpol} = E_x \tag{6.11}$$

Simulations use 5000 injected electrons which are scaled to the known bunch charge of 131 pC. The electric fields after scaling and transforming coordinates are shown in Figure 6.15.

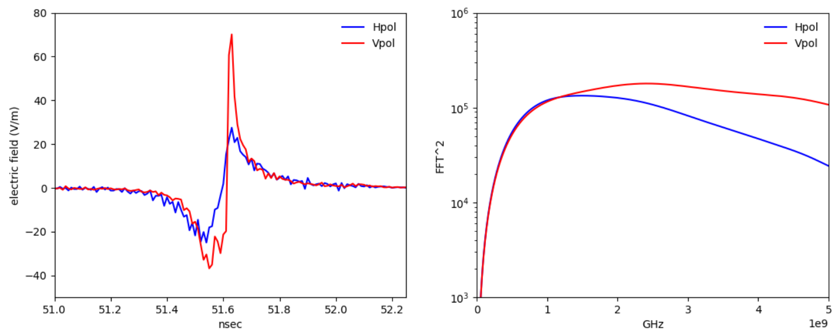

Figure 6.15: Raw electric field from endpoint formalism at position (0,1329,747) cm from the beginning of the target.

Now, according to the transfer function (eq. 6.9), we need the total system response, which can be considered the antenna response convolved with the cable response. The antenna response used in this example, which is close to bore sight, is shown in Figure 6.16.

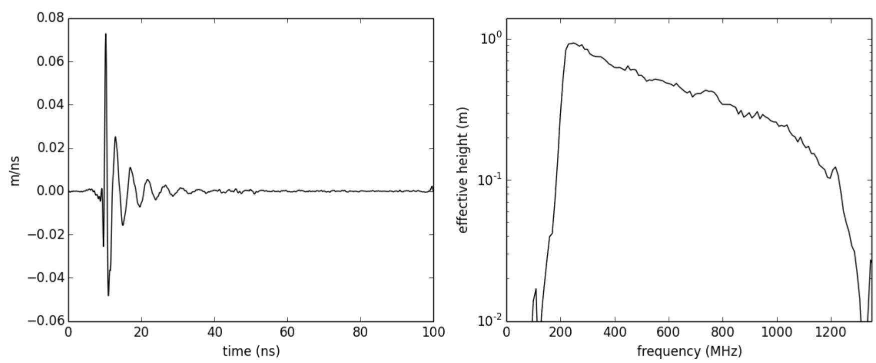

Figure 6.16: Antenna response, which is applied in the frequency domain, but data is stored in the time domain.

Using the convolution theorem we can say, with $\mathcal{F}$ denoting a Fourier transform,

$$\mathcal{F}(\mathbf{h_e}(\mathbf{t}) * \mathbf{E}(\mathbf{t})) = \mathcal{F}(\mathbf{h_e}(\mathbf{t})) \cdot \mathcal{F}(\mathbf{E}(\mathbf{t})). \tag{6.12}$$

Doing the convolution in the frequency domain and then transforming back to the time domain, we arrive at the simulated voltage at the antenna. Figure 6.17 shows the final convolved voltage (right) at the oscilloscope compared to the original electric field (left). System ringing is evident, as is typical of a filtered RF signal.

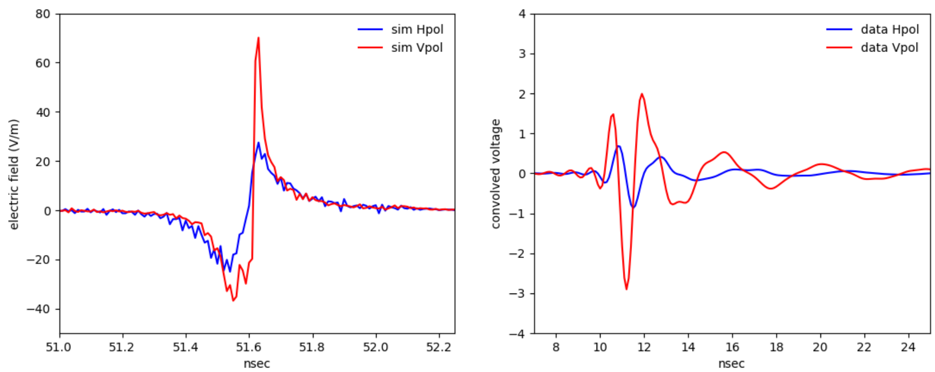

Figure 6.17: Left: Simulated electric field. Right: Electric field convolved with the system response, resulting in the simulated voltage at the oscilloscope. The time base for the left panel is relative to the start of the simulation. The time base for the right panel is arbitrary.

6.4 T-510 Data

Data was recorded on a Tectronix oscilloscope, with 4 traces per scope logged. Raw data was calibrated with scaling coefficients saved in the oscilloscope output file. There could be some contamination from one polarization into the other. In the experimental set up, it may be that the antenna array was not perfectly aligned in the vertical direction. This will cause some horizontally polarized signal to read as vertically polarized, and visa versa. The antenna itself may also have some natural leakage due to the proximity of horizontal and vertical feeds and their finite size.

To estimate the magnitude of the leakage we look at the horizontally polarized signal at the 652 cm antenna position with a 0 G magnetic field. In theory, there should be no signal, and any signal could be attributed to leakage of some sort. In fact, the peak amplitude of the horizontally polarized signal at this point is less than a percent of the vertically polarized signal for the same position and magnetic field. This is compared to the full strength magnetic field, where the horizontal signal amplitude is $\sim 40\%$ of the vertical signal amplitude. Because this leakage seems to be small, it is not corrected for and instead included in the systematic uncertainties, as part of the antenna alignment.

6.4.1 Systematic Uncertainties

In order to directly compare experimental data and simulations, it is necessary to understand the systematic uncertainties of each. As discussed in Chapter 5, there are many quantities that are estimated, but not fully known in the experimental set up. This includes things like the index of refraction of the target, the dimensions of the lead, and digitization effects in the oscilloscope. In order to continue with this analysis, we don't consider errors due to the uncertainties in these values and consider their effects to be small. We do account for systematic uncertainties with known effects, like the fluctuations in magnetic field and beam charge. Similarly, we don't have numerical estimates for all the systematic errors in the simulations, including numerical noise. To study the quantitative effects of these errors, it will be necessary to run simulations altering each parameter to see how the resulting emission changes.

We choose to take the peak voltage of each trace as the value to compare between experimental data and simulation. This quantity is chosen because it is straight forward to determine, and is relatively stable compared to the power in the trace, which is more heavily influenced by ringing due to filters and reflections in the target. Comparing the peak voltages, after the known systematics are taken into account, we still see a discrepancy between data and simulation. This problem prompted the study of reflections in the target, which is discussed in Section 6.5.4.

In the mean time, we consider the known systematic errors. These include beam charge calibration, magnetic field measurements, and antenna geometry measurements. As discussed in Chapter 5, the beam charge was continuously monitored with the ICT. The average charge was 131 pC with standard deviation of 3 pC. The charge was also measured with the ICT in different locations relative to the end of the beam pipe. These measurements yield a 2% systematic uncertainty overall in charge bunch. Waveforms shown in this chapter are for specific events, with the 2% systematic uncertainty assumed. The magnetic field was measured in a 5x5 cm grid with a precision of 3.64 G, which was the minimum precision of the magnetic field probe used. The field was monitored at the same point in the target for all runs, resulting in a 72 G RMS for full strength magnetic field. This adds a 6% uncertainty. Uncertainties introduced in measurements of the antenna geometry are harder to quantify. The antenna array was adjusted manually with ropes and fixed by eye with reference to ground markers. Once in place, the height was measured with a laser measure. Most of the uncertainty is in the antenna angle relative to the target. This error is estimated to be 6%, as the antenna response does not change significantly for angular differences below 10°.

The known systematic uncertainties in simulations are due to the difference between endpoint and ZHS formalisms, the assumption of ray optics, and the validity of assuming the antennas are in the far field of the emission from the target when calculating the transmission coefficients, as discussed in Section 6.2.2. These contributions to the systematic uncertainties are summarized in Tables 6.1 and 6.2.

Error	uncertainty	percent
beam charge	3 pC	2%
magnetic field	72 G	6%
antenna alignment	–	6%

Table 6.1: Summary of systematic uncertainties in the T-510 data.

Error	uncertainty	percent
ZHS vs. endpoint	–	7%
propagation	–	5%

Table 6.2: Summary of systematic uncertainties in the T-510 simulations.

Summing in quadrature, the measured signal has a 8.7% systematic uncertainty, and the simulation a 8.6% systematic uncertainty.

6.5 Results

6.5.1 Comparing Simulation and Data

A comparison of simulated and experimental data is shown in Figure 6.18 for the horizontally polarized signal at the point of peak emission (z=652 cm) and in Figure 6.19 for the vertically polarized signal at the same location. It is clear that while the basic features of the SLAC data are recovered, the maximum amplitude of the reconstructed pulse differs by about 30%. The maximum amplitude, or peak voltage, is the quantity that is used to compare simulations to data and is the quantity to which the systematic errors are applied. For plotting purposes, the simulated voltage and measured data are aligned by the position of peak voltage, although there is no absolute time base for the simulations after convolution. The difference is primarily attributed to the reflection of the signal off of the bottom of the target, which is not accounted for in simulations. Ringing effects are seen in both data and simulation, due to the filters. The structure after the main pulse is more complicated for data, which is also likely due to reflection effects. For both polarizations, there are different structures in the FFT for data and simulation. The simulations show stronger power at low frequencies, with the power tapering off across the band. There is an interference pattern evident in the data FFT, which again is attributed to reflections in the target. Further discussion of reflections is found in Section 6.5.4.

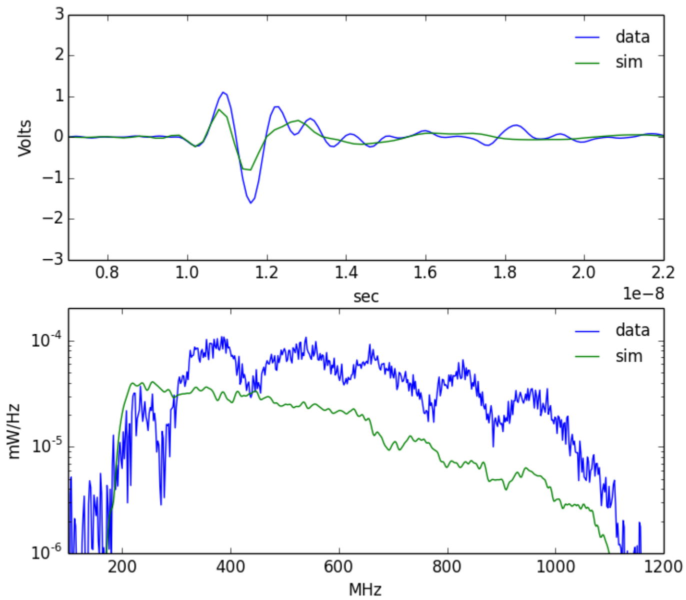

Figure 6.18: Top: Waveforms for horizontally polarized data and simulation at an antenna position of 652 cm, which is close to the point of peak field intensity, and B=970 G. Bottom: Power spectra of the same data.

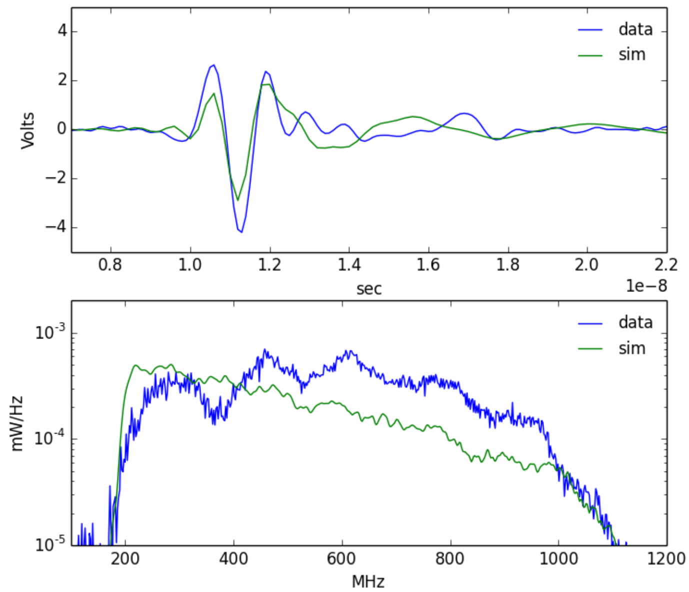

Figure 6.19: Top: Waveforms for vertically polarized data and simulation at an antenna position of 652 cm, which is close to the point of peak field intensity, and B=970 G. Bottom: Power spectra of the same data.

6.5.2 Mapping the Radiation Pattern

One of the goals of T-510 was to map the emission from the particle cascade in a dense medium which was predicted to be beamed into a Cherenkov cone. As discussed in Sections 6.2.2 and 6.2.3, for the T-510 setup, the antennas are not far away, and so the finite size and shape of the shower is important. A cone like radiation pattern is expected, but the details can only come from simulation. Figure 6.20 shows measured and simulated peak voltages for antenna positions spanning the radiation pattern in a vertical slice containing the beam axis. Horizontally and vertically polarized signal amplitudes are plotted for full strength and zero strength magnetic fields. There is no substantial horizontally polarized signal for the B=0 G case, as expected, since signals in the x=0 vertical plane are magnetically induced. The vertically polarized signal remains unchanged for zero and maximum magnetic fields. We also see that there is a radiation map for the horizontally polarized signal in the case of B=970 G that peaks in the same location as the vertical map. Although the simulated amplitudes are systematically lower, the shape of the radiation pattern is consistent.

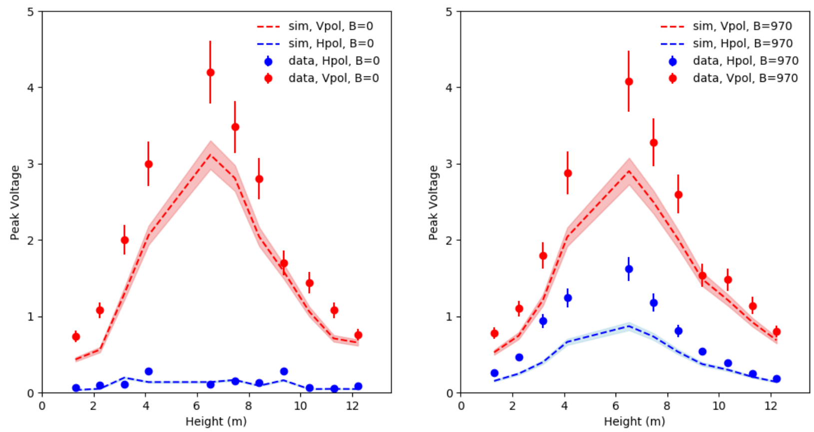

Figure 6.20: Radiation is mapped by peak amplitude of the signal. Left: Vertical and horizontal polarizations in the case B=0 G. Right: Vertical and horizontal polarizations in the case B=970 G. Note, the antenna heights referenced on the x-axis do not all lie at the same distance from the target, but are offset as seen in Figure 6.4.

Figure 6.21 shows the simulated and measured peak amplitude for B=970 G normalized by maximum amplitude so as to compare the shape of the radiation pattern. For both polarizations, the shapes of the measured and simulated patterns are consistent. The results from simulation were calculated only at the locations of actual antennas. The shaded bands show a linear interpolation between points. One data point at 513 cm above the beam is missing, due to a bad data run. This affects the visual impression of the simulation. Presumably, a true data point at 513 would lie above the linear interpolation, and produce a smoother result. There is a visible shift in the radiation pattern between data and simulation, with the simulated cone being slightly lower in height than the data. This feature is not yet understood.

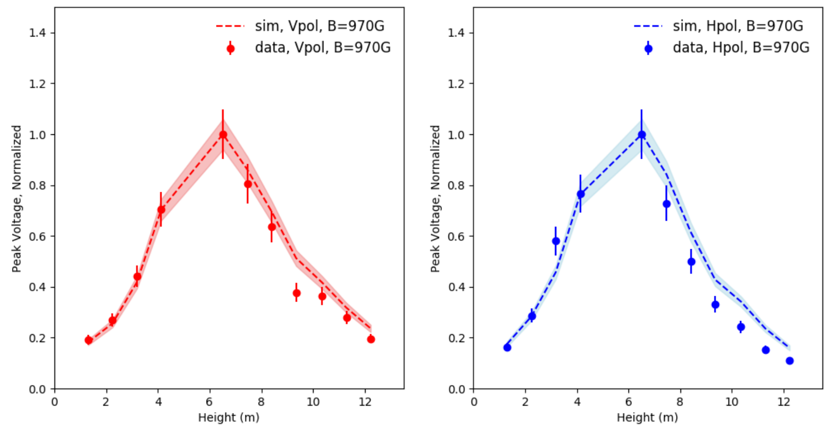

Figure 6.21: The radiation pattern is mapped by peak amplitude of the signal, normalized by maximum amplitude.

Due to coherence effects, we expect the Cherenkov cone width to be frequency dependant. The width of the cone, $\delta\theta$, is inversely proportional to the observing frequency and the longitudinal size of the cascade, as $\delta\theta = \frac{1}{fL_{\parallel}}$. Although we are not observing strictly Cherenkov effects, this trend is evident in Figures 6.22 and 6.23, where the power in different frequency bands in horizontal and vertical polarizations is plotted as a function of antenna height. Each band is normalized so that the sum of all the power is equal to one. The radiation pattern is narrowest in the 900-1200 MHz band and the widest in the 300-600 MHz band for both polarizations.

In the case of air showers, the Cherenkov angle is small (on the order of 1°) compared to the T-510 Cherenkov angle, and the longitudinal dimensions of the shower are longer (on the order of $L_{\parallel} = 5\frac{X_0}{\rho}$). For this reason, the Cherenkov cone shape is lost for the lower frequencies, where the width of the cone is larger than the Cherenkov angle. At higher frequencies where the width of the cone is narrower, a Cherenkov ring is seen [220][221].

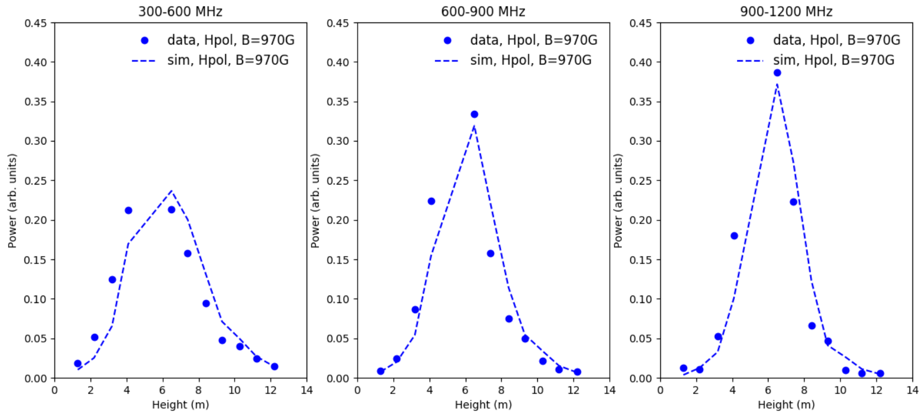

Figure 6.22: Power for horizontally polarized signals (B=970 G), for frequency bands 300-600 MHz, 600-900 MHz, and 900-1200 MHz, as a function of antenna height. Each profile is normalized by total power.

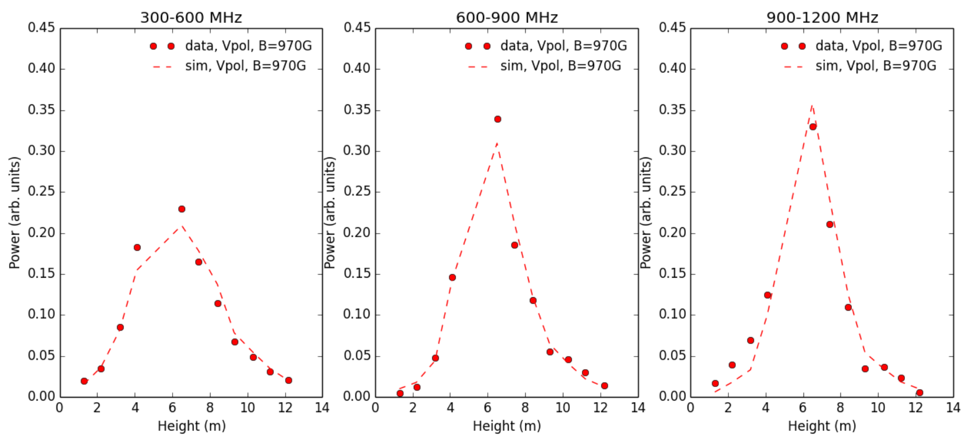

Figure 6.23: Power for vertically polarized signals (B=970 G), for frequency bands 300-600 MHz, 600-900 MHz, and 900-1200 MHz, as a function of antenna height. Each profile is normalized by total power.

6.5.3 Magnetic Effects

SLAC T-510 was the first experiment to directly measure radio emission from a particle cascade in a magnetic field. We expect the radiation to scale linearly with magnetic field, and indeed, we see the signal strength increase linearly with the strength of the magnetic field. The peak amplitude also changes polarity with the polarity of the applied magnetic field. This corresponds to the transverse current induced in the cascade flowing in the opposite direction. Figure 6.24 shows that the geomagnetic signals for positive and negative magnetic fields are inverses to each other.

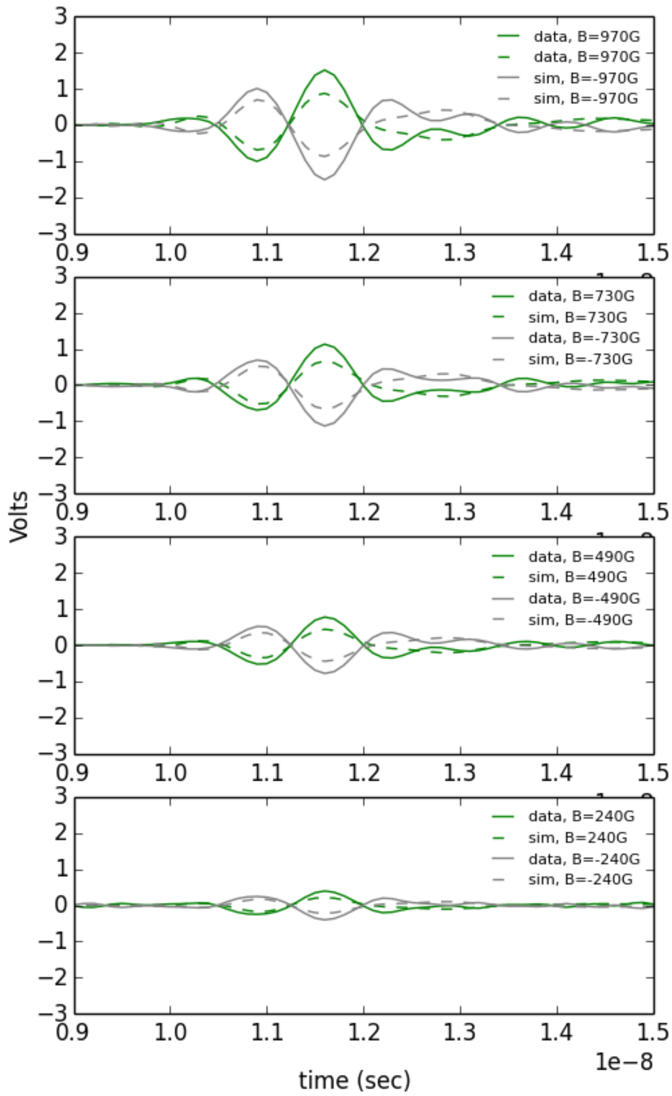

Figure 6.24: Horizontally polarized data and simulations for magnetic field strengths of ±970,±730,±490,±240 G, and at antenna position of 652 cm above beam height.

Because the amplitude of the data voltage is systematically higher than the simulated voltage (presumably due to the reflection problem), we look at the ratio of horizontally polarized to vertically polarized signals to compare the scaling with magnetic field. Figure 6.25 shows this ratio plotted against the magnetic field strength. For the antenna position at 652 cm, the best fit line to the measured data differs by $\sim 20\%$ from the simulated data.

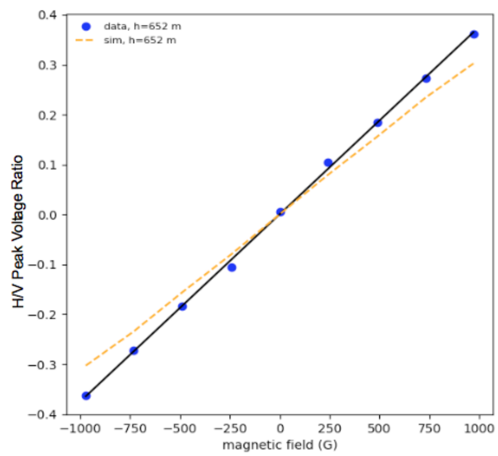

Figure 6.25: The ratio of horizontally polarized signal to vertically polarized signal is shown for the antenna at 652 cm. The dashed line is the simulated ratio, and the black line is the linear fit to measured data.

6.5.4 Reflections

The T-510 target was placed on an RF absorbing mat during the experiment. From the measured data, we see that the measured voltage is systematically larger that the simulated voltage by roughly 35%. This discrepancy is thought to be due to reflections from the bottom of the target interfering with the main signal. Figure 6.26 shows a schematic of the target and antenna positions. A given antenna sees multiple reflections. The first reflection from the bottom of the target is separated from the main pulse by about 1 ns, and therefore interferes with the signal in a way that is complicated to correct. Second and third reflections are separated by more than 6 ns.

These reflections are responsible for the interference pattern seen in the frequency domain with a beating every 150 MHz.

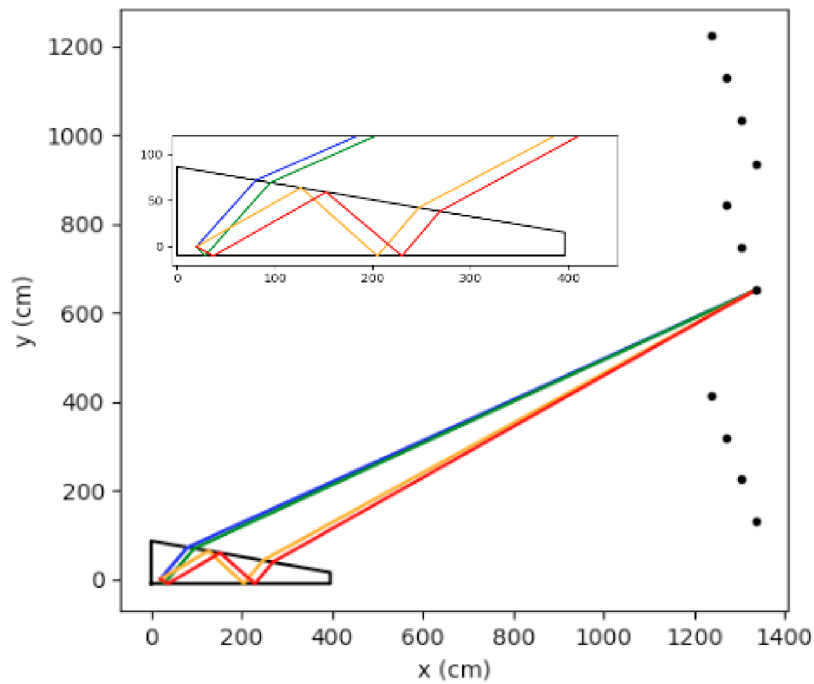

Figure 6.26: Reflections seen in SLAC data. Black points represent antenna positions. This diagram shows reflections that land in the antenna at 652 cm above beam height. The primary signal is shown in blue, the first reflection in green, and second and third reflections in yellow and red.

Three reflections are modeled in Figure 6.26, but there are also reflections from the back of the target that are not taken into consideration in this analysis, but discussed in Appendix E. At the time of the experiment, the characteristics of the mat were unknown. Since then, measurements have been done that indicate the mat has a reflection coefficient close to one in the T-510 frequency band. This is discussed in Appendix D. We take the approach of adding full reflections to the simulations in order to compare them to data. To do this we need to know the shape and amplitude of each reflection. The timing of each reflection can be calculated directly using known geometry. To find the shape of the antennas we start at the antenna position use ray tracing to find the angle of emission for the ray that would start at the same place as the primary emission and reflect and hit the antenna. Then, with that emission angle we find where a direct ray would land in the antenna plane. Data is only available for discrete antenna positions, so we use the simulated data for the antenna position closest to the predicted location. For the first reflection this is the same antenna. For the second and third antennas this emission angle is offset by approximately 20°, twice the tilt of the target surface. Then, the reflected signal is added to the primary signal in the time domain, with the calculated time delay, as

$$V_{total}(t) = V_{primary}(t) + R_{mat} \times V_{reflected}(t + t_{delay}). \tag{6.13}$$

Here, R_{mat} is the reflection coefficient of the mat. Since the point of the reflected signal in the antenna plane is close to that of the primary signal, the same pulse shape is used for both, and $V_{primary} = V_{reflected}$. Figures 6.27 and 6.28 show the results of adding one reflection with $R_{mat} = -1$ to produce simulated voltages. The choice of -1 is appropriate for reflection from a perfect reflector or a medium with very large dielectric constant. The first reflection is closest to the main pulse in time, so it has the most influence on the amplitude of the signal.

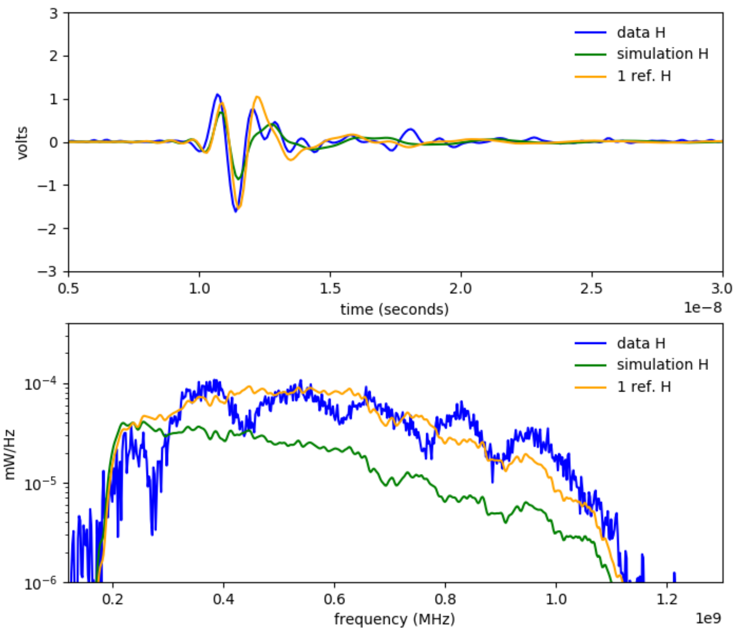

Figure 6.27: Horizontal signal at B=970 at a position of 652 cm above the beam height. The blue line indicates the measured signal. The green line indicates the simulation, and the orange line indicates the simulation with the addition of the first reflection.

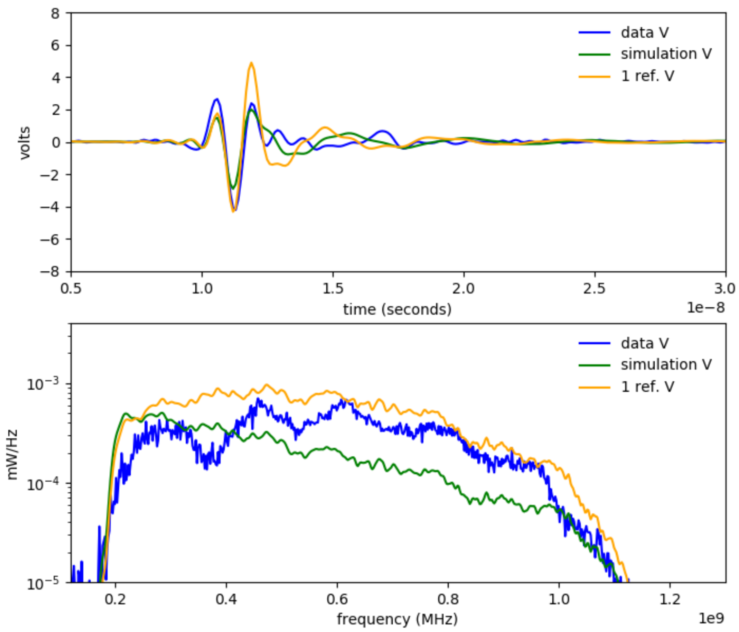

Figure 6.28: Vertical signal at B=970 at a position of 652 cm above the beam height. The blue line indicates the measured signal. The green line indicates the simulation, and the orange line indicates the simulation with the addition of the first reflection, $\sim$ 1 ns delayed from the primary signal, inverted with a reflection coefficient of 1.0 at the mat.

Including the first reflection boosts the amplitude of the simulated peak data to that of the measured data. It also increases the power content of the entire signal, most notably in the higher frequencies where the discrepancy is the largest. For horizontal signals, the shape of the time domain signal reconstructs well. For vertical signals, including the reflection produces a reasonable amplitude for the primary pulse (at -4 V in Figure 6.28), but introduces more ringing in the signal.

To do a quantitative estimate of the effect of the reflections on the frequency spectum, we look at the simulated electric field $E_0(\omega)$. Adding a phase shifted, reflected signal, E_1, gives

$$\begin{aligned} E(\omega) &= E_0 + E_1 \\ &= E_0 - e^{i\omega t} E_0 \\ &= E_0(1 - e^{i2\pi f t}). \end{aligned} \tag{6.14}$$

This gives a power of

$$P = 2P_0(1 - \cos(2\pi f t)), \tag{6.15}$$

which peaks when $\cos(2\pi f t) = -1$, or equivalently, when $ft = 1/2$. From Figures 6.27 and 6.28, the peak power ratio, P/P_0, can be estimated to be around 700 MHz, which gives a time delay for the first reflection of

$$t = \frac{1}{2f} = \frac{1}{1.4\,\mathrm{GHz}} = 0.7\,\mathrm{ns}. \tag{6.16}$$

This estimate is very close to the calculated delay time of 0.78 ns for the antenna position at 652 cm.

Looking at the peak amplitudes of the simulated signal with one reflection across the radiation pattern, it seems that the reflection does account for the much of the discrepancy between simulation and data. However, we still see the shift in the radiation pattern between data and simulation. These results are seen in Figure 6.29.

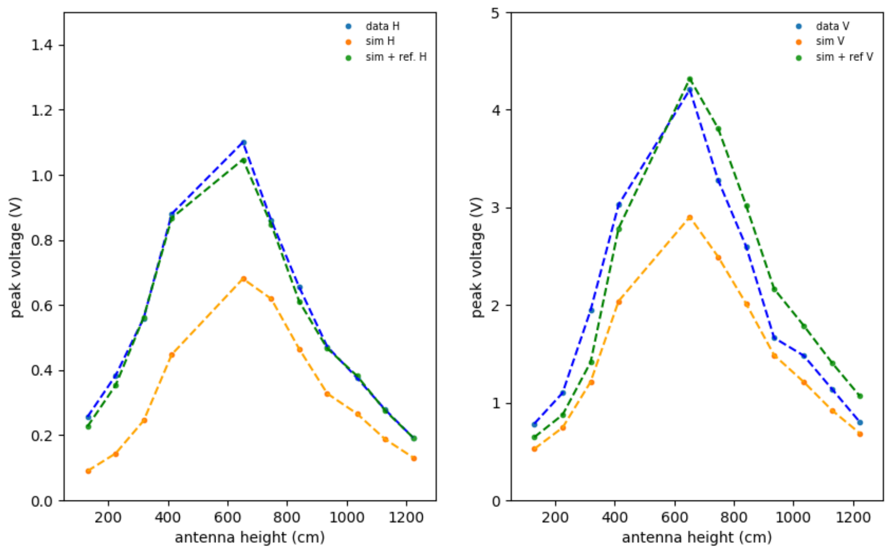

Figure 6.29: Radiation pattern mapped by peak amplitude of signal. Amplitudes are shown for data (blue), simulation (orange), and simulation corrected for the first reflection (green). Left: horizontally polarized data with magnetic field B=970 G. Right: vertically polarized data with magnetic field B=970 G.

Figures 6.30 and 6.31 show the power in the pulses split into frequency bands and normalized. It is clear that adding reflections changes the amplitudes and power of the pulses, however the shape of the simulated emission pattern over the antenna plane is similar with and without reflections.

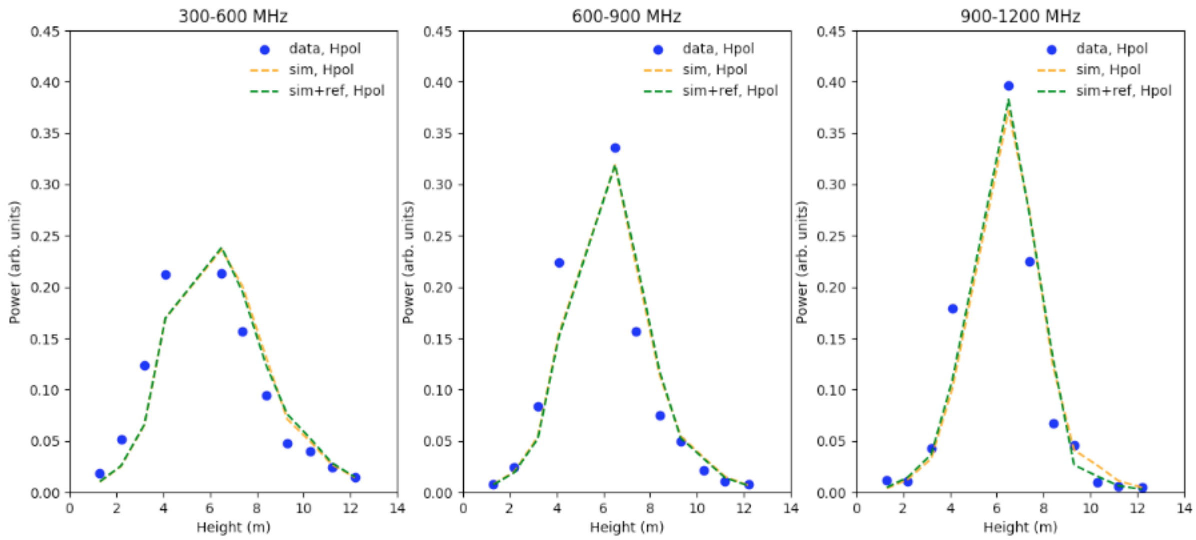

Figure 6.30: Power for horizontally polarized signals (B=970 G), for frequency bands 300-600 MHz, 600-900 MHz, and 900-1200 MHz, as a function of antenna height. Each profile is normalized its total power.

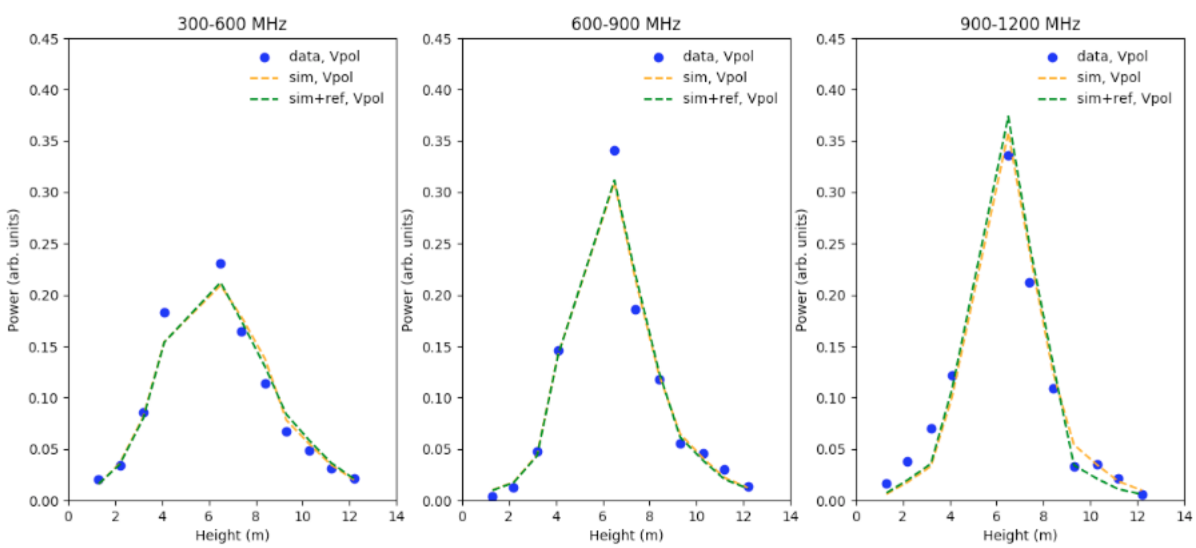

Figure 6.31: Power for vertically polarized signals (B=970 G), for frequency bands 300-600 MHz, 600-900 MHz, and 900-1200 MHz, as a function of antenna height. Each profile is normalized by its total power.

The addition of a reflection also brings the ratio of horizontal to vertical peak amplitude into closer agreement, as seen in Figure 6.32.

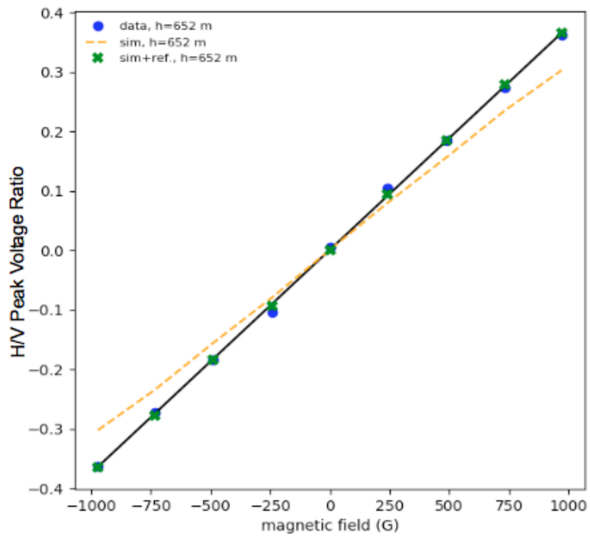

Figure 6.32: The ratio of horizontally polarized signal to vertically polarized signal is shown for the antenna at 652 cm. The dashed line is the simulated ratio without reflection, and the black line is the linear fit to measured data, and the green crosses indicate the simulation with the first reflection added.

The second reflection is delayed between 5 and 9 ns with respect to the first, depending on antenna position and assumed point of emission within the target. The third reflection is a further ~ 2 ns after the second. These don't contribute to the peak amplitude of the time domain signal, but do create the interference pattern seen in the frequency domain. In order to find the correct shape of the reflected pulses, we again find the emission angle of each reflected signal that reaches the antenna. Using that angle, we trace the trajectory of the emission as if it was not reflected to determine where it would land in the antenna plane. Then, we use the shape of the pulse from the closest simulation we have to that point. For the antenna at 652 cm, the second and third reflections would land in the antenna at 319 cm. The second and third reflections are added in the same manner as the first, with the extra consideration that the reflection and transmission coefficients at the top of the target now have to be recalculated for each trajectory.

From the figures showing contributions from difference segments along the target (i.e. Figure 6.8), we estimate that most of the emission comes from a point roughly 30 cm into the target. In reality, the emission comes from the entire track, but we use this point as a reference to find the time delay between the main signal and second reflection. (This distinction isn't as important for the first reflection, which has a time delay less dependant on emission point.) The interference pattern created by the second and third reflections is very sensitive to the time delay. Also, here we use the same emission point for both vertically and horizontally polarized signals, although as discussed in Section 6.2.4, this is not necessarily the case. The effects of adding the second and third reflections are shown in Figures 6.33 and 6.34. An interference pattern is evident in both polarizations. There could also be a contribution to the signal from a reflection off the back of the target. This would be more pronounced for the vertical signal, since presumably it evolves closer to the beginning of the target. The back reflection analysis is beyond the scope of this work.

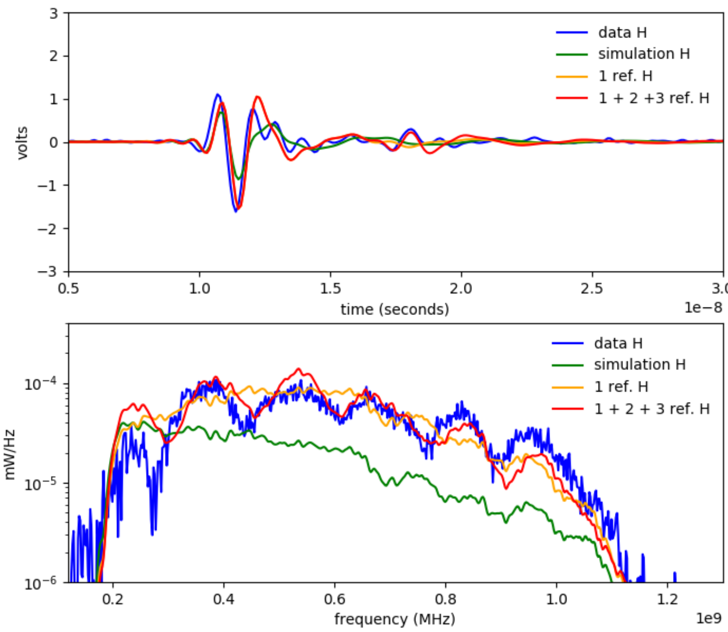

Figure 6.33: Horizontal signal at B=970 G at a position of 652 cm above the beam height. The blue line indicates the measured signal. The green line indicates the simulation. The orange line indicates the simulation with the addition of the first reflection, and the red line indicates the addition of the second and third reflections.

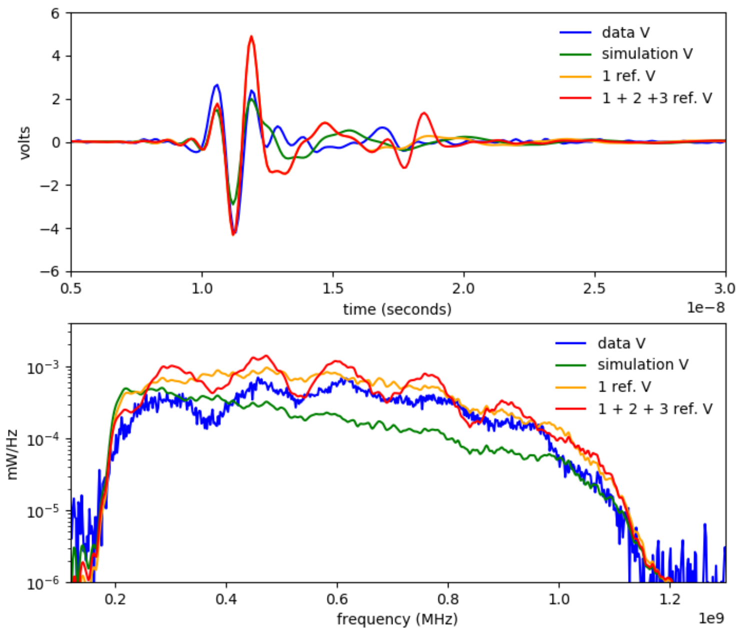

Figure 6.34: Vertical signal at B=970 G at a position of 652 cm above the beam height. The blue line indicates the measured signal. The green line indicates the simulation. The orange line indicates the simulation with the addition of the first reflection, and the red line indicates the addition of the second and third reflections.

In summary, adding the first reflection to simulated data recovers the difference in amplitude between simulated and measured data. Adding second and third reflections indicate that the inference pattern evident in the data is also due to reflections in the target. Because we know that the three primary reflections have a large influence on the data, it could also be that other reflections, such as the reflection from the back of the target, also influence the shape of the pulse. To model this further, more simulations would have to be done which carefully include these effects.

6.5.5 Wavefront

The previous sections focus on finding the amplitude of radiation from a particle cascade at different antenna positions in order to understand the radiation pattern and cascade development. Studying the shape of the radio wavefront is also a promising way to understand cascade development, and is used to extract X_{max} from cosmic ray data [222] by comparing the timing of the experimental data to simulations. Figure 6.35 shows the relative arrival times of signals at antenna positions across the radiation pattern. The arrival time at each position is found by taking the timing of the peak of each voltage trace. The times are then corrected for geometric antenna offsets, so as to be aligned into the same plane. The data from the antenna at 513 cm is used here (although not in the previous analysis), because the timing of the pulse was able to be extracted from the data, although pulse amplitude was not. The data from the 747 cm antenna is not used because of unknown timing offsets in the cables. There is a clear non-planar wavefront. In order to characterize the shape of the wavefront more precisely, it will be necessary to recalibrate T-510 timing delays in the antennas, and fully understand the timing of the simulated electric fields after they are convolved into voltages. There is also an apparent small timing offset between polarizations. This results in a small circularly polarized signal, which is explored further in [214].

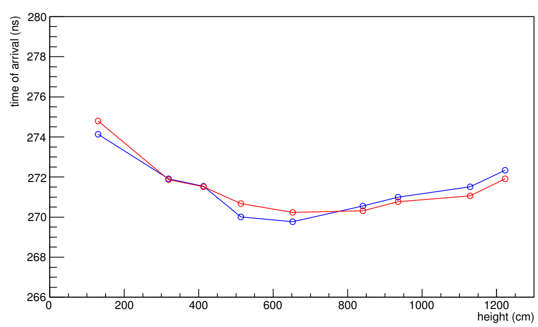

Figure 6.35: Relative arrival times of horizontally (blue) and vertically (red) polarized signals for different antenna positions.

6.6 Conclusions

The T-510 experiment produced radio emission in a controlled experimental setting with a magnetic field present. This data was compared to simulations that track the cascade development at the particle-level and use first principles to simulate emission without relying on any assumptions about emission mechanisms. The same techniques are used to simulated radio emission from cosmic ray air showers.

First, the paradigm of magnetically induced radiation was studied. Measured radiation shows a conical pattern that narrows with increasing frequency in both magnetically induced and charge excess signals. The magnitude of the magnetically induced radiation scales linearly with magnetic field strength while the Askaryan signal remains unchanged.

However, when comparing the amplitudes of simulated and measured signals, it was seen that they differed by an amount that can't be attributed to the known systematic uncertainties. For this reason, reflections within the target were considered. We have shown that including realistic, full reflections in the simulations reproduces the data well, with a first reflection correcting the amplitude and spectrum of the signal and the second and third reflections producing an interference pattern seen in the data. The agreement between data and simulations demonstrated in the T-510 experiment confirms that these simulation techniques are appropriate to use in the reconstruction of cosmic ray air showers.

In order to confirm the agreement of absolute scaling between data and simulation, we need a better study of the experimental and simulation systematic errors. This effort will require quantifying uncertainty in parameters that we have taken as known quantities in this study, such as the index of refraction of the target, the cascade development in the lead, effects of the digitization in the oscilloscopes used, etc. Then, with complete systematic errors for both data and simulation, the magnitudes of each can be compared to place a bound on the absolute simulation uncertainty.

Chapter 7

ANITA 3

7.1 Introduction

The results of the SLAC T-510 experiment will be critical input to radio experiments such as ANITA. The ANITA 3 preparation and flight took place at the same time as T-510 experiment and data analysis. ANITA data analysis efforts rely heavily on radio simulation packages, validated by the T-510 experiment. In the following chapter I discuss the ANITA 3 concepts and various components of the experiment, as well as initial thoughts of the ANITA 3 flight that took place in the austral summer of 2014-2015.

7.2 ANITA 3 Concept

ANITA (Antarctic Impuslive Transient Antenna) is a radio interferometer that flies balloon borne over the Antarctic ice. ANITA's antennas see a 360° view of Antarctic ice and detect Askaryan radiation from neutrino induced particle cascades in ice and geomagnetic radiation from cosmic ray induced particle cascades in the Earth's atmosphere. Radio signals from such events are faint, but can also travel far distances without attenuation. This makes ANITA ideal for detecting rare UHE neutrino and cosmic ray events.

ANITA 3 is the third flight of the ANITA program, with changes made to the triggering system, the antenna sensitivity in frequency and coverage, and instrument box layout. The ANITA 1 flight occurred in the austral summer of 2006-2007 and had 32 antennas divided into 16 phi sectors. For this first flight the instrument implemented a triggering system that mixed vertical and horizontal signals into left and right handed circular polarization. The linear Askaryan radiation would then be present in both polarizations. Each signal was also banded into four frequency ranges, resulting in eight inputs. The trigger requirement was 3 out of 8 inputs above individual noise-riding thresholds, with at least one input from each polarization. This requirement captured broad band signals and discriminated against CW. Unexpectedly, including the horizontal polarization opened the window to observations of UHECR signals.

ANITA 2 flew in the austral summer of 2008-2009. This instrument included an additional 8 antennas for a total of 40. The trigger only included vertically polarized inputs to increase sensitivity to neutrino signals. The signal was divided into three subbands and one full band input. A trigger occurred when the full band and two of the three subbands had a signal amplitude over the given threshold, protecting against CW triggers. The discovery of the ANITA 1 cosmic rays was not made until after the ANITA 2 instrument was established. The scientific results of the first two ANITA flights are discussed in Chapter 3.

ANITA 3 builds off the legacy of the first two flights. There were a total of 48 antennas, with an addition drop down antenna to detect low frequency signals. The trigger system used separate vertical and horizontal polarizations and the entire bandwidth to increase the signal to noise ratio. CW noise sources would be minimized using dynamic phi masking instead of coincidences in different frequency bands. ANITA 3 flew in the austral summer of 2014-2015.

7.3 ANITA Gondola

The ANITA gondola is the framework that houses the rest of the experiment. Figure 7.1 shows the ANITA 3 gondola with all components included and deployed. The three tiers of antennas, the instrument box, solar panels and the ALFA (ANITA Low Frequency Antenna) are all visible.

Figure 7.1: Fully assembled ANITA 3 gondola at the hang test in Palestine, TX.

ANITA 3 used new carbon fiber tubing technology to build the frame that held antennas, instrument box, and communication equipment. Previous ANITA gondolas were constructed from aluminium, and the change was made to save on weight restrictions. The gondola was constructed from the top down and was completely painted white to prevent overheating. Powered components and the instrument box were covered with reflective tape and grounded to the gondola frame to redirect heat to be radiated. Figure 7.2 shows an overhead view schematic of the gondola layout.

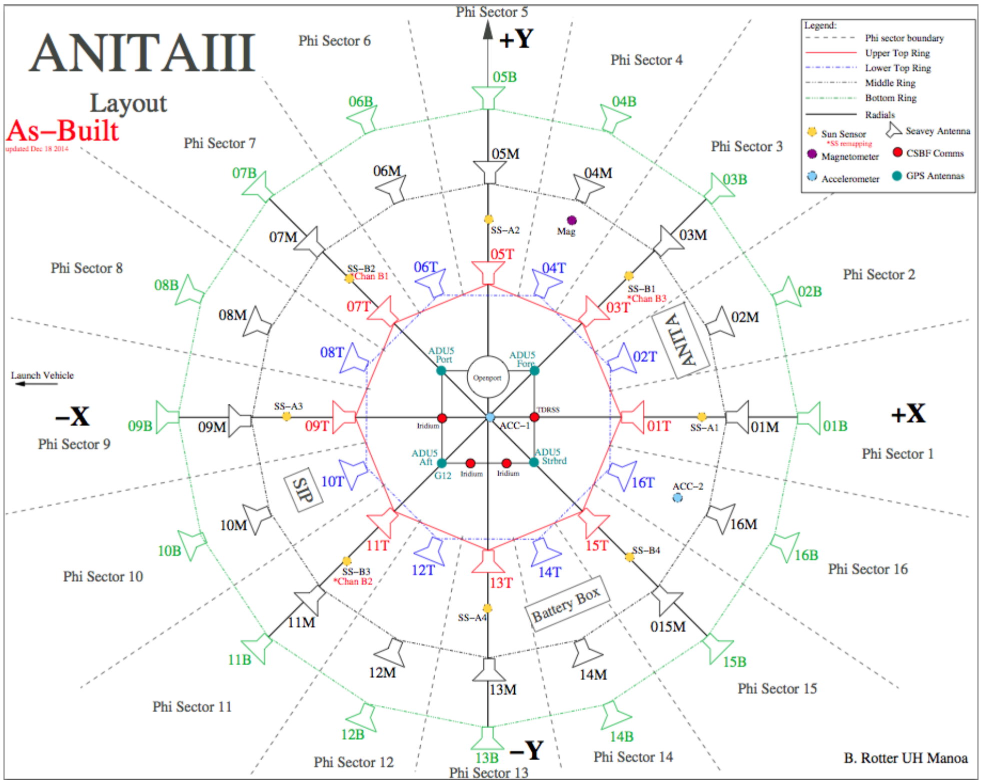

Figure 7.2: Layout of the ANITA 3 payload.

48 antennas were arranged in three tiers, the top tier consisting of two sub tiers. The instrument box, magnetometer, and sun sensors were situated between the top and second tier. Solar panels were installed as drop down units to be released below the lowest tier of antennas after launch. This was done as a space saving requirement, as the gondola had to be built in a limited size hanger and launched from a limited size vehicle. Finally, a large drop down low frequency antenna was built to be stored inside the antenna array and deploy after the solar panels. This antenna hung 2 meters below the solar panels so as to not interfere with the tiered antennas. The Columbia Scientific Balloon Facility (CSBF) Science Instrument Package (SIP) was located on the opposite side of the gondola as the ANITA instrument box. Communications equipment and Global Positioning System (GPS) antennas were on the very top of the payload, including Iridium and OpenPort communication equipment. These features of the experiment will be discussed further in the following sections.

7.4 RF Signal Chain

The radio frequency (RF) signal chain is a critical part of the ANITA experiment that propagates the electric field created by a neutrino or cosmic ray cascade to the heart of the triggering and data writing systems. The signal observed by each antenna needs to be filtered, amplified and digitized for storage. This section gives an overview of all the components of the ANITA 3 signal chain between the front-end antennas and triggering and digitization.

7.4.1 Seavey Antennas

The first stage of the ANITA signal chain is the antenna. ANITA 3 consisted of 48 quad ridged, dual polarization Seavey horn antennas. Antennas were customized to have maximum efficiency between $200 - 1200$ MHz, the frequency band expected to be produced by Askaryan radiation. Antennas were arranged on the gondola in phi sectors spanning 22.5 degrees and tilted downwards 10° to have good coverage of the Antarctic ice. The 3 dB point of the antennas (averaged over the $200 - 1200$ MHz range) is 30°, which allows a total of 40° downwards coverage of the ice. Most of the ice volume is near the horizon, so 40° coverage is suitable.

Seavey antennas have been used for all ANITA flights and have been well characterized. New antennas were used for the ANITA 3 campaign and gain and S21 values for each were individually measured at the CSBF facility. The beam pattern was also measured for select antennas to ensure consistency with previous flights.

Figure 7.3 shows the beam pattern for vertical and horizontal antenna polarizations. In Figure 7.4 we see the Seavey gain, which is flat in the 200-1200 MHz region. At 3dB, the bandwidth is 200-1280 MHz, ensuring we see the expected neutrino and cosmic ray event frequencies.

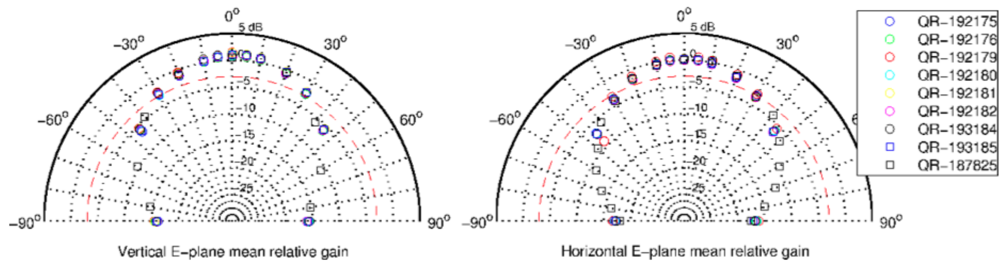

Figure 7.3: Seavey antenna beam pattern. Antenna gain is measured for each antenna of each ANITA flight, but anechoic chamber beam pattern measurements were only made for ANITA 1 [223].

Seavey antennas are the same models used in the T-510 experiment and were characterized in the same way. Figure 7.5 shows the effective height measured for a sample of ANITA antennas.

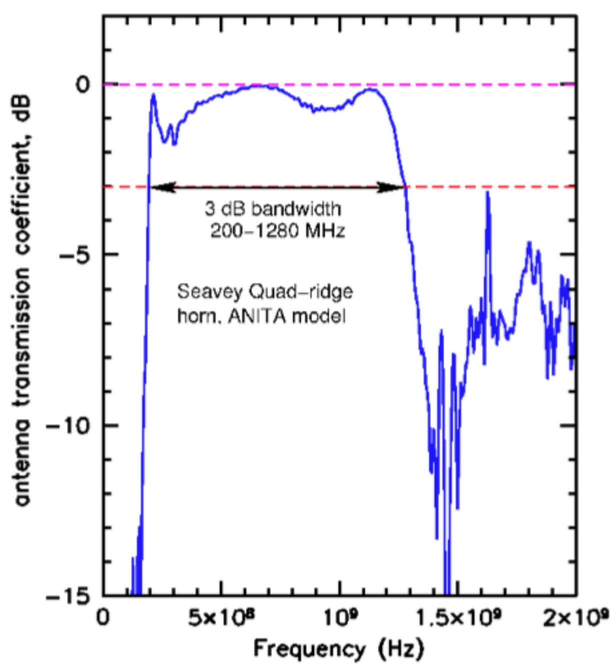

Figure 7.4: Seavey antenna gain for ANITA 1 antennas [223].

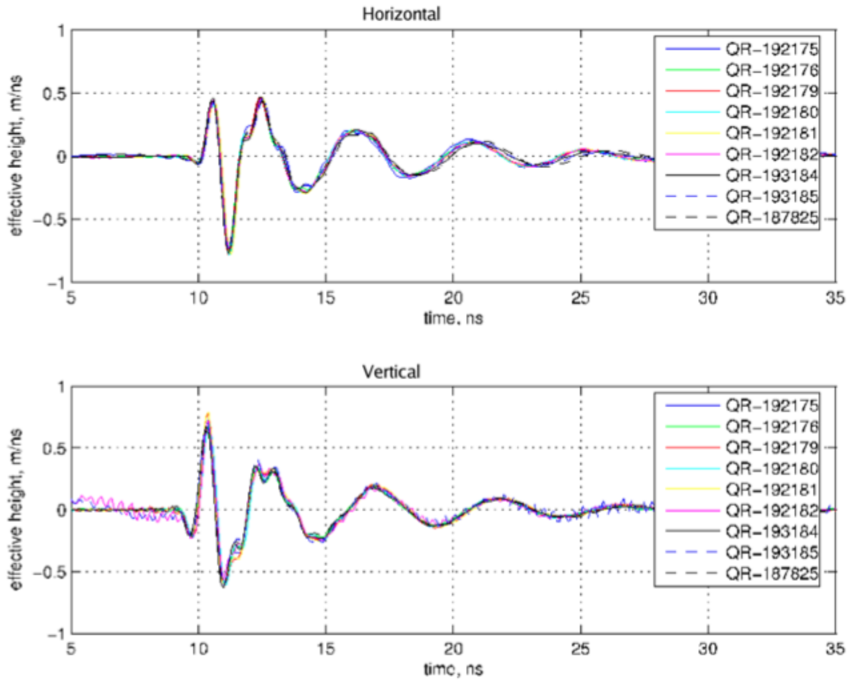

Figure 7.5: Effective height measured for Seavey antennas for ANITA 1, also used for the T-510 experiment [223].

7.4.2 ANITA Instrument Box

The second stage of the signal chain is amplification. Attached to each antenna is an AMPA (antenna-mounted pre-amplifier) which amplifies the weak signal before it gains noise in the bulk of the signal chain. The signal travels from the AMPA through 12 feet of Heliax cable and enters the instrument box, which contains the rest of the electronics. A schematic of the RF signal chain inside the box is shown in 7.6, where the signal enters through the AMPAs.

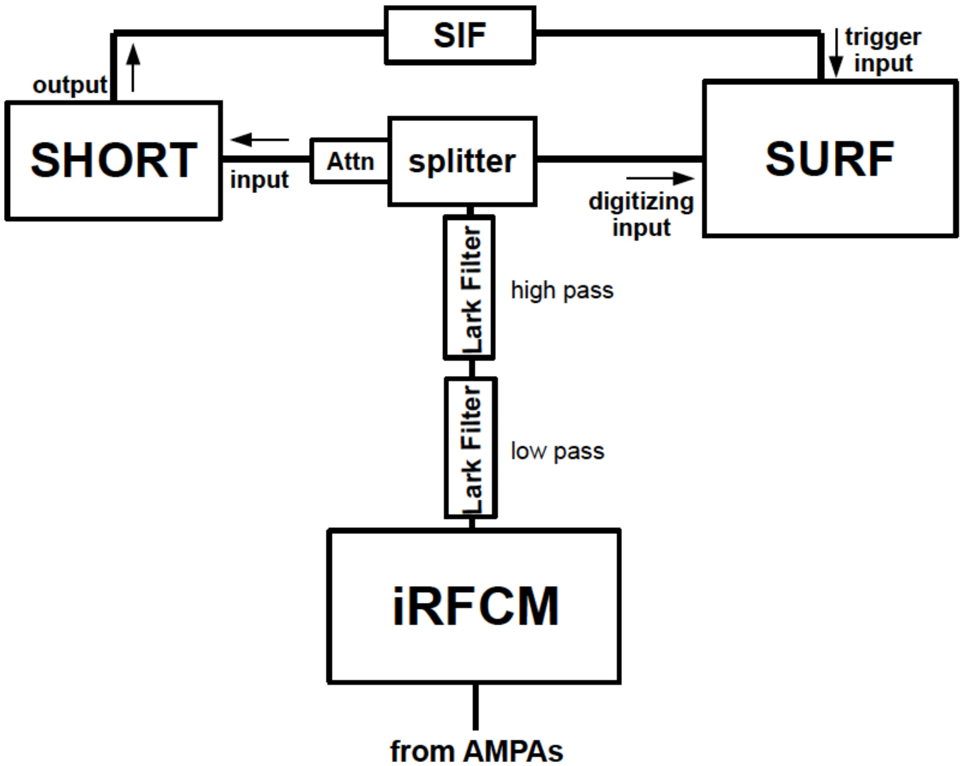

Figure 7.6: ANITA 3 signal chain. Radio signal enters AMPAs directly after going through Seavey antennas.

The signal goes directly into the iRFCMs (internal Radio Frequency Conditioning Module, modified from ANITA 2 to go inside the instrument box), seen in Figure 7.7 with the radio safe box open. The iRFCMs have further amplification and filtering.

Figure 7.7: Internal Radio Frequency Conditioning Module in production.

From there the signal goes through Lark filters, filtering between 200 MHz and 1200 MHz. Prior to the flight, the total power for each channel is measured, and different attenuators are placed on every channel according to its gain. The signal is split, with half the signal going to the triggering electronics, and half going to the digitizing electronics. The digitizing signal goes into the SURF (Sampling Unit for Radio Frequencies), and the triggering signal goes into the SHORT (SURF High Occupancy RF Trigger, Figure 7.8) board, which squares the signal with a tunnel diode, and then into the TURF (Triggering Unit for Radio Frequencies). If a trigger is detected the SURF is alerted via the SIF (SURF InterFace), and data is recorded to the flight hard drives. Details of the SURF and TURF are discussed later in this section.

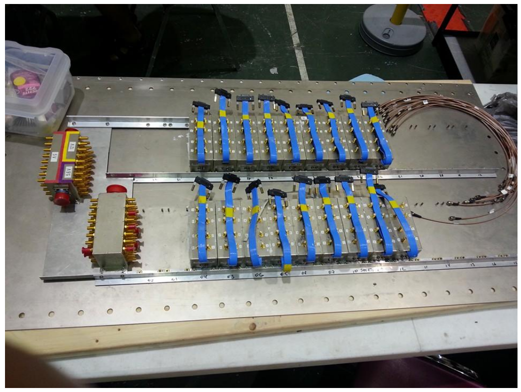

Figure 7.8: SHORT boards mounted on the lid of the instrument box. Photo by Ryan Hupe.

Each piece of the signal chain was characterized at the CSBF facility in Palestine, Texas in the summer of 2014. Characterization included testing S21 for each component on a Network Analyzer, and noise figures for relevant parts. For example, the AMPA gains and noise figures as a function of frequency are shown in Figure 7.9. The 200-1200 MHz bandpass is evident.

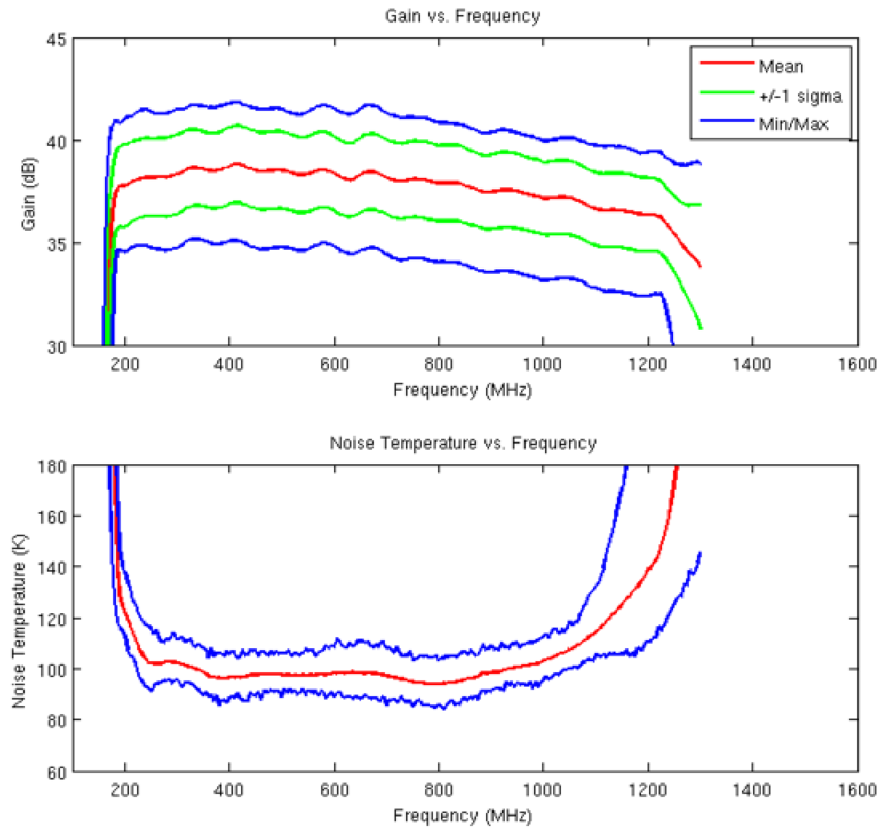

Figure 7.9: AMPA responses, measured in Palestine.

Similarly, the iRFMC S21 measurements show appropriate gain for the desired frequencies.

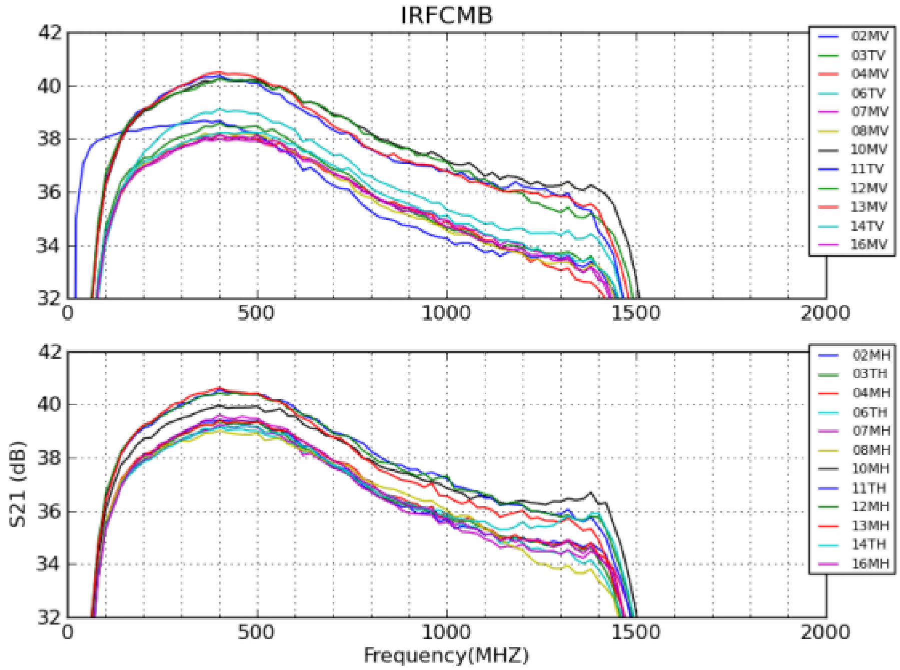

Figure 7.10: iRFCM responses, measured in Palestine.

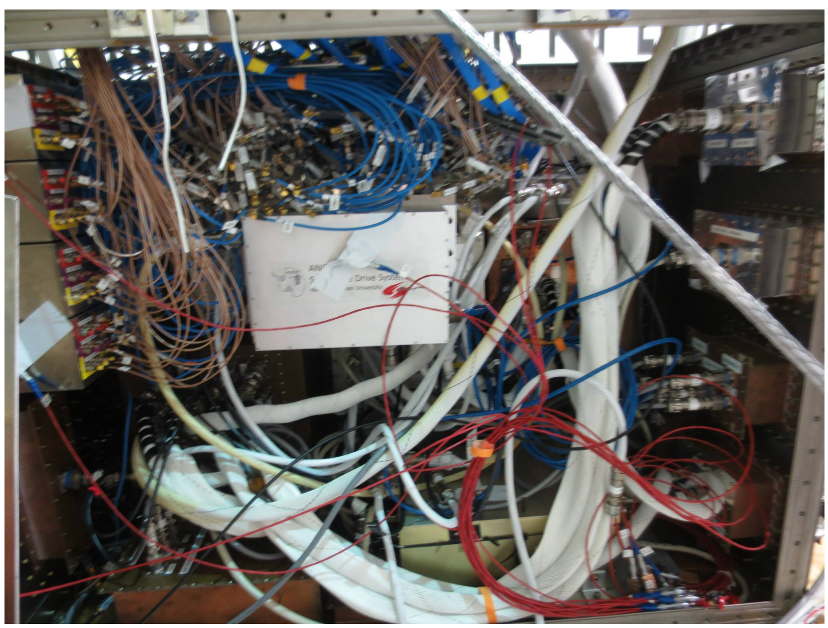

Figure 7.11: Inside of the instrument box.

The inside of the instrument box is shown in Figure 7.11. Cables are carefully guided and strain relieved between each signal chain component. The iRFCM units are seen on the left edge of the box. SHORT, SURF, and TURF units are in the upper back area, hidden by blue cables and filters. Towards the bottom right we can see the housekeeping box and GPS units, discussed below. Temperature sensors were placed on a selection of components to monitor their performance during flight.

7.4.3 Sampling and Data Acquisition

As seen in Figure 7.6, the RF signal is split into a sampling path and a triggering path. The analog ANITA data is continuously sampled until a trigger is seen, and then the data is digitized and saved. The 12 SURF boards house the data sampling. Each SURF board contains eight channels, 4 hpol and 4 vpol. Care is taken that no adjacent SURF channels have signals from adjacent antennas to avoid cross talk effects. ANITA has a specifically designed chip for data acquisition as no commercially available chip could handle both the large quantity of data ANITA collects and the limited power budget. This LABRADOR chip, four of which are mounted on each SURF board, has a 260 element SCA (Switched Capacitor Array) that continuously samples data at a rate of 2.6 GSPS. Each channel is sampled by four LABRADOR chips simultaneously. When a trigger is detected (details given in the next section), the SCA on one LABRADOR is frozen and the contents sent to a digitizer, a process that takes 30 ms. Since 4 LABRADOR chips are used at the same time, the other three can sample, minimizing dead time [224].

7.4.4 Trigger System

Half of the ANITA signal enters the triggering system. The system is designed to be flexible to adjust trigger criteria for different environmental conditions. The first components in the triggering pathway are the SHORT boards. Each SHORT board has eight channels that amplify each signal using a tunnel diode, which squares the incoming signal. The output of the SHORT board is sent into an FPGA (Field Programmable Gate Array), which determines if the signal is above a threshold. This threshold is variable which allows it to stay just above the thermal noise floor. The threshold is determined on the flight computer, which continuously calculates the trigger rate and adjusts the threshold accordingly. The signal in any channel crossing the trigger threshold is considered an L1 trigger. The output trigger logic from the FPGAs is sent to the TURF board.

The TURF unit contains a second FPGA which compares the trigger patterns from the L1 trigger. The next level "phi-sector" trigger is formed when two out of three channels in the same phi-sector and of the same polarization have an L1 trigger. Next, a "polarization" trigger is formed if two adjacent phi-sectors have "phi-sector" triggers. Polarization triggers of either hpol or vpol constitute a global trigger which is sent to the SURFs to initiate digitization.

Trigger masking was implemented for ANITA 2 and ANITA 3. If the payload passes a noisy area the trigger can be swamped with false signals. Trigger masking allows specific phi sectors to be eliminated from the trigger logic. The decision to mask a phi sector was again made on the flight computer, which continuously monitored the direction and rate of triggers.

The ANITA 3 trigger efficiency was measured at the Long Duration Balloon (LDB) Facility in Palestine, TX. Varying strength signals were fed into each channel with timing delays corresponding to different positions of the source signal. Trigger efficiency was 50% at 3 SNR, seen in Figure 7.12.

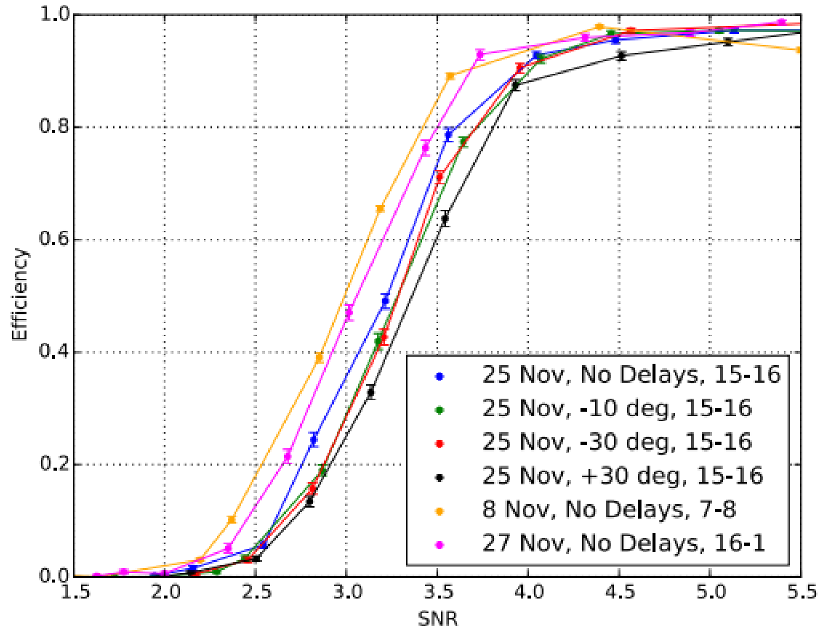

Figure 7.12: Trigger efficiency, as measured at LDB.

7.5 Flight Software

The ANITA flight computer is housed inside the instrument box. Commands can be set to the computer via telemetry, discussed later in this chapter. An acquisition daemon (Acqd) maintains trigger thresholds, phi masking, and is responsible for acquiring waveform and housekeeping data from the SURFs. The event daemon (Eventd) and archive daemon (Archived) write the data to three local hard drives. A prioritizer daemon (Prioritizerd) uses a cross correlation method to assign a priority level to each event associated with the likelihood of it being a neutrino or cosmic ray. High priority events are sent North via telemetry.

7.6 GPS and Positioning

Position and attitude information is critical for ANITA analysis and event reconstruction. Orientation and location of the payload over Antarctica can confirm or reject reconstructed events as cosmic rays and neutrinos. The gondola included 3 differential GPS units related to ANITA, as well as one for CSBF systems. There was one Thales G12 unit that gives position and altitude information. Two independent Magellan ADU5 units gave position, altitude and attitude information, which includes heading, pitch, and roll. The G12 unit requires one antenna, and the ADU5 units each require 4 antennas to reach an attitude solution. These antennas were mounted on the top of the gondola in a square configuration for maximum separation between antennas. The ADU5 units are capable of giving attitude information to within 0.1°. The GPS antenna locations were calibrated using Ashtec Evaluate software at the LDB facility at McMurdo station. Sun sensors, magnetometers, and even solar panels can also yield position and attitude information. Redundancy for position information is necessary because it is mission critical.

7.7 Power System

The ANITA instrument was optimized to run on as little power as possible, as it can only live on battery power for about 6 hours after launch. Since the ANITA instrument was in full view of the sun during the full flight, solar power was utilized for charging the batteries. Eight solar panels, with full azimuthal coverage, dropped down below the last tier of antennas. Power was converted to rechargeable batteries through a charge converter. A power distribution box sends the required voltages to systems including the SHORT boards, computer CPU, and any components requiring power.

7.8 Communication Systems

Communication with the payload during the flight was critical to send commands to the instrument, monitor housekeeping information (system temperature, location, etc.), and receive prioritized data, or data that had a high likelihood of coming from a calibration pulser or a cosmic ray or neutrino event. Commands include forcing triggers, requesting configuration files, changing phi masking requirements, and changing trigger thresholds, among others. The instrument could also be power cycled via commanding, and flight software could be updated when the Openport (discussed below) connection was operational.

ANITA 3 used 3 communication methods. LOS (line of sight) was the most efficient way to send data (at 300 kbps), however it was only available at the very beginning of the flight before the payload went over the horizon, and if the payload circled near McMurdo again. TDRSS (Tracking and Data Relay Satellite System) and IRIDIUM satellite constellations were used after ANITA left LOS contact. The IRIDIUM constellation was used both for Openport (new for ANITA 3) and standard data packets. Openport offered data rates of $\sim$20 kbps. The IRIDIUM Openport uplink failed mid flight, so TDRSS was the main source of communication with the instrument, with data rates of $\sim$6 kbps.

During LOS, information was relayed through GSE machines based in McMurdo that sent information to Palestine, TX. That information was forwarded to collaboration universities to be read by the data viewing software. Data from satellite uplinks was sent north directly. ANITA events require about 56 kb of space, and about three events were sent via satellite every minute (along with house keeping information), which is approximately 0.1% of events written to disk.

After the flight, the ANITA hard drives were recovered near Davis Sation. The drives were shipped to Hobart, Australia, and hand carried to North America.

7.9 Data Viewing Software

Viewing data in real time was important to the experiment's success. ANITA collaborators took 6 hour shifts for the entire flight so that someone was always monitoring the instrument to look for anomalous behavior so that it could be corrected in flight. Various software was used to view housekeeping and event data.

Anitaviewer, TrigMon and SlowMo, are linux based executables that were created for ANITA 1 and have since been modified for successive flights. These viewers accessed data from sql databases updated with telemetered data. The AWARE web based monitoring system was useful as an independent data monitoring system and used telemetered data in ROOT format.

7.10 System Calibration and Testing

7.10.1 EMI Testing

Because ANITA signals are small, any EMI leakage inside this instrument can cause problems. All components are sealed in EMI safe boxes, as seen in Figures 7.7 and 7.8, however, leakage can occur. EMI testing for both the CSBF SIP and instrument box was performed at LDB using UH's EMI-shielded tent. The instrument under testing was completely inside the tent, along with a Discone antenna (Telewave ANT2805) attached to an AMPA (AMPA 25, gain 34.75 dB at 300 MHz). Power to the AMPA and instrument under testing was located outside the tent, as was a monitoring oscilloscope. Baseline measurements were taken without power to the system, and no differences were detected in the spectra or the waveform RMS of the monitoring antenna when the instruments were powered on. The RF shield testing set up is shown in Figure 7.13.

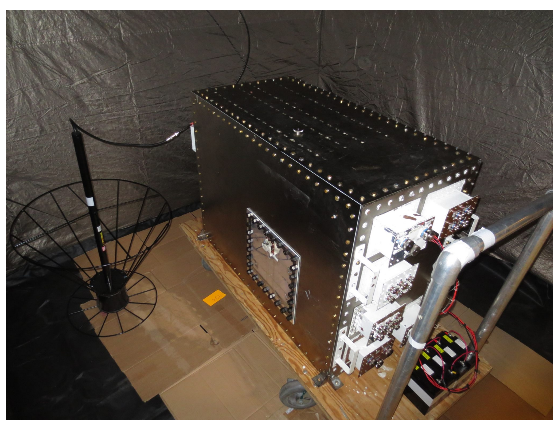

Figure 7.13: RF shield testing inside a EMI-shielded tent. Both the ANITA instrument box and the CSBF SIP were tested. Photo by David Saltzsberg.

7.10.2 Instrument Calibration

Reconstruction of ANITA events depends on precise knowledge of timing between channels. Antenna signals are distributed over 12 SURF units. Each SURF has a clock, but the clocks in different SURFs are not necessarily in sync. Also, each signal travels though a unique signal path and through different attenuators, so exact voltage amplitude needs to be known from start to finish.

The final calibration data was taken at LDB after the ANITA payload was fully assembled. At any time two signal chains were monitored- one for testing and one for reference. The same reference channel was used to compare to the remaining 95 channels. A signal was sent through a variable attenuator and was split and fed into each AMPA. An oscilloscope monitored signals before the attenuator and directly before the signal reached the SURF. The system was triggered externally with a picosecond pulser. Three attenuator setting were used, and 4000 samples were collected for each signal chain. The calibration test setup is documented in Figure 7.14.

Corrections were made for temperature fluctuations, clock jitters, and wrap around differences in the SCA read out.

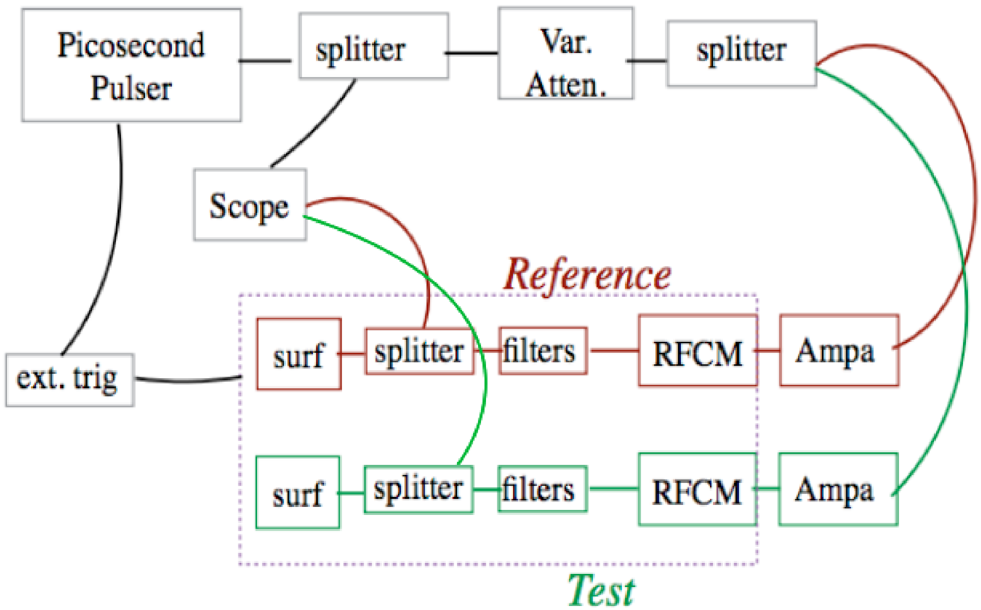

Figure 7.14: Callibration schematic as set up at the LDB facility.

7.10.3 Ground Pulsers

The ANITA instrument cannot be fully turned on until it is well away from McMurdo and loud radio noise. This means that the instrument cannot be fully calibrated end to end before launch. It is necessary to have known signals reach the instrument in flight to finish the calibration process. Ground pulsers were installed at McMurdo station, WAIS Divide, and Siple Dome.

Three pulsers (2 kV, 6 kV, and 10kV) combined with Hpol bicones, a Vpol discone, and a Seavey pointed at the payload were used at LBD. Remote pulsing stations used solar panels to power pulsers fed to vertically and horizontally polarized bicone antennas. A sample LDB calibration pulser configuration is shown in 7.15.

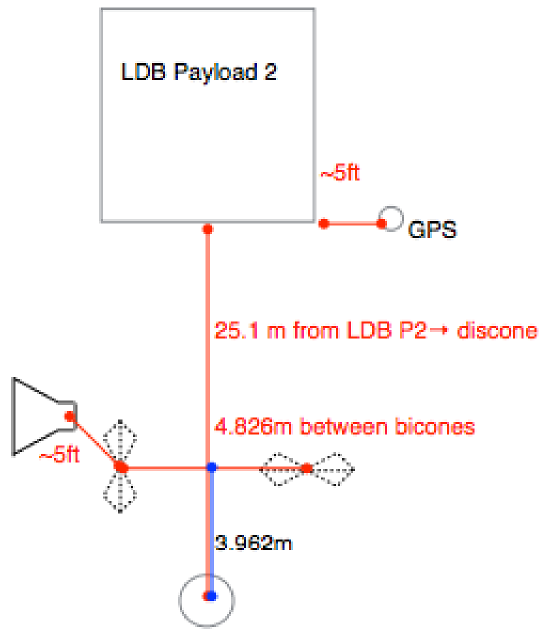

Figure 7.15: ANITA ground pulser system at LDB. Here LDB Payload 2 refers to a position of the ANITA instrument when it was taken outside the hanger.

7.10.4 HiCal

A balloon borne calibration pulser was flown shortly after the ANITA instrument launched. This was done to help calibrate cosmic ray events that may have reflected off of the ice surface. HiCal consisted of a peizo lighter with a bandwidth similar to ANITA-like pulses, a battery, and a GPS unit. Battery power was limited to 50 hours of operation in the event commanding was lost during flight. The first HiCal launch attempt failed, but a second payload launched two days after ANITA and followed the ANITA flight path. A third HiCal launch was also successful and followed the ANITA payload as it passed McMurdo on its second circuit around the continent. Hpol HiCal pulses were detected in flight. HiCal, along with two of it's primary experimenters, is shown in Figure 7.16.

Figure 7.16: HiCal instrument, flown shortly after ANITA launched, with builders Jessica and Mark Stockham.

7.11 Analysis and Simulation

ANITA 3 data is in analysis during the writing of this dissertation, so this section will give an overview of the general ANITA analysis procedure used for ANITA 1 and 2. ANITA uses a blind analysis strategy, where events from calibration pulses are injected into the data set. Good reconstruction of known "events" confirms that the analysis procedure works. In the first stage of analysis bad data is removed. Bad data includes events with incomplete waveforms, flagged GPS stamps, events with a saturated SURF signal, etc. The incoming direction of the remaining events is then reconstructed. Interferometric techniques use the timing between signals in different antenna pairs to calculate the direction of the incoming plane wave signal. Further quality cuts are made to remove events that don't reconstruct properly. Thermal noise events are incoherent, so while the waveforms in each antenna may look impulsive, they do not add coherently. The incoming direction of the remaining events are propagated back to the continent to find the origin of the signal. Events with known anthropogenic sources are removed. Remaining events comprise the detected signal.

A clustering method is used to estimate the background signal. Since it is unlikely that more than one neutrino comes from the same location on the ice, events that originate from the same location (within 40 km) are considered to come from a man made source. The background signal, $N_{unknown,single}$, can be estimated by comparing the number of multiple events from an unknown source, $N_{unknown,unknown}$, to the ratio of the number of single events from known sources, $N_{known,single}$ to the number of multiple events from known sources, $N_{known,multiple}$,

$$\frac{N_{unknown,single}}{N_{unknown,multiple}} = \frac{N_{known,single}}{N_{known,multiple}}. \tag{7.1}$$

For ANITA 2, the background single rate was 0.6 ± 0.39 Vpol events and 0.25 ± 0.19 Hpol events. The reconstruction efficiency can then be determined by opening the blind box and seeing how well injected signals reconstructed. Again, for ANITA 2, 8 of 11 injected events were reconstructed [23].

The effective volume and reconstruction efficiency of the instrument are also simulated. ANITA uses multiple Monte Carlo simulation packages, including SAM (SADE ANITA Monte Carlo) [167], UH Monte Carlo, and IceMC. Simulations generate neutrino events in ice and propagate the electric field to the ANITA payload. The signal then passes through a model of the signal chain to produce the observed signal. In the case of cosmic rays, the ZHAireS simulation package (discussed in Chapter 4) is used to generate a realistic cosmic ray signal that is propagated to the instrument and passed through the signal chain. The simulation process is critical to understanding the reconstruction efficiency and the effective volume of the instrument, which determines the limits on the UHE neutrino flux set by the experiment and the inclusion of ANITA UHECRs on the cosmic ray flux spectrum. Details of analysis and simulation can be found in [166][223].

7.12 2015 Flight

Figure 7.17: ANITA 3 launch on December 17, 2014.

ANITA 3 launched on December 17, 2014. The payload flew for 22 days, until it was brought down in East Antarctica near Davis Station for fear of losing the balloon over the ocean. The drop down solar panels and ALFA antenna deployed correctly. There was a consistent CW signal at 260 MHz, presumably from several satellites. The SHORT boards were modified to be full bandwidth, so the CW resulted in high L1 trigger rates for the half of the payload that faced the source. The Openport system failed mid-flight, but TDRSS remained operational. The hard drives worked well, with 84 million events on disk, and were recovered and sent back to the University of Hawaii. The instrument experienced ~60% livetime with an event rate of ~50 Hz. Pulses were seen from HiCal, LDB, and WAIS Divide. The phi masking system suffered from problems with the return rate of threshold triggers that caused phi sectors to unmask prematurely. This resulted in more dead time for data collection, as the digitizing and data readout was overwhelmed. At the time of writing, ANITA 3 data is in analysis.

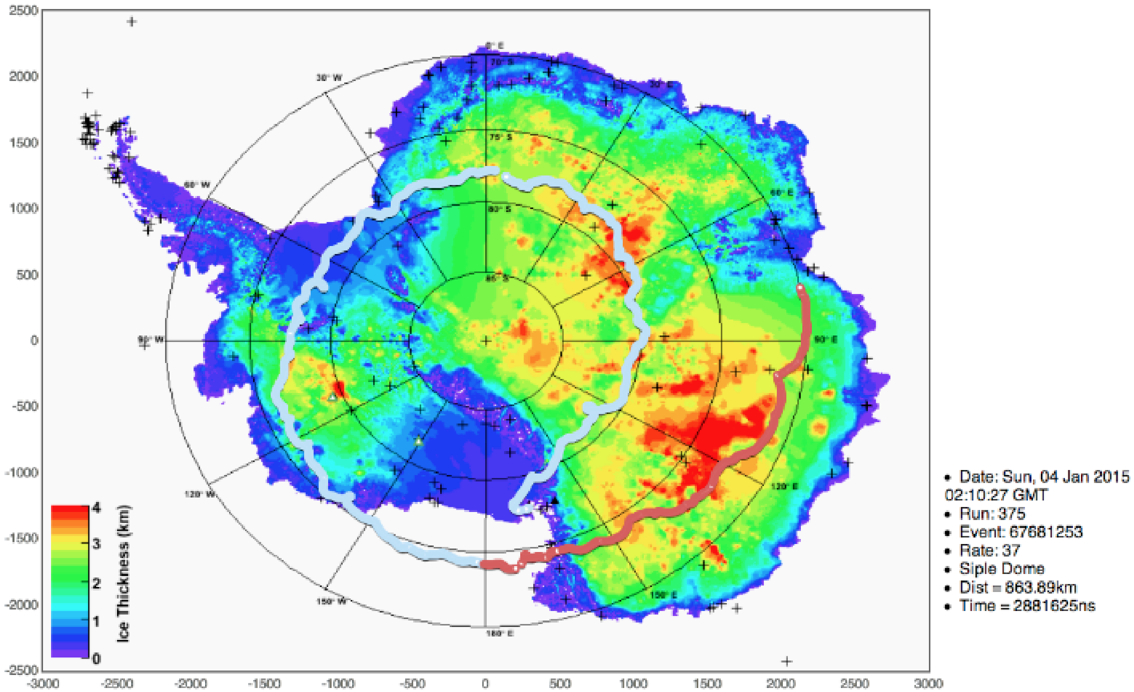

Figure 7.18: Trajectory of ANITA 3 flight.

Chapter 8

ANITA CONTRIBUTIONS

8.1 Introduction

Contributions to ANITA 3 started in early 2013, with the flight date still scheduled for December 2013. Contributions included Delaware responsibilities of GPS and temperature sensor preparation, and modifications to existing hardware, which started at the University of Hawaii but continued at the University of Delaware. I also participated in integration at CSBF in Palestine and the flight campaign at McMurdo station. In this chapter I describe in detail the impact these contributions had on the 2014-2015 ANITA flight.

8.2 GPS Calibrations

Exact knowledge of payload latitude, longitude, altitude, pitch, and roll are critical for reconstruction of ANITA events. Three GPS units are used on ANITA flights. One G12 unit measures position, and two ADU5 units (labeled ADU5A and ADU5B) measure position and attitude. There are other navigation instruments, including magnetometers and sun sensors, but the GPS units are the primary tools for tracking the payload time, orientation, and position. The ADU5B unit malfunctioned halfway through the ANITA 2 flight, and it's protective box was damaged during subsequent shipping. A discussion of GPS operations is given in Appendix G.

University of Delaware was responsible for GPS navigation during the ANITA 3 flight. A major effort in preparing the GPS systems was troubleshooting the ADU5B unit. This effort involved creating a model support stand for the GPS antennas that mimicked the relative position of the antennas on the ANITA payload. ADU5A and ADU5B units were always tested in unison for comparison purposes. For example, the signal may reflect off various local obstructions before it gets to one of our antenna and if the reflected signals are strong enough they can confuse the receiver and cause erroneous measurements due to the multipath of the signal, depicted in Figure 8.1. Multipath interference occurs when the GPS antenna receives two or more signals from the same source by different pathways. This difference is phase dependent, and causes uncertainty in the reconstructed location because the timing of the incoming satellite signal is altered [225]. These issues were minimized by doing the testing on the roof of the university parking garage, but still existed in some form.

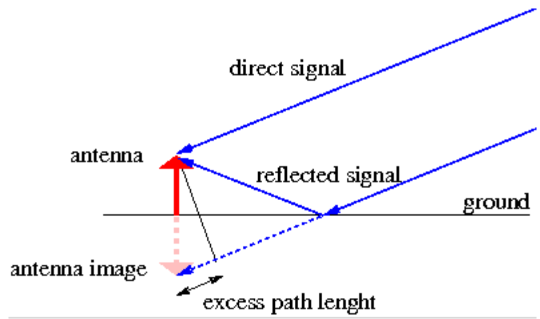

Figure 8.1: Multipath interference created by the difference of the path length between the direct signal and the reflected signal [225].

The primary problem with the ADU5B unit is what we called “signal dropouts,” where the attitude signal would disappear for a length of time and then reappear. This generated an error flag in the data. Many attempts were made to fix this problem, including changing the antenna array position, changing the antennas themselves, and running different software. The unit was eventually sent back to the manufacturer, where it was determined that one channel’s printed circuit board had a damaged voltage control oscillator. The unit was returned and confirmed to work according to specifications.

The GPS units also had to be cleared for altitude and speed limitations. Commercial GPS units have limitations on the altitude and speed to prevent units from being used on illegal equipment like missiles. To make sure the limitations were removed we brought the units to Wallops Flight Facility in Wallops, VA, where they have a flight simulator and Bemco Vacuum chamber to test the units' performance under flight conditions. The units passed thermal cycling and altitude tests, indicating they should work as expected in flight.

8.3 SHORTs

Before discussing contributions to ANITA hardware it will be useful to review the ANITA signal chain discussed in Chapter 7. Radio signals enter the signal chain through the Seavey horn antennas and are amplified in the AMPA units. The signal is further conditioned in the iRFMC module, and then filtered and split into triggering and sampling paths. The sampling path goes into the SURF unit, and the triggering path goes through the SHORT boards and into the TURF. If a trigger is detected, the SURF is notified and the data is recorded to the flight hard drives. Figure 7.6 shows the signal chain.

The same SHORT boards have been used in all three ANITA flights with various modifications. The board takes 8 incoming channels, puts each through a tunnel diode, and then filters out extra noise that may have been added. In ANITA 1 and 2 the boards also filtered the signals into 4 frequency bands. For ANITA 1, one antenna's worth of signal could be put into one SHORT: 4 frequency bins of two polarizations. In ANITA 2, since only vertical polarization was used for triggering, two antennas could use one board. It was decided that ANITA 3 would not use the frequency banding, so when that part of the chain was removed, four antennas could be fed into one SHORT. However, the SHORT boards and their encasing boxes were not designed to have eight different inputs, but rather two that would be split into different frequency bands on the board itself. For the boards to be useful, new inputs had to be soldered directly onto the boards and the cases modified to handle the new inputs.

8.3.1 Hardware Adjustments

Space on the board is extremely limited for adjustments, so the new connectors had to be very small. The w.fl connector was chosen, and soldered directly onto the SHORT board before the tunnel diode and it's neighboring capacitor. The w.fl connectors were surface mount, and not correctly shaped for the board location, so care was taken to interrupt the signal chain before the input and to ground everything properly. The connectors were strain relieved with circuit board stickers that were tested to withstand 50 g's. Holes were drilled into the lids of the existing SHORT boxes and the previous input connectors were terminated. Each channel was checked at the Bartol Lab at UD for proper S11 and output signal functionality.

Figure 8.2 shows the SHORT boards before alteration. Boards are double sided, and originally included four frequency bins stemming from one input signal.

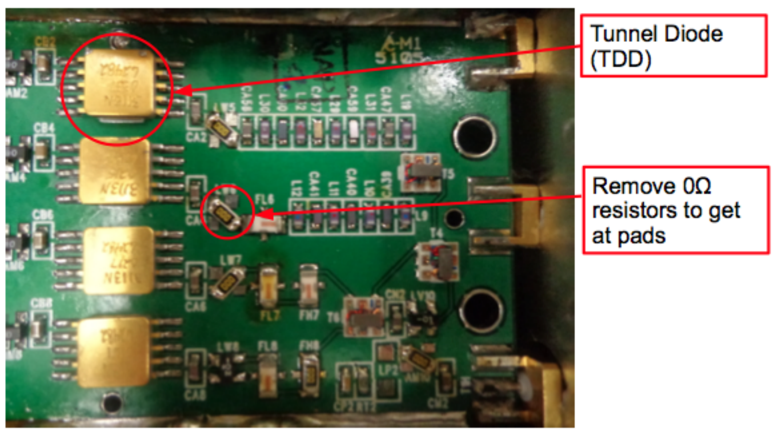

Figure 8.2: SHORT boards before alteration. The circled resistors were removed, and the existing signal chain was broken to avoid signal contamination.

Figure 8.3 shows a sample SHORT board after alteration. The 0Ω resistors have been replaced with the new signal input.

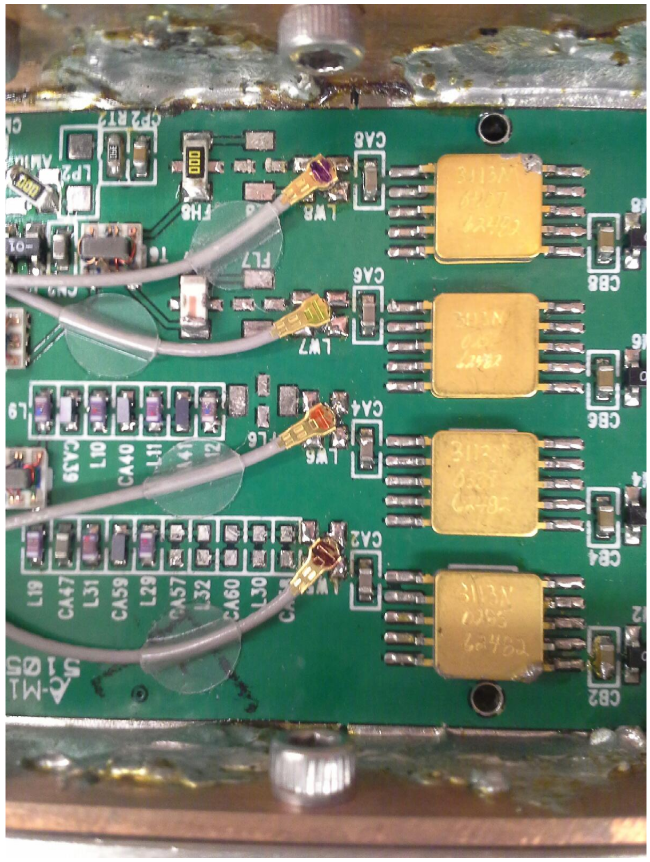

Figure 8.3: SHORT boards after alteration. The circled resistors were removed, and the existing signal chain was broken to avoid signal contamination.

The SHORT S11 measurement is shown in Figure 8.4. These results indicate that the SHORT boards and attached cables are performing adequately after modifications.

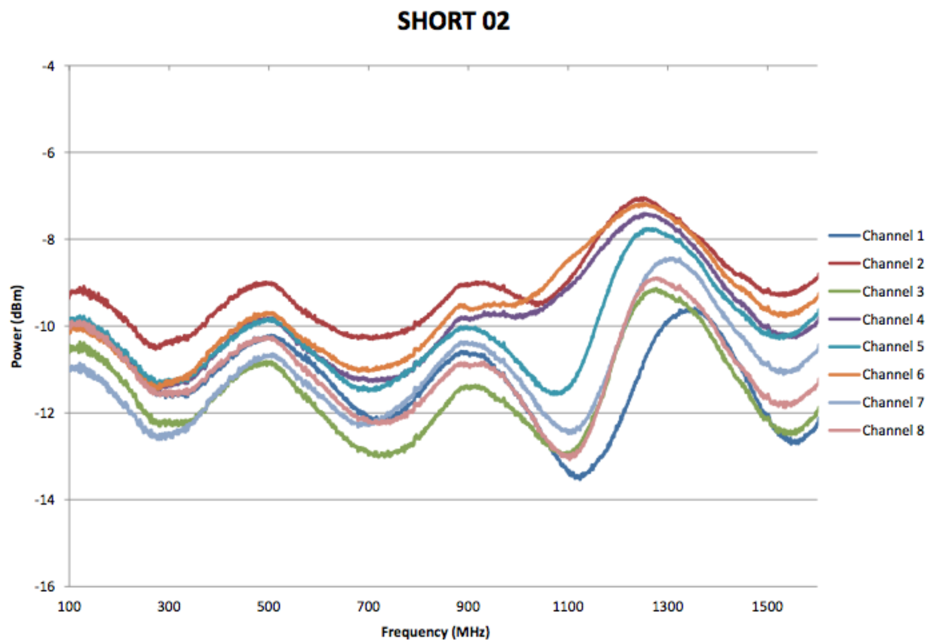

Figure 8.4: Sample SHORT S11 measurement. Substantial power is not lost in the w.fl cable over the relevant frequency band.

8.3.2 Tunnel Diode Gains and Range of Operation

Tunnel diodes use quantum tunneling to achieve very fast operation. This is important for ANITA because the signals they are amplifying are very short and fast. ANITA uses the tunnel diode to square the incoming signals, making them all unipolar, to send a more robust pulse into the trigger logic. It is important to characterize how each tunnel diode operates and find the best input voltage region to work in. This keeps the response of the tunnel diodes linear and well known.

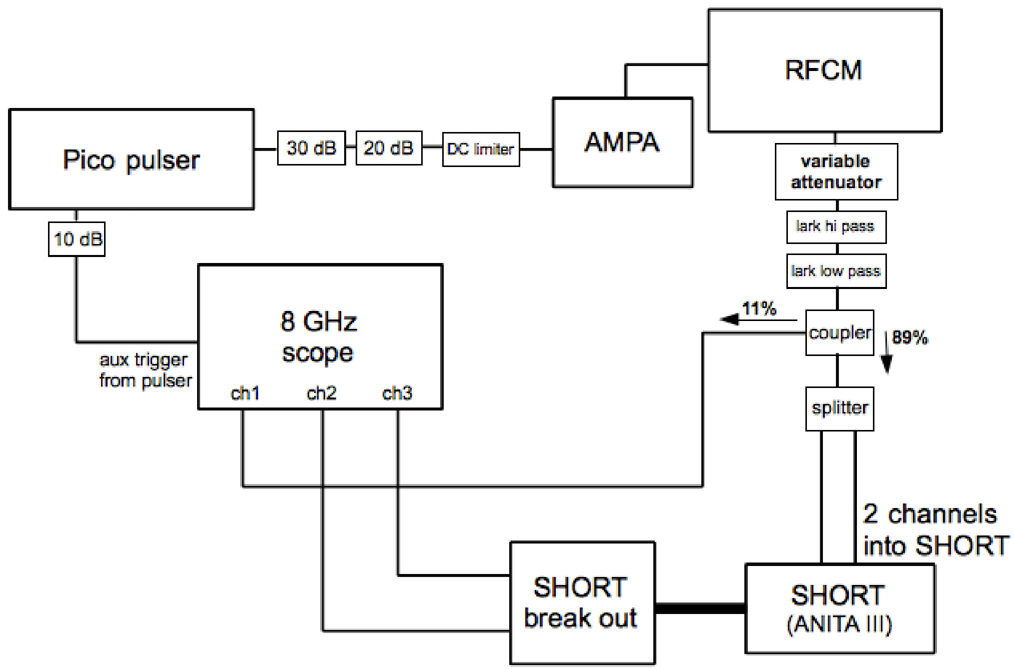

Figure 8.5: SHORT testing setup.

Testing of the SHORT boards was done in Palestine, TX. A picosecond pulser was used to generate a sharp signal (on a neutrino-like time scale) that was sent through the ANITA signal chain, including AMPA, iRFCM, and appropriate filters. That signal was split, sending 11 percent to monitoring scope (which was triggered by the pico pulser), and the other 89 percent was split into two SHORT channels, which were also sent into the monitoring scope after going through the SHORT. A variable attenuator was placed in the signal chain so many different strength signals could be characterized. All SHORT channels were shown to be consistent.

SHORT number 34, channel 2 is shown as an example in Figure 8.6. Filters were used to achieve the different frequency bins, and no filtering was done by the SHORTs themselves. The quantities compared are the diode (SHORT output) peak to peak divided by the RMS of the signal and the raw RF input peak to peak divided by the RMS and also divided by two, because it is a bipolar signal. There are two linear regions of operation, and the frequency dependence widens at higher SNR.

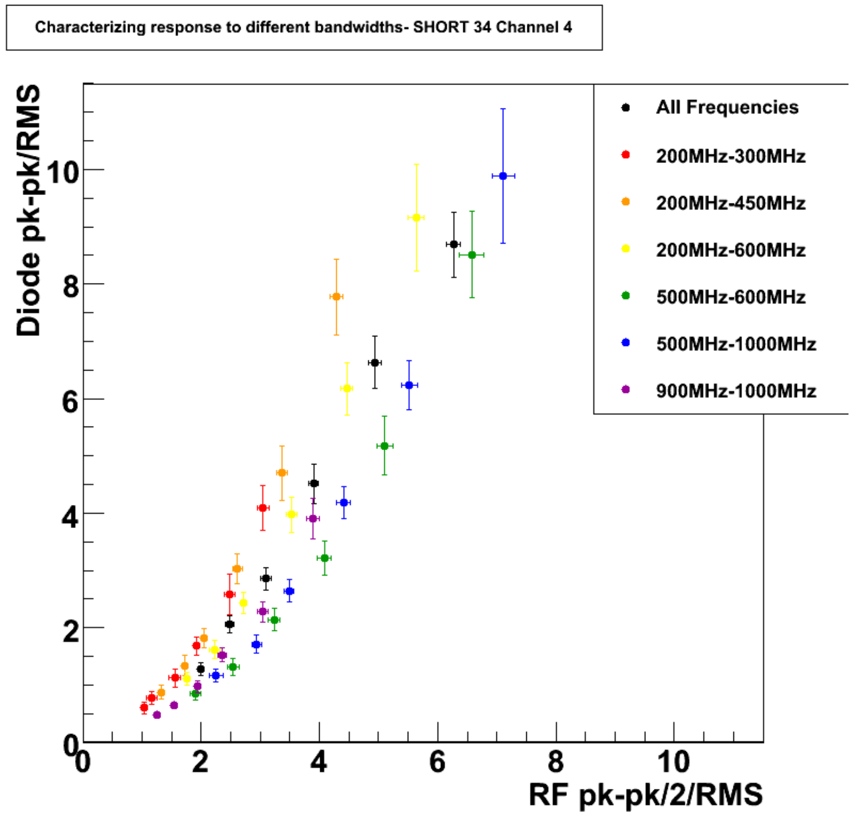

Figure 8.6: SHORT SNR response.

Figure 8.7 shows the SHORT output RMS (no pulse) versus the RF input RMS. This test was done to determine the appropriate operating range of the SHORTs, and which attenuators would be necessary in the signal chain. The known operating region of the SHORTS is shown by the black curve (linear in log space). The maximum input voltage was then 26 mV, and 10 mV was the value used in the ANITA 3 instrument.

8.4 Temperature Sensors

Monitoring the temperature of different system components during flight allows housekeeping monitors to have a good diagnostic of the health of the system. The University of Delaware was responsible for manufacturing and installing temperature sensors. Christopher Elliott (UD) assembled temperature sensors for both internal

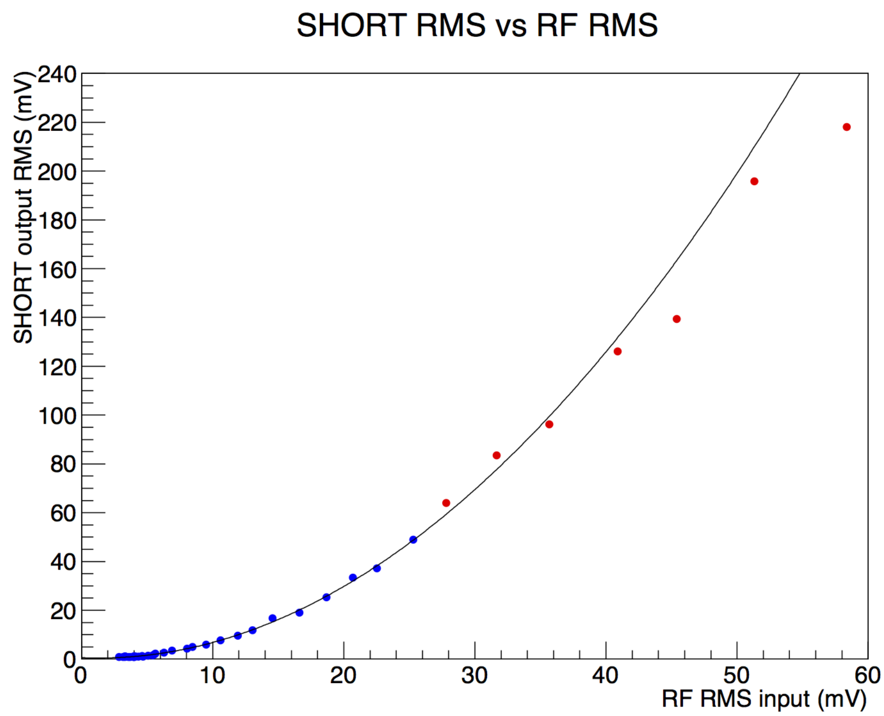

Figure 8.7: SHORT output RMS compared to the input RMS, used to determine proper operating range.

and external monitoring. External sensors are enclosed in a copper box to avoid RF contamination. Sensors consist of a simple contact AD590 component, and the voltage output can be scaled to a Celsius temperature. These sensors are accurate to within a degree. Figure 8.8 shows a temperature sensor before the AD590 component is included.

ANITA is designed to include 25 sensors external to the instrument box and 15 sensors inside the instrument box. Wiring was only completed for 15 external sensors. Internal sensors were epoxied onto a sampling of active components, including iRFMCs, SHORTs, Helium drives, the CPU crate, and the radiator plate. External sensors monitored AMPAs, the instrument box, photovoltaic panels, and the battery box. All sensors performed properly during flight.

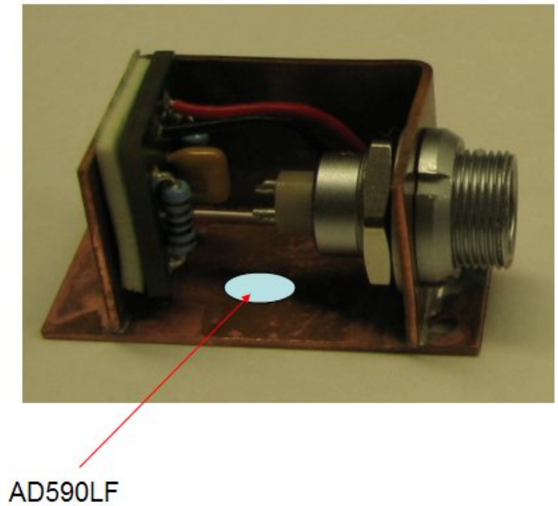

Figure 8.8: Temperature sensor for ANITA.

8.5 ANITA 3 Integration and Campaign

The ANITA 3 instrument was integrated and fully functional for the first time in the summer of 2014, a few months before the schedule flight. Integration took place at the CSBF facility in Palestine, TX between mid June and mid August, 2014. There, the gondola was constructed for the first time, new Seavey antennas were tested and characterized, the ALFA antenna was built and tested, and the entire instrument was assembled and tested. Instrument assembly involved installation of various components, including SHORTs, AMPAs, iRFCMS, and all hardware that was contained inside the instrument box. Signal chain testing and characterization occurred here, as a first pass. The entire functional instrument box was tested inside a Bemco chamber to ensure low temperature and air density conditions would not change the instrument performance, that is, that the electronics could withstand operating at very high and low temperatures without air circulation. All external RF cables were also manufactured at CSBF. The final step of instrument integration is the “hang test,” where the entire instrument is assembled and wired up. Especially important here is the communication systems. The hang test is considered a success when all instrumentation and communication equipment work. The deployable aspects of the payload (solar panels and ALFA) were also tested. After passing the hang test the instrument is boxed up and sent to McMurdo. The LDB Facility at McMurdo Station, Antarctica, housed all the preparations and launch site for the ANITA experiment. The instrument was reassembled and final calibrations were performed. At launch, the team at McMurdo tracked the location and performance of the instrument until it was out of the line of sight.

During the campaign I wrote for the Scientific American Expeditions blog, found at https://blogs.scientificamerican.com/expeditions/neutrinos -on-ice-how-to-build-a-balloon/. A total of 6 blog entries cover the scientific goals of the ANITA project, the logistics of launching a balloon payload in Antarctica, and the details of preparing the instrument for launch.

Chapter 9

SUMMARY

Radio techniques have proven to be effective in the detection of UHE cosmic ray and neutrino induced particle cascades. Such events are rare, and radio emission from cascades provides a wealth of information about the primary and can be detected across a large volume. While it has been known that radio emission from particle cascades existed since the 1960s, it is only recently that efforts have been made to characterize the radiation and understand the emission mechanisms. The goal of this dissertation was to present the results of the SLAC T-510 experiment, which was the first to characterize radio emission from a particle cascade in the presence of a magnetic field and compare the results to simulations, and to describe the ANITA 3 experiment, which aims to measure UHE cosmic rays and neutrinos.

An introduction to cosmic rays and neutrinos was given in Chapter 2, including the history of detection, spectra, sources, propagation, and detection. Indirect detection methods were of particular interest to this work. Experiments that use radio techniques to detect particle cascades were then introduced in Chapter 3. This includes the historical beam experiments at SLAC that laid the groundwork for T-510, as well as ANITA and ground based radio detectors which rely on knowledge of radio emission mechanisms.

Chapter 4 provided a theoretical background of radio emission from particle cascades. Radio emission is generated in the electromagnetic components of the cascade through the Askaryan and geomagnetic mechanisms. Askaryan radiation is due to a charge excess that develops with the cascade front, and geomagnetic emission is caused by a transverse current due to the development of the cascade in a magnetic field. These emission mechanisms provide radio signatures that can be used to reconstruct properties of the primary. Prior to T-510, the Askaryan effect had been observed in a controlled setting, but without a magnetic field the geomagnetic mechanism was untested. Also, the particle level simulations that predict radio emission from cascades had never been compared to data collected from a cascade developing in known conditions. The importance of trusted radio simulations became clear as radio detection of UHECR developed. The need to confirm simulations and understand magnetically induced emission mechanisms led to the SLAC T-510 experiment.

Chapter 5 provided the logistical details and experimental setup of T-510, and Chapter 6 described simulation techniques and data analysis. The overall goal of the experiment was to simulate an electromagnetic cascade in a magnetic field, and compare the results with experimental data. In particular, it was important to map the Askaryan and magnetically induced radiation patterns and confirm the scaling of magnetically induced radiation with magnetic field strength. The ZHS and endpoint simulation packages were used, and agreed to within 7% for the peak amplitude of emission. The simulated electric fields were convolved with the system response to produce a voltage that was comparable with measured data. Differences between the simulations for magnetically induced radiation are small, but not yet well understood.

Qualitative features of the T-510 data are well understood. The width of the radiation pattern narrows with increasing frequency, and the magnitude of the magnetically induced radiation increases linearly with the applied magnetic field and changes polarity with the sign of the field. The radiation due to charge excess in the cascade does not depend on the magnetic field.

A first comparison between simulation and data indicated that the predicted radiation was roughly 60% of the measured radiation. The simulations did produce the same qualitative features as the measured data. The discrepancy in magnitudes is ultimately thought to be due to a reflection from the bottom surface of the T-510 target that was not accounted for in simulations. Adding reflections to simulations reproduced the overall magnitude of the measured data well, and largely corrected for the differences between data and simulation. The results of this experiment demonstrate that particle level simulations can be used to predict radio emission from air showers.

The ANITA 3 experiment was discussed in Chapters 7 and 8. Chapter 7 focused on the ANITA 3 instrument, including antennas, instrument box, data acquisition and sampling, trigger system, and signal chain. Other mission critical components such as flight software, the GPS system, communication systems and data viewing software were introduced. My personal contributions to the experiment, including GPS calibration, hardware modification, temperature sensor application, and the ANITA 3 integration and campaign were expanded on in Chapter 8.

ANITA, and all other experiments that use radio techniques to detect cosmic rays, rely on simulations to understand measured data. These simulations have now been validated by the results of SLAC T-510, and can be used with confidence.

Appendix A
ACRONYM GUIDE

The following acronyms are used in this work:

AERA Auger Engineering Radio Array

AGN Active Galactic Nuclei

ALFA ANITA Low Frequency Array

AMPA Antenna-Mounted Pre-Amplifier

ANITA Antarctic Impulsive Transient Antenna

ARA Askaryan Radio Array

ASTA Accelerator Structure Test Area

CODALEMA Cosmic ray Detection Array with Logarithmic ElectroMagnetic Antennas

CPU Central Processing Unit

CSBF Columbia Scientific Balloon Facility

CTA Cherenkov Telescope Array

CW Continuous Wavelength

EAS Extensive Air Shower

EMI Electromagnetic Interference

ESTB End Station Test Beam

FACET Facility for advanced Accelerator Experiment Tests

FFT Fast Fourier Transform

FFTW Fastest Fourier Transform in the West (FFT package)

GEANT GEometry ANd Tracking (simulation package)

GPS Global Positioning System

GSE Ground Support Equiptment

GSPS Giga-Samples Per Second

GZK GreisenZatsepinKuzmin limit on cosmic ray energy

HDPE High-Density Polyethlyne

ICT Integrating Current Transformer

IRFCM Internal Radio-Frequeny Conditioning Module

KASCADEKArlsruhe Shower Core and Array DEtector

LCLS Linac Coherent Light Source

LOFAR Low-Frequency Array for Radio astronomy

LDB Long Duration Balloon Facility at McMurdo

LOPES LOFAR Prototype Station

LOS Line of Sight (telemetry)

LPDA Logarithmic Periodic Dipole Antenna

NLCTA Next Linear Collider Light Source

PMT Photo-Multiplier Tube

RF Radio Frequency

REAS Radio Emission from Air Shower

RMS Root Mean Squared (statistical measurement)

SHORT SURF High Occupancy Radio Frequency

SIP Science Instrument Package (from CSBF)

SKA Square Kilometer Array

SLAC Stanford Linear Accelerator (now SLAC National Accelerator Laboratory)

SNR Signal-to-Noise Ratio

SURF Sampling Unit for Radio-Frequencies

TDRSS Tracking and Data Relay Satellite System (telemetry)

TURF Triggering Unit for Radio-Frequencies

UHE Ultra-High Energy

UHECR Ultra-High Energy Cosmic Ray

WAIS Divide West Antarctic Ice Sheet (Divide)

ZHS Zas, Halzen, Stanev Simulation Code

Appendix B

T-510 RUN INFORMATION

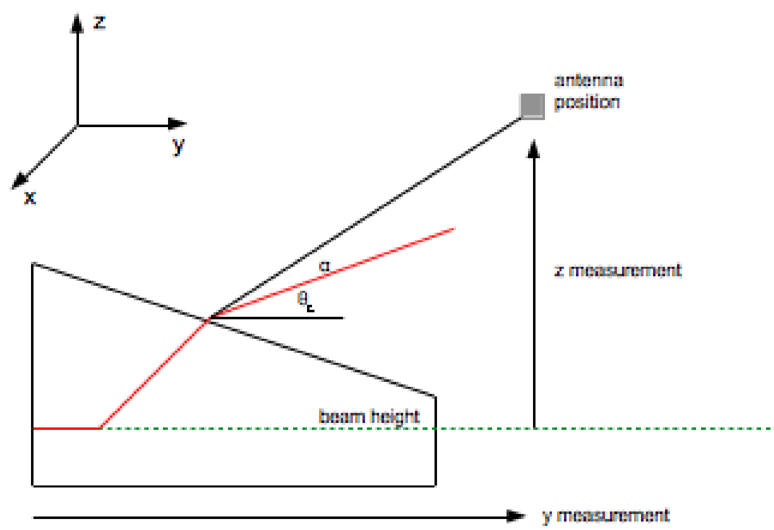

Figure B.1: Measuring the antenna positions.

Figure B.1 shows the points from which the T-510 antenna positions were measured. The y position measurement was taken from the beginning of the target to the the antenna face. The z position was taken from the beam height to the center of the antenna face. The angle α indicates how far the antenna is off the Cherenkov angle. The following tables list the (x,y,z) positions of the antennas for the runs analyzed in Chapter 5. The three run numbers listed indicate 0, positive (+970 G), and negative (-970 G) magnetic fields. The vertical and horizontal antenna polarizations were in the same position for the Seavy runs. The Bicone and LPDA runs required different antennas for each polarization, so the positions are listed separately.

Run No.	X (cm)	Y (cm)	Z (cm)	Angle α
218, 219, 220	0	1338	130	$-22.89°$
218, 219, 220	0	1304	225	$-18.81°$
218, 219, 220	0	1271	319	$-14.56°$
218, 219, 220	0	1237	413	$-10.15°$
223, 224, 225	0	1338	513	$-6.72°$
210, 211, 212	0	1338	652	$-1.20°$
210, 211, 212	0	1304	747	$2.89°$
210, 211, 212	0	1271	841	$6.91°$
210, 211, 212	0	1338	935	$10.87°$
215, 216, 217	0	1304	1035	$12.81°$
215, 216, 217	0	1271	1129	$16.36°$
215, 216, 217	0	1237	1223	$19.80°$

Table B.1: T-510 Run Geometry for Seavey Antennas.

Run No.	X (cm)	Y (cm)	Z (cm)	Angle α
343	0	1346	40.1	$-29.00°$
340	0	1346	257	$-18.8°$
332	0	1346	458	$-9.91°$
319	0	1346	662	$1.74°$
316	0	1346	863	$5.29°$
313	0	1346	1060	$11.2°$
309	0	1346	1264	$16.4°$

Table B.2: T-510 Run Geometry for Vpol Bicone antennas.

Run No.	X (cm)	Y (cm)	Z (cm)	Angle α
343	0	1296	-145	$-37.10°$
340	0	1296	72	$-27.60°$
332	0	1296	273	$-18.84°$
319	0	1296	477	$-10.42°$
316	0	1296	678	$2.86°$
313	0	1296	875	$3.71°$
309	0	1296	1079	$9.63°$

Table B.3: T-510 Run Geometry for Hpol Bicone antennas.

Run No.	X (cm)	Y (cm)	Z (cm)	Angle α
369	0	1346	286	$-17.36°$
366	0	1346	416	$-11.53°$
363	0	1346	515	$-7.32°$
360	0	1346	619	$-3.15°$
349	0	1346	736	$1.21°$
353	0	1346	818	$4.06°$
357	0	1346	918	$7.30°$
372	0	1346	1023	$10.43°$
375	0	1346	1118	$13.05°$

Table B.4: T-510 Run Geometry for Vpol LPDA antennas.

Run No.	X (cm)	Y (cm)	Z (cm)	Angle α
369	0	1296	107	$-25.79°$
366	0	1296	237	$-19.64°$
363	0	1296	336	$-15.10°$
360	0	1296	440	$-10.49°$
349	0	1296	557	$-5.61°$
353	0	1296	639	$-2.38°$
357	0	1296	739	$1.31°$
372	0	1296	884	$4.92°$
375	0	1296	939	$7.95°$

Table B.5: T-510 Run Geometry for Hpol LPDA antennas.

Appendix C

CALCULATION OF ANTENNA RESPONSE

The effective height relates the voltage produced by an antenna to the electric field of the same polarization entering the antenna. This is of pivotal importance to SLAC T-510, because we only see the voltage output of our antenna system, which we need to compare to the electric field predicted by simulations at the antennas. The Seavey and VHF antennas we used have been characterized at UCLA and the University of Hawaii. The primary equations for this derivation come from [226].

C.1 Derivation

The primary relation between the electric field at the front end of an antenna to the voltage at the back end is

$$V(t) = \mathbf{h_e}(\mathbf{t}) * \mathbf{E}(\mathbf{t}) \tag{C.1}$$

where $\mathbf{h_e}(\mathbf{t})$ is the effective height. The $*$ symbol identifies the convolution process, defined as

$$[f * g](t) = \int_{-\infty}^{\infty} f(\tau)g(t-\tau)d\tau. \tag{C.2}$$

The Convolution Theorem makes it easier to work in the fourier domain. Let $\mathcal{F}$ denote a fourier transform.

$$\mathcal{F}(f * g) = \mathcal{F}(f) \cdot \mathcal{F}(g) \tag{C.3}$$

and

$$f * g = \mathcal{F}^{-1}(\mathcal{F}(f) \cdot \mathcal{F}(g)). \tag{C.4}$$

Therefore,

$$V(t) = \mathbf{h_e(t)} * \mathbf{E(t)} = \mathcal{F}^{-1}(\mathcal{F}(h_e(t)) \cdot \mathcal{F}(E(t))). \tag{C.5}$$

The transmitted power, P_T, from voltage V_T by antennas with radiation resistance R_r matched to the load is given as

$$P_T(f) = \frac{1}{2}\frac{V_T(f)^2}{R_r} = \frac{h^2(f)E^2(f)}{2R_r}. \tag{C.6}$$

A more general parameter uses the effective aperture, A_e. By definition,

$$P(f) = S(f)A_e(f) = \frac{E^2(f)A_e(f)}{Z_0} \tag{C.7}$$

where S is the power density of the plane wave incident on the antenna and Z_0 is the impedance of free space, 377Ω. For a perfect antenna, the effective area would be equal to the physical area of the mouth of the antenna.

The effective height and effective aperture are related by

$$A_e(f) = \frac{h_e(f)^2 Z_0}{4R_r}. \tag{C.8}$$

The effective height must be measured for any of the above to be useful. We can measure the effective height by relating the a known power transmitted and a known power received from two antennas at a known distance apart. The Friis Equation relates those two quantities, and can be stated in the following ways:

$$\frac{P_R(f)}{P_T(f)} = \frac{A_{eT}(f)A_{eR}(f)}{r^2\lambda^2} \tag{C.9}$$

$$\frac{P_R(f)}{P_T(f)} = \frac{G_T(f)G_R(f)c^2}{(4\pi Rf)^2} \tag{C.10}$$

since the gain of the antennas is defined as

$$G(f) = \frac{4\pi A_e(f)}{\lambda^2}. \tag{C.11}$$

Here λ is the wavelength and r is the separation between the two antennas. The power transmitted and received is defined as

$$P(f) = \frac{1}{4}\frac{V^2(f)}{R_r}. \tag{C.12}$$

Using the relation between effective height and effective area, we can derive an expression for the effective height in terms of Z_0, R_r, r, f, and the transmitted and received voltages.

$$h_e^2(f) = \frac{R_r}{Z_0}\frac{rc}{f}\frac{V_R(f)}{V_T(f)}. \tag{C.13}$$

The resulting effective height is measured in meters.

C.2 Seavey Data

Data was taken to calculate the effective height in 2005 in an anechoic chamber at the University of Hawaii. Figure C.1 shows the measurement set up. Pulses of known power were transmitted using a Seavey reference horn (Figure C.2). A receiving horn recorded the observed signal (Figure C.3). The orientation both the transmitting and receiving antenna were rotated to measure the antenna response at varying angles off boresight.

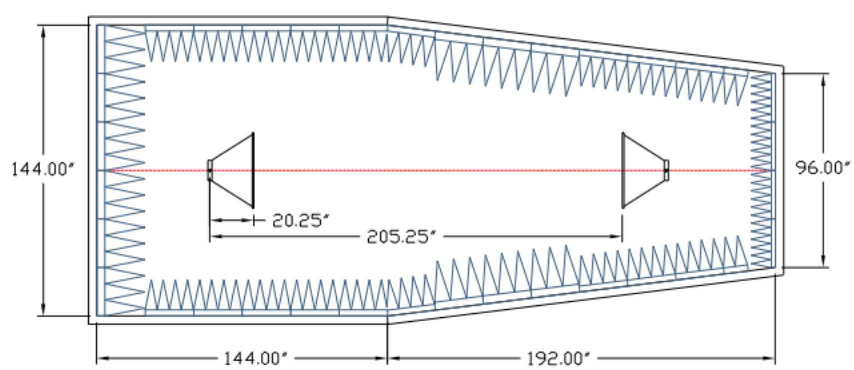

Figure C.1: Experimental Setup for Seavey Effective Height measurements taken at UH.

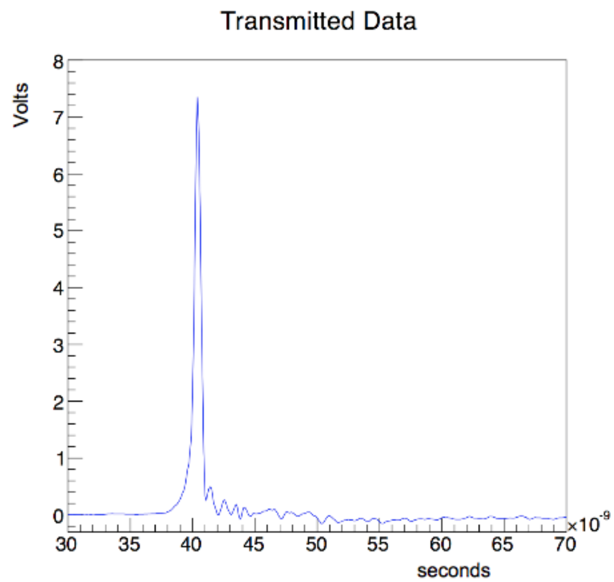

Figure C.2: Transmitted pulse from Seavey antenna, used to calculate antenna response.

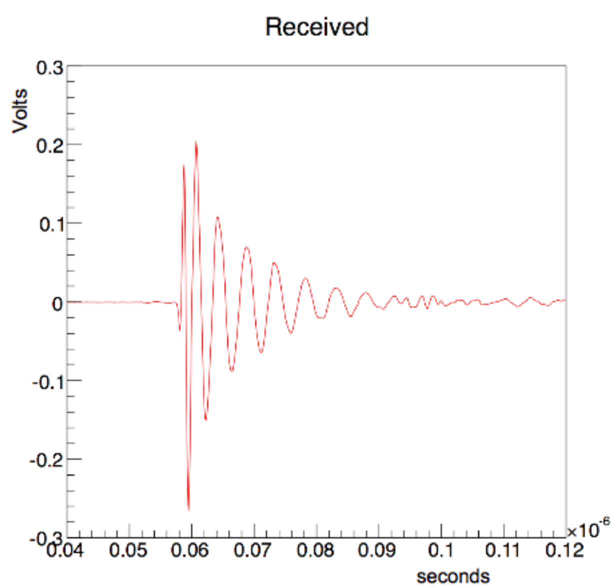

Figure C.3: Received pulse from Seavey antenna, used to calculate antenna response.

Appendix D

REFLECTION MEASUREMENT

The primary source of uncertainty in SLAC T-510 data was a reflection off of the bottom of the target. An RF absorbing mat was placed under the target, but the properties of the mat were unknown. To address this problem, a follow-up experiment was designed to measure the reflection coefficient of the mat, and preformed by members of the T-510 collaboration at Cal Poly in August, 2017. The same target used in T-510 was constructed on top of the RF absorbing mat, which itself was on top of a piece of plywood and metal foil. A dipole transmitting antenna was placed inside the target, and a receiving antenna (Seavey, same type as used in the T-510 experiment) was placed in the far field of the transmitting antenna. The antenna in the target was roughly at beam height and in the region of cascade development during the T-510 runs. The transmitting antenna was oriented to emit in the horizontally polarized direction. Data was taken with the mat in place and without the mat. Without the mat, a full reflection is expected. The difference between runs with and without the mat indicate the absorption of the mat. A schematic of the experiment is shown in Figure D.1.

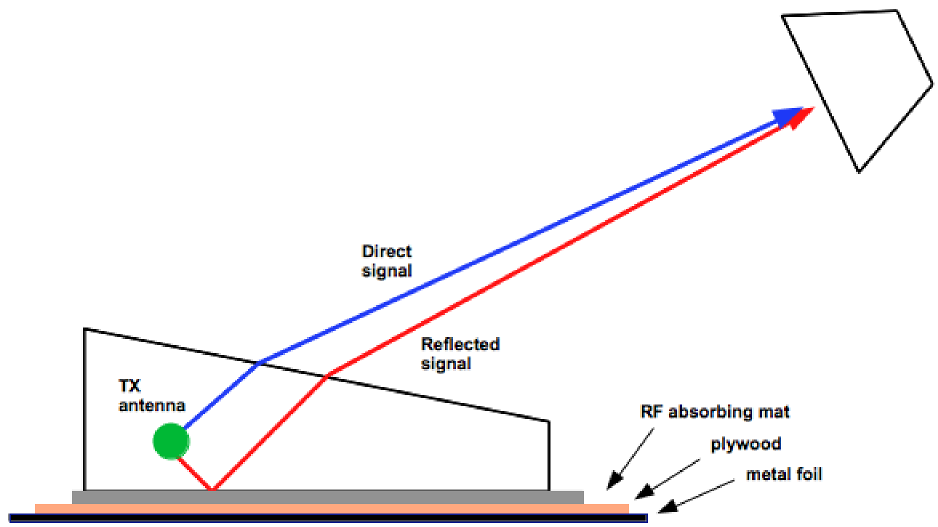

Figure D.1: Schematic of the reflection measurement set up (S. Wissel).

Figure D.2 shows the results of the experiment. The blue trace indicates the received signal with no mat, and the green trace indicates the signal with the mat in place. To first order, there appears to be little difference between signals. There is an ongoing effort to carefully characterize the reflection coefficient of the mat, but for the purposes of this work, we take this as a confirmation that using a reflection coefficient of $R = -1$ is reasonable. This is what is used in Section 6.5.4 when handling the reflections when comparing T-510 data to simulation.

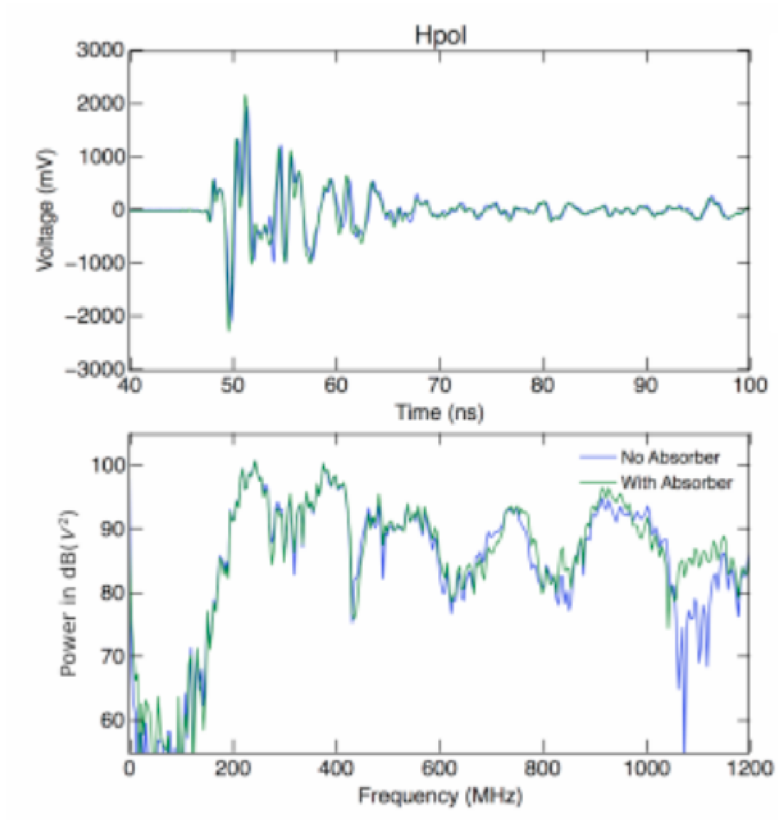

Figure D.2: Horizontally polarized reflection measurement signals. The blue line indicates the signal without absorber, and the green with absorber (C. Paciaroni and S. Wissel).

Appendix E

REFLECTIONS FROM THE BACK OF THE TARGET

In addition to the reflections off the bottom of the target discussed in Section 6.5.4, there is a contribution from reflections off the back of the target. Up until roughly 80 cm into the target, emission from each track point fully reflects off the back of the target and reaches the same antenna as the primary emission. At the front of the target the direct and back reflected radiation arrive almost simultaneously, while they are increasingly separated in time as the radiating shower front moves further away. Sample back reflection trajectories are shown in Figures E.1 and E.2. It isn't possible to fully understand the impact of these reflections without doing further dedicated simulations, since the emission at each track point was not separately recorded. As shown, adding a full reflection from the bottom of the target brings the data and simulation into close agreement. It is possible that the outstanding discrepancies can be described by including reflections from the back of the target.

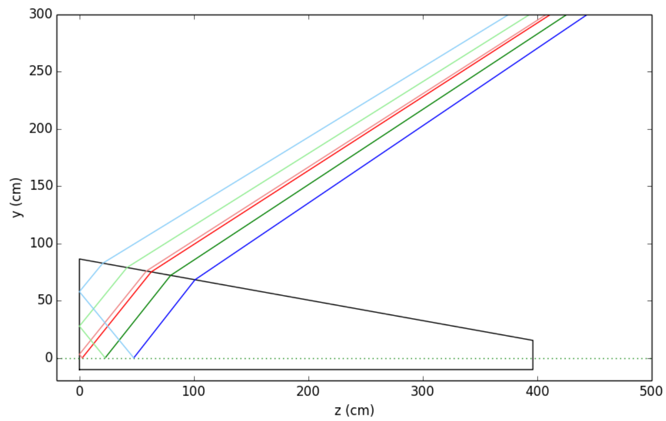

Figure E.1: Close up view of back reflections within the target. Dark colors indicate a direct path, and light indicate reflected paths.

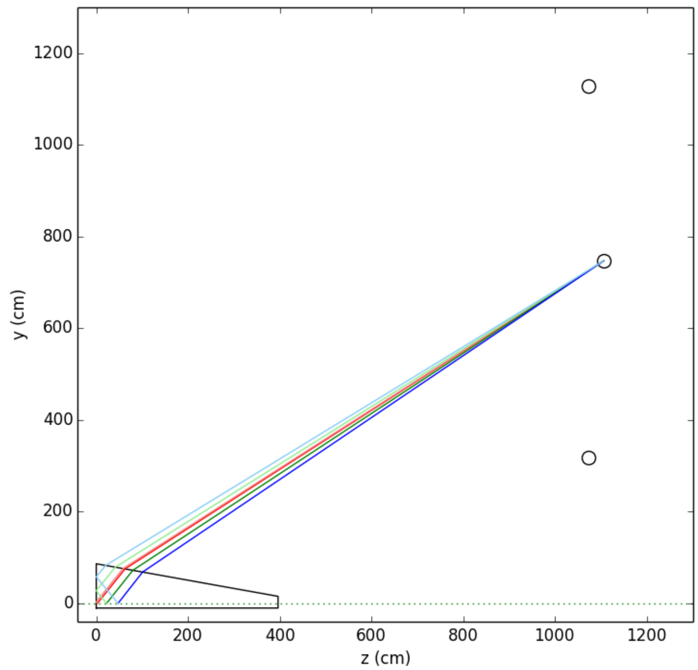

Figure E.2: Reflections from the back of the target seen in SLAC data. Black points represent antenna positions. Different color trajectories represent different paths emission can take to the antennas. Dark colors indicate a direct path, and light indicate reflected paths.

Appendix F

VHF DATA

Data was also taken with Bicone antennas in the VHF (20-200 MHz) range and LPDA antennas in the S-band range (1-3 GHz). Data from the LPDA runs appears to be flawed, so it is not considered here. Figure F.1 shows the signal for a VHF at 662 cm for Vpol and 678 cm for Hpol. The reflection interference pattern is evident in both polarizations. Figure F.2 shows the mapping of the radiation pattern. VHF data is not compared to simulations because antenna responses have not yet been measured for the Bicone antennas.

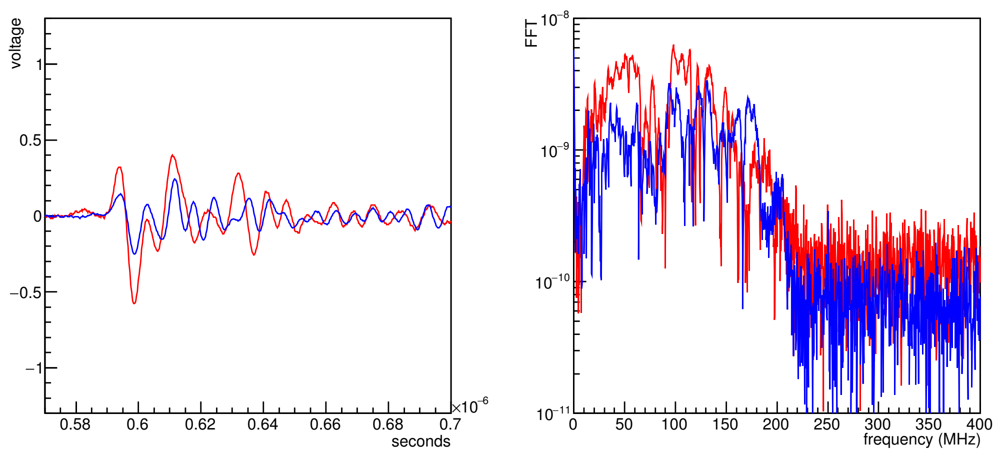

Figure F.1: VHF waveform (left) and power spectrum (right) for antennas at 662 cm for Vpol and 678 cm for Hpol, B=970 G. Vertically polarized data is shown in red and horizontally polarized in blue.

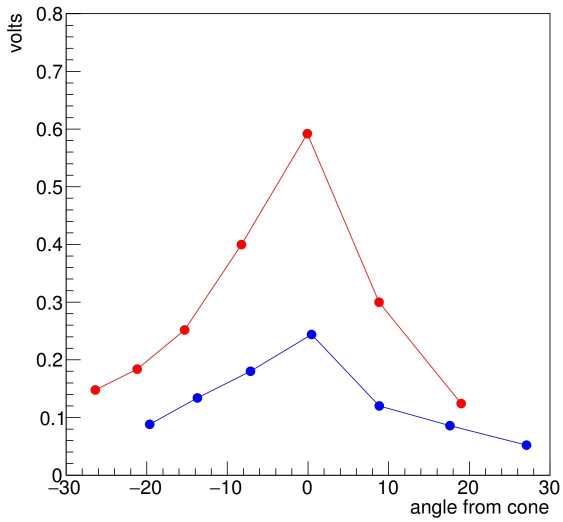

Figure F.2: Mapping of the Cherenkov cone with VHF antennas, with B=970 G. 0° is at the peak of the radiation pattern. Vertically polarized data is shown in red and horizontally polarized in blue.

Appendix G

GLOBAL POSITIONING SYSTEM OPERATIONS

The Global Positioning System is a constellation of 27 satellites that orbit the Earth. The position of the satellites at any given time is catalogued in an almanac that is managed by the US Department of Defense. A GPS receiver receives signals from at least four satellites and uses temporal data necessary for the process of trilateration, whereby the relative time between the satellites and receiver is used to triangulate the position of the receiver [227]. Differential GPS units include information from a known location on Earth that is also known to the satellites. This extra data helps correct for inaccuracies in signal propagation reconstruction and almanac information.

The G12 units used during the ANITA flight work as described above. One antenna can provide information about position, velocity, altitude, and timing. The unit calculates these variables at a rate of 20 Hz and outputs data every second [228].

ANITA required attitude information in addition to position information for accurate pointing. The ADU5 units used consist of 4 antenna arrays and can determine pitch and roll to an accuracy of 0.2° and 0.4° degrees, respectively. The attitude is determined by the relative positions of three antennas to one reference antenna. The ADU5 units refresh at a rate of 5 Hz and read out data every second.

Bibliography

[1] Victor F. Hess and Carl D. Anderson. *The Nobel Prize in Physics 1936*.

[2] R. Davis. "Solar neutrinos. II: Experimental". In: *Phys. Rev. Lett* 13 (1964), p. 303. DOI: https://doi.org/10.1103/PhysRevLett.12.303.

[3] B. P. Abbott et al. "Astrophysical Implications of the Binary Black-Hole Merger GW150914". In: *Astrophys. J.* 818.2 (2016), p. L22. DOI: 10.3847/2041-8205/818/2/L22. arXiv: 1602.03846 [astro-ph.HE].

[4] Kumiko Kotera et al. "The Astrophysics of Ultrahigh Energy Cosmic Rays". In: *Ann.Rev.Astron.Astrophys* 49 (2011), pp. 119–153. DOI: 10.1146/annurev-astro-081710-102620.

[5] Kenneth Greisen. "End to the cosmic ray spectrum?" In: *Phys. Rev. Lett.* 16 (1966), pp. 748–750.

[6] G. T. Zatsepin and V. A. Kuzmin. "Upper Limit of the Spectrum of Cosmic Rays". In: *J. Exp. Theor. Phys. Lett.* 4 (1966), p. 78.

[7] G. A. Askaryan. "Excess negative charge of an electron photon shower and its coherent radio emission". In: *J. Exptl. Theoret. Phys.* 41 (1962), pp. 616–618.

[8] J.V. Jelley et al. "Radio Pulses from Extensive Cosmic-Ray Air Showers". In: *Nature* 205 (1965), pp. 327–328.

[9] Frank G. Schrder and Pierre Auger Collaboration. "Radio detection of high-energy cosmic rays with the Auger Engineering Radio Array (PISA 2015)". In: *Nucl. Instr. Meth. A* 824 (2016).

[10] H. Flacke et al. "Detection and imaging of atmospheric radio flashes from cosmic ray air showers". In: *Nature* 435 (2005).

[11] Didier Lebrun. "CODALEMA: A Cosmic Ray Radio Detection Array". In: *Proceedings, 30th International Cosmic Ray Conference (ICRC 2007): Merida, Yucatan, Mexico, July 3-11, 2007*. Vol. 4. 2007, pp. 187–190. URL: http://indico.nucleares.unam.mx/contributionDisplay.py?contribId=161&confId=4.

[12] P. Schellart et al. "Detecting cosmic rays with the LOFAR radio telescope". In: *Astron. Astrophys.* 560 (2013), A98. DOI: 10.1051/0004-6361/201322683. arXiv: 1311.1399 [astro-ph.IM].

[13] Alice Bean. "Rice limits on the diffuse ultrahigh energy neutrino flux". In: *AIP Conf. Proc.* 870 (2006). [,212(2006)], pp. 212–214. DOI: 10.1063/1.2402620.

[14] P. Allison and the ARA collaboration. "Design and Initial Performance of the Askaryan Radio Array Prototype EeV Neutrino Detector at the South Pole". In: *Instrumentation and Methods for Astrophysics* (2011). DOI: 10.1016/j.icarus.2012.05.028.

[15] Spencer R. Klein. "ARIANNA: A radio detector array for cosmic neutrinos on the Ross Ice Shelf". In: *IEEE Trans. Nucl. Sci.* 60.2 (2013), pp. 637–643. DOI: 10.1109/TNS.2013.2248746. arXiv: 1207.3846 [astro-ph.IM].

[16] P. W. Gorham et al. "The Antarctic Impulsive Transient Antenna Ultra-high Energy Neutrino Detector Design, Performance, and Sensitivity for 2006-2007 Balloon Flight". In: *Astropart. Phys.* 32 (2009), pp. 10–41. DOI: 10.1016/j.astropartphys.2009.05.003. arXiv: 0812.1920 [astro-ph].

[17] J. D. Bray et al. "Limit on the ultrahigh-energy neutrino flux from lunar observations with the Parkes radio telescope". In: *Phys. Rev.* D91.6 (2015), p. 063002. DOI: 10.1103/PhysRevD.91.063002. arXiv: 1502.03313 [astro-ph.HE].

[18] Peter W. Gorham et al. "Experimental limit on the cosmic diffuse ultrahigh-energy neutrino flux". In: *Phys. Rev. Lett.* 93 (2004), p. 041101. DOI: 10.1103/PhysRevLett.93.041101. arXiv: astro-ph/0310232 [astro-ph].

[19] T. R. Jaeger, R. L. Mutel, and K. G. Gayley. “Project RESUN, a radio EVLA search for UHE neutrinos”. In: *Astropart. Phys.* 34 (2010), pp. 293–303. DOI: 10.1016/j.astropartphys.2010.08.008. arXiv: 0910.5949 [astro-ph.IM].

[20] O. Scholten et al. “Improved flux limits for neutrinos with energies above 10^{22} eV from observations with the Westerbork Synthesis Radio Telescope”. In: *Phys. Rev. Lett.* 103 (2009), p. 191301. DOI: 10.1103/PhysRevLett.103.191301. arXiv: 0910.4745 [astro-ph.HE].

[21] A. Connolly et al. “Status of SalSA”. In: *ARENA Proceedings, 2010* (2010).

[22] S. Hoover et al. “Observation of Ultrahigh-Energy Cosmic Rays with the ANITA Balloon-Borne Radio Interferometer”. In: *Phys. Rev. Lett.* 105 (2010).

[23] P. W. Gorham et al. “New Limits on the Ultra-high Energy Cosmic Neutrino Flux from the ANITA Experiment”. In: *Phys. Rev. Lett.* 103 (2009), p. 051103. DOI: 10.1103/PhysRevLett.103.051103. arXiv: 0812.2715 [astro-ph].

[24] E. Zas, F. Halzen, and T. Stanev. “Electromagnetic pulses from high-energy showers: Implications for neutrino detection”. In: *Phys. Rev. D* 45 (1992).

[25] David Saltzberg et al. “Observation of the Askaryan effect: Coherent microwave Cherenkov emission from charge asymmetry in high-energy particle cascades”. In: *Phys. Rev. Lett.* 86 (2001), pp. 2802–2805. DOI: 10.1103/PhysRevLett.86.2802. arXiv: hep-ex/0011001 [hep-ex].

[26] P. W. Gorham et al. “Accelerator Measurements of the Askaryan effect in Rock Salt: A Roadmap Toward Teraton Underground Neutrino Detectors”. In: *Phys.Rev. D* 72 (2004). DOI: 10.1103/PhysRevD.72.023002.

[27] P. W. Gorham et al. “Observations of the Askaryan Effect in Ice”. In: *Phys.Rev.Lett.* 99 (2007). DOI: 10.1103/PhysRevLett.99.171101.

[28] K.Belov et al. “Accelerator measurements of magnetically-induced radio emission from particle cascades with applications to cosmic-ray air showers”. In: *Phys.Rev. D* (2015). DOI: SLAC-PUB-16338.

[29] D. Allard, E. Parizot, and A. V. Olinto. "On the transition from Galactic to extragalactic cosmic-rays: spectral and composition features from two opposite scenarios". In: *Astropart.Phys.* 27 (2007). DOI: 10.1016/j.astropartphys.2006.09.006.

[30] C. D. Anderson. "The Positive Electron". In: *Phys. Rev.* 43 (1933), pp. 491–494. DOI: 10.1103/PhysRev.43.491.

[31] Seth H. Neddermeyer and Carl D. Anderson. "Note on the Nature of Cosmic-Ray Particles". In: *Physics Review Letters* 51 (1937).

[32] Pierre Auger et al. "Extensive cosmic ray showers". In: *Rev. Mod. Phys.* 11 (1939), pp. 288–291. DOI: 10.1103/RevModPhys.11.288.

[33] John Linsley. "Evidence for a Primary Cosmic-Ray Particle with Energy 10^{20} eV". In: *Phys. Rev. Lett.* 10 (1963).

[34] John Linsley. "Very High Energy Cosmic Rays". In: *Symposium - International Astronomical Union* 94 (1981).

[35] E. Fermi. "On the Origin of the Cosmic Radiation," in: *Physical Review* 75 (1949).

[36] P. Meyer. "Cosmic Rays in the Galaxy". In: *Annual Review of Astronomy and Astrophysics* 7 (1969), p. 1.

[37] F. W. Stecker. "Diffuse Cosmic Gamma rays: Present Status of Theory and Observations". In: *nature physical science* 241 (1973).

[38] V.S. Berezinsky and G.T. Zatsepin. "On the Origin of Cosmic Rays at High Energies". In: *Phys. Lett.* 28B (1969).

[39] HiRes Collaboration. "First Observation of the Greisen-Zatsepin-Kuzmin Suppression". In: *Phys.Rev.Lett.* 100 (2008).

[40] W. Pauli. "Open letter to the group of radioactive people at the Gauverein meeting in Tbingen". In: (2030).

[41] F. Wilson. “Fermi’s Theory of Beta Decay”. In: *American Journal of Physics* 36 (1968).

[42] C. L. Cowan et al. “Detection of the free neutrino: A Confirmation”. In: *Science* 124 (1956), pp. 103–104. DOI: 10.1126/science.124.3212.103.

[43] B. Pontecorvo. “Electron and Muon Neutrinos”. In: *Sov.Phys.JETP* 10 (1960).

[44] Royal Swedish Academy of Sciences. *Press Release: The 1995 Nobel Prize in Physics*. 1995.

[45] J. N. Bachall. “Solar Neutrinos I. Theoretical”. In: *Phys. Rev. Lett.* 12 (1964), pp. 300–302.

[46] Royal Swedish Academy of Sciences. *Press Release: The 2015 Nobel Prize in Physics*. 2015.

[47] F. Reines et al. “Evidence for high-energy cosmic-ray neutrino interactions”. In: *Phys. Rev. Lett.* 15 (1965), 429433.

[48] M. R. Krishnaswamy et al. “The Kolar Gold Fields Neutrino Experiment. II. Atmospheric Muons at a Depth of 7000 hg cm-2”. In: *Proceedings of the Royal Society of London. Series A, Mathematical and Physical Sciences* 323 (1971), pp. 511–522.

[49] Y. Fukuda et al. “Evidence for Oscillation of Atmospheric Neutrinos”. In: *Phys. Rev. Lett* 81 (1998).

[50] K. Hirata et al. “Observation of a Neutrino Burst from the Supernova SN 1987a”. In: *Phys. Rev. Lett.* 58 (1987). [,727(1987)], pp. 1490–1493. DOI: 10.1103/PhysRevLett.58.1490.

[51] T. J. Haines et al. “OBSERVATION OF A NEUTRINO BURST FROM SN1987A IN IMB”. In: *THE STANDARD MODEL. THE SUPERNOVA SN1987A. PROCEEDINGS, LEPTONIC SESSION OF THE 22ND RENCONTRES DE MORIOND, LES ARCS, FRANCE, MARCH 8-15, 1987. VOL. 1.* [,735(1987)]. 1987, pp. 735–

738. URL: http://inspirehep.net/record/255998/files/Pages_from_C87-03-08_735-738.pdf.

[52] E. N. Alekseev et al. "Detection of the Neutrino Signal From SN1987A in the LMC Using the Inr Baksan Underground Scintillation Telescope". In: *Phys. Lett.* B205 (1988), pp. 209–214. DOI: 10.1016/0370-2693(88)91651-6.

[53] K. Nomoto and T. Shigeyama. "Supernova 1987A: Constraints on the Theoretical Model". In: *Supernova 1987A in the Large Magellanic Cloud* 595 (1988), pp. 273–288.

[54] Eun-Suk Seo. "Measurement of galactic cosmic ray proton and helium spectra during the 1987 solar minimum". PhD thesis. Louisiana State U., 1991. URL: http://wwwlib.umi.com/dissertations/fullcit?p9200090.

[55] V. V. Akimov et al. "Measurements of the primary cosmic ray spectra in the 10-to-the-10 to 10-to-the-14 ev energy range from proton-1, 2, 3 satellites". In: *Conf. Proc.* C690825 (1969), pp. 517–520.

[56] A.V.Glushkov et al. "Energy Spectrum of Primary Cosmic Rays in the Energy Region of 10^{17} to 10^{20} eV by Yakutsk Array Data". In: *Proceedings of the 28th International Cosmic Ray Conference* (2003).

[57] R.M. Tennent. "The Haverah Park extensive air shower array". In: *Proceedings of the Physical Society* 92 (1967).

[58] Gustavo A. Medina-Tanco. "The Energy spectrum observed by the AGASA experiment and the spatial distribution of the sources of ultrahigh-energy cosmic rays". In: *Astrophys. J.* 510 (1999), p. L91. DOI: 10.1086/311814. arXiv: astro-ph/9810366 [astro-ph].

[59] R. M. Baltrusaitis et al. "THE UTAH FLY'S EYE DETECTOR". In: *Nucl. Instrum. Meth.* A240 (1985), pp. 410–428. DOI: 10.1016/0168-9002(85)90658-8.

[60] S. C. Corbato et al. “HiRes: A High resolution Fly’s Eye detector”. In: *Nucl. Phys. Proc. Suppl.* 28B (1992). [,36(1992)], pp. 36–39. DOI: 10.1016/0920-5632(92)90106-3.

[61] R. Pesce. “Measuring the spectrum of UHECR with the Pierre Auger Observatory”. In: *Nucl. Instrum. Meth.* A692 (2012), pp. 83–87. DOI: 10.1016/j.nima.2011.12.090.

[62] Andrew W. Strong, Igor V. Moskalenko, and Vladimir S. Ptuskin. “Cosmic-Ray Propagation and Interactions in the Galaxy”. In: *Annu. Rev. Nucl. Part. Sci.* 57 (2007).

[63] W. Baade and F. Zwicky. “Supernovae and Cosmic Rays”. In: *Proceedings of the National Academy of Sciences of the United States of America* 20 (1934).

[64] S.P. Swordy. “The Energy Spectra and Anisotropies of Cosmic Rays”. In: *Space Science Reviews* 99 (2001).

[65] W. Hanlon. “The Energy Spectrum of Ultra High Energy Cosmic Rays Measured By the Hgih Resolution Fly’s Eye Observatory in Stereoscopic Mode”. PhD thesis. University of Utah, 2008.

[66] M. Aguilar et al. “Observation of New Properties of Secondary Cosmic Rays Lithium, Beryllium, and Boron by the Alpha Magnetic Spectrometer on the International Space Station”. In: *Phys. Rev. Lett.* 120.2 (2018), p. 021101. DOI: 10.1103/PhysRevLett.120.021101.

[67] M. Meneguzzi, J. Audouze, and H. Reeves. “The production of the elements Li, Be, B by galactic cosmic rays in space and its relation with stellar observations”. In: *Astronomy and Astrophysics* 15 (1971), pp. 337 –359.

[68] Thomas K. Gaisser. *Cosmic Rays and Particle Physics*. Caimbridge University Press, 1990. ISBN: 978-0521339315.

[69] P.S. Swordy et al. "Relative Abundances of Secondary and Primary Cosmic Rays at High Energies". In: *Proceedings of the 21st International Cosmic Ray Conference* 3 (1990).

[70] K. Lodders. *Solar system abundances of the elements*. University Lecture. 2010.

[71] P. Goret et al. "A comparison of the elemental abundances in the cosmic ray sources with local galactic and solar energetic particle abundances". In: *International Cosmic Ray Conference, 17th, Paris, France* 9 (1981).

[72] J.S. George et al. "Elemental Composition and Energy Spectra of Galactic Cosmic Rays During Solar Cycle 23". In: *Astrophysics Journal* 698 (2009).

[73] C. Patrignani et al. *The Review of Particle Physics*. Vol. 40. Chin. Phys. C, 2014.

[74] Michael Unger. "Cosmic Rays above the Knee". In: *Invited talk at the 21st European Cosmic Ray Symposium* (2008).

[75] R. Aloisio et al. "A dip in the UHECR spectrum and the transition from galactic to extragalactic cosmic rays". In: *Astropart. Phys.* 27 (2007), pp. 76–91. DOI: 10.1016/j.astropartphys.2006.09.004. arXiv: astro-ph/0608219 [astro-ph].

[76] D. Hooper, S. Sarkar, and A. M. Taylor. "The intergalactic propagation of ultra-high energy cosmic ray nuclei". In: *Astropart.Phys* 27 (2007), pp. 199–212.

[77] R. Aloisioa, V. Berezinsky, and A. Gazizov. "Transition from galactic to extra-galactic cosmic rays". In: *Astroparticle Physics* (2012).

[78] Greisen, Zatsepin, and Kuzmin. "Upper Limit of the Spectrum of Cosmic Rays". In: *Journal of Experimental and Theoretical Physics Letters* 4 (1066), pp. 78–80.

[79] W. D. Apel et al. "Reconstruction of the energy and depth of maximum of cosmic-ray air-showers from LOPES radio measurements". In: *Physical Review D* 47 (2014), pp. 142–153.

[80] Roger Blandford and David Eichler. “Particle Acceleration at Astrophysical Shocks: A Theory of Cosmic Ray Origin”. In: *Physics Reports* 154 (1987).

[81] V.L. Ginzburg and Nauk Usp. Fiz. In: *Sov. Phys, Usp.* 51 (1953).

[82] Luis Alfredo Anchordoqui. “Ultrahigh Energy Cosmic Rays: Facts, Myths, and Legends”. In: *6th CERN-Latin-American School of High-Energy Physics, Natal, Brazil* (2011).

[83] F. Fraschetti. “On the acceleration of ultra-high-energy cosmic rays”. In: *Phil. Trans. R. Soc. A* 366 (2008).

[84] H. J. de Vega and N. Sanchez. “Extreme Energy Cosmic Rays: Bottom-up vs. Top-down Scenarii”. In: *Fourth International Workshop on New Worlds in Astroparticle Physics* (2002).

[85] M. Kachelriess. “Lecture notes on high energy cosmic rays”. In: *17th Jyvaskyla Summer School* (2008).

[86] M. S. Longair. *High Energy Astrophysics, Vol. 2: Stars, the Galaxy and the Interstellar Medium*. Cambridge University Press, 2008.

[87] M. Bustamante et al. “High-energy Cosmic-Ray Acceleration”. In: *CERN Latin American School on High Energy Physics* (2009). eprint: https://cdsweb.cern.ch/record/1249755/files/p533.pdf.

[88] *CERN Document Server*. URL: http://cds.cern.ch/record/1342390/plots.

[89] P.O. Lagage and C.J. Cesarsky. “The maximum energy of cosmic rays accelerated by supernova shocks”. In: *Astronomy and Astrophysics* 125 (1983), pp. 249–257.

[90] S. Thoudam et al. “Cosmic-ray energy spectrum and composition up to the ankle: the case for a second Galactic component”. In: *Astronomy & Astrophysics* 595 (2016).

[91] K. M. Schure et al. "Diffusive Shock Acceleration and Magnetic Field Amplification". In: *Space Sci Rev* 173 (2012), pp. 491–519. DOI: 10.1007/s11214-012-9871-7.

[92] T. Antoni et al. "KASCADE measurements of energy spectra for elemental groups of cosmic rays: Results and open problems". In: *Astropart.Phys* 24 (2005), pp. 1–25. DOI: 10.1016/j.astropartphys.2005.04.001.

[93] V. Ptuskin. "Cosmic ray transport in the Galaxy". In: *Journal of Physics: Conference Series* 47 (2006). eprint: http://www.cosmic-ray.org/conf/papers/014_cosmic2005.pdf.

[94] A. Meli. "Relativistic Jets and Cosmic Ray Acceleration". In: *European Conference on Laboratory Astrophysics* 58 (2012), pp. 27–31.

[95] Rafael Alves Batista et al. "CRPropa 3 - a Public Astrophysical Simulation Framework for Propagating Extraterrestrial Ultra-High Energy Particles". In: *JCAP* (2016).

[96] Vladimir Ptuskin. "Propagation of galactic cosmic rays". In: *Astroparticle Physics* 39-49 (2012), 4451.

[97] V.L. Ginzburg and S.I. Syrovatskii. *The Origin of Cosmic Rays*. Pergamon Press and Macmillan Company, 1964. ISBN: 978-0080108582.

[98] H. S. Ahn et al. "MEASUREMENTS OF THE RELATIVE ABUNDANCES OF HIGH-ENERGY COSMIC-RAY NUCLEI IN THE TeV/NUCLEON REGION". In: *Astrophys. J.* 715.2 (2010), pp. 1400–1407. DOI: 10.1088/0004-637X/715/2/1400.

[99] S. Karajula and W. Tkaczyk. "The formation of the cosmic ray energy spectrum by a photon field". In: *Astroparticle Physics* 1 (1993), pp. 229–237.

[100] D. Kuempel. "Extragalactic Propagation of Ultra-High Energy Cosmic Rays". In: *astro-ph.HE* (2014).

[101] T.Stanev. “Neutrino production by UHECR proton interactions in the infrared background”. In: *Physics Letters B* 595 (2004), pp. 50–54. DOI: 10.1016/j.physletb.2004.05.075.

[102] S. H. Sposato. “The Trans-Iron Galactic Element Recorder (TIGER): A Balloon-borne Cosmic-Ray Experiment”. In: *Proceedings of the 26th International Cosmic Ray Conference* (1999).

[103] W. R. Binns et al. “The SuperTIGER Instrument: Measurement of Elemental Abundances of Ultra-Heavy Galactic Cosmic Rays”. In: *Astrophys. J.* 788 (2014), p. 18. DOI: 10.1088/0004-637X/788/1/18.

[104] H. S. Ahn et al. “MEASUREMENTS OF THE RELATIVE ABUNDANCES OF HIGH-ENERGY COSMIC-RAY NUCLEI IN THE TeV/NUCLEON REGION”. In: *Astrophys. J.* 715.2 (2010), pp. 1400–1407. DOI: 10.1088/0004-637X/715/2/1400.

[105] Y. S. Yoon et al. “Cosmic-Ray Proton and Helium Spectra from the First CREAM Flight”. In: *Astrophys. J.* 728 (2011), p. 122. DOI: 10.1088/0004-637X/728/2/122. arXiv: 1102.2575 [astro-ph.HE].

[106] M. Boezio et al. “The space experiment PAMELA”. In: *Nucl. Phys. Proc. Suppl.* 134 (2004). [,39(2004)], pp. 39–46. DOI: 10.1016/j.nuclphysbps.2004.08.006.

[107] F. Barao. “AMS: Alpha Magnetic Spectrometer on the International Space Station”. In: *Nucl. Instrum. Meth.* A535 (2004), pp. 134–138. DOI: 10.1016/j.nima.2004.07.196.

[108] R. Battiston. “The Alpha Magnetic Spectrometer (AMS)”. In: *Nucl. Instrum. Meth.* A409 (1998), pp. 458–463. DOI: 10.1016/S0168-9002(98)00126-0.

[109] J. Abraham et al. “Observation of the Suppression of the Flux of Cosmic Rays above 4 x 10^{19} eV”. In: *Physical Review Letters* 101.6 (2008). DOI: http://dx.doi.org/10.1103/PhysRevLett.101.061101.

[110] Telescope Array Collaboration. "Telescope Array Experiment". In: *Nuclear Physics B* 175-176 (2008), 221226.

[111] P. Tinyakov. "Latest results from the telescope array". In: *Nuclear Instruments and Methods in Physics Research A* 742 (2014), pp. 29–34.

[112] S. F. Berezhnev et al. "Energy spectrum and mass composition of cosmic rays, by the data of the Tunka-133 array". In: *Bull. Russ. Acad. Sci. Phys.* 79.3 (2015). [Izv. Ross. Akad. Nauk Ser. Fiz.79,no.3,377(2015)], pp. 344–347. DOI: 10.3103/S1062873815030090.

[113] Frank G. Schroder. "Radio detection of Cosmic-Ray Air Showers and High-Energy Neutrinos". In: *Progress in Particle and Nuclear Physics* (2016).

[114] M. G. Aartsen et al. "Measurement of the cosmic ray energy spectrum with IceTop-73". In: *Phys.Rev.D* 88 (2013), p. 042004. DOI: 10.1103/PhysRevD.88.042004.

[115] W.M. Yao et al. (Particle Data Group). "Review of Particle Physics: Quarks". In: *Journal of Physics G.* 33 (2013), p. 1. DOI: 10.1088/0954-3899/33/1/001. eprint: http://pdg.lbl.gov/2006/reviews/quarkmodrpp.pdf.

[116] D. Griffiths. *Introduction to Elementary Particles*. 2nd ed. Wiley, 2008. ISBN: 978-3-527-40601-2.

[117] J. Konya and N. Nagy. *Nuclear and Radiochemistry*. 1st ed. Elsevier, 2012. ISBN: 9780123914309.

[118] N. Jelle, A. B. McDonald, and R.G. Hamish Robertson. "The Sudbury Neutrino Observatory". In: *Annu. Rev. Nucl. Part. Sci.* 59 (2009), pp. 431–465.

[119] Z. Maki, M. Nakagawa, and S. Sakata. "Remarks on the Unified Model of Elementary Particles". In: *Progress of Theoretical Physics* 28 (1962), pp. 870–880.

[120] L. Wolfenstein. "Neutrino Oscillations in Matter". In: *Phys. Rev.* D17 (1978), pp. 2369–2374. DOI: 10.1103/PhysRevD.17.2369.

[121] W.C. Haxon. "Neutrino Astrophysics". In: *Nuclear Theory* (2008).

[122] U. F. Katz and Ch. Spiering. "High-Energy Neutrino Astrophysics: Status and Perspectives". In: *Prog. Part. Nucl. Phys.* 67 (2012), pp. 651–704. DOI: 10.1016/j.ppnp.2011.12.001. arXiv: 1111.0507 [astro-ph.HE].

[123] J. Bahcall. "Solar Neutrinos: A Popular Account". In: *Encyclopedia of Physics*. Ed. by (Wiley-VCH. 3rd ed. 2005. URL: arXiv:physics/0411190.

[124] B. T. Cleveland et al. "Measurement of the solar electron neutrino flux with the Homestake chlorine detector". In: *Astrophys. J.* 496 (1998), pp. 505–526. DOI: 10.1086/305343.

[125] SNO Collaboration. "Direct Evidence for Neutrino Flavor Transformation from Neutral-Current Interactions in the Sudbury Neutrino Observatory". In: *Phys. Rev. Lett.* 89 (2002). DOI: https://doi.org/10.1103/PhysRevLett.89.011301.

[126] D. Casper et al. "Measurement of atmospheric neutrino composition with the IMB-3 detector." In: *Phys. Rev. Lett.* 66 (1991), pp. 2561–2564.

[127] Y. Fukuda et al. "Atmospheric ν_μ/ν_e ratio in the multi-GeV energy range". In: *Phys. Lett. B* 335 (1994), 237245.

[128] Takaaki Kajita. "Atmospheric neutrinos and discovery of neutrino oscillations". In: *Proc. Jpn. Acad. Ser. B Phys. Biol. Sci.* 86 (2010), 303321. DOI: 10.2183/pjab.86.303.

[129] T. Stanev T.K. Gaisser F. Halzen. "Particle astrophysics with high energy neutrinos". In: *Physics Reports* 258 (1995), pp. 173–236.

[130] E. Waxman. "Viewpoint: The Beginning of Extra-Galactic Neutrino Astronomy". In: *Physics* 7 (2014).

[131] M. G. Aartsen et al. "Observation of High-Energy Astrophysical Neutrinos in Three Years of IceCube Data". In: *Phys. Rev. Lett.* 113 (2014), p. 101101. DOI: 10.1103/PhysRevLett.113.101101. arXiv: 1405.5303 [astro-ph.HE].

[132] M. G. Aartsen et al. "The IceCube Neutrino Observatory - Contributions to ICRC 2015 Part II: Atmospheric and Astrophysical Diffuse Neutrino Searches of All Flavors". In: *Proceedings, 34th International Cosmic Ray Conference (ICRC 2015): The Hague, The Netherlands, July 30-August 6, 2015*. 2015. arXiv: 1510.05223 [astro-ph.HE]. URL: http://inspirehep.net/record/1398539/files/arXiv:1510.05223.pdf.

[133] F.W. Stecker. "Cosmic Physics: The High Energy Frontier". In: *Journal of Physics G* 29 (2003).

[134] V. Berezinsky. "Extragalactic cosmic rays and their signatures". In: *Astropart. Phys.* 53 (2014), pp. 120–129.

[135] Amy Connolly and Abigail G. Vieregg. "Radio Detection of High Energy Neutrinos". In: 2017, pp. 217–240. DOI: 10.1142/9789814759410_0015. arXiv: 1607.08232 [astro-ph.HE]. URL: http://inspirehep.net/record/1478333/files/arXiv:1607.08232.pdf.

[136] Y. Fukuda et al. "Evidence for Oscillation of Atmospheric Neutrinos". In: *Phys. Rev. Lett.* 81 (1998).

[137] S. Fukuda et al. "Constraints on Neutrino Oscillations Using 1258 Days of Super-Kamiokande Solar Neutrino Data". In: *Phys. Rev. Lett* 86 (2001).

[138] IceCube Collaboration. "Evidence for High-Energy Extraterrestrial Neutrinos at the IceCube Detector". In: *Science* 342 (2013).

[139] IceCube Collaboration. "Probing the origin of cosmic-rays with extremely high energy neutrinos using the IceCube Observatory". In: *Physical Review D* 88 (2013).

[140] IceCube Collaboration. "Search for dark matter annihilations in the Sun with the 79-string IceCube detector". In: *Phys. Rev. Lett.* 110 (2013).

[141] IceCube Collaboration. *IceCube South Pole Neutrino Observatory*. 2016. URL: https://icecube.wisc.edu/ (visited on 2016).

[142] S. Adrin-Martnez et al. "Letter of Intent for KM3NeT 2.0". In: *Journal of Physics G: Nuclear and Particle Physics* 43 (2016).

[143] KM3NeT collaboration. *KM3NeT the next generation neutrino telescope*. 2016. URL: https://www.km3net.org/ (visited on 2016).

[144] S. Soucatos. "ANTARES, a large underwater neutrino detector". In: *Phys. Atom. Nucl.* 61 (1998). [Yad. Fiz.61,989(1998)], pp. 897–909.

[145] I. A. Belolaptikov et al. "The Baikal underwater neutrino telescope: Design, performance and first results". In: *Astropart. Phys.* 7 (1997), pp. 263–282. DOI: 10.1016/S0927-6505(97)00022-4.

[146] T. Huege. "Radio detection of cosmic ray air showers in the digital era". In: *Phys. Rept.* 620 (2016), pp. 1–52. DOI: 10.1016/j.physrep.2016.02.001. arXiv: 1601.07426 [astro-ph.IM].

[147] K.D. de Vries et al. "Coherent Cherenkov Radiation from Cosmic-Ray-Induced Air Showers". In: *Phys.Rev.Lett.* 107 (2011). DOI: 10.1103/PhysRevLett.107.061101.

[148] T.J. Stubbs. "Evidence of Radio–224 ,Pulses at 2 MHz fr,om Cosmic Ray Air Showers". In: *Nature* 230 (1971). DOI: 10.1038/physci230172a0.

[149] D.J. Fegan and D.M. Jennings. "UHF Radio Pulses from the Zenith associated with Extensive Air Showers". In: *Nature* 223 (1969). DOI: 10.1038/223722a0.

[150] Fruin J. H. Charman W. N. and Jelley. In: *Canad. J. Phys.* 46 (1968), p. 220.

[151] H.R. Allan, R.W. Clay, and J.K. Jones. "Radio Pulses from Extensive Air Showers". In: *Nature* 227 (1970). DOI: 10.1038/2271116a0.

[152] F. Kakimoto et al. In: *Proceedings of the 22nd ICRC* (1991).

[153] C. Castagnoli et al. In: *Proc. 23rd ICRC (Calgary)* 4 (1993), pp. 258–261.

[154] F. D. Kahn and I. Lerche. “Radiation from cosmic ray air showers”. In: *Proceedings of the Royal Society of London A: Mathematical, Physical and Engineering Sciences* 289.1417 (1966), pp. 206–213. ISSN: 0080-4630. DOI: 10.1098/rspa.1966.0007. eprint: http://rspa.royalsocietypublishing.org/content/289/1417/206.full.pdf.

[155] F. Halzen, E. Zas, and T. Stanev. “Radiodetection of cosmic neutrinos: A Numerical, real time analysis”. In: *Phys. Lett.* B257 (1991), pp. 432–436. DOI: 10.1016/0370-2693(91)91920-Q.

[156] J. Alvarez-Muniz, R. A. Vazquez, and E. Zas. “Calculation methods for radio pulses from high-energy showers”. In: *Phys. Rev.* D62 (2000), p. 063001. DOI: 10.1103/PhysRevD.62.063001. arXiv: astro-ph/0003315 [astro-ph].

[157] Soebur Razzaque et al. “Coherent radio pulses from GEANT generated electromagnetic showers in ice”. In: *Phys. Rev.* D65 (2002), p. 103002. DOI: 10.1103/PhysRevD.65.103002. arXiv: astro-ph/0112505 [astro-ph].

[158] Roman V. Buniy and John P. Ralston. “Radio detection of high-energy particles: Coherence versus multiple scales”. In: *Phys. Rev.* D65 (2002), p. 016003. DOI: 10.1103/PhysRevD.65.016003. arXiv: astro-ph/0003408 [astro-ph].

[159] Heino Falcke and Peter Gorham. “Detecting radio emission from cosmic ray air showers and neutrinos with a digital radio telescope”. In: *Astropart. Phys.* 19 (2003), pp. 477–494. DOI: 10.1016/S0927-6505(02)00245-1. arXiv: astro-ph/0207226 [astro-ph].

[160] O. Scholten, K. Werner, and F. Rusydi. “A Macroscopic Description of Coherent Geo-Magnetic Radiation from Cosmic Ray Air Showers”. In: *Astropart. Phys.* 29 (2008), pp. 94–103. DOI: 10.1016/j.astropartphys.2007.11.012. arXiv: 0709.2872 [astro-ph].

[161] T. Huege, M. Ludwig, and C. W. James. "Simulating radio emission from air showers with CoREAS". In: *AIP Conf. Proc.* 1535 (2013), p. 128. DOI: 10.1063/1.4807534. arXiv: 1301.2132 [astro-ph.HE].

[162] Jaime Alvarez-Muniz, Washington R. Carvalho Jr., and Enrique Zas. "Monte Carlo simulations of radio pulses in atmospheric showers using ZHAireS". In: *Astropart. Phys.* 35 (2012), pp. 325–341. DOI: 10.1016/j.astropartphys.2011.10.005. arXiv: 1107.1189 [astro-ph.HE].

[163] Marianne Ludwig and Tim Huege. "REAS3: Monte Carlo simulations of radio emission from cosmic ray air showers using an 'end-point' formalism". In: *Astropart. Phys.* 34 (2011), pp. 438–446. DOI: 10.1016/j.astropartphys.2010.10.012. arXiv: 1010.5343 [astro-ph.HE].

[164] S. J. Sciutto. "AIRES: A System for air shower simulations. User's guide and reference manual. Version 2.2.0". In: (1999). arXiv: astro-ph/9911331 [astro-ph].

[165] W. Ralph Nelson, H. Hirayama, and David W. O. Rogers. "The Egs4 Code System". In: (1985).

[166] Stephen Hoover. "A Search for Ultrahigh-Energy Neutrinos and Measurement of Cosmic Ray Radio Emission with the Antarctic Impulsive Transient Antenna". PhD thesis. University of California Los Angeles, 2010.

[167] A. Javaid. "Monte Carlo simulation for radio detection of Ultra High Energy air shower cores by ANITA-II". PhD thesis. University of Delaware, 2012.

[168] S. Barwick et al. In: *J.Glaciol.* 51 (2005), p. 173.

[169] Andrea Silvestri et al. "Status of ANITA and ANITA-lite". In: *NATO Sci. Ser. II* 209 (2005). [,297(2004)], pp. 297–306. DOI: 10.1007/1-4020-3748-1_23. arXiv: astro-ph/0411007 [astro-ph].

[170] O. Kalashev et al. "Ultrahigh-energy cosmic rays. Propagation in the galaxy and anisotropy". In: *Mod.Phys.Lett A* 16 (2001), pp. 2505–2515. DOI: astro-ph/0006349.

[171] H. Schoorlemmer et al. “Energy and Flux Measurements of Ultra–High Energy Cosmic Rays Observed During the First ANITA Flight”. In: *astro–ph.HE* (2016). DOI: 10.1016/j.astropartphys.2016.01.001.

[172] P. W. Gorham et al. “Characteristics of Four Upward-pointing Cosmic-ray-like Events Observed with ANITA”. In: *Phys. Rev. Lett.* 117.7 (2016), p. 071101. DOI: 10.1103/PhysRevLett.117.071101. arXiv: 1603.05218 [astro-ph.HE].

[173] T. Antoni et al. “The Cosmic ray experiment KASCADE”. In: *Nucl. Instrum. Meth.* A513 (2003), pp. 490–510. DOI: 10.1016/S0168-9002(03)02076-X.

[174] D. Ardouin et al. “Radio-Detection Signature of High Energy Cosmic Rays by the CODALEMA Experiment”. In: *Nucl. Instrum. Meth.* A555 (2005), p. 148. DOI: 10.1016/j.nima.2005.08.096. arXiv: astro-ph/0504297 [astro-ph].

[175] Herv Carduner et al. “The CODALEMA/EXTASIS experiment: Contributions to the 35th International Cosmic Ray Conference (ICRC 2017)”. In: (2017). arXiv: 1710.02487 [astro-ph.HE].

[176] S. Thoudam et al. “Measurement of the cosmic-ray energy spectrum above 1016 eV with the LOFAR Radboud Air Shower Array”. In: *Instrumentation and Methods for Astrophysics* (2015). DOI: 10.1016/j.astropartphys.2015.06.005.

[177] S. Buitink et al. “A large light-mass component of cosmic rays at 10^{17} – $10^{17.5}$ eV from radio observations”. In: *Nature* 531 (2016), p. 70. DOI: 10.1038/nature16976. arXiv: 1603.01594 [astro-ph.HE].

[178] Astronomy institute Netherlands Institute for Radio Astronomy Astron. 2016. URL: http://www.astron.nl/general/lofar/lofar.

[179] The ARIANNA Collaboration. “A First Search for Cosmogenic Neutrinos with the ARIANNA Hexagonal Radio Array”. In: *Astropart.Phys.* 70 (2015), pp. 12–26. DOI: 10.1016/j.astropartphys.2015.04.002.

[180] Matt Williams. *What is Lunar Regolith?* URL: http://www.universetoday.com/20360/lunar-regolith/.

[181] Justin Bray et al. "Lunar detection of ultra-high-energy cosmic rays and neutrinos with the Square Kilometre Array". In: *PoS* AASKA14 (2015), p. 144.

[182] O. Scholten et al. "Detecting UHE Cosmics and Neutrinos off the Moon". In: *Journal of Physics, Conference Proceedings* (2006). DOI: arXiv:astro-ph/0609179v2.

[183] M.H. Reno C. Quigg and T.P. Walker. "Interactions of Ultrahigh-Energy Neutrinos". In: *Phys. Rev. Lett.* 57 (1986).

[184] O.C. Alkofer. "Introduction to Cosmic Radiation". In: *Verlag Karl Thiemig* (1975).

[185] W. Heitler. *The Quantum Theory of Radiation, third ed.* Oxford University Press, 1954.

[186] E. Longo and I.Sestili. "Monte Carlo calculation of photon-initiated electromagnetic showers in lead glass". In: *Nucl. Instrum. Methods* 128 (1975), pp. 283–307.

[187] W.R. Nelson et al. "Electron Induced Cascade showers in Copper and Lead at 1 GeV". In: *Phys. Rev.* 149 (1966), pp. 201–208.

[188] K. Kamata and J. Nishimura. "The Lateral and the Angular Structure Functions of Electron Shower". In: *Prog. Theoret. Phys. Suppl* 6 (1958), p. 93.

[189] S.Lafebre et al. "Universality of electronpositron distributions in extensive air showers". In: *Astroparticle Physics* 31 (2009), pp. 243–254. DOI: 10.1016/j.astropartphys.2009.02.002.

[190] R. Engel R. Ulrich and M. Unger. "Hadronic multiparticle production at ultrahigh energies and extensive air showers". In: *Phys. Rev. D* 83 (2011). DOI: 10.1103/PhysRevD.83.054026.

[191] J. Matthews. "A Heitler model of extensive air showers". In: *Astroparticle Physics* 22 (2004).

[192] et al. S. Razzaque. "Signal Characteristics from Electromagnetic Cascades in Ice". In: *AIP Conference Proceedings* 579 (2001), p. 1390146.

[193] L. Landau, I. Pomeranchuk, and Dokl. Akad. Nauk. "Electron-cascade processes at very high energies". In: *SSSR* 92 (1953).

[194] T. Stanev et al. "DEVELOPMENT OF ULTRAHIGH-ENERGY ELECTROMAGNETIC CASCADES IN WATER AND LEAD INCLUDING THE LANDAU-POMERANCHUK-MIGDAL EFFECT". In: *Phys. Rev.* D25 (1982), pp. 1291–1304. DOI: 10.1103/PhysRevD.25.1291.

[195] John David Jackson. *Classical Electrodynamics*. Wiley, 1998. ISBN: 978–0471309321.

[196] Jaime Alvarez-Muniz, Andres Romero-Wolf, and Enrique Zas. "Practical and accurate calculations of Askaryan radiation". In: *Phys.Rev. D* 84 (2011).

[197] Jaime Alvarez, Andres Romero Wolf, and Enrique Zas. "Cherenkov radio pulses from electromagnetic showers in the time-domain". In: *Phys.Rev. D* (2010). DOI: Phys.Rev.D81:123009.

[198] P.A. Cherenkov. "Visible emission of clean liquids by action of radiation". In: *Doklady Akademii Nauk SSSR* 451 (1934).

[199] H. Falcke, P. Gorham, and R.J. Protheroe. "Prospects for radio detection of ultra-high energy cosmic rays and neutrinos". In: *New Astron.Rev.* 48 (2004). DOI: 10.1016/j.newar.2004.09.028.

[200] A. Aab et al. (Pierre Auger Collaboration). "Testing Hadronic Interactions at Ultrahigh Energies with Air Showers Measured by the Pierre Auger Observatory". In: *Phys. Rev. Lett.* 117 (2016). DOI: 10.1103/PhysRevLett.117.192001.

[201] D. Heck et al. "CORSIKA: A Monte Carlo code to simulate extensive air showers". In: *FZKA 6019* (1998).

[202] Geant4 Collaboration. "Geant4a simulation toolkit". In: *Nuclear Instruments and Methods in Physics Research Section A* (2003).

[203] E. Zas et al. "Radiodetection of cosmic neutrinos. A numerical, real time analysis". In: *Phys. Rev. B* 257 (1991).

[204] T. Huege et al. "General description of electromagnetic radiation processes based on instantaneous charge acceleration in endpoints". In: *Phys.Rev. E* (2011). DOI: 10.1103/PhysRevE.84.056602.

[205] Klaus Werner and Olaf Scholten. "Macroscopic Treatment of Radio Emission from Cosmic Ray Air Showers based on Shower Simulations". In: *Astropart. Phys.* 29 (2008), pp. 393–411. DOI: 10.1016/j.astropartphys.2008.04.004. arXiv: 0712.2517 [astro-ph].

[206] T. Huege et al. "The convergence of EAS radio emission models and a detailed comparison of REAS3 and MGMR simulations". In: *roceedings of the ARENA2010 conference,* (2010).

[207] J. Alvarez-Muniz and E. Zas. "Cherenkov radio pulses from EeV neutrino interactions: the LPM effect". In: *Phys.Lett. B* 411 (1997).

[208] Time Huege. "The renaissance of radio detection of cosmic rays". In: *Proceedings of the 33rd International Cosmic Rays Conference* (2013).

[209] F.G. Schroeder and Pierre Auger Collaboration. "A Comparison of LOPES Lateral Distributions of the Air-shower Radio Signal with REAS 3.11 and CoREAS Simulations". In: *Proceedings of the 33rd International Cosmic Rays Conference* (2013).

[210] S. Hoover et al. "Observation of Ultrahigh-Energy Cosmic Rays with the ANITA Balloon-Borne Radio Interferometer". In: *Nature* 435 (2005). DOI: 0.1038/nature03614.

[211] *SLAC National Accelerator Laboratory.* 2015. URL: https://www6.slac.stanford.edu/about/slac-overview.aspx.

[212] M. Tigner and F. Zimmermann. *Handbook of Accelerator Physics and Engineering*. World Scientific Publishing Company, 2013. ISBN: 9814417173.

[213] D. Saeedkia. *Handbook of Terahertz Technology for Imaging, Sensing and Communications*. WP Woodhead Publishing, 2013. ISBN: 0857092359.

[214] Anne Zilles. "Emission of Radio Waves in Particle Showers: Validation of microscopic simulations with the SLAC T-510 experiment and their potential in the future Square Kilometre Array". PhD thesis. Karlsruhe Institute of Technology, 2016. DOI: 10.5445/IR/1000065046.

[215] D. Williams. "The Askaryan Effect and Detection of Ex-tremely High Energy Neutrinos in the Lunar Regolth and Salt". PhD thesis. University of California, Los Angeles, 2004.

[216] Nikolai G. Lehtinen et al. "FORTE satellite constraints on ultrahigh energy cosmic particle fluxes". In: *Phys.Rev. D* (2004). DOI: 10.1103/PhysRevD.69.013008.

[217] Wayne Storr. *Butterworth Filter Design*. URL: http://www.electronics-tutorials.ws/filter/filter_8.html.

[218] Konstantin Belov. "Radio emission from Air Showers. Comparison of theoretical approaches". In: *AIP Conf. Proc.* 1535 (2013), p. 157. DOI: 10.1063/1.4807540. arXiv: 1303.3313 [astro-ph.HE].

[219] Anne Zilles et al. "Modelling of radio emission in the SLAC T-510 Experiment using microscopic Geant4 simulations". In: *PoS* ICRC2015 (2016), p. 313.

[220] A. Nelles et al. "Measuring a Cherenkov ring in the radio emission from air showers at 110190 MHz with LOFAR". In: *Astropart. Phys.* 65 (2015), pp. 11–21. DOI: 10.1016/j.astropartphys.2014.11.006. arXiv: 1411.6865 [astro-ph.IM].

[221] A. Nelles et al. “The radio emission pattern of air showers as measured with LOFARa tool for the reconstruction of the energy and the shower maximum”. In: *JCAP* 1505.05 (2015), p. 018. DOI: 10.1088/1475-7516/2015/05/018. arXiv: 1411.7868 [astro-ph.HE].

[222] A. Corstanje et. al. “The shape of the radio wavefront of extensive air showers as measured with LOFAR”. In: *Astroparticle Physics* (2014).

[223] A. Vieregg. “The Search for Astrophysical Ultra-High Energy Neutrinos Using Radio-Detection Techniques”. PhD thesis. UCLA, 2010.

[224] M. Mottram. “A Search for Ultra-high Energy Neutrinos and Cosmic-Rays with ANITA-2”. PhD thesis. UCL, 2012.

[225] European Space Agency. *Multipath*. 2012. URL: http://www.navipedia.net/index.php/Multipath.

[226] John D. Kraus. *Antennas*. McGraw-Hill Companies, 1988. ISBN: 978-0070354227.

[227] Marshall Brain and Tom Harris. *How GPS Receivers Work*. 2006. URL: http://electronics.howstuffworks.com/gadgets/travel/gps.htm.

[228] *G12 OEM Board and Sensor Reference Manual*. 2002.